FLORIDA INTERNATIONAL UNIVERSITY

Miami, Florida

MEASUREMENT OF SINGLE SPIN ASYMMETRY AND FIFTH STRUCTURE FUNCTION FOR THE $p(\vec{e}, e'K^+)\Lambda$ REACTION WITH CEBAF LARGE ACCEPTANCE SPECTROMETER (CLAS)

A dissertation submitted in partial fulfillment of the

requirements for the degree of

DOCTOR OF PHILOSOPHY

in

PHYSICS

by

Rakhsha Nasseripour

2004

To: Dean R. Bruce Dunlap
. College of Arts and Sciences

This dissertation, written by Rakhsha Nasseripour, and entitled Measurement of Single Spin Asymmetry and Fifth Structure Function for the $p(\vec{e}, e'K^{+})\Lambda$ Reaction with CEBAF Large Acceptance Spectrometer (CLAS), having been approved in respect to style and intellectual content, is referred to you for judgment.

We have read this dissertation and recommend that it be approved.

Pete E.C. Markowitz

Elton Smith

Laird H. Kramer

Misak Sargsian

Brian A. Raue, Major Professor

Date of Defense: July 9, 2004

The dissertation of Rakhsha Nasseripour is approved.

Dean R. Bruce Dunlap
College of Arts and Sciences

Dean Douglas Wartzok
University Graduate School

Florida International University, 2004

.

.

DEDICATION

To the memory of my father who inspired me to be an independent woman and passed me the passion for learning and exploring the world.

ACKNOWLEDGMENTS

I didn't do it alone! Ever since I started my great journey in graduate career, I have been blessed with my friends' and family's support and I have met many wonderful people who have helped me going through the ups and downs. Their encouragement, support, and friendship have been the most important ingredient of surviving and accomplishing the hard work.

I cherish my mother's, Rakhshandeh, friendship and ceaseless support at my life decisions. Thank you mom, for your forbearance and for being always supportive and understanding of the necessity of my desire “to go”. My sister, Tiba, inspired me with her interest in science, encouragement, and forever affection, and her gifts too. Thank you!

I truly value the ever-lasting friendship, love, support and helpful deeds of my dear friends Mahdokht, Aida, Mahasty, and Maria, who have always been there for me, with their heart-warming support, encouragement, and understanding in difficult times. Thanks for believing in me and continuously sustaining me down the path to the “doctorhood”!

I would like to thank my major professor, Dr. Brian Raue, who has fostered my development in graduate career and directed my original steps toward my research work. It is impossible for me to relate the significance of his guidance, wisdom, patience, and support throughout my research work and graduate studies. He introduced me to the field of particle physics and kaon electroproduction experiments, helped me develop my research skills and launched me to the world of scientific research. His understanding nature and caring attitude has sustained me through the long and arduous dissertation process. He is a great mentor, colleague, and a true friend. Brian, thanks for being such a wonderful inspiring advisor, and for allowing me to continue my professional development at FIU for which I am truly grateful. My heartfelt thanks also go to your lovely wife, Patti, for her kindness, support, hosting wonderful parties, and helping me feel at home.

I have high esteem for Dr. Daniel Carman for his solid guidance that has been a significant contribution in my research work as he challenged me to meet high standards. Thanks Dan!

I wish to thank Dr. Elton Smith both for his integrated vision and comments throughout my dissertation work and as a member of my dissertation committee. Thank you Elton! It has been a great opportunity working with you.

Thanks go to Pawel Ambrozewicz, my friend and colleague whom I will always value his encouragement, openness to share his experience and knowledge, and good humor. And thanks for shooing the birds behind the window so I wouldn't envy their freedom!

My gratitudes go to the members of my dissertation committee, Dr. P. Markowitz, Dr. L. Kramer, and Dr. M. Sargsian, who have supported me academically and professionally. Thank you for your constructive criticism and comments throughout my graduate studies.

I would also like to recognize the invaluable support of the faculty and staff at the FIU physics department who have greatly contributed to the progress of my academic career.

My research was funded by Department of Energy and supported by Jefferson National Laboratory. I would like to thank Dr. Latifa Elouadrhiri, Dr. Volker Burkert, Dr. Bernhard Mecking, Dr. Mac Mestayer, and Dr. Kyungseon Joo and entire CLAS collaboration for allowing me the opportunity to work and develop my professional skills at Jefferson National Laboratory. It was a great experience, working at Jefferson Laboratory and making a lot of good friends...

.

"One sees clearly only with the heart. Anything essential is invisible to the eyes."

Antoine de Saint-Exupery

ABSTRACT OF THE DISSERTATION

MEASUREMENT OF SINGLE SPIN ASYMMETRY AND FIFTH STRUCTURE FUNCTION FOR THE $p(\vec{e}, e'K^+)\Lambda$ REACTION WITH CEBAF LARGE ACCEPTANCE SPECTROMETER (CLAS)

by

Rakhsha Nasseripour

Florida International University, 2004

Miami, Florida

Professor Brian A. Raue, Major Professor

The single spin asymmetry, $A_{LT'}$, and the polarized structure function, $\sigma_{LT'}$, for the $p(\vec{e}, e'K^+)\Lambda$ reaction in the resonance region have been measured and extracted using the CEBAF Large Acceptance Spectrometer (CLAS) at Jefferson Lab. Data were taken at an electron beam energy of 2.567 GeV. The large acceptance of CLAS allows for full azimuthal angle coverage over a large range of center-of-mass scattering angles. Results were obtained that span a range in Q^2 from 0.5 to 1.3 GeV^2 and W from threshold up to 2.1 GeV and were compared to existing theoretical calculations. The polarized structure function is sensitive to the interferences between various resonant amplitudes, as well as to resonant and non-resonant amplitudes. This measurement is essential for understanding the structure of nucleons and searching for previously undetected nucleon excited states (resonances) predicted by quark models. The W dependence of the $\sigma_{LT'}$ in the kinematic regions dominated by s and u channel exchange ($\cos\theta_k^{cm}$= -0.50, -0.167, 0.167) indicated possible resonance structures not predicted by theoretical calculations. The $\sigma_{LT'}$ behavior around $W =$

1.875 GeV could be the signature of a resonance predicted by the quark models and possibly seen in photoproduction. In the very forward angles where the reaction is dominated by the t-channel, the average $\sigma_{LT'}$ was zero. There was no indication of the interference between resonances or resonant and non-resonant amplitudes. This might be indicating the dominance of a single t-channel exchange. Study of the sensitivity of the fifth structure function data to the resonance around 1900 MeV showed that these data were highly sensitive to the various assumptions of the models for the quantum number of this resonance. This project was part of a larger CLAS program to measure cross sections and polarization observables for kaon electroproduction in the nucleon resonance region.

TABLE OF CONTENTS

LIST OF TABLES

TABLE PAGE

LIST OF FIGURES

FIGURE PAGE

1 Introduction

1.1 Strangeness Production

Study of the electromagnetic production of strange quarks, in the resonance region plays an important role in understanding the strong interaction processes. Currently, a number of experiments at TJNAF (Thomas Jefferson National Accelerator Facility) are involved in studies of kaon electroproduction in which strange hadrons are produced off non-strange baryon targets. Understanding the coupling of non-strange baryons to strange hadrons is of importance in understanding these processes and the development of theoretical models.

Kaon electroproduction in the $p(\vec{e}, e'K^+)\Lambda$ reaction involves the production of strange particles $\Lambda(uds)$ and $K^+(u\bar{s})$ in the final states via strange quark-pair ($s\bar{s}$) creation. While the quantum chromodynamic (QCD) description of quark interactions and creation is well accepted at high energies with perturbative theory, it cannot be used in the non-perturbative regimes that involve lower energies. Instead, a number of theoretical models have been developed to describe the quark-pair creation in these energy regimes. Most of these models describe the interaction as producing non-strange baryons that decay to a strange baryon and a strange meson. These states are called intermediate states including Born and resonant terms that couple to the final states particles.

"Hadrodynamic" models are the first class of these models in which, hadrons are considered as elementary particles and the strong hadronic decay is described in

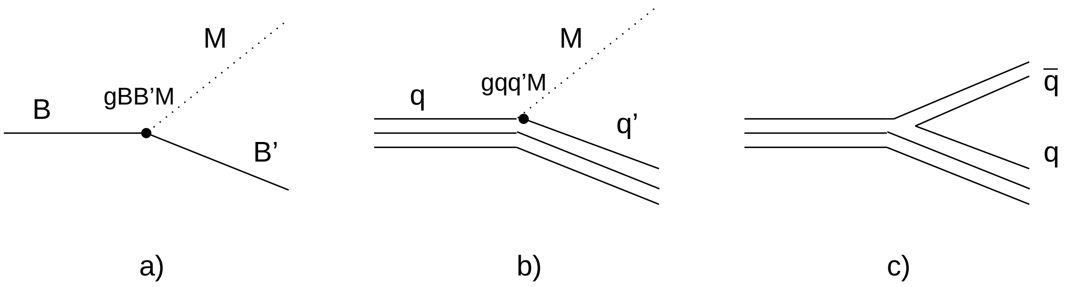

Figure 1: Baryon decay as an elementary meson emission from a baryon B (a), as an elementary meson emission from a quark q (b), and in a quark pair ($q\bar{q}$) creation model (c). $g_{BB'M}$ and $g_{qq'M}$ denote the couplings for baryon-meson and quark-meson vertices.

terms of phenomenological coupling constants while using SU(3) flavor symmetry arguments to obtain relationships between various couplings (Fig. 1(a)). These models are discussed in detail in section 1.3.

In the second class of theoretical models, the decay of baryons is considered to take place through "elementary meson emission" [1] which is illustrated in Fig. 1(b). In these types of models, the mesons are emitted from the quark lines.

The third class of models includes the "pair creation models" [2, 3]. In these models, the decay of the baryon is possible by the creation of a quark-antiquark pair in the hadronic medium. The quark of the created pair becomes part of the decay baryon while the antiquark of the created pair combines with a quark of the decaying baryon and creates a decay meson. (Fig.1(c)).

In a quark pair creation model, the intermediate baryonic spectrum is obtained by solving the Schrodinger equation in a space consisting of the valence quarks. A relativised Hamiltonian is used with a potential that includes the Coulomb, spin-spin, and spin-orbit interactions. The wave functions are obtained in a harmonic

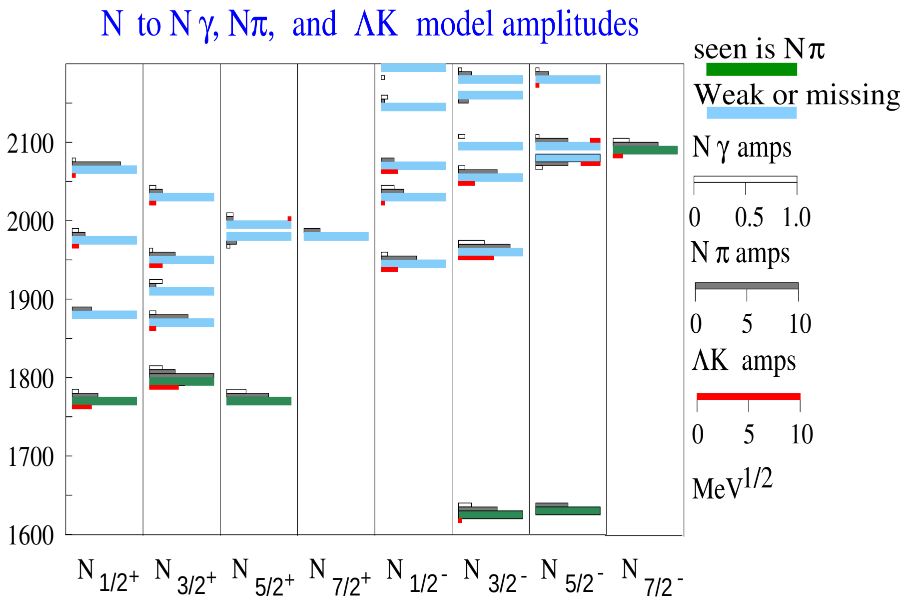

Figure 2: Quark Model predictions for nucleon resonances up to 2.2 GeV, sorted by spin and parity [4]. The bars show the location of the mass on the y-axis and the quantum number of the predicted resonance state, N_{JP}, on the x-axis where J and P denote the spin and parity of the state. The bars also show the status of establishment of these states, seen in Nπ (green), weak or missing (blue). The decay amplitudes for each state and decay channel is proportional to the length of the bars and are shown for $K\Lambda$ (red), Nπ (grey), and Nγ (white) decay channels.

oscillator basis and then particles are grouped according to their spin and parity. The wave functions for mesons and baryons are a product of terms including space, spin, flavor, and color. Thus, the models must include a considerable number of possible baryon and meson wave functions with many possible mixings.

Using the wave function described above, the decay amplitude $A \to BC$ for baryon A is evaluated by calculating the matrix element $M = \langle BC|T|A\rangle$, where T is the pair production operator [3]. Fig. 2 shows the prediction of a quark model by Capstick and Roberts [4] for ΛK decay amplitudes for nucleon resonances up to 2.2 GeV. Some of these states have been seen in pion production data but some of them are “missing” or have not yet been experimentally seen.

Because of the relatively high threshold for ΛK final states compared to πN and $\pi\pi N$, these decays are particularly important in searching for missing and undiscovered non-strange baryons (resonance states) with higher masses and negative parity. Furthermore, the density of states that decay to ΛK is less than πN which leads to a better chance of separating out individual states.

The fifth or polarized structure function is particularly sensitive to the interferences between these nucleonic resonances as well as to the interferences between resonant and non-resonant amplitudes. It can provide essential information in searching for evidence of missing resonances. It is sensitive to the small contributions of the background channels that are too small to be seen in the unpolarized cross section measurements. High-precision cross section and polarization measurements in kaon electroproduction experiments also provides information about the coupling of these resonances to final states like ΛK and ΣK and are essential for examining the structure of the nucleons.

1.2 Basic Electroproduction Formalism

1.2.1 Kinematics

The schematic of electroproduction of $K^+\Lambda$ off a fixed hydrogen target is given in Fig. 3. The angle between the incident and scattered electron is θ_e while the angle between the electron scattering plane and hadron production plane is defined as ϕ. In the one-photon exchange approximation, the interaction between the incident electron beam and the target proton is mediated by a virtual photon, γ^*. The virtual

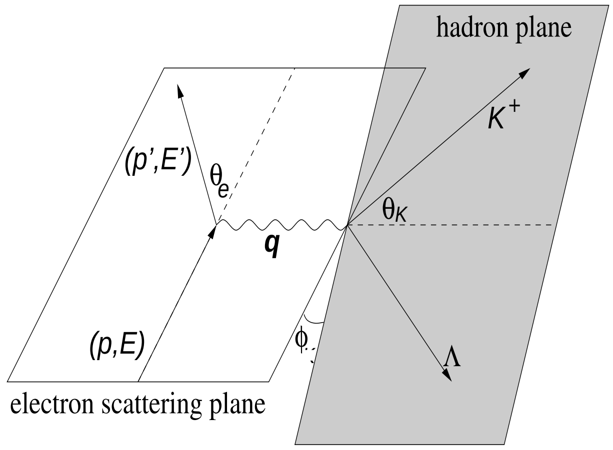

Figure 3: Kinematic diagram for kaon-hyperon electroproduction.

photon four momentum, is obtained from the difference between the four momenta of the incident, $e_\mu = (E, \mathbf{p}_e)$, and scattered electrons, $e'_\mu = (E', \mathbf{p}'_e)$ as:

$$q_\mu = e_\mu - e'_\mu = (\nu, \mathbf{q}) \tag{1}$$

The four momentum transfer squared, Q^2, is an invariant quantity:

$$Q^2 = -(q_\mu)^2 = -(\nu^2 - \mathbf{q}^2) = 4\mathrm{EE}' \sin^2(\theta_\mathrm{e}/2) \tag{2}$$

where

$$\nu = E - E' \tag{3}$$

is the energy transfer. The invariant mass of the intermediate hadronic state is defined as:

$$W^2 = s = (q_\mu + p_\mu)^2 = M_p^2 + 2M_p\nu - Q^2, \tag{4}$$

where p_μ is the four momentum of the target proton with the mass of M_p. Also, the invariant Mandelstam variables t and u are defined as:

$$t = (q_\mu - K_\mu)^2 = (p_\mu - Y_\mu)^2 = q_\mu^2 + K_\mu^2 - 2q_\mu.K_\mu \tag{5}$$

$$u = (q_\mu - Y_\mu)^2 = (p_\mu - K_\mu)^2 = q_\mu^2 + Y_\mu^2 - 2q_\mu.Y_\mu \tag{6}$$

where K_μ and Y_μ are the four momenta of the out going kaon and hyperon respectively. These two invariant variables can also be written in terms of the scattering angle of the out going kaon and hyperon, θ_K and θ_Y, as follows:

$$t = -Q^2 + M_K^2 - 2(\nu\sqrt{M_K^2 + |\mathbf{K}|^{\mathbf{2}}}) + 2|\mathbf{q}||\mathbf{K}|\cos\theta_{\mathrm{K}} \tag{7}$$

$$u = -Q^2 + M_Y^2 - 2(\nu\sqrt{M_Y^2 + |\mathbf{Y}|^{\mathbf{2}}}) + 2|\mathbf{q}||\mathbf{Y}|\cos\theta_{\mathrm{Y}} \tag{8}$$

Throughout this analysis we describe the kinematics of the reaction in terms of five variables, Q^2, W, ϕ, the angle between hadronic plane and electron scattering plane, θ_K^{cm}, the kaon angle in the center-of-mass frame with respect to the direction of the virtual photon momentum, and ϵ, the virtual photon polarization (see next section). W is the invariant energy available to the system, while the values of Q^2 show the level of deep inelasticity of the reaction. The θ_K^{cm} dependence of the cross section is related to the t dependence and also related to the multipoles that contribute to the final or intermediate states. The importance of the measurement of the ϕ angle is crucial for extracting the structure functions (see Sec. 1.2.2).

1.2.2 Cross Section

The cross section for the electromagnetic interaction of a relativistic electron beam with a hadron target is obtained by calculating the transition probability of the process. Fig. 4 shows the one-photon exchange diagram for electron scattering. The transition probability is given by the square of the scattering matrix S_{fi}, averaged over all the initial states and summed over the final states and over the spin of the outgoing electron [5]:

$$\begin{aligned}\sum_{spin}\bar{\sum_{i}}\int\sum_{f}|S_{fi}|^2 &= e^2e_T^2\frac{1}{Q^4}\sum_{\lambda\lambda'}\sum_{spin}j_\lambda j^*_{\lambda'}\bar{\sum_{i}}\int\sum_{f}J_\lambda J^*_{\lambda'}(2\pi)^4\delta^4(p_f-p_i-q)\\ &= 2\pi e^2e_T^2\frac{1}{Q^4}\sum_{\lambda\lambda'}\frac{1}{4EE'}L_{\lambda\lambda'}W_{\lambda\lambda'} \qquad (9)\end{aligned}$$

where j_λ and J_λ are the four-vector charge and current densities for the electron and the hadron, respectively. The cross section is obtained by multiplying Eq. 9 by the appropriate phase space and dividing by the incoming flux and can be written in the form of a contraction between leptonic and hadronic tensors that contain the electron variable and hadron variable separately, $L_{\lambda\lambda'}$ and $W_{\lambda\lambda'}$. This is very important since it will make it possible to study the electromagnetic probe and hadronic structure separately and clarify various aspects of the reaction mechanisms.

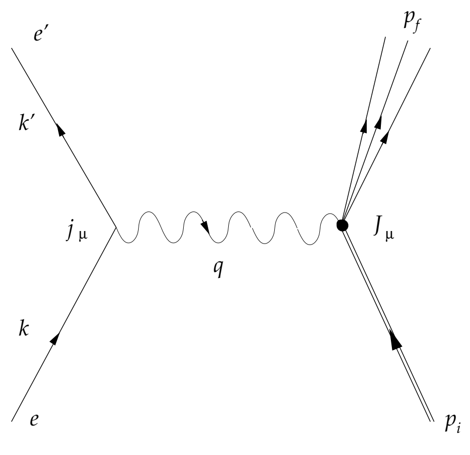

Figure 4: One-photon exchange diagram for electron scattering.

The explicit calculation of the lepton tensor components are tabulated in Appendix A as expressed in Ref. [5] for different processes. In general, the lepton tensor can be written in terms of a density matrix of virtual photon polarization,

ρ_{ab}, that contains a symmetric helicity-independent part and an anti-symmetric helicity-dependent part:

$$\rho_{ab} = \begin{pmatrix} \frac{1}{2}(1+\epsilon) & -ih\frac{1}{2}\sqrt{1-\epsilon^2} & -\frac{1}{\sqrt{2}}\sqrt{\epsilon_L(1+\epsilon)} \\ ih\frac{1}{2}\sqrt{1-\epsilon^2} & \frac{1}{2}(1-\epsilon) & -ih\frac{1}{\sqrt{2}}\sqrt{\epsilon_L(1-\epsilon)} \\ -\frac{1}{\sqrt{2}}\sqrt{\epsilon_L(1+\epsilon)} & ih\frac{1}{\sqrt{2}}\sqrt{\epsilon_L(1-\epsilon)} & \epsilon_L \end{pmatrix}$$

with $a, b = x, y, z$ and with the z axis along q. The polarization parameter, virtual photon transverse polarization component is defined as:

$$\epsilon = \left(1 + 2(1 + \frac{\nu^2}{Q^2}) \tan^2 \frac{\theta_e}{2}\right)^{-1} \tag{10}$$

and

$$\epsilon_L = \frac{Q^2}{\nu^2}\epsilon \tag{11}$$

is the longitudinal polarization component.

The anti-symmetric part contributes to the cross section only when the hadron tensor also contains an anti-symmetric part, which is the case of an unpolarized target and detection of the final state hadron in coincidence with the scattered electron. The anti-symmetric part vanishes for the case of unpolarized electrons ($h = 0$) and reduces the density matrix of the virtual photon to:

$$\rho_{ab} = \begin{pmatrix} \frac{1}{2}(1+\epsilon) & 0 & -\frac{1}{\sqrt{2}}\sqrt{\epsilon_L(1+\epsilon)} \\ 0 & \frac{1}{2}(1-\epsilon) & 0 \\ -\frac{1}{\sqrt{2}}\sqrt{\epsilon_L(1+\epsilon)} & 0 & \epsilon_L \end{pmatrix}$$

As seen, no helicity information can be obtained with an unpolarized electron beam.

The explicit calculation of the hadron tensor components, $W_{\lambda\lambda'}$, is more complicated and depends on the specific process under investigation. They are usually written in terms of functions of independent kinematical variables that describe the internal structure of the hadrons or "structure functions" [5].

Following the notation of Ref. [6, 7], the differential cross section for electroproduction in the center-of-mass frame is given by:

$$\frac{d^5\sigma}{dE' d\Omega'_e d\Omega_K} = \Gamma_\nu \frac{d\sigma_\nu}{d\Omega_K} \tag{12}$$

where Γ_ν is the virtual photon flux given by

$$\Gamma_\nu = \frac{\alpha}{4\pi^2}\frac{kE'}{Q^2 E}\left(\frac{2}{1-\epsilon}\right), \tag{13}$$

$\frac{d\sigma_\nu}{d\Omega_K}$ is the virtual photon cross section, E and E' are the incident and scattered electron energies respectively, and

$$k = \frac{W^2 - M^2}{2M} \tag{14}$$

is the "photon equivalent energy", the laboratory energy necessary for a real photon to excite a hadronic system with c.m. energy of W. The virtual photon cross section for the case of no target and recoil polarizations is:

$$\begin{aligned}\frac{d\sigma_\nu}{d\Omega_K} = \sigma_T + \epsilon_L\sigma_L + \sqrt{2\epsilon_L(1+\epsilon)}\sigma_{LT}\cos\phi + \epsilon\sigma_{TT}\cos 2\phi \\ +h\sqrt{2\epsilon_L(1-\epsilon)}\sigma_{LT'}\sin\phi\end{aligned} \tag{15}$$

where σ_i are the structure functions that measure the response of the hadronic system and $i = T, L, LT, TT$, and LT' represent transverse, longitudinal and the various interference terms of structure functions. In contrast to the case of virtual photons, where the pure longitudinal and transverse response functions and the interference terms occur, for real photons there is only the pure transverse response.

In the most general case for all types of polarization, the virtual photon cross section in terms of response function is [7]:

$$\begin{aligned}
\frac{d\sigma_\nu}{d\Omega_K} &= K\mathbf{P}_\alpha\mathbf{P}_\beta\{\mathrm{R}_{\mathrm{T}}^{\beta\alpha} + \epsilon_{\mathrm{L}}\mathrm{R}_{\mathrm{L}}^{\beta\alpha} \\
&+ [2\epsilon_L(1+\epsilon)]^{\frac{1}{2}}({}^cR_{TL}^{\beta\alpha}\cos\phi + {}^sR_{TL}^{\beta\alpha}\sin\phi) \\
&+ \epsilon({}^cR_{TT}^{\beta\alpha}\cos 2\phi + {}^sR_{TT}^{\beta\alpha}\sin 2\phi) \\
&+ h[2\epsilon_L(1-\epsilon)]^{\frac{1}{2}}({}^cR_{TL'}^{\beta\alpha}\cos\phi + {}^sR_{TL'}^{\beta\alpha}\sin\phi) \\
&+ h(1-\epsilon^2)^{\frac{1}{2}}R_{TT'}^{\beta\alpha}\} \qquad (16)
\end{aligned}$$

where β and α denote target and recoil polarizations respectively. We have defined

$$K = \frac{|\mathbf{k}|}{k}$$

where $|\mathbf{k}|$ is the c.m. momentum of the kaon and $\mathbf{P}_\alpha$ and $\mathbf{P}_\beta$ are the polarization projection operators for the target and the recoil particles. A table containing the response functions for various cases of beam, target and recoil polarizations is given in Appendix D.

In the case of only polarized electron beam and no target and recoil polarization, $\alpha = \beta = 0$, only R_i^{00} terms contribute and we can write the structure functions as follows:

$$\sigma_L = KR_L^{00},\ \ \sigma_T = KR_T^{00},\ \ \sigma_{LT} = KR_{LT}^{00},\ \ \sigma_{TT} = KR_{TT}^{00},\ \ \sigma_{LT'} = KR_{LT'}^{00} \quad (17)$$

The response functions in turn, can be written in terms of their multipole expansions, CGLN amplitudes or helicity amplitudes [7]. Here are the five structure functions in terms of helicity amplitudes:

$$\begin{aligned}
\sigma_L &= K(|H_5|^2 + |H_6|^2), \\
\sigma_T &= K\frac{1}{2}(|H_1|^2 + |H_2|^2 + |H_3|^2 + |H_4|^2), \\
\sigma_{LT} &= K\frac{1}{\sqrt{2}}Re(H_5^* H_1 - H_5^* H_4 + H_6^* H_2 + H_6^* H_3), \\
\sigma_{TT} &= K Re(-H_1^* H_4 + H_2^* H_3), \\
\sigma_{LT'} &= K\frac{1}{\sqrt{2}}Im(-H_5^* H_1 + H_5^* H_4 - H_6^* H_2 - H_6^* H_3).
\end{aligned} \tag{18}$$

1.2.3 Polarized Structure Function

The possibility of separating the different components of the electromagnetic interaction in the cross section in the one-photon exchange approximation allows one to measure the structure functions and to consider them as observables. As seen in previous sections, the differential cross section for kaon electroproduction in inelastic scattering of longitudinally polarized electrons off unpolarized protons is expressed as a sum of five structure functions, one more than in the case of coincidence experiments with unpolarized electrons. With polarized electrons, the lepton tensor, $L_{\mu\nu}$ contains both a symmetric and an antisymmetric part. However the antisymmetric part contributes to the cross section only when the hadron tensor, $W_{\mu\nu}$, also contains an antisymmetric part. An antisymmetric part arises with unpolarized targets when an emitted particle is detected in coincidence with the scattered electron (in this case a kaon). The electron polarization therefore produces a fifth structure function that corresponds to the helicity asymmetry:

$$A_{LT'} = \frac{\frac{d\sigma}{d\Omega}^+ - \frac{d\sigma}{d\Omega}^-}{\frac{d\sigma}{d\Omega}^+ + \frac{d\sigma}{d\Omega}^-} = \frac{\sqrt{2\epsilon_L(1-\epsilon)}\sigma_{LT'}\sin\phi}{\sigma_0} \tag{19}$$

where

$$\sigma_0 = \sigma_T + \epsilon_L \sigma_L + \sqrt{2\epsilon_L(1+\epsilon)}\sigma_{LT}\cos\phi + \epsilon\sigma_{TT}\cos 2\phi \tag{20}$$

is the unpolarized cross section. The $\pm$ superscripts on $\frac{d\sigma}{d\Omega}$ correspond to electron helicity states of ± 1.

The fifth or polarized structure function $\sigma_{LT'}$ is intrinsically different from the four structure functions of the unpolarized cross section. This term is generated by the imaginary part of terms involving the interference between longitudinal and transverse components of the hadronic and leptonic current [5]. In the absence of multiple resonances or interference between resonant and non-resonant processes, the fifth structure function is zero. It will be non-zero in the case of multiple reaction channels and will provide new and unique information on the interference between resonant and non-resonant amplitudes [8]. It thereby provides a means of measuring the contributions of small background channels that are often too weak to be observed directly in the unpolarized cross-section measurements. The sensitivity of the fifth structure function to different resonances and to the interference between the resonant and non-resonant amplitudes is important in searching for "missing resonances" that contribute to $K\Lambda$ production.

1.3 Theoretical Calculations– Hadrodynamic Models

The strong interaction can be described by pQCD at high energies where a perturbative approach can be used to calculate the interaction based on the quark-gluon degrees of freedom. However, at low energies, where mesons and baryons are con-

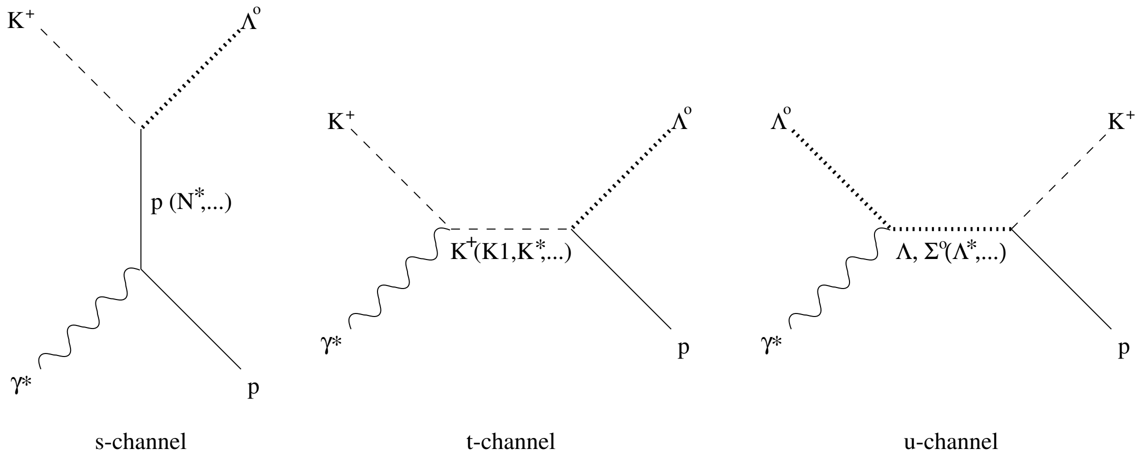

Figure 5: Feynman diagrams for $K^+\Lambda$ electroproduction for s, t, and u channel reactions. The Born terms are shown where the exchange particle can be either a proton, kaon or lambda. The nucleonic, kaonic and hyperonic resonances are shown in the parentheses.

sidered eigenstates of the strong interaction, the perturbative techniques cannot be used and the transition between these eigenstates cannot be explained. Hadrodynamic calculations are a class of phenomenological models that have been developed to describe the strong interaction in non-perturbative regimes. In these models, the scattering amplitude is calculated in terms of hadronic degrees of freedom based on Feynman diagrammatic techniques. Fig. 5 illustrates Feynman diagrams for some of the elementary production processes for kaon electroproduction. s, t, and u channels contribute to the electroproduction process in varying degrees depending on the kinematics and each may go through any number of intermediate resonances. Two different types of hadrodynamic models are discussed here. First, the single-channel isobar calculations and second, the Regge models.

1.3.1 Single-channel Isobar Calculations

The single-channel isobar calculations include the contributions of the diagrams corresponding to the exchange of one particle or resonance in the intermediate state by constructing an effective Lagrangian from the sum of Born terms and extended Born terms in the s, t, and u channels. The s-channel represents the propagation of a nucleonic state, while the u and t channels account for the exchange of the hyperonic and kaonic resonances, respectively. The scattering amplitude is written in terms of a Lorentz-invariant matrix element, [9, 10, 11, 12, 13], which consists of the invariant amplitudes that explicitly express the contribution of each intermediate state and reaction channel. These amplitudes contain the corresponding coupling constants and propagators for each state and channel. The contribution of each diagram is weighted by the propagator of the exchanged particle which is proportional to:

$$\frac{1}{(q^2 - M_x^2 + iM_x\Gamma_x)} \tag{21}$$

where q is one of the s, t, or u variables depending on the diagram, and M_x and Γ_x are the mass and the decay width of the exchanged particle x. For Born terms, the term $iM_x\Gamma_x$ is zero since the exchange particle does not decay. The Lorentz-invariant matrix element can also be written in terms of CGLN amplitudes [7] that are suitable for the purpose of multipole analysis.

The currently available single-channel isobar calculations compared in this study are Adelseck and Wright [9, 10]; Williams, Ji, and Cotanch [11]; Mart and Bennhold [13, 14]; and Janssen [15, 16]. These calculations use the same framework but different choices for the intermediate meson and baryon exchanges. Appendix B shows a table of resonances included in each of these models. Furthermore, these calculations employ different parameterizations of kaon charge form factors, kaon transition form factors, form factors associated with the hadron vertex, and the direct coupling of the photon to the hadron. These form factors describe the charge and current distributions in the hadron and determine the kinematic dependence of the couplings. Since the kaon and hyperon form factors are not well known, there are several different approaches employed in these calculations.

These models also have different choices for the coupling constants at the interaction vertices that determine the strength of the interactions between the different hadronic states. One may treat the coupling constants either as free parameters or constrain them by the ranges given by the SU(3) symmetry of the underlying interaction. In the following, we will briefly describe some of the recent models.

Adelseck and Wright (1988):

In this model, the amplitudes that describe the hadronic current were calculated by solving Feynman diagrams for Born terms and resonant states in s, t, and u channels. These states are summarized in the Appendix B. This model includes an additional kaonic resonance, the second kaon resonance $Q1$, which is a pseudovector state. For kaon form factors, a vector meson dominance (VMD) model is used [9, 10]. In a VMD model the virtual photon can couple directly to a virtual vector meson with the same quantum numbers and four-momentum that then interacts with the hadron. In this model, all of the coupling constants describing the strength of the reaction vertices are obtained by a least-squares fit to the available photo- and electroproduction data. The explicit definition of all the vertex factors is given in Ref [17].

William, Ji, and Cotanch (WJC) Model (1992):

The resonances and intermediate states included in the WJC model are given in Appendix B. The coupling constants were all determined by the fits to the data available at the time for both $K\Lambda$ and $K\Sigma^0$ production. The electromagnetic form factors for kaon and K^*K transition form factors are modeled based on an extended VMD model, EVMD [11]. The EVMD approach is based on a smooth transition from the vector meson picture at low Q^2 to direct interactions between the constituent quarks of the interacting hadron and the photon for high Q^2. The most general EVMD expression for the kaon charge form factor, $F_{K^+}(q^2)$ is given in Ref. [11] as:

$$F_{K^+}(q^2) = \gamma F_\gamma(q^2) + \sum_v F_v(q^2)(\frac{g_v}{f_v})\frac{M_v^2}{(M_v^2 - q^2 - iM_v\Gamma_v)} \tag{22}$$

where $F_v(q^2)$ and $\gamma F_\gamma(q^2)$ are the intrinsic form factor for the hadronic vertex, and the form factors associated with the direct coupling of the photon to the hadron. M_v and Γ_v are the mass and the width of the vector meson, γ is the normalization factor, and $\frac{g_v}{f_v}$ is the effective vector meson coupling to the hadron. Also, for the proton electric and magnetic form factors, $G_E^p(q^2)$, and $G_M^p(q^2)$, the EVMD parameterization is used. It is important to mention that by using a sum rule on the coupling constants, and taking all the strong form factors to be constant, the EVMD would be equal to the simple VMD model.

Mart and Bennhold Model (1999-2001):

This model [13], has a different approach for selecting baryon resonances in the intermediate states than other models. In the previous models, usually the resonances are selected empirically by their relative contribution to the overall χ^2 of the fit to the data. The choice of the resonances in this model is based on constructing an amplitude with a minimum number of resonances that are consistent with multichannel analyses. The multi-channel calculation includes the re-scattering terms that can contribute to the production of the final state [18, 19]. Furthermore, unlike the previous models, this model includes only Born terms in the u-channel.

In this calculation, the SU(3) values are used for the Born couplings while all the other coupling constants for $p(\gamma, K^+)\Lambda$ were determined by a fit to the available differential photoproduction cross section and recoil polarization data. The choice of the electromagnetic form factors are the same as those of WJC model. However, this model uses a different type of hadronic form factor based on a new prescription that is consistent with gauge invariance. The necessity of this new form of hadronic form factor was due to the high strength of the t-channel Born terms in the total cross section calculations. The general form for the hadronic form factor is given by [13]:

$$F(\Lambda, q^2) = \frac{\Lambda^4}{\Lambda^4 + (q^2 - m^2)^2} \tag{23}$$

where $q^2 = s$, t, or u and m is the mass of the intermediate particle. The cut off mass, Λ, is a free parameter determined by the fit to the experimental data. In this model an additional cut off function was used to reduce the strength of the Born

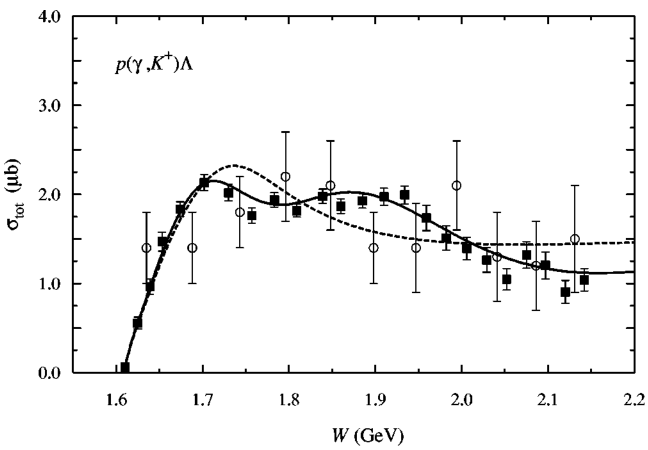

Figure 6: The total photoproduction cross section new (squares) and old (circles) data from SAPHIR [20]. The solid (dashed) line shows Mart and Bennhold model with (without) including $D_{13}(1960)$ resonance in the model.

terms in t-channel. This function is multiplied by the production amplitude and has the monopole form of:

$$F(\Lambda, t) = \frac{\Lambda^2 - m_K^2}{\Lambda^2 - t} \tag{24}$$

where m_K is the mass of kaonic resonance.

This model was used to fit the photoproduction $p(\gamma, K^+)\Lambda$ SAPHIR data [20] in which a resonance structure was seen. Fig. 6 shows the result of the fit of this model, with and without including a resonance $D_{13}(1960)$ [14]. This resonance was predicted by the quark models [2]. However, it is possible to explain the shoulder by additional hyperon resonance in u-channel [21]. It is suggested that the measurement of the photon asymmetry can be used to further study of this resonance [14].

Janssen Model (2001):

In this model, the standard form of the electromagnetic form factors and propagators are used and coupling constants are treated as free parameters that are extracted from the global fit to the available complete data set of SAPHIR [20], SPring-8, Hall C, and older data from Harvard-Cornell and Orsay. The values of coupling constants obtained from the fit are then compared to the quark-model predictions. This model is very similar to that of Mart and Bennhold except that instead of using a cut off function in the prescription of the hadronic form factors to reduce the strength of the Born terms, it introduces hyperon resonances in the u-channel, as summarized in Appendix B. It was shown that the u-channel hyperon resonances destructively interfere with the Born terms and reduce their strength to the level of the experimental data [15, 16].

To extract reliable resonance information from the available data, it is necessary to include theoretical uncertainties and also use appropriate fitting strategies of the model to the data. Janssen has employed a new fitting procedure based on a "genetic algorithm" [22]. In this method, first a set of random solutions were generated. Then each solution was used to evaluate χ^2. The population of the solutions were then "evolved", by mixing values (cross over) or by changing the values at random (mutation). These values were then used to find a global minimum χ^2. Fig. 7 shows the result of the fit to the SAPHIR photoproduction data where all curves represent equally good fits to the experimental data.

1.3.2 Guidal Regge Model

The Regge models are also based on the Feynman diagram calculations, however, in the Regge approach, a single-channel exchange particle in the t-channel, is replaced by the exchange of a Regge trajectory that represents a family of particles with the

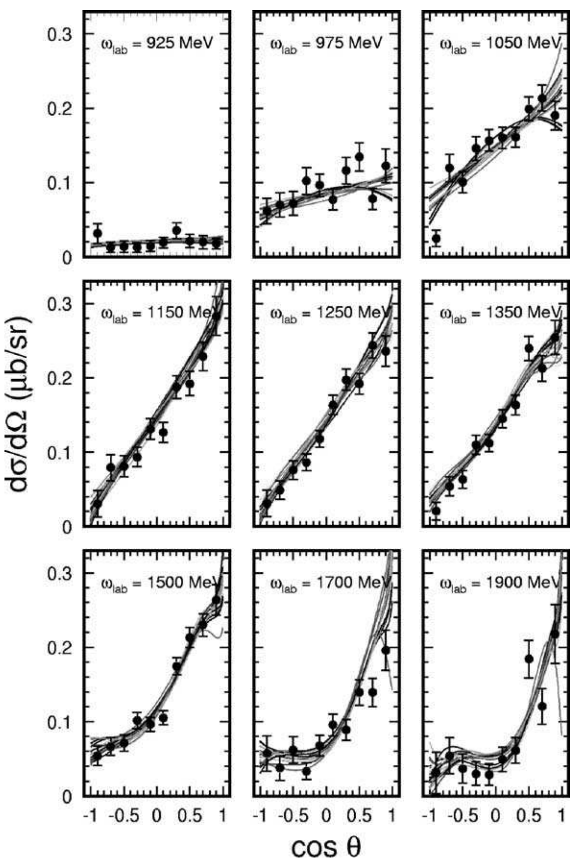

Figure 7: Calculations from Janssen model for the angular distribution of the differential cross section for Λ photoproduction. Data is from SAPHIR [20]. The curves correspond to various solutions with comparable χ^2.

same internal quantum numbers. Therefore, the pole-like Feynman propagator is replaced by Regge propagator.

The Guidal Regge model for photo- and electroproduction of $K^+\Lambda$ is described in Ref. [23, 24] and is based on two "Reggeized" t-channel K and K^* exchanges. The special feature of this model is the assignment of the same electromagnetic form factors to the t and s-channel diagrams to keep gauge invariance. This approach is different than the previous calculations in which different electromagnetic form factors were assigned to the t and s-channel diagrams– monopole and dipole forms

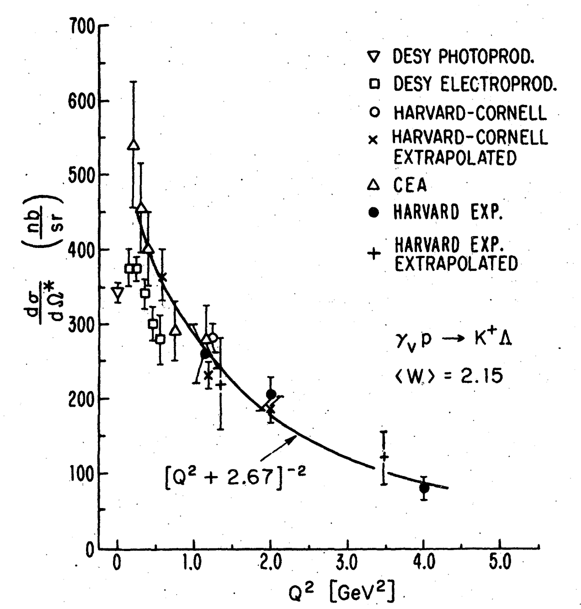

Figure 8: The Q^2 dependence of $K^+\Lambda$ cross section. Data from Ref. [26, 27, 28, 29].

respectively. To extend the model from photoproduction to electroproduction, the K and K^* t-channel diagrams were multiplied by a monopole form factor of the form:

$$F_{K,K^*}(q^2) = \frac{1}{1 + \frac{q^2}{\Lambda^2_{K,K^*}}} \tag{25}$$

with the choice of $\Lambda^2_K = \Lambda^2_{K^*} = 1.5$ GeV^2. This new feature, has resulted in a successful description of the recent experimental data [25].

1.4 Previous Measurements

The development of the theoretical models has been highly based on the availability of the experimental measurements. Experimental results of precise cross section– and, eventually polarization observable– measurements are important for constraining the free parameters of these models.

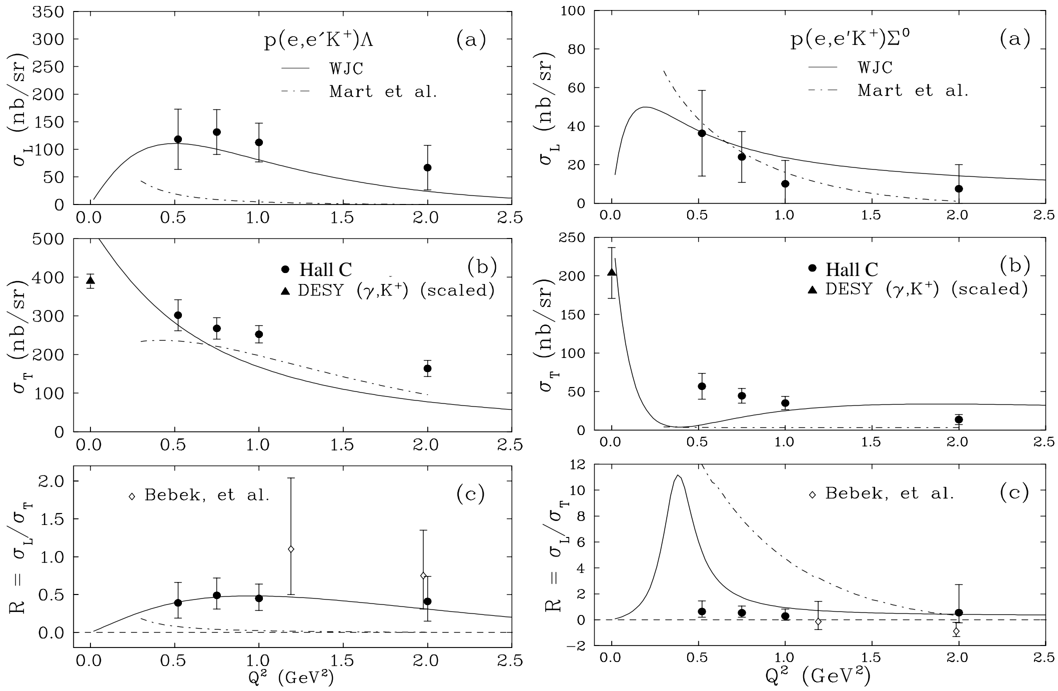

Figure 9: Longitudinal (a) and transverse (b) cross sections for $K^+\Lambda$ (left) and $K^+\Sigma^0$ (right) as a function of Q^2. The ratio is shown in panel (c). Figures from Ref. [30].

Electroproduction:

The first measurement of the kaon electroproduction goes back to 1972 in which the reactions $e+p \rightarrow K^+ + \Lambda(\Sigma^0)$ were studied [26]. The final state electron and kaon were detected in coincidence using the two-arm spectrometer system at Cambridge Electron Accelerator (CEA). The cross sections were measured as a function of W from 1.85 to 2.60 GeV, virtual photon mass squared from 0.18 to -1.2 GeV^2, and θ_K^{cm} from 0 to 28°. The Λ and Σ^0 cross sections were extracted by fitting the Λ and Σ^0 peaks in the missing-mass spectrum. The result showed a strong Q^2 dependence. A few years later in 1974, Bebek and his collaboration (Harvard-Cornell) performed similar experiments at the Wilson Synchrotron Laboratory at Cornell university at four Q^2 and W values of (0.6, 2.67), (1.2, 2.67), (2.0, 2.67), and (1.2, 2.15) in

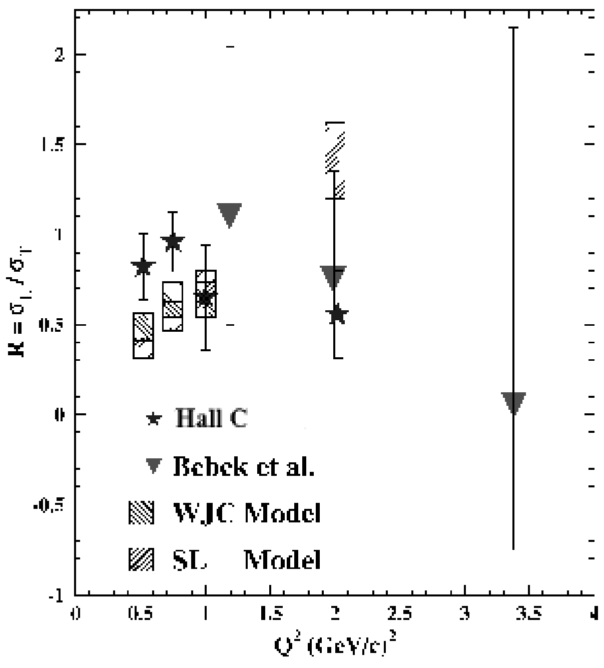

Figure 10: The ratio $R = \sigma_L/\sigma_T$ versus Q^2 (GeV)^2 from Ref. [25].

(GeV^2, GeV) and ϵ range of 0.86 to 0.94 [27]. The result of these measurements were in good agreement with those made at CEA and indicated that the Σ^0 cross section has a more rapid fall off than Λ as Q^2 increases. Fig. 8 shows the result of these two experiments along with the result of another measurement in 1977 at Harvard by the same group [28] repeating the same experiment but for lower ϵ range from 0.35 to 0.50. The figure also compares these results to some early photo- and electroproduction measurements at DESY in 1972 [29].

Recently, the results of high quality measurements at Jefferson laboratory, have become available over a wide range of kinematics. The most recent published data are the result of two similar analysis, [25] and [30], on the separation of longitudinal and transverse cross sections, σ_L and σ_T, in the electroproduction of kaons on a hydrogen target in Hall C. The experimental setup was such that data were taken at four values of Q^2 between 0.5 and 2.0 GeV^{2}and for each Q^2 value, there were three measurements at different values of the virtual photon polarization, ϵ. This made it possible to separate longitudinal, σ_L, and transverse, σ_T, structure functions by performing a linear fit to the combined longitudinal and transverse cross sections, $\sigma_T + \epsilon\sigma_L$, while integrating the differential cross section over ϕ cancels out the interference terms, σ_{LT} and σ_{TT} (Eq. 15). L/T separations currently provide the most stringent constraints on the K^+ electromagnetic form factor. The result of these two analyses on the measurement of the differential cross section both agree with those of previous measurements. However, Fig. 9 and 10 show the result of these two analyses on the L/T ratio are not quite in agreement with each other. The graphs also show the previous data on this measurement.

Another published electroproduction result is the first measurement of the transferred polarization for $\vec{e}p \to e'K^+\vec{\Lambda}$ measured in Hall B of the Jefferson Laboratory with the CLAS. The Λ hyperon polarization was measured using a longitudinally polarized electron beam of 2.567 GeV energy on a hydrogen target over Q^2 from 0.3 to 1.5 (GeV)^2, W from threshold to 2.15 GeV and over full kaon center-of-mass angular range [31] (this is the same data set which has been analyzed for this dissertation). The self-analyzing nature of the Λ weak decay to $p\pi^-$ has an asymmetric angular distribution with respect to the Λ spin direction and allows the measurement of Λ polarization via:

$$\frac{dN^{\pm}}{d\cos\theta_p} = N[1 + \alpha(P^0 \pm P_b P')\cos\theta_p] \tag{26}$$

where P_b is the electron beam polarization, α is the weak decay constant, and P^0 and

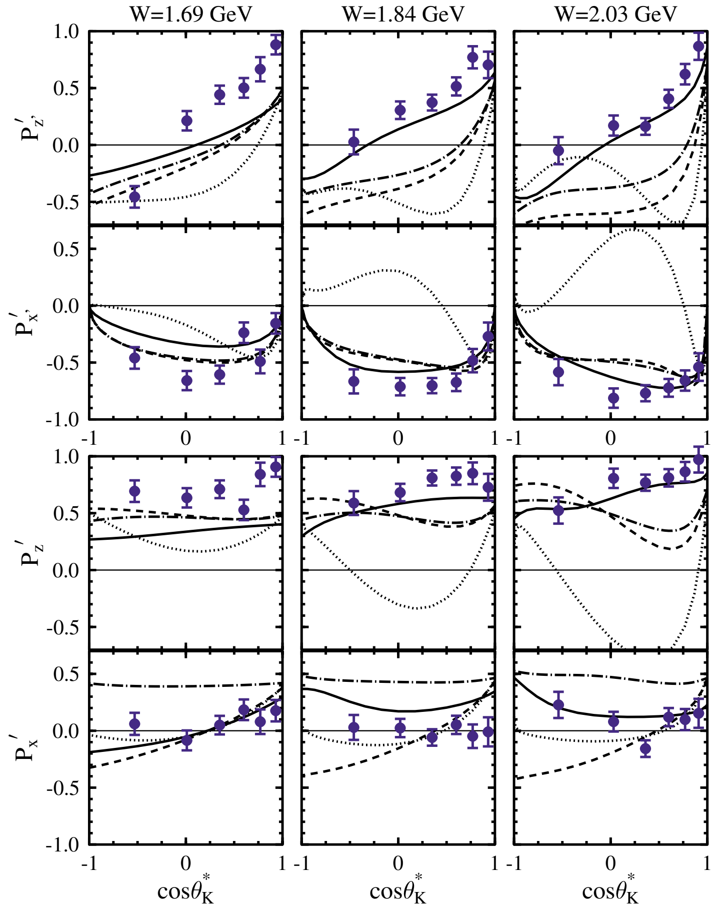

Figure 11: Two component of Λ transferred polarization in two coordinated systems, one associated with the electron plane (x, y, z) and the other one associated with the hadron plane (x', y', z'), at beam energy of 2.567 GeV, versus $\cos\theta_K^{cm}$ for three W values and summed over Q^2 from Ref. [31]. The curves correspond to the hadrodynamic models: WJC 1992 (dotted), Bennhold and Mart 1998 (dashed), Bennhold and Mart 2002 (solid), Janssen 2002 (dot-dashed).

P' are the induced and transferred Λ polarization respectively. Fig. 11 shows the result of this measurement compared to some of the theoretical calculations. One result of this analysis indicates that the transferred Λ polarization along the virtual photon direction is maximal. Within a simple quark model of strange quark pair creation, the spin of the Λ is carried by the s quark. Therefore, one can conclude that the spin of the strange quark pair were anti-aligned when they were created.

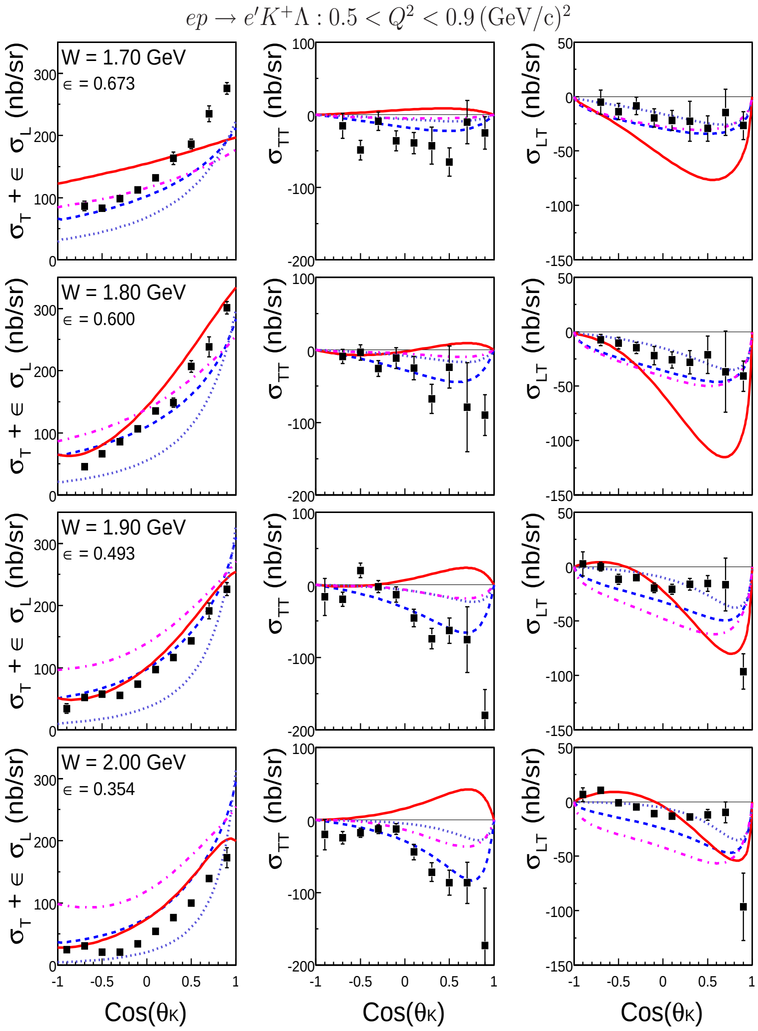

Figure 12: The structure functions for Λ electroproduction from Ref. [33]. The curves are calculation from Bennhold (solid), Janssen (dot-dashed), Guidal (dashed), and a version of Guidal calculation excluding K^* exchange (dotted).

These data have also been used to extract the ratio of longitudinal to transverse structure functions [32]. In that analysis, it is shown that at $\cos\theta_K^{cm} = 1$, the ratio $R = \frac{\sigma_L}{\sigma_T}$ is smaller than what is obtained by Rosenbluth method.

In another analysis of the same CLAS data [33], the $K^+\Lambda$ and $K^+\Sigma^0$ electroproduction unpolarized cross section, σ_0, and structure functions were measured over a wide kinematic range, Q^2 between 0.5 to 1.5 $(\mathrm{GeV})^2$, W from threshold to 2.05

GeV, and nearly complete angular coverage in the center-of-mass frame with an electron beam energy of 2.567 GeV. In this analysis, the $\sigma_u = \sigma_T + \epsilon\sigma_L$ and σ_{TT} and σ_{LT} terms are extracted and compared to the recent theoretical calculations that qualitatively are in agreement with the data but cannot describe the details of the angular distributions and resonant-like behavior (Fig. 12, these results will be used in our extraction of $\sigma_{LT'}$). It is important to mention that none of the CLAS electroproduction data have yet been included in the theoretical models.

Photoproduction:

The SAPHIR collaboration has recently published total and differential cross section data for photoproduction of hyperons. The data were taken using the SAPHIR detector at the electron stretcher ring ELSA in Bonn (Fig. 6 and 7). As seen in Fig. 6, the total cross section as a function of W shows a rise from threshold up to 1.7 GeV, which possibly corresponds to the mass of $N^*(1650)$ or $N^*(1710)$ resonances that decay into $K^+\Lambda$. The differential cross sections were fit with a polynomial of the form:

$$\frac{d\sigma}{d\Omega} = (\frac{q}{k})[a_0 + a_1 \cos\theta_K^{cm} + a_2 \cos^2\theta_K^{cm} + a_3 \cos^3\theta_K^{cm}], \tag{27}$$

where $\frac{q}{k}$ is the ratio of the kaon and photon momenta in the center-of-mass frame. The fit indicated a large s-wave contribution and also a non-negligible s–p-wave interference. The total cross section for $K^+\Lambda$ also shows a bump at 1.9 GeV. A similar polynomial fit to the angular distributions of the differential cross section at this energy indicates contributions from s, p, and d-waves.

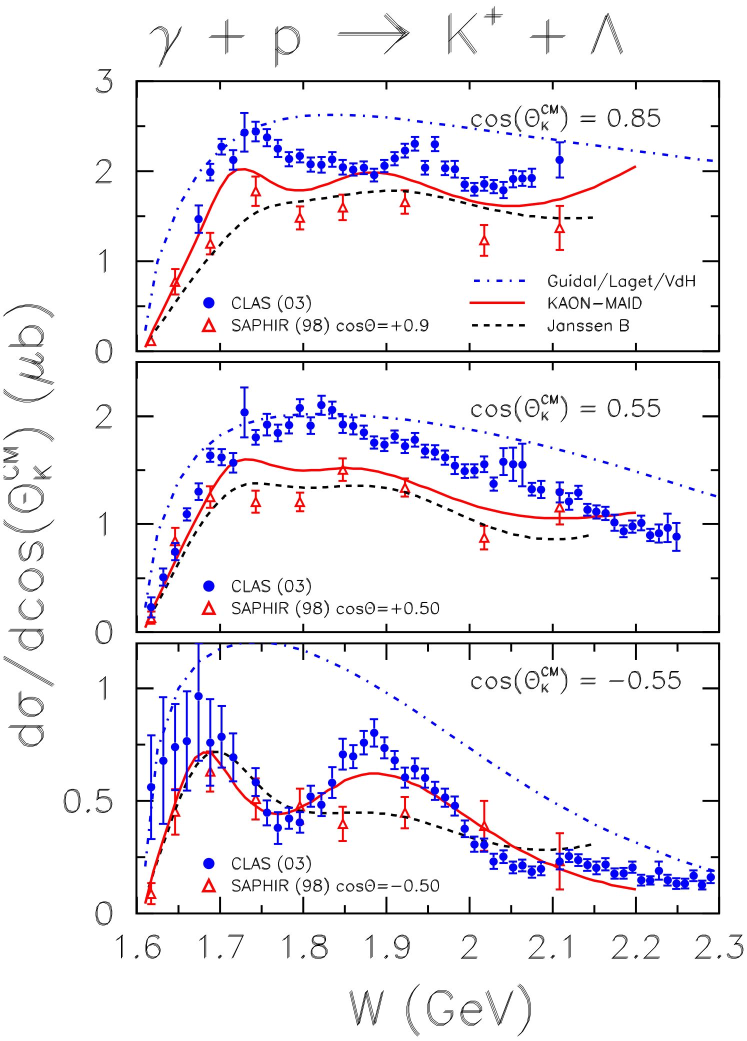

Figure 13: W dependence of the Λ differential cross section for forward, intermediate forward, and backward kaon center-of-mass angles from Ref. [34].

Published data also exist from analysis of Hall B data at Jefferson Laboratory on the photoproduction of $K^+\Lambda$ and $K^+\Sigma^0$ [34]. In that analysis, the differential cross section and hyperon recoil polarization were measured for photon energies from threshold up to 2.3 GeV. The results (Fig. 13) show larger cross sections in the middle to forward angles compare to the results of SAPHIR. The angular distribution of the measured cross sections are also more backward peaking which could be from hyperon resonance contributions in the u-channel. However, the resonance structure seems to be more complicated for s and t channels . Moreover, in the measurement of Λ recoil polarization, a structure around $W = 1.9$ GeV in the backward angles was seen that might be again a sign of a resonance contribution in that region.

There are a number of other analyses in progress based on Jefferson Laboratory experiments on electromagnetic production of kaons. For example, experiment number 98-108 in Hall A aims to separate the longitudinal and transverse structure functions for Q^2 up to 3 GeV^2 through detection of kaons along the direction of virtual photon where only these terms contribute to the cross section. That analysis also includes the study of the t-dependence of cross sections over a large range of t.

Another example is the ongoing analysis of the five structure functions for kaon electroproduction as part of the Hall B experiment E00-112. The "five structure function group" aims to provide the world's most complete set of data for $K^+\Lambda$ and $K^+\Sigma^0$ in the nucleon resonance region.

1.5 Contents of Thesis

There is no previous measurement on the fifth structure function, $\sigma_{LT'}$, for kaon electroproduction. In the following chapters, we will describe in detail, a measurement of the single spin asymmetries and polarized or fifth structure function, $\sigma_{LT'}$, for $p(\vec{e}, e'K^+)\Lambda$ reaction using the CLAS detector in Hall B of Jefferson Laboratory. The large angular acceptance of CLAS enables us to study the reaction and measure the single spin asymmetries and polarized structure function over varying kinematical regions covering four-momentum transfer $0.5 \leq Q^2 \leq 1.3$ GeV^2 and invariant mass $1.6 \leq W \leq 2.1$ GeV over a full angular range in $\cos\theta_K^{cm}$ and ϕ^{cm}.

We will describe the experimental setup, event selection from the experimental data sets, particle identification procedures, the detector fiducial cuts, kinematic and background corrections necessary for extracting the reaction yields. The measurement of the single spin asymmetries and extraction of the polarized structure functions including acceptance and radiative corrections will be discussed and the results will be presented and discussed in relation to the available theoretical models.

2 Experimental Setup

2.1 The CEBAF Accelerator

Jefferson Lab's Continuous Electron Beam Accelerator Facility, (CEBAF), Fig. 14, is designed to continuously accelerate electron beams up to 6 GeV for nuclear and particle physics experiments. CEBAF consists of two Superconducting Radio-Frequency (SRF) linear accelerators (linacs) that are connected at both ends by a set of five recirculating arcs. There are 338 SRF niobium cavities in CEBAF that are grouped into eight, forming a total of $42\frac{1}{4}$ cryomodules, twenty in each linac and $2\frac{1}{4}$ at the injector. The cryomodules are immersed in a bath of liquid helium at a temperature of -271 C (2.08 K) [37]. An electromagnetic field is applied to the cavities inducing a charge on the interior surface of the cavities. The electromagnetic field oscillates in time, with a frequency of 1497 MHz, such that electrons always see a net positive charge in front of them as shown in Fig. 15. Therefore, the electrons accelerate throughout the cavity with a beam energy spread of $\frac{\Delta E}{E} \leq 10^{-4}$. Before delivery to the three experimental halls, the electron beam is circulated through the two linacs for up to five passes. The electrons gain up 600 MeV for each pass through one of the linacs. The CEBAF accelerator has a 100% duty factor which makes it possible to have a high luminosity while the instantaneous rate of incident electrons on the target is low. This reduces the accidental background rate in coincidence measurements of small cross section processes. The continuous electron beam is composed of three interlaced, variable intensity beams that can be independently directed after up to five passes to any of the three experimental halls. This allows

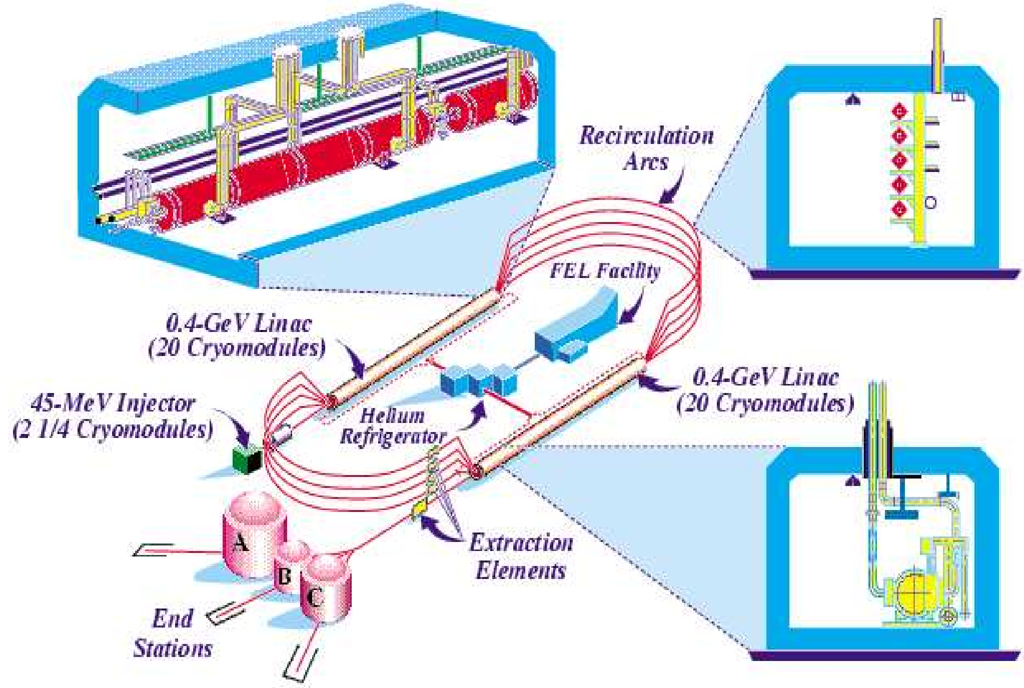

Figure 14: The main components of the CEBAF accelerator: the injector, the north and south linacs, the recirculating arcs and the separator.

three simultaneous experiments at the same (only in case of full five pass beam) or different energies and currents. This is done using a RF separator at the beam switch-yard such that each experimental hall receives every third bunch of electron packets at a frequency of 499 MHz, or every 2.004 ns.

Each of the three experimental halls at Jefferson lab are equipped with spectrometers specialized for complementary experimental programs. Hall A contains double-arm, identical, high-resolution spectrometers, HRS, ($\frac{\delta p}{p} \leq 10^{-4}$) with a maximum momentum of 4 GeV. Each arm can be use for either electron or hadron detection. Hall C houses a high momentum spectrometer, HMS, with medium resolution ($\frac{\delta p}{p} \leq 10^{-3}$) and a short orbit spectrometer, SOS, designed to detect short-lived

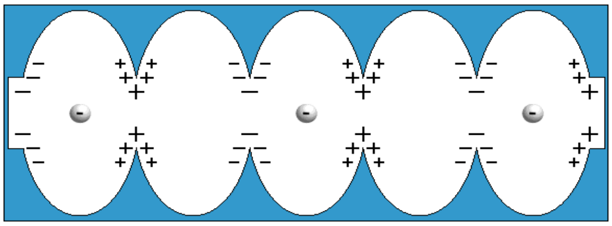

Figure 15: Schematic of charge configuration on a typical acceleration cavity [37].

hadrons. CLAS, the CEBAF Large Acceptance Spectrometer, is located in Hall B and will be discussed in the later sections.

2.2 The Polarized Electron Beam

The electron beam at CEBAF begins at the injector and can be delivered in a highly spin-polarized state. Linearly polarized electrons are emitted from a GaAs photocathode that is illuminated with circularly polarized light from a pulsed diode laser. Three diode lasers are biased with an radio frequency (RF) of 499 MHz, $\frac{1}{3}$ of the accelerating cavity frequency, which allows each of the experimental halls to choose the beam current and energy. The light from the lasers is then optically combined to form a 1497 MHz pulse train [35, 36] and the electrons are accelerated up to 45 MeV and injected into the north linac. A beam polarization of up to 80% can be obtained with this technique. The electron beam polarization is measured via Møller polarimetry in the experimental halls. The helicity of the electron beam was flipped at the rate of 30 Hz for the current experiment.

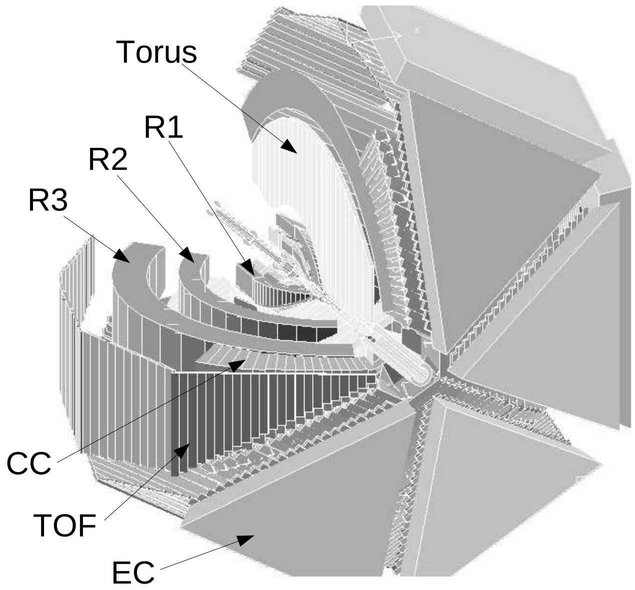

Figure 16: Three dimensional representation of CLAS with a portion of the system cut away to highlight the elements of the detector system.

2.3 CLAS in Hall B

The CEBAF Large Acceptance Spectrometer (CLAS) is a nearly 4π sr detector used for investigating the structure of the nucleons and nuclear matter by observing multi-particle final-states.

Schematic views of the CLAS are shown in Fig. 16 and Fig. 17. Six superconducting coils generate a toroidal magnetic field around the target with azimuthal symmetry about the beam axis. The coils divide CLAS into six sectors, each functioning as an independent magnetic spectrometer. Each sector is instrumented with multi-wire drift chambers (DC) to determine charged-particle trajectories, scintillator counters for time of flight (TOF) measurements, and in the forward region, a gas-filled threshold Čerenkov counter (CC) for electron/pion separation, and an

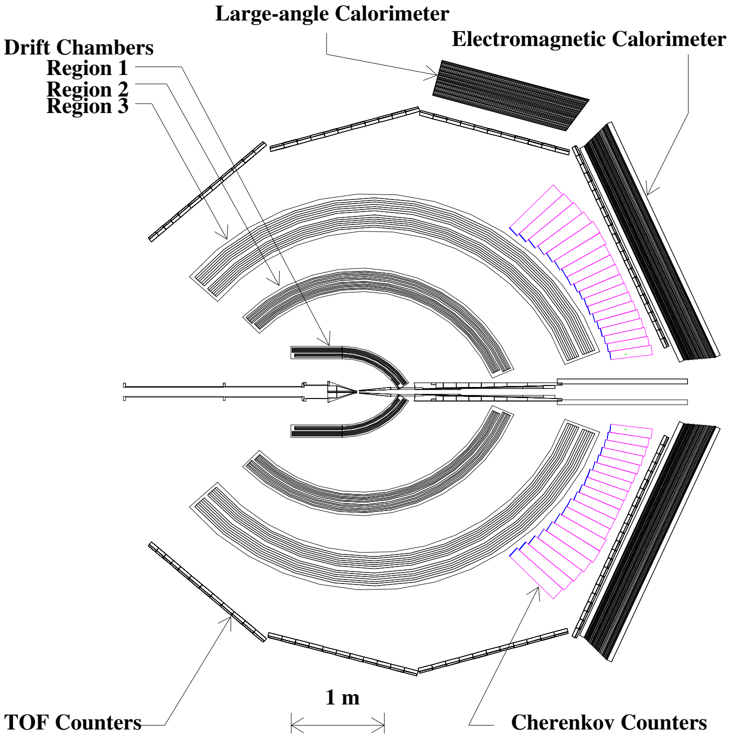

Figure 17: Mid-plane slice of the CLAS detection system.

electromagnetic calorimeter (EC) to identify and measure the energy of electrons and high-energy neutral particles.

2.3.1 The Toroidal Magnetic Field

The toroidal magnetic field generated by the main torus induces a curvature in the path of the charged particles and allows the measurement and analysis of their momenta. The toroidal magnetic field is such that the charged particles are bent in θ, the angle between the beam line and particle's trajectory, while their azimuthal angle about the beam direction, Φ, remains largely unaffected. This simplifies the charged particle's track reconstruction.

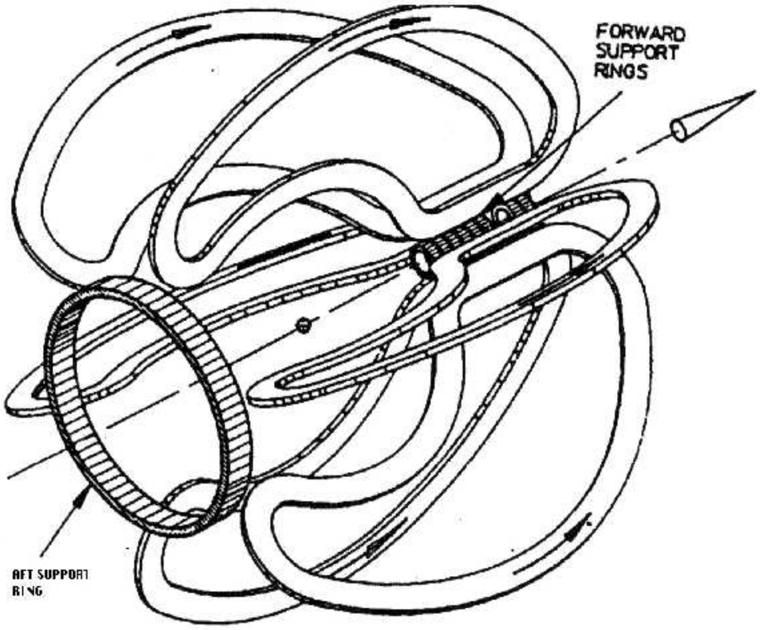

Figure 18: Configuration of the CLAS torus coils.

The torus consists of six superconductive iron free coils with a maximum design current of 3860 A, placed about the beam line (Fig. 18) and was build by Oxford Instrumentation Corporation. The coils are 5m long and 3m tall made of an aluminum stabilized NbTi/Copper conductor and sealed within an aluminum cryostat. The torus is kept at operational temperature of 4.5 K with a flow of supercritical helium through cooling tubes [38]. The magnetic field lines normally run counterclockwise around the beam axis as viewed from upstream, such that the negative (positive) charged particles bend toward (away from) the beamline, Fig 19. The current can be reversed as dictated by the experiments. The magnetic field peaks at 3.5 T with an integral magnetic field of 2.5 T·m in the forward direction [38]. It has been observed that the electron beam moves as a function of the torus cur-

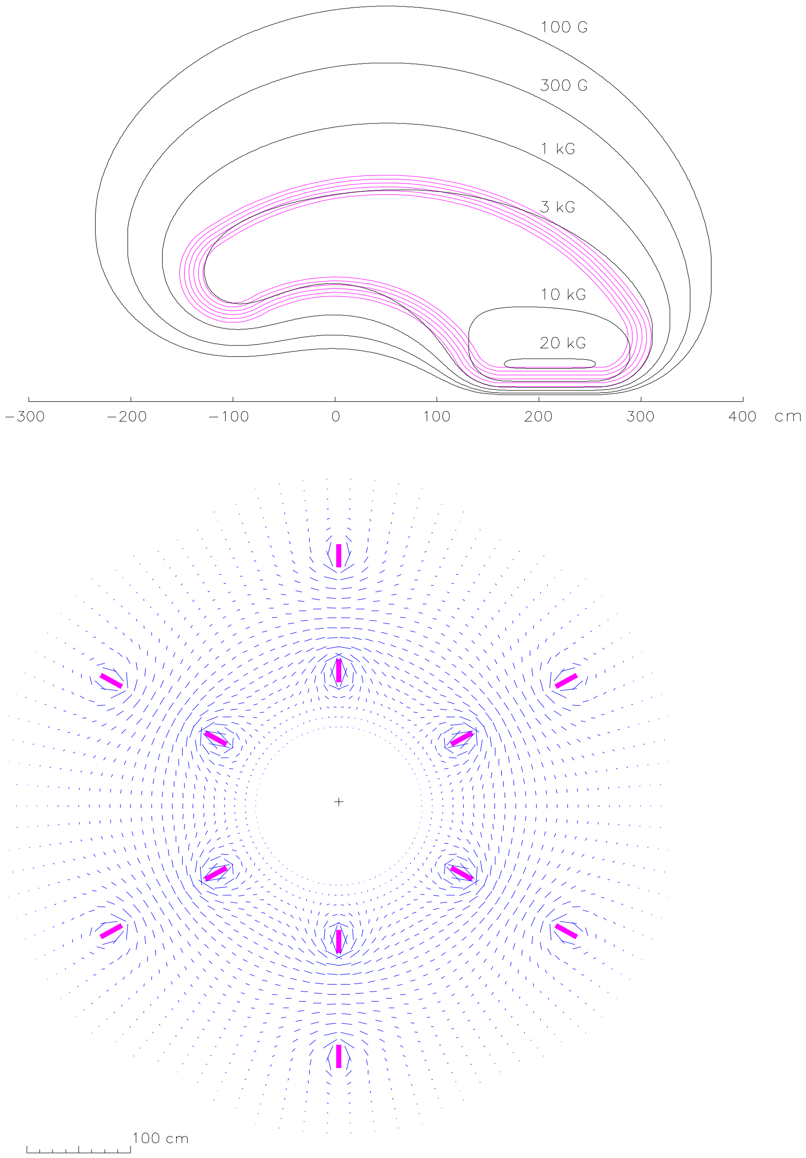

Figure 19: Top: The magnetic field contours for the main torus at the maximum current setting. Bottom: Magnetic field vectors for the CLAS toroid transverse to the beam in a plane centered on the target.

rent. Therefore, the position of the torus coils must not have been installed at their ideal position. Methods have been developed to analyze data with this non-ideal magnetic field, which will be discussed in section 3.6.

Møller scattered electrons from the target are the dominant source of the background hits in the inner drift chambers. Therefore, a mini torus is used to generate a weak magnetic field around the target to protect the drift chambers from these low-energy electrons. The mini torus coils are made of normal conducting material and only occupy space inside the shadows of the main torus. It provides a minimal obstruction to particles passing through CLAS. The polarity of the mini torus is such that the low energy electrons are bent back toward the beam line and out of the acceptance of CLAS.

2.3.2 Drift Chambers

The CLAS tracking system consists of 18 separate multi-layer drift chambers with similar basic design elements, located at three radial regions in each of the six sectors of CLAS. The track of charged particles from the fixed target is measured at three locations or regions (labeled R1, R2 and R3 in Fig. 20). The geometry of these 18 chambers provides for good tracking resolution and efficiency with large acceptance [39]. The CLAS multi-wire drift chambers consist of many parallel anode wires (sense wires) acting as independent detectors. To achieve a good spatial and time resolution, a large number of wires are required. A schematic representation of a typical drift chamber sector is shown in Fig. 20. The chamber bodies were designed to support field and sense wires running between two end-plates. Each end-plate contains thousands of holes into which the wire-fixture assemblies were placed with nearly 130,000 wires forming hexagonal drift cells (Fig. 21). The sense wires for all chambers is 20-μm-diameter gold-plated tungsten and the field wire is

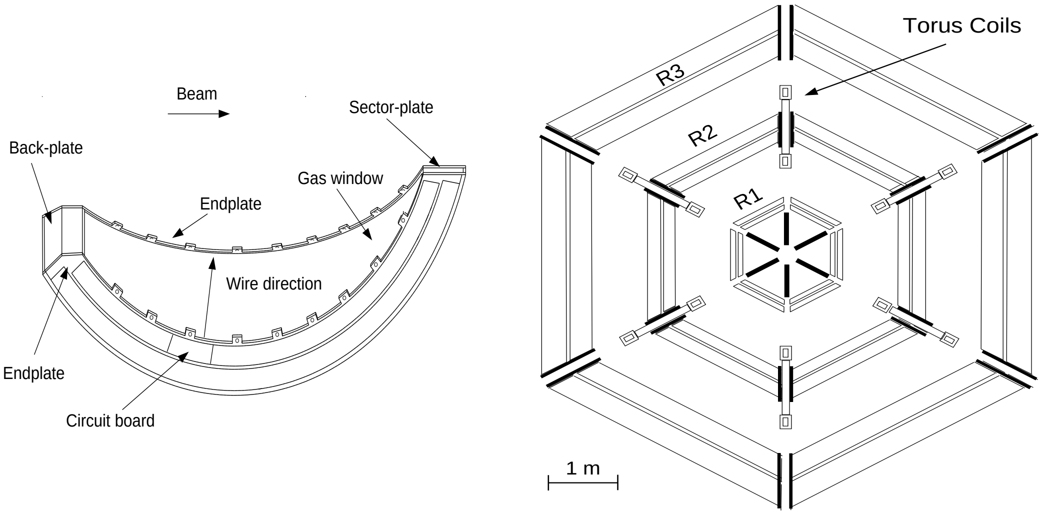

Figure 20: Left: Schematic representation of a typical drift-chamber sector. Right: Vertical cut through the drift chambers transverse to the beam line at the target location.

140-μm-diameter gold-plated aluminum alloy. The chamber gas is 90% argon 10% CO_2 mixture which results in minimal multiple scattering. The reconstruction of charged-particle tracks is performed in two stages (as illustrated by Fig. 21). In the first stage, individual tracks are fit only to hit-wire positions and data are combined into track segments and then linked together to form tracks across the three regions within one sector. The size of the drift cells are comparatively small and the number of wire layers are large, therefore the particle momenta can already be reconstructed with a resolution of $\frac{\Delta p}{p} \approx 3\%$ to 5%. Additional information on these tracks, derived from the Čerenkov, time of flight, and electromagnetic calorimeter detectors, allows for determination of the identities and speeds of the charged particles. In the second stage of the analysis, flight-time information of the particles from the target to the outer scintillators is used to correct the measured drift times [40]. The determined

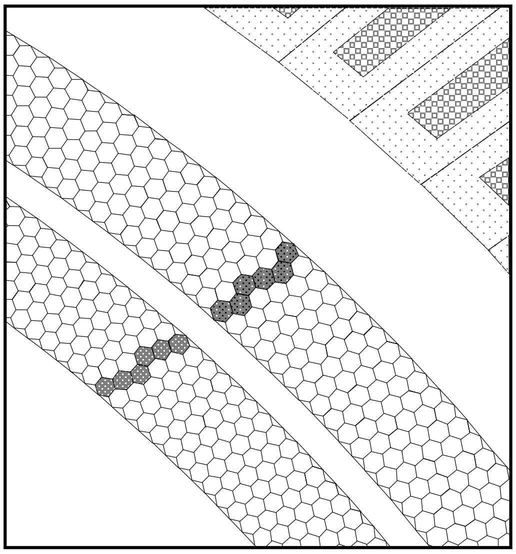

Figure 21: A portion of an R3 sector showing the layout of its two super-layers. The sense wires are at the center of each hexagon and the field wires are at the vertices. The shaded cells indicate hit-wires for a charged particle track ($\sim$ 1cm in radius).

drift times then are converted to drift distances and precise track information is reconstructed.

2.3.3 Time-of-flight Scintillator Counters

Scintillation counters are used to measure the time-of-flight(TOF) of particles from the target [40]. Since good momentum reconstruction depends on the timing resolution, the time-of-flight system requires good timing information for particle identification and, as we will show, the separation of pions and kaons up to 2 GeV/c. The system provides signals for the CLAS trigger electronics and timing analysis. It also has adequate granularity to give a uniform response for selecting individual particles reaching the time-of-flight detectors.

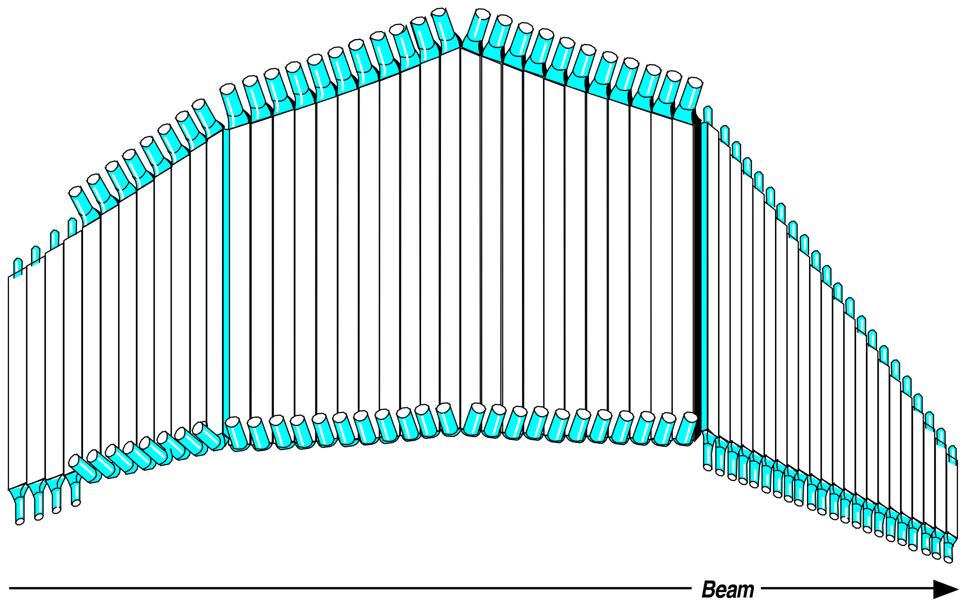

Figure 22: Time of flight counters.

Forty-eight scintillation counters per sector cover the polar angular range from 10 to 165 degrees. The scintillator counters are mounted in four panels in each of the six sectors. The material of the scintillators was chosen to have fast time response and low light attenuation. Fig. 22 presents a view of the TOF counters in one sector showing the grouping into four panels. Each scintillation counter is individually wrapped and assembled with two photomultiplier tubes and light guides. The integrated charge of the pulses from the photomultipliers is recorded by analog-to-digital converters (ADCs) and the timing information is provided via TDCs (time-to-digital converters). In order to identify particles by TOF, it is necessary to determine the flight time of particles of known momenta through a known trajectory. Therefore, precise timing information is achieved in the off-line software analysis using the momentum and position measured with the drift chambers.

The corrected TOF is obtained by using a radio frequency(RF) gated start signal, and the TOF scintillators to determine the time at the end of the particle trajectory through the detector. The electron beam comes in bunches at a rate of 499 MHz corresponding to the RF of the accelerator. The correct signal for each trigger is determined by identifying the final-state electron and tracing back to the interaction point. The TOF resolution is 150-250 ps allowing for unambiguous selection of the correct beam bunch, which is separated by 2.004 ns from the neighboring ones. As will be shown in section 4.2.2, the TOF information is combined with tracking information to determine particle speed, which is then combined with particle momentum information to determine particle identification.

The TOF system is also used for energy-loss measurements. Pulse height information, being proportional to the energy loss in the counter, provides an independent means for the identification of slow particles.

2.3.4 Čerenkov Counters

The Čerenkov detectors serve the function of separating electrons and pions in CLAS and is part of the electronics trigger. The Čerenkov effect happens when the velocity, βc, of the particle exceeds c/n, where n is the refractive index of the medium. The Čerenkov light is emitted in the form of a coherent wavefront at a fixed angle with respect to the trajectory. The wavefront forms the surface of a cone with the particle trajectory as the axis, such that

$$\cos\alpha = \frac{ct/n}{\beta ct} = \frac{1}{\beta n} \tag{28}$$

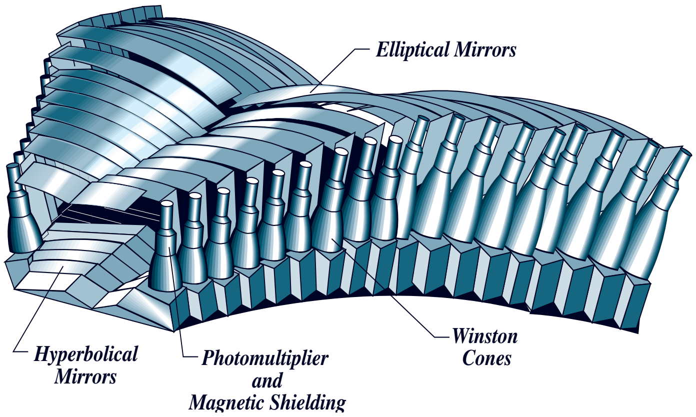

Figure 23: A schematic drawing of the array of the optical modules in one of the six sectors.

Therefore, the measurement of the angle in the above equation provides a direct measurement of the velocity.

The Čerenkov detectors in CLAS consist of 216 optical modules and are designed to maximize the coverage in each of the six sectors out to $\theta = 45°$. This is done by covering as much of the available space as possible with mirrors and placing light collecting cones and photomultiplier tubes in appropriate positions. Each sector is divided into 18 regions of θ, and each θ segment is divided into two modules about the symmetry plane bisecting each sector, Fig. 23. This results is a total of 12 identical sub-sectors around the Φ direction for each θ interval and a total of 216 light collection modules. The optics of each θ module is designed to focus the light onto a photomultiplier tube associated with that module. The optical elements consists of two focusing mirrors, a collection cone, and cylindrical mirror at the base of the cone. The trajectory of the light produced by a typical electron passing through the Čerenkov detector is also illustrated in Fig. 24.

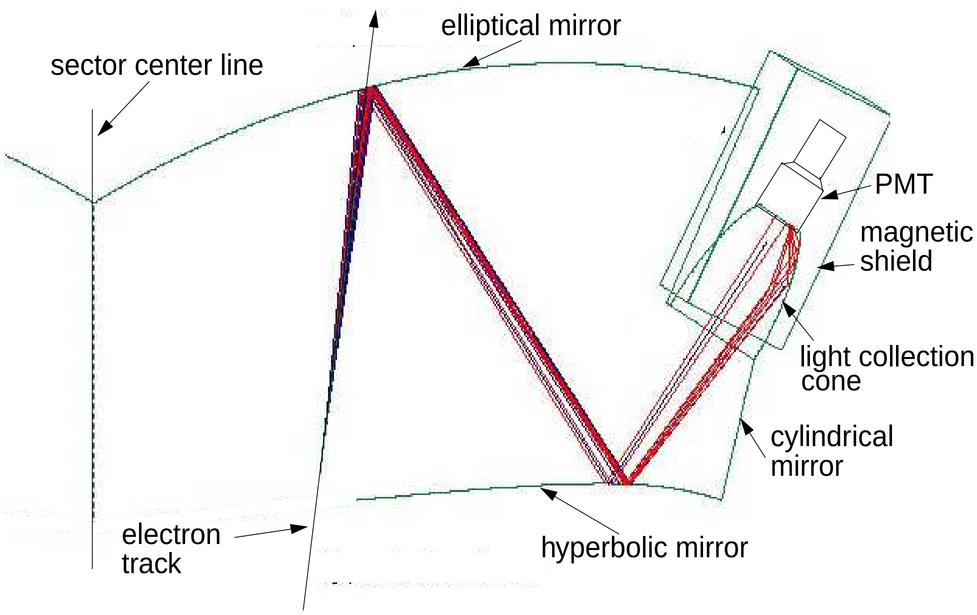

Figure 24: Optical arrangement of one of 216 optical modules of the CLAS Cerenkov detector, showing the optical and light collection components.

The radiator gas for Čerenkov counters in CLAS is C_4F_{10}, chosen for its light transmission properties and high index of refraction $n = 1.00153$. It results in a high photon yield and a high pion momentum threshold [41].

The photomultiplier signals provide one of the inputs for the CLAS trigger system. The Čerenkov ADC and TDC information is read out together with data from the other detector components using the CEBAF Online Data Acquisition system (CODA). During electron beam operation, a CC-EC coincidence indicates a valid electron scattering event.

2.3.5 Electromagnetic Calorimeter

The forward region ($8^\circ < \theta < 45^\circ$) of each sector is equipped with a lead-scintillator electromagnetic sampling calorimeter (EC). The main function of EC in CLAS is to

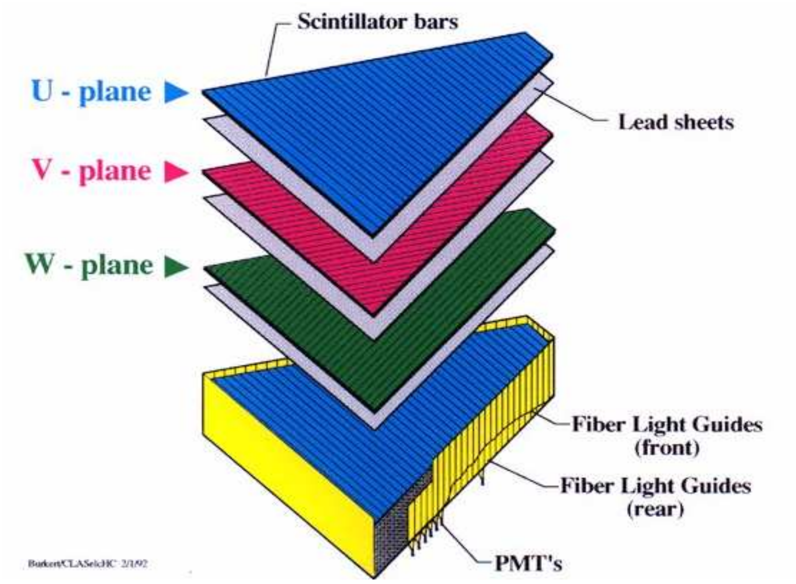

Figure 25: Exploded view of one of the six CLAS EC modules.

detect and trigger on electrons at energies above 0.5 GeV. The total energy deposited in the EC is available at the trigger level to reject minimum ionizing particles or to select a particular range of scattered electron energies. Electromagnetic calorimeters are the essential devices for measuring the energy and position of particles that produce electromagnetic showers. In the absorption process, the incident particle interacts in a large detector mass, generating secondary, less energetic particles and photons that in turn generate particles, so that all of the incident energy appears as ionization or excitation in the medium. The electromagnetic calorimeters provide fast "total energy" signals useful for quick decisions on event selection.

The CLAS EC is made of alternating layers of scintillator strips and lead sheets. There are 39 layers in the sandwich, each consisting of a 10-mm thick scintillator followed by a 2.2-mm thick lead sheet forming a triangular pyramid with a projected apex pointing at the CLAS target. Each scintillator layer is made of 36 strips parallel

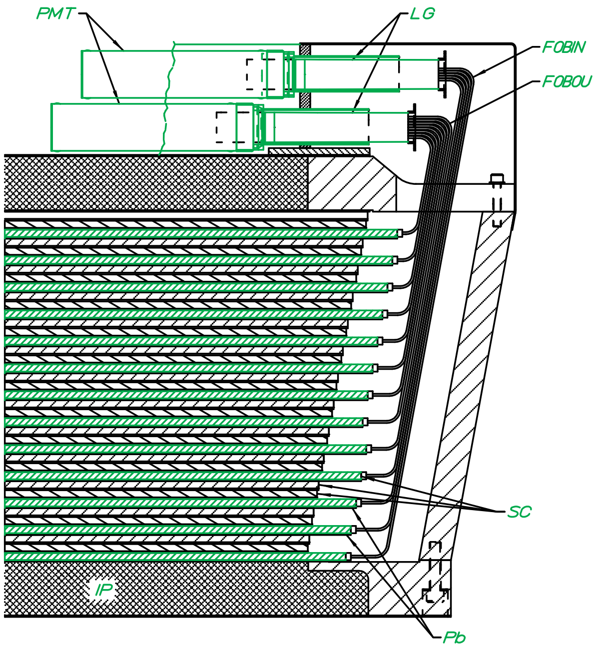

Figure 26: Schematic vertical cut of EC light readout system.

to one of the sides of the triangle, with the orientation of the strips rotated by 120 in each successive layer. Thus there are three orientations or views (U,V,W), each containing 13 layers, that provide information on the location of energy deposition. Each view is further subdivided into an inner (5 layers) and outer (8 layers) stack (Fig. 25) to provide longitudinal sampling of the shower for hadron identification. Each module thus requires $36(strips) \times 3(views) \times 2(stacks) = 216$ photomultipliers. A fiber-optic light readout system is used to transmit the scintillator light to the PMTs. Fig. 26 displays the schematic side view and vertical cut of the fiber-optic readout unit for a single inner and outer stack of the calorimeter module.

Electron triggers in CLAS require a signal based on the total energy deposited in the calorimeters. This is accomplished with a fast analog sum of all 216 PMTs in each EC module. Electronic NIM modules provide further summing in various combinations of U,V,W views for both inner and outer stacks. The CLAS electron trigger accepts only events that deposit more than minimum ionizing energy in the calorimeters, which, together with the Čerenkov counters, helps to reject pions. The response of the EC to a fixed deposited energy is uniform and independent of the position of the hit [42], provided the entire shower is contained within the volume of the EC.

2.4 Liquid Hydrogen Target

The target is positioned inside CLAS at the center of curvature of the inner toroidal coil. This is done using support structures that are inserted from the upstream end and are independent of the detector itself.

For the E1C running period, two different liquid hydrogen targets were used. The first target was a 5-cm-long Al cell with a wall thickness of 150 μm, and a window thickness of 1.0 μm. The target had a density of 0.0730 g/cm^3 and was kept at a temperature of 18 K. The second target was a 3.8-cm-long Al cell with a wall thickness of 120 μm, and a window thickness of 1.6 μm. The target had a density of 0.0695 g/cm^3 at a temperature of 20.5 K.

2.5 Trigger configuration and Data Acquisition

The signals from different parts of the CLAS detector are recorded by the data acquisition system when the chosen trigger condition is satisfied. The trigger system for CLAS is a two level system that is overseen by the Trigger Supervisor electronics.

Detector	Threshold (mV)
EC inner	60
EC outer	100
EC total	80
CC	20
SC	100

Table 1: CLAS detector thresholds for E1C running period. The Trigger condition was EC-inner, EC-total and CC coincidence.

The level 1 trigger provides a fast signal from the fast PMT-based detectors, such as CC and EC and then the level 2 trigger selects events with charged particles based on the preliminary track identification from DC hits. The signals from the two trigger levels are then passed to the trigger supervisor.

For this data set, only the level 1 trigger was used. The level 1 trigger requires hits in the EC and CC in the same sector that satisfy the detector thresholds summarized in Table. 1. With this trigger configuration, 45% of the electron-like events, were actual electron events. The remaining events consist of events in which the trigger is due to the noise in the CC counters or due to the hadrons that interact with the detector's structure producing showers.

The coincidence between the CC and EC initiates the CLAS data acquisition readout of all of CLAS. The TDC and ADC information from each detector component are written to a BOS data structure [43]. For the E1C running period, the typical data rate was about 8 MB/s with an event rate of 2 kHz. For the data set used in this analysis, at a beam energy of 2.567 GeV, the total number of triggers collected were 520 M and 390 M for torus settings of 1500 A and 2250 A respectively.

3 Event Selection for $p(\vec{e}, e'K^+)\Lambda$ Reaction

3.1 Data Sets

The data used is this analysis were from the CLAS E1C running period which took place from January to April 1999. Data were taken at various running conditions. We have included runs at an electron-beam energies of 2.567 GeV with torus current settings of 1500 and 2250 A. A complete list of the runs is in Appendix C. The electron beam was polarized with an average beam polarization of approximately 70%. Details of the beam polarization measurements are in Sec. 5.3. The kinematic coverage of this data set for the $p(\vec{e}, e'K^+)\Lambda$ reaction is shown in Fig. 27.

3.2 Event Reconstruction

The raw TDC and ADC values recorded in the BOS data files are converted to physical quantities using the CLAS standard reconstruction package and calibration constants [44]. In this process, the information from each detector is combined for track reconstruction, particle identification, and to finally reconstruct each physics event.

The event reconstruction is performed in several steps. First, the tracking process is done by fitting individual tracks to the hit-wire positions in the drift chambers ("hit-base" tracking). The track segments are then combined within each superlayer and across the three regions in each sector to identify the charge, target vertex position, and three-momentum vectors of each charged particle. The hits in the other detectors are then matched with these tracks to help the particle identification by

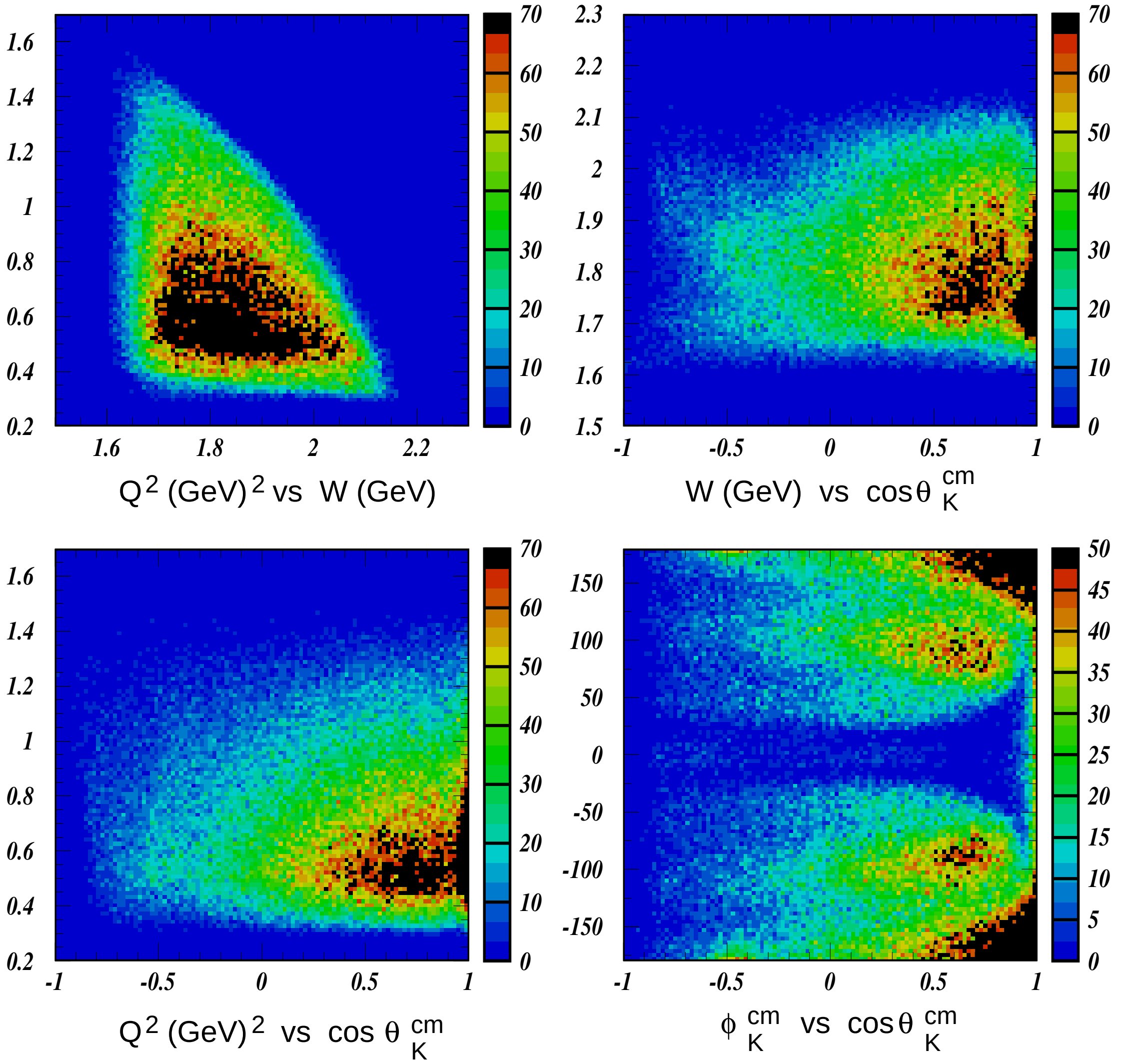

Figure 27: CLAS kinematic coverage for 2.5 GeV data. Top: Q^2 (GeV)^2 versus W (GeV) (left), W (GeV) versus $\cos(\theta_K^{cm})$ (right). Bottom: Q^2(GeV)^2 versus $\cos(\theta_K^{cm})$(left), ϕ versus $\cos(\theta_K^{cm})$ (right).

measuring the time-of-flight, energy loss, and Čerenkov light of the charged particles.

At this stage, comparing the track to a special track dictionary determines the approximate momentum of the particle with a 3-5% resolution. To improve the tracking resolution, the timing information of the electron track for each event is used. The "time-base" tracking is done by determining the drift time of the ionization electrons from the charged particles path to the nearest sense wire. Using an appropriate function to parameterize the drift time, it will determine the distance of closest approach, DOCA, of the charged particle track to the sense wire.

3.3 Detector Calibration

Before the final event reconstruction, each detector package must be calibrated to ensure the quality and accuracy of the detector response. This is usually done using a small portion of the actual data that is sampled from throughout the run period. In general, calibration is the parameterization of particular functions representing the measured quantities by each detector component such as time, energy, and position in terms of TDC and ADC values. These parameters or "calibration constants" are then stored in the proper calibration data bases to be used by event reconstruction codes.

For example, the CLAS drift chambers are calibrated by the parametrization of the drift velocity function for each superlayer in each sector [45]. This is done by fits to DOCA versus drift time plots. As mentioned in the previous section, DOCA values are obtained from fits that include all the layers by parametrization of the drift time, in time-base tracking. There are also several correction functions that are included in the actual functional form.

As for the TOF system, the reconstructed time and energies are determined by parameterization of adjusted time and normalized pulse heights of the left and right PMTs [46]. The Calibration constants are obtained to convert raw time in the units of TDC channels to the real time in nanoseconds, to determine the delay between left-right counters, and time-walk corrections [47], to determine the position of the hit in the scintillator, and to determine the effective velocity of light in the scintillator.

The energy and time calibration of each detector package results in sets of parameters that are adjusted to ensure the complete and accurate behavior of the detector. This procedure is done for each data set to account for different running conditions and hardware modifications.

3.4 Filtered Data

Due to the fact that most of the CLAS data do not contain kaons, a pre-selection of the kaon events was done using a kaon filtering program that skimmed through the data files and extract kaon events based on preliminary particle identification. In this analysis, the kaon candidates were selected by choosing positively charged particles with a reconstructed mass between 0.3 and 0.7 GeV^2/c^2 with the invariant mass greater than 1.5 GeV–slightly below the hyperon production threshold. Due to the huge amount of CLAS data and relatively low rate of kaon events, the skimming process increased the speed of the subsequent data analysis procedure.

3.5 Electron Identification

The final-state particle identification for the $p(\vec{e}, e'K^+)\Lambda$ reaction requires every event to have an electron candidate. The electrons are identified by looking for particles that satisfy EC-CC coincidence condition and have a negative DC track that is matched with the hit position of the TOF detector. Since these requirements have relatively loose cuts, the electron candidate sample is still contaminated with other negative particles. Therefore, software cuts are applied to improve the electron identification.

3.5.1 Energy deposition in the Electromagnetic Calorimeter

In electron scattering experiments, a large fraction of triggers are induced by pions. Pions with energy up to 2.5 GeV are mostly rejected in the threshold CC. To distinguish the higher energy pions from electrons, we can use the characteristic behavior of pions in the EC. Energetic π^- are minimum ionizing in the EC and therefore the total energy deposited in the EC by pions is proportional to the thickness of the detector and independent of the pion energy. On the other hand, electrons produce an electromagnetic shower and deposit an energy that is proportional to their energy. Fig. 28 shows the correlation between the energy deposited in the inner and outer layers of the calorimeter for tentatively identified pions and electrons. Using this feature we can remove the minimum ionizing pions by selecting electrons with a cut on the measured energy deposited in the inner layer of the EC as $EC_{inner} \geq 0.045$ GeV.

A large fraction of the electron energy is deposited in the lead sheets of the EC and not detected by the active elements. The sampling fraction is a characteristic of the detector and has been measured to be about 0.3. The sampling energy, E_{samp}, is defined as the total energy measured by the EC divided by the sampling fraction. This energy must be consistent with the momentum, p_e, as measured by

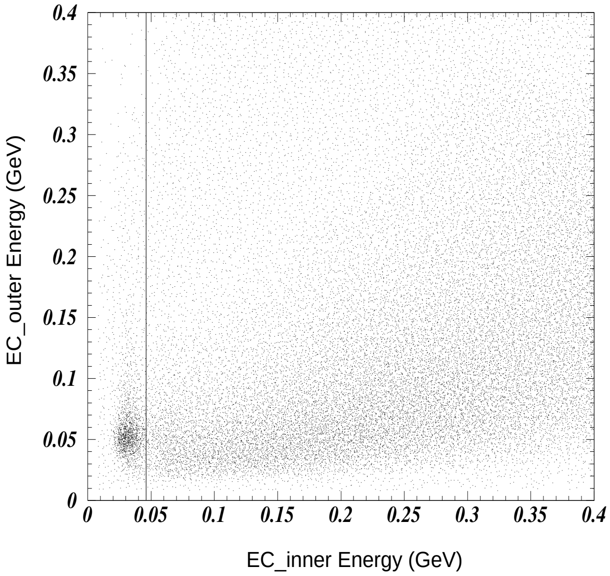

Figure 28: Correlation between energy loss in inner and outer EC layers for tentatively identified pions.

the tracking system. Fig. 29 shows the correlation between p_e and E_{samp} as well as the distribution of the ratio E_{samp}/p_e, which should be approximately one. The deviations from one in these plots corresponds to those pions that have triggered the CC and made their way into the electromagnetic calorimeter. The energy deposited by these pions equals to the minimum ionization energy and does not depend on the momentum of the pions. To remove these pions from the electron sample, we employed a cut on this ratio of $0.7 \leq E_{samp}/p_e \leq 1.4$.

We have also applied a cut on the EC trigger threshold due to the amplitude fluctuations in the EC hardware response near threshold. This cut was determined [48] to be

$$E_{EC}(\text{MeV}) \geq 214 + 2.47 \times (EC_{total} \ \text{ threshold in mV}).$$

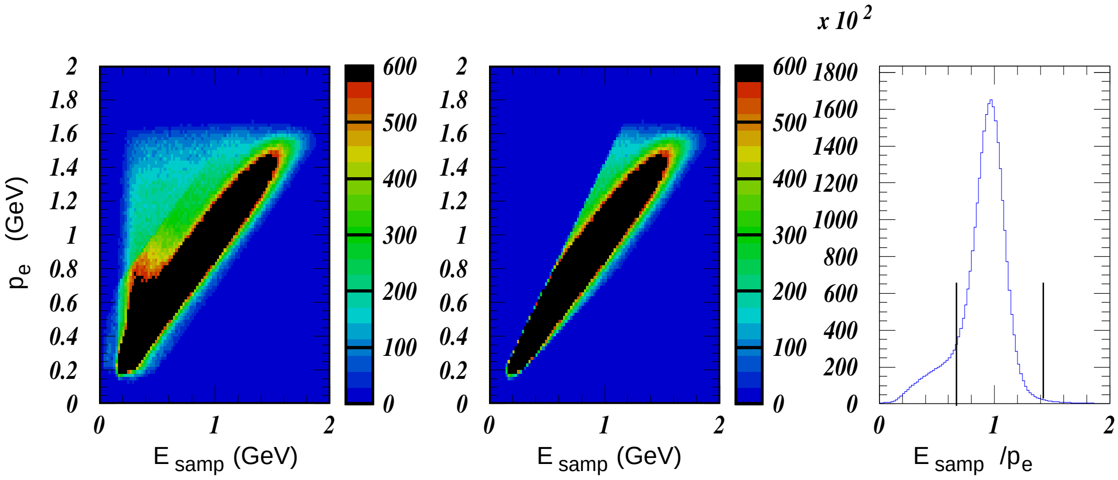

Figure 29: Electron momentum (GeV) measured by DC versus the energy deposited in EC by electron (GeV) before (left) and after (middle) the sampling fraction cut. Ratio of E_{samp}/p_e for electrons (right). The vertical lines show the cuts applied in this analysis.

3.5.2 Reconstructed Vertex Position

The coordinates of the target vertex are reconstructed by tracking the particle position back from the TOF detector to the target with information from the DC. As shown in 30 (left), the reconstructed z-vertex distribution of the target has a sector dependent offset. This is due to the fact that the target and the beam are not exactly on the central axis of the torus. In order to use a general vertex cut for all sectors for each running condition, the individual z-vertex distributions for each sector were plotted and fit with a function of the form

$$y = \frac{1}{a + b^{-c(z_e+d)}} \tag{29}$$

where y is the vertical axis, and d will be the sector-dependent offset that aligns the distributions. The z-vertex distributions are shown in Fig. 30 before and after the alignment. The general cut, $-2.9 \leq z_e \leq 2.2$ cm, are then applied to the distributions.

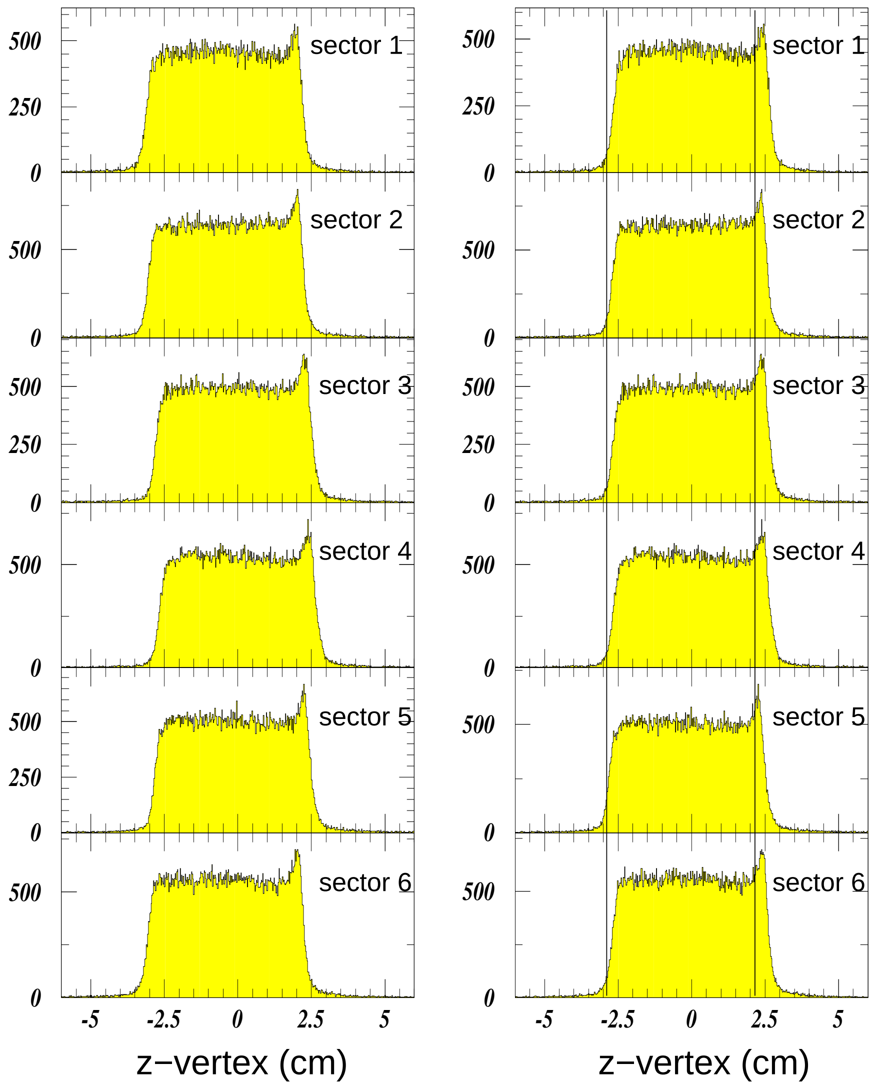

Figure 30: z-component of electron vertex position for 2.567 GeV for all six sectors of CLAS. Left (Right): before (after) the alignment. The $-2.9 \leq z_e \leq 2.2$ cm cut was applied after the alignment. (The bump is caused by the insulation layer around the target.)

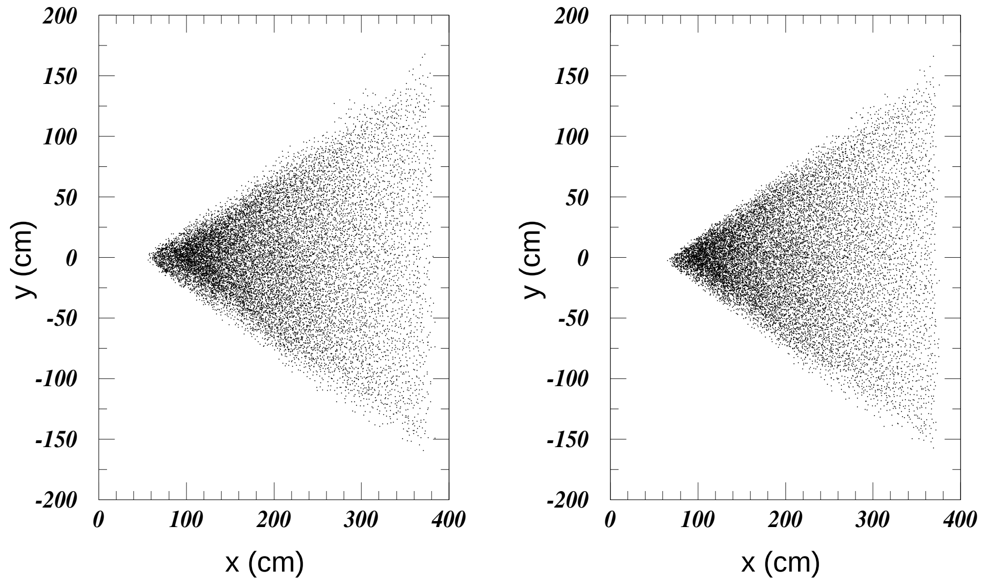

Figure 31: EC reconstructed event distribution, y versus x position on the face of the forward calorimeter for sector one before (left) and after (right) the EC fiducial cuts.

3.5.3 EC Fiducial Cuts

For events very close to the edges of EC the detection efficiency is non-uniform and the energy reconstruction is inaccurate due to the leakage. To ensure that the electromagnetic shower occurs fully within the EC sector, additional cuts were applied that require the event to be at least 10 cm away from the U, V, W edges of EC. For this purpose, we have used a subroutine written by S. Stepanyan [49] and the following cut:

$$20 \text{ cm} \leq U_{EC} \leq 400 \text{ cm}, \quad V_{EC} \leq 375 \text{ cm}, \quad W_{EC} \leq 405 \text{ cm}.$$

Fig. 31 shows the result of this cut.

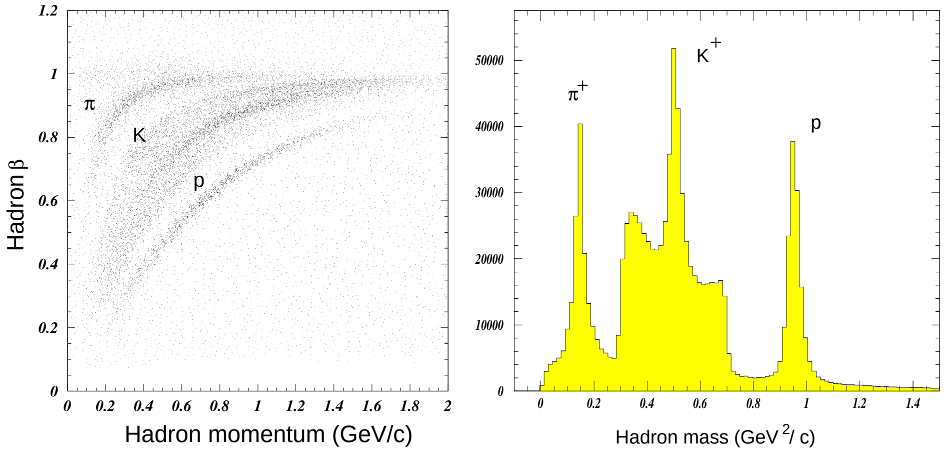

Figure 32: Left: β versus momentum for hadrons. Right: hadron mass spectrum. Data are shown are from kaon filtered (skimmed) data sample.

3.6 Hadron Identification

Hadrons are identified by calculating their mass from the measured momentum, p, and velocity, βc, according to

$$m_h = \frac{p}{\gamma \beta c}. \tag{30}$$

The momentum is calculated using tracking information from the drift chambers and the velocity is determined from the measured time of flight t and particle path length, l, which is also obtained from tracking information. The velocity is given in the usual way by

$$\beta c = l/t \tag{31}$$

Fig. 32 shows the β versus momentum versus momentum distribution for positively charged particles. The momentum and timing measurements will be discussed separately.

3.6.1 Time of Flight Measurement and Corrections

Particle time of flight is determined using the timing signal from the TOF detectors, t_{TOF}, the beam-target interaction time, or start time, t_{start}, and a correction necessary to match the start time with the proper beam burst, or RF bucket, t_{RF}.

$$t = t_{TDC} - t_{start} + t_{RF} \tag{32}$$

Since the electrons are identified independent of the TOF information as discussed above, we can reconstruct the event start time from the electron's measured time-of-flight. When the electron is identified, its signal in the TOF can be used as reference time, which along with the electron path-length, l^e, is used to reconstruct the start time:

$$t_{start} = t^e_{TOF} - \frac{l^e}{\beta^e c}, \tag{33}$$

where $\beta^e \approx 1$.

In order to improve the determination of the start time, the RF structure of the beam should be considered. The electrons ride on the top of the RF wave with a bunch length of a few picoseconds. The electron buckets are spaced by 2.004 ns (RF_{struc}). The time difference between the event-reconstructed start time and the arrival time of the closest bunch (a signal is recorded in the data stream with the arrival of the electron bunches) gives the RF correction, e.g. the mean of the remainder of the differences to RF signal [50]:

$$t_{RF} = MOD(t_{TDC} - \frac{l}{\beta c} - T_{RF}, RF_{struc}) - \frac{RF_{struc}}{2} \tag{34}$$

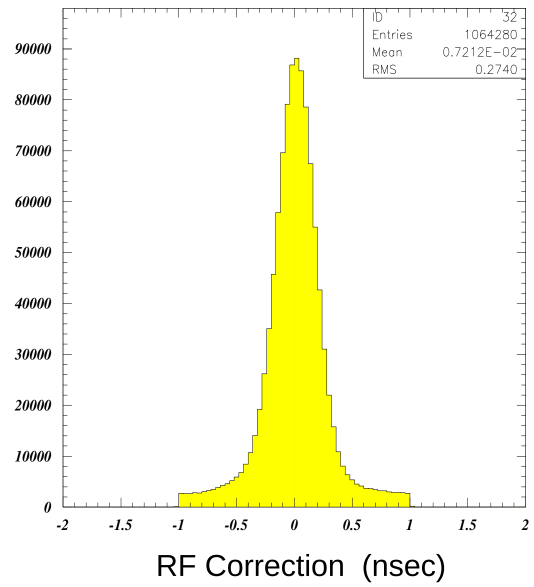

Figure 33: RF timing correction distribution for electrons (nsec).

The width of RF correction distribution (Fig. 33) around zero gives the TOF resolution.

3.6.2 Momentum-dependent Kaon Selection

As seen in Fig. 34 and Fig. 35, the hadron mass distribution varies with momentum. This is due to the loss of TOF resolution as the particle momentum increases ($\beta \rightarrow 1, \gamma \rightarrow 0$), Eq. 30. At high momentum the relative TOF uncertainty is large resulting in large mass uncertainty. This leads to the need for a momentum dependent mass cut which takes the form

$$m_K \geq 0.5 + 4.8 \times (0.005 + 0.00005 \times p_K + 0.01 \times {p_K}^2)$$
$$m_K \leq 0.5 - 4.8 \times (0.005 + 0.00005 \times p_K + 0.01 \times {p_K}^2) \qquad (35)$$

This functional form was suggested by the Saclay group [51].

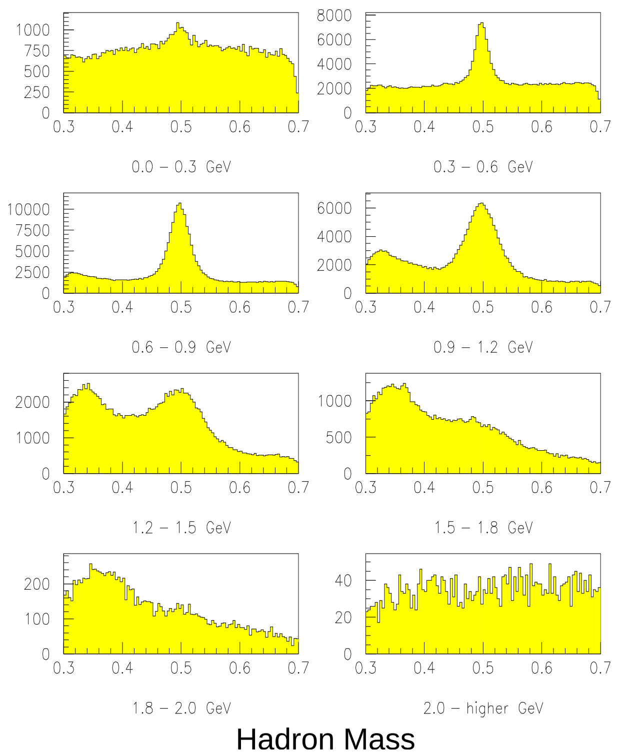

Figure 34: Hadron mass distributions for various hadron momentum cuts.

3.6.3 Reconstructed z-Vertex for Kaons

Using tracking information, we can reconstruct the kaon creation point along the beamline similar to the way this was done for the electron. We have employed a cut on this reconstructed z component of the vertex position for kaons to ensure that the selected kaons came from the liquid hydrogen target:

$$-3.5 \text{ cm} \leq z_K \leq 3.5 \text{ cm} \tag{36}$$

Fig. 36 shows the distribution of the z-vertex of kaons for each sector. Because of finite resolution effects, this vertex differs slightly from the electron vertex position and a wider cut was used.

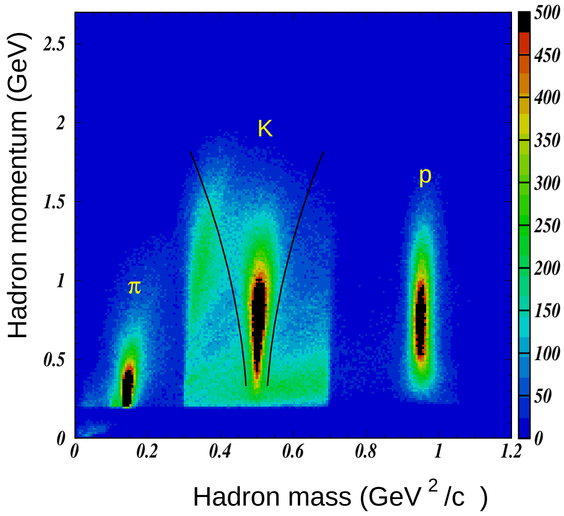

Figure 35: Hadron momentum versus mass. The overlaid curves show the kaon mass cut used in this analysis.

3.7 TOF Bad Paddle Removal

The poorly performing TOF scintillators are removed from this analysis. This includes the dead or noisy paddles that do not respond to the signals or have poor resolution. Fig. 37 and 38 show the RF correction distribution versus SC paddle number for each sector of CLAS and for electrons and kaons respectively. The poorly performing SC paddles have RF correction distributions that are too wide or non-Gaussian. Events in which any of these bad scintillators are involved for electrons and kaons are removed from the analysis. The list of paddles that are disregarded in this work are given in the table 2.

3.8 Fiducial Volume Cuts

The fiducial volume cuts are geometrical cuts dependent upon laboratory angles θ and ϕ, momentum, and field settings. The good acceptance defined by these cuts

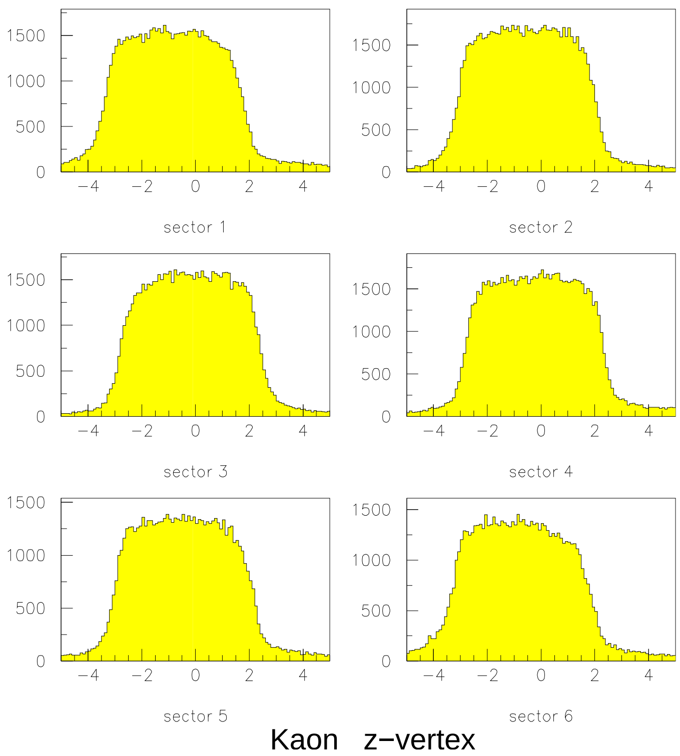

Figure 36: Z-vertex distribution for kaons along the beam line for the six sectors.

are different for electrons and kaons. The general form of these cuts are the result of work by C. Smith [52]. These cuts are used to ensure that these particles are detected within the volume of CLAS where the detection efficiency is relatively large and flat. The accepted ϕ regions for electrons are

$$\begin{aligned} \Delta\phi_e &= 30.0 \times \sin\left(\theta_e - \theta_{min}\right)^x \\ \theta_{min} &= 8.5 + 17.5/(p_e \times I_{max}/I + 0.15) \\ x &= 0.35 \times \left(p_e \times I_{max}/I\right)^{0.333} \end{aligned} \tag{37}$$

where I_{max}/I represents the ratio of the maximum torus current setting, $I_{max} = 3375$ A, to the nominal setting, I, θ_{min} is the minimum scattering angle, which is a function of momentum for in-bending electrons, p_e is the electron momentum, θ_e,

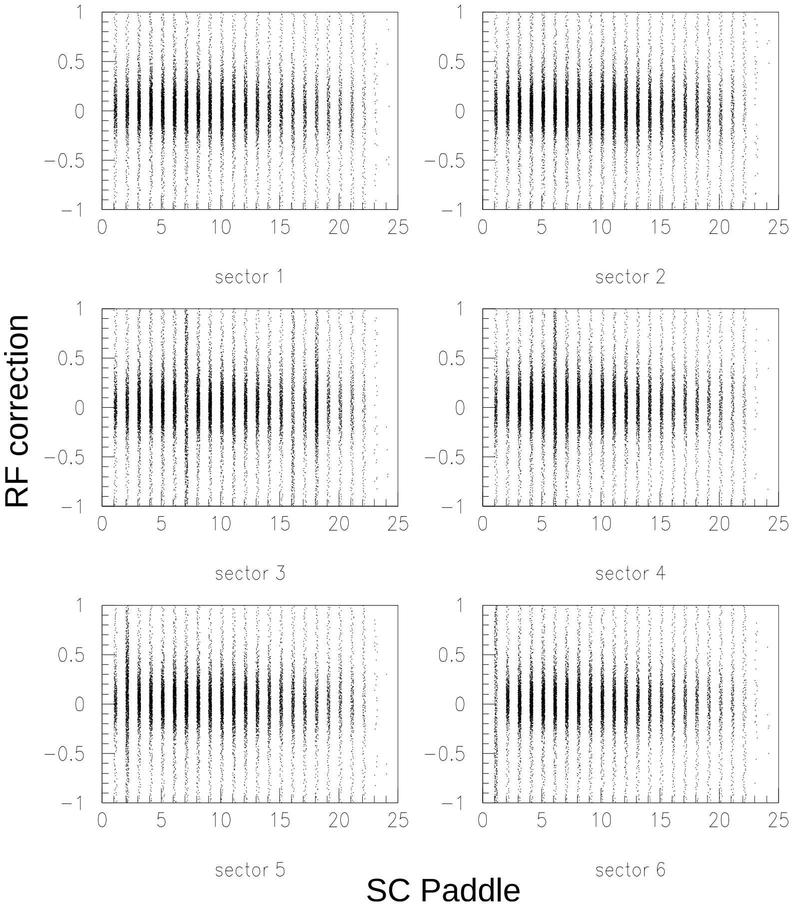

Figure 37: RF correction versus SC paddle number for electron). The poorly performing paddles in each sector can be distinguished in the histogram.

and ϕ_e are the polar and azimuthal electron angles. The following cuts are used for kaons:

$$\Delta\phi_h = 25.0 \times (1 - \exp(-0.15 \times (\theta_h - 9.0))) \tag{38}$$

Fig. 39 and Fig. 40 show θ versus ϕ distribution before and after the above cuts for electrons and hadrons respectively.

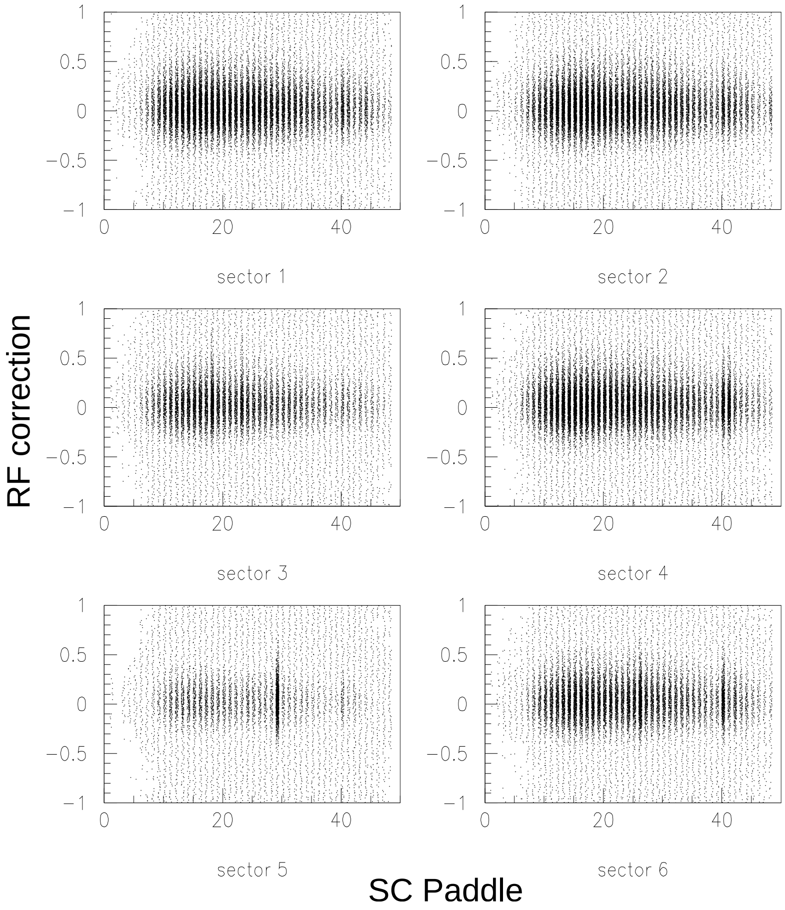

Figure 38: RF correction versus SC paddle number for kaons. The poor performing paddles in each sector can be distinguished in the histogram.

3.9 Momentum Corrections

Due to the uncertainties in the description of the drift chamber position in the tracking code as well as in the magnetic field map, there is an artificial angular dependence to the position of the ep elastic scattering peak in the W spectrum as seen in the left of Fig. 41. The fact that the fixed value of elastic peak in the W spectrum ($W = 0.937$ GeV) is independent of the kinematics of the reaction of interest, can be used as an indicator to check the quality of the tracking and therefore calibrate the reconstructed electron and hadron momenta.

Sector	Bad Paddles for 2.5 GeV data
1	≥ 40
2	≥ 40, 6
3	≥ 40, 7, 16, 18, 23, 37, 38
4	≥ 40
5	≥ 40, 2, 29
6	≥ 40, 1, 29

Table 2: List of the TOF paddles that are removed from the analysis.

This analysis uses the general momentum correction for CLAS suggested by the University of Pittsburgh group to adjust the magnitudes of the reconstructed electron and hadron momenta [53]. For a uniform magnetic field, the detector misalignments lead to a shift in the curvature of the particle's track in CLAS that is proportional to $\frac{qB}{p}$, where B is the magnetic field, and q and p are the particle's charge and momentum respectively. In general, this mismeasurement is shown to be in the form of:

$$\Delta(\frac{q\int Bdl}{p}) = \alpha + \beta\frac{q\int Bdl}{p} \tag{39}$$

where α and β are functions of θ and ϕ that depend on the residual drift chamber misalignments and errors in the magnetic field map respectively (see Ref. [53] for details). α and β parameters are determined for ep elastic scattering but can be generally applied.

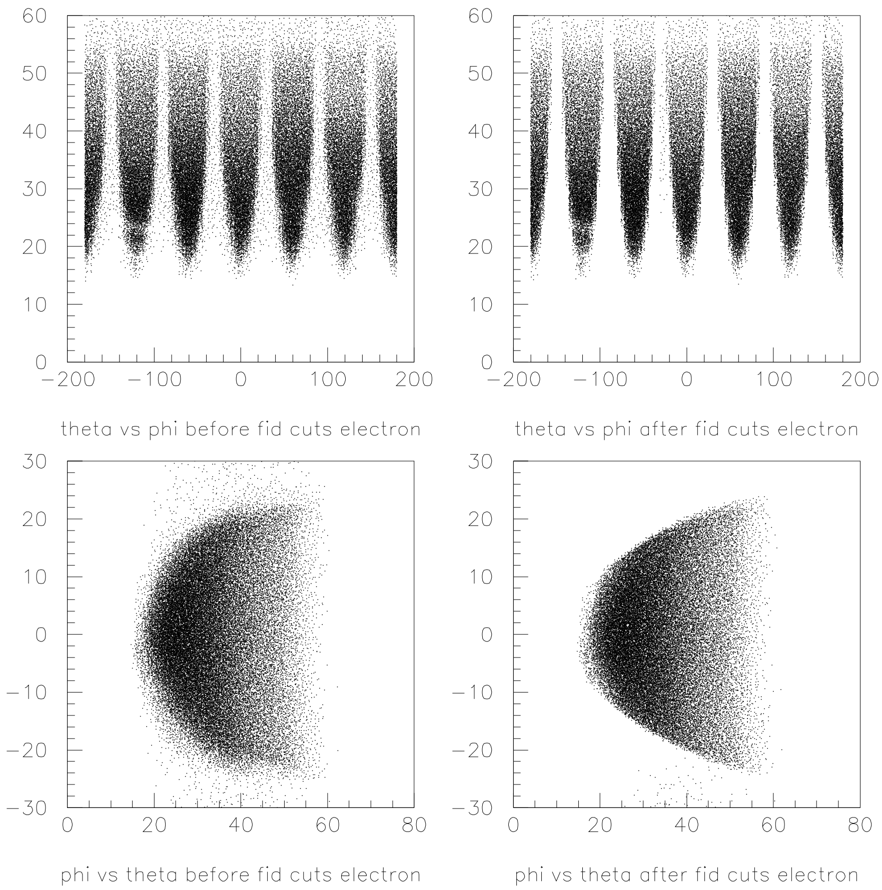

Figure 39: Top: θ_e distribution versus ϕ_e before (left) and after (right) the fiducial cuts. Bottom: ϕ_e versus θ_e , sector 1, before (left) and after (right) the fiducial cuts for electrons.

The momentum correction is applied to both electrons and hadrons. The reconstructed electron and kaon momenta are plotted in Fig. 42 and Fig. 43 versus the change in the momenta after applying the above correction function. The order of these corrections is about 1%. These corrections not only improve the position and resolution of the elastic peak in W versus ϕ, as shown in Fig. 41 but also improves the resolution of the hyperon missing mass spectrum (Fig. 44) reducing the width of lambda peak from $\sigma = 7.2$ MeV to 5.9 MeV.

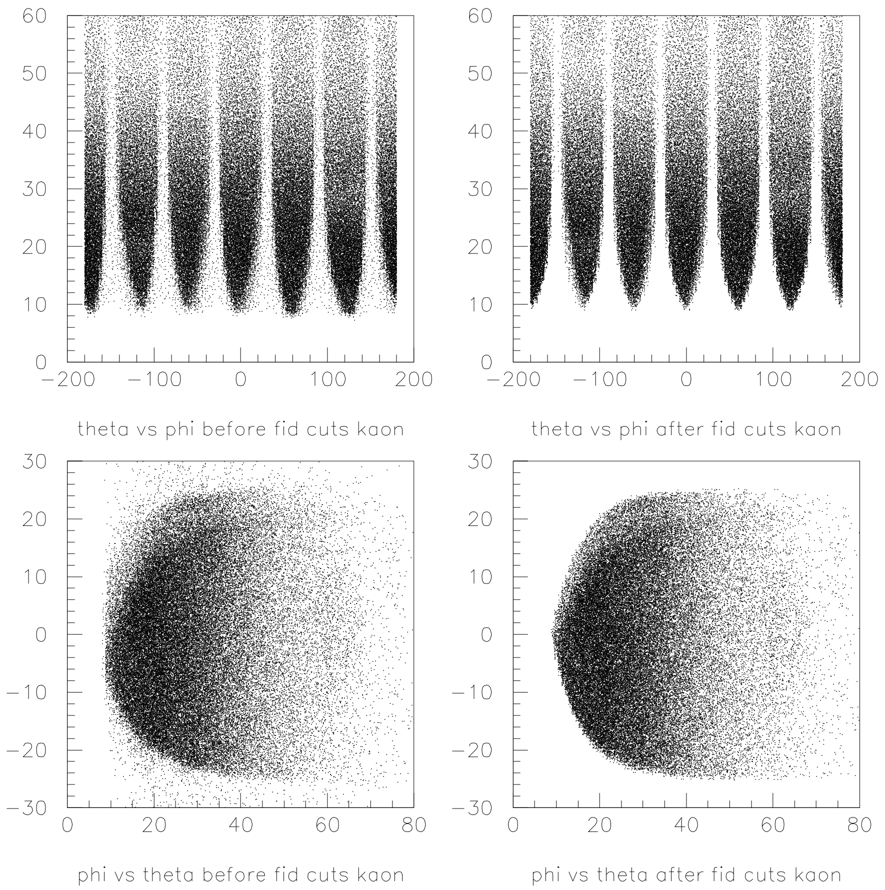

Figure 40: Top: θ_K distribution versus ϕ_K before (left) and after (right) the fiducial cuts. Bottom: ϕ_K θ_K , sector 1, before (left) and after (right) the fiducial cuts for kaons.

3.10 Hyperon Missing Mass

The hyperons are identified by the reconstruction of missing-energy, Y_0, and missing-momentum, $\mathbf{Y}$, of the $e'K^+$ final-state. The final state kaon's momentum in the laboratory frame is measured to be $K_\mu = (K_0, \mathbf{K})$. Therefore, the inferred hyperon four momentum is:

$$Y_\mu = q_\mu + p_\mu - K_\mu \tag{40}$$

$$\mathbf{Y} = \mathbf{q} - \mathbf{K} \tag{41}$$

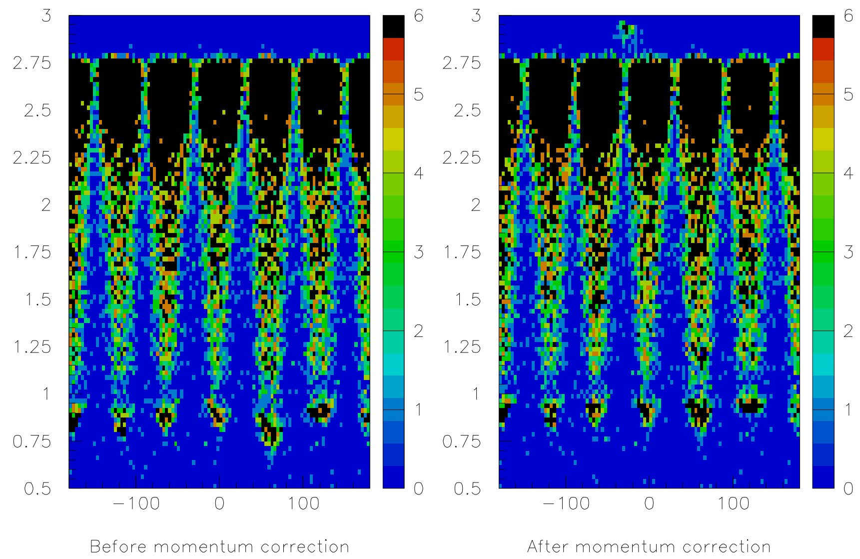

Figure 41: W versus ϕ before (left) and after (right) momentum corrections. The *ep* elastic peaks are aligned for all the 6 sectors after the electron momentum correction.

$$Y_0 = \nu + M_p + K_0 \tag{42}$$

$$M_m^2 = Y_0^2 - |\mathbf{Y}|^2 \tag{43}$$

where K_0 and $\mathbf{K}$ are the energy and momentum of the detected hadron–a kaon in this case–and M_p is the mass of target proton. Fig. 44 shows the reconstructed missing-mass spectrum summed over all kinematic variables. The missing-mass distribution for selected kinematic bins can be found in Fig. 45. These figures show distributions in which backgrounds have not been removed. A detailed discussion of background subtraction is found in section 4.1.

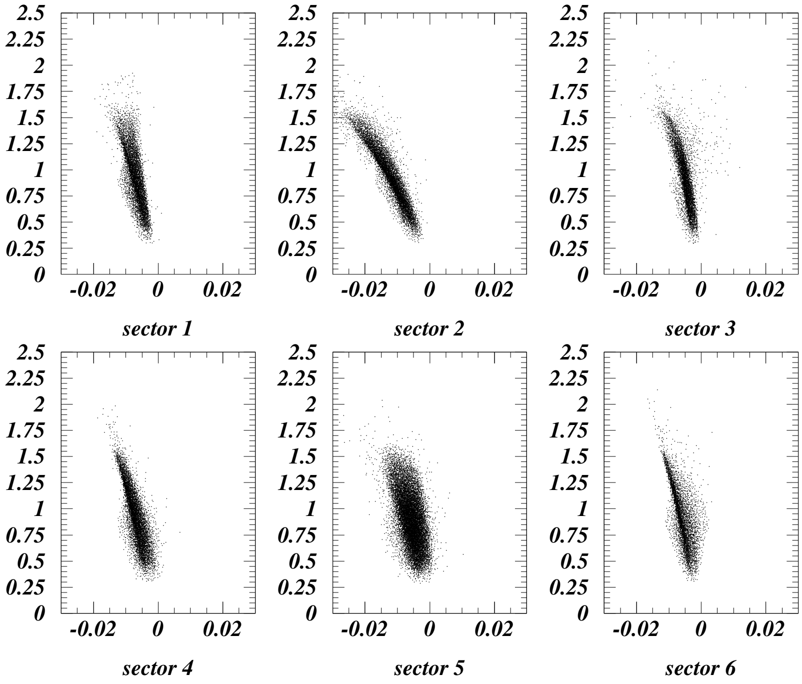

Figure 42: Reconstructed electron momentum (GeV/c) after momentum correction plotted versus the momentum correction (GeV/c) applied for all six sectors.

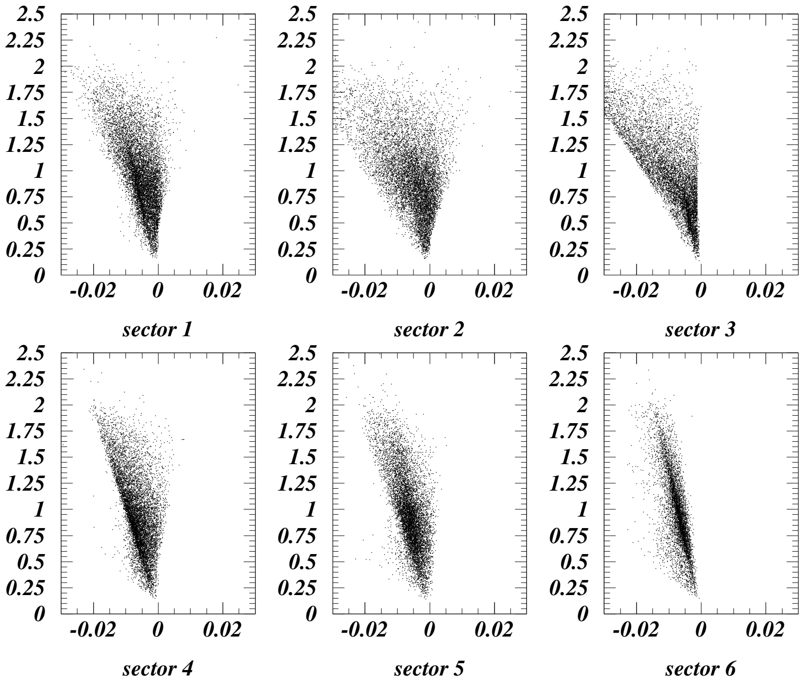

Figure 43: Reconstructed kaon momentum (GeV/c) after momentum correction plotted versus the momentum correction (GeV/c) applied for all six sectors.

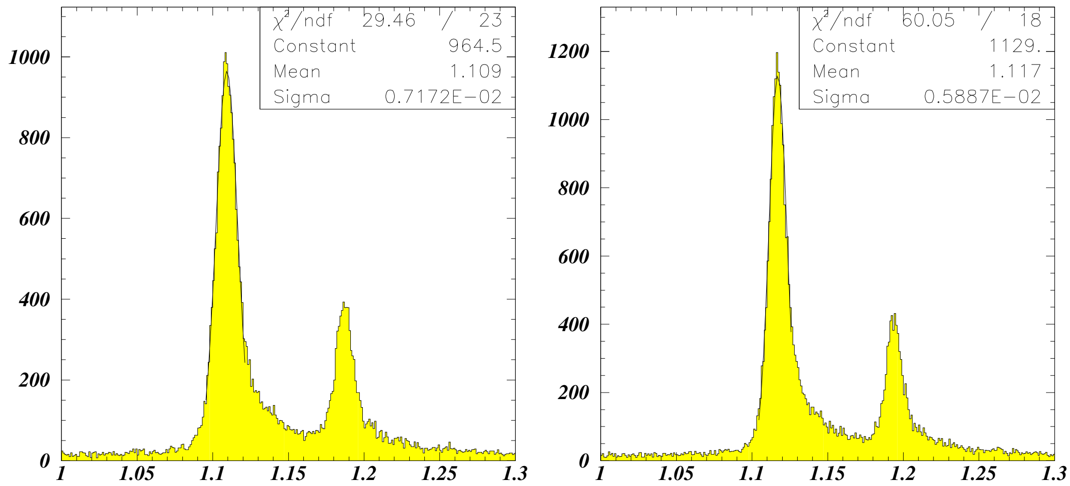

Figure 44: Hyperon missing mass spectrum (GeV) generated for $\vec{e} + p \to e'K^+Y$ events. Left (Right) figure is before (after) the application of the momentum corrections. The fitted width of the Λ peak is reduced from 7.2 MeV to 5.9 MeV.

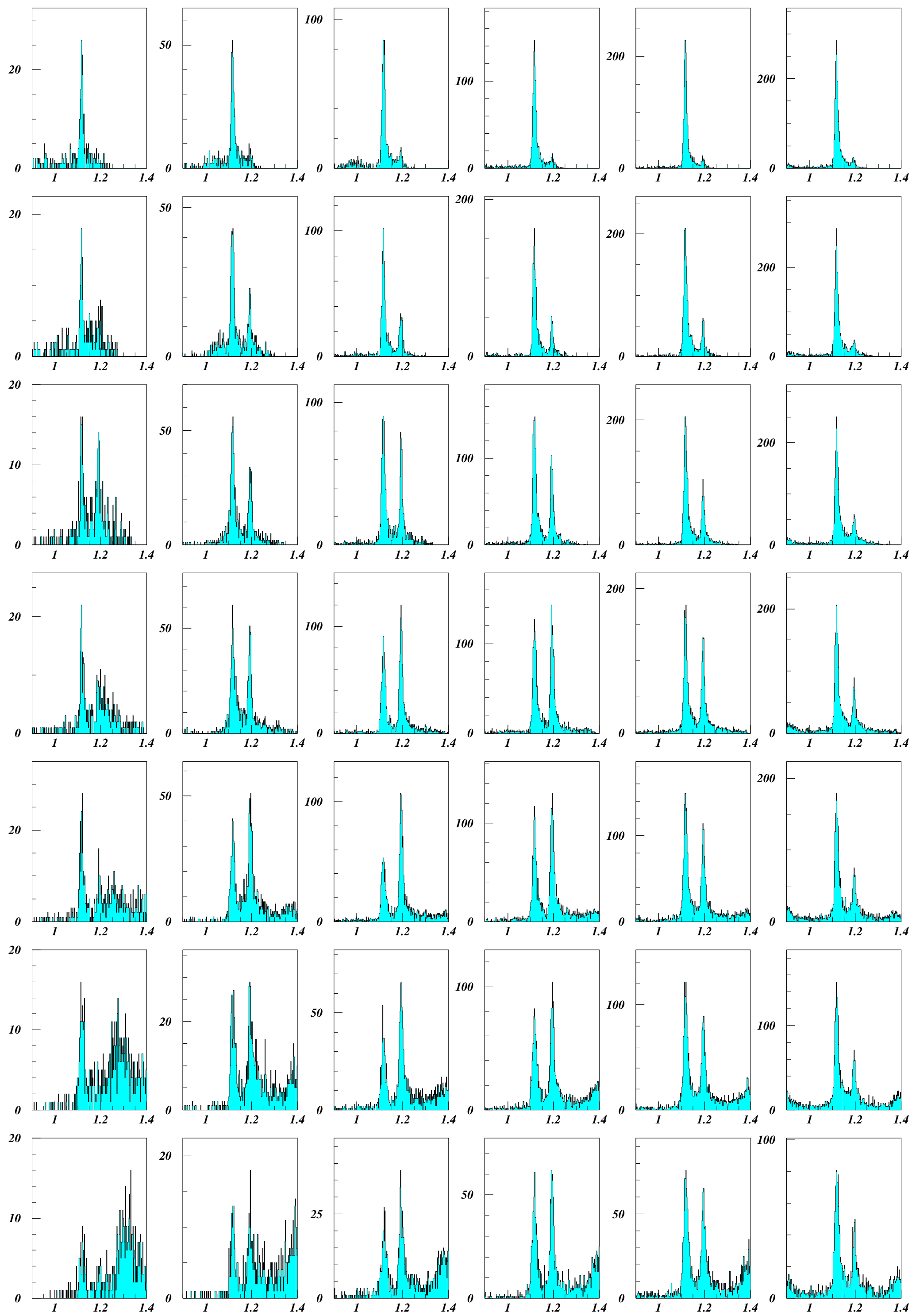

Figure 45: Missing mass (GeV) distributions for $Q^2 = 0.7$ GeV^2 and (left-to-right) $\cos\theta_K^* = -0.833, -0.500, -0.167, 0.167, 0.500, 0.833$ and (top-to-bottom) $W = 1.725, 1.775, 1.825, 1.925, 1.975, 2.025$ GeV and helicity +1.

4 Yield Extraction for $p(\vec{e}, e'K^+)\Lambda$ Reaction

The yields of the $ep \rightarrow e'K^+\Lambda$ reaction are extracted from the missing-mass distributions sorted for each helicity state and binned over the kinematic variables, Q^2, W, $\cos\theta_K^{cm}$ and ϕ. In this chapter, we will explain in detail, the procedure for extracting the background subtracted yields for the $p(e, e'K)\Lambda$ reaction for each kinematic bin as well as yield corrections that must be considered such as detector acceptance and radiative corrections.

4.1 Background Corrections

The background contributing to the missing-mass histograms (Fig.46) comes from the misidentified pions and protons in the selected kaon sample (Fig. 32). To study the effect of this contamination, the following possible background reaction channels are considered: for the case that a π^+ has been misidentified as a kaon, the reactions are

- $e + p \rightarrow e' + n + \pi^+$

and for the case of a proton in the final state,

- $e + p \rightarrow e' + p + \eta$
- $e + p \rightarrow e' + p + \omega$
- $e + p \rightarrow e' + p + \rho^0$
- $e + p \rightarrow e' + p \quad$ (elastic)

These final-state reactions have kinematics determined by the masses of the interacting particles at a fixed W. This means that the final-state particles are kinematically

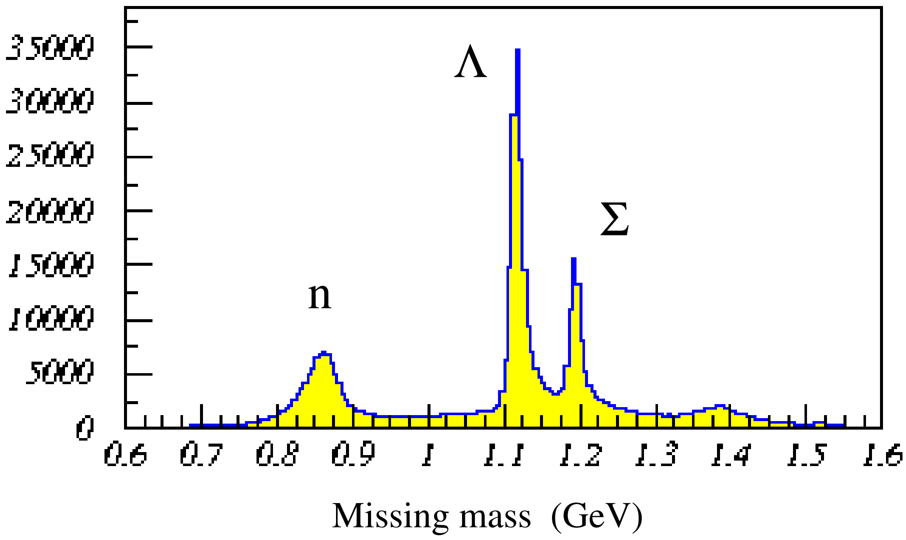

Figure 46: Missing mass spectrum for $e'K^+Y$ final state showing the Λ and Σ peaks with a uniform background. The shifted neutron peak, corresponding to the $e'\pi^+n$ final state, is also seen. The shift in the neutron missing mass is due to the pions being misidentified as kaons.

constrained and therefore, it is possible to remove these channels by using kinematic cuts. The upper panel of Fig. 47 shows the distribution of the proton (left) or π^+ (right) center-of-mass angle with respect to the virtual photon direction, θ_p^{cm} and θ_π^{cm}, versus missing mass for the case that a π^+ or a proton is detected along with the scattered electron in the final state. The distributions show clearly the mass of the undetected or missing particles. However, the lower panel of the same figure show the same distribution for the case that a π^+ or a proton is misidentified with a kaon i.e. the pions or protons are selected as kaons and are assigned the kaon mass. The signature of the contribution of these misidentified particles can be seen in lower left panel of Fig. 48. The $e'n\pi^+$ events are in the correlated band around 0.85 GeV.

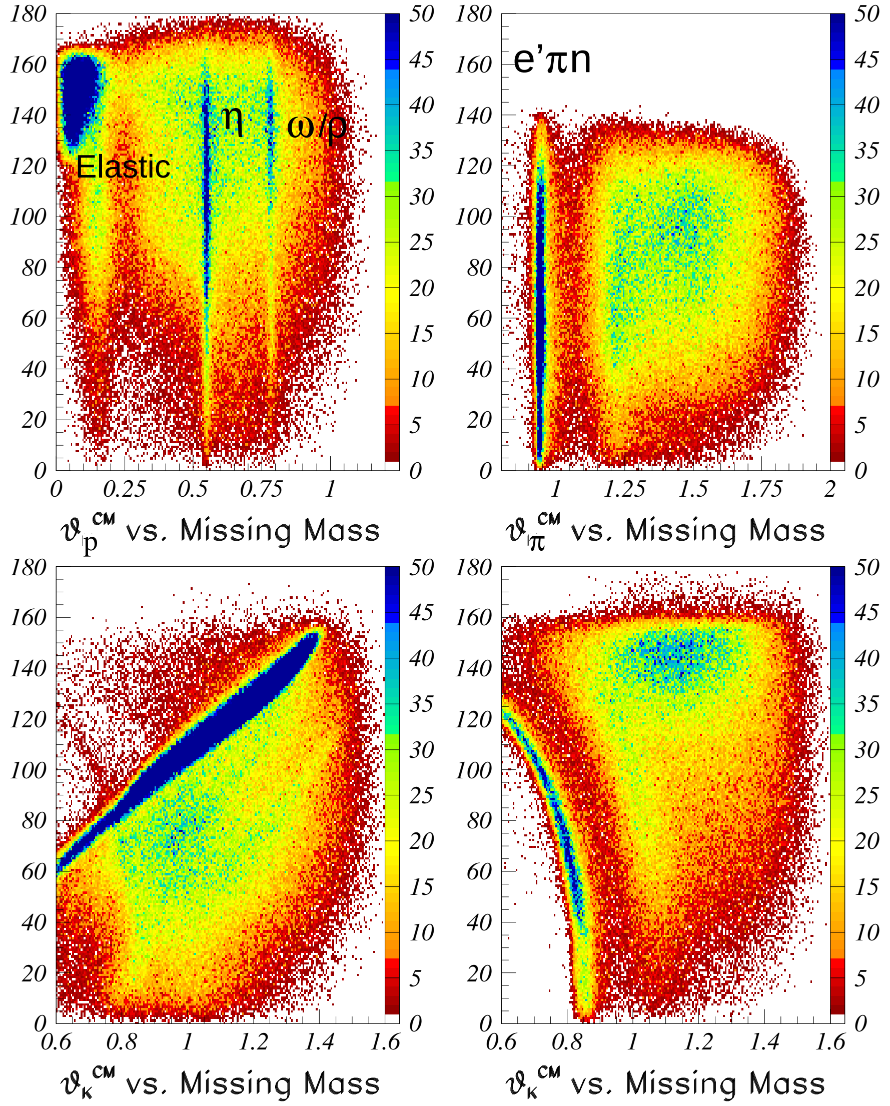

Figure 47: Top: the angular distributions of the detected hadrons with respect to the direction of the virtual photon in the center-of-mass frame versus the missing mass for $e'pX$ (left) and $e'\pi^+X$ (right) final states. Bottom: the same final states but assigning the kaon mass to protons (left) and pions (right).

The $e'p$ elastic events fall in the diagonal band that extends from 0.6 to 1.4 GeV. To remove the background reaction channel corresponding to the $e'\pi^+n$ final states, a cut is used on the missing mass distribution shown in upper left panel of Fig. 48. This distribution is obtained by selecting all the hadrons in the final state

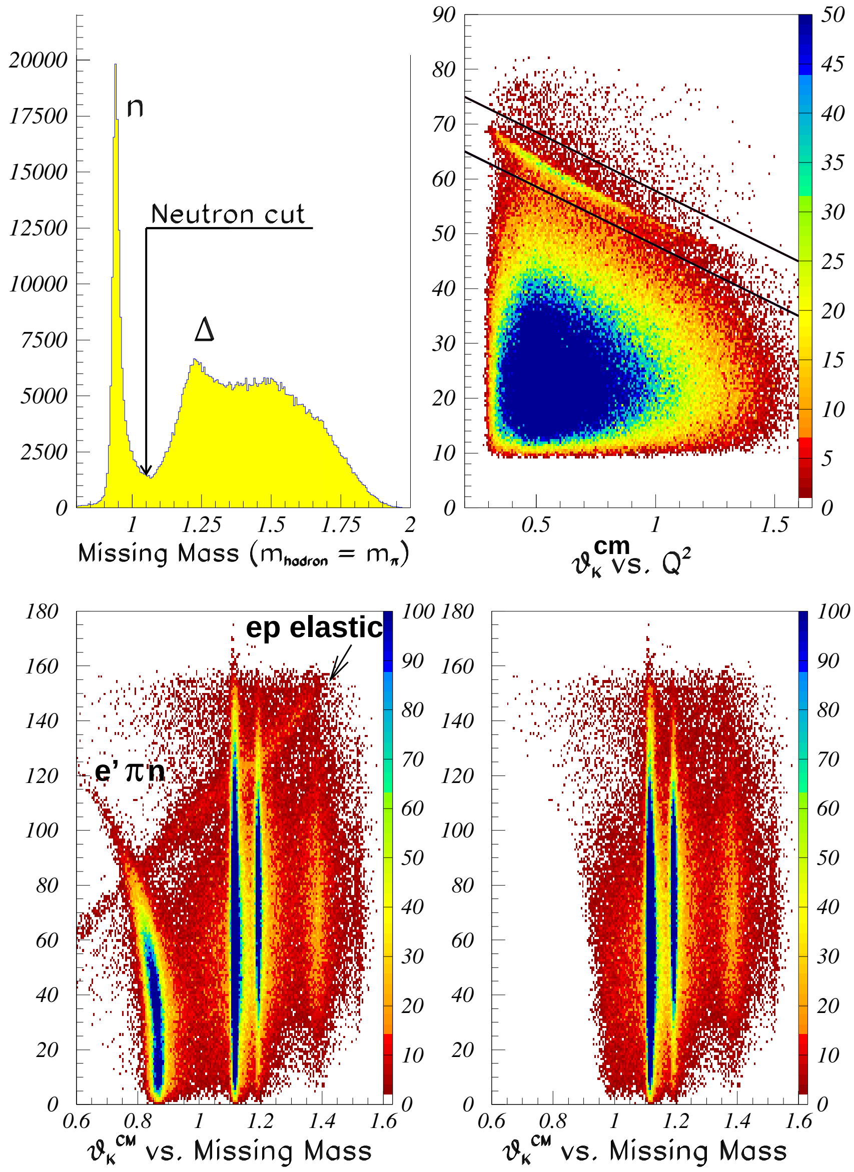

Figure 48: Cuts applied to remove the background channels. Top left: cut on the neutron missing mass to remove the $e'\pi^+n$ final states. Top right: cut on θ_K^{cm} to remove the elastic events. Bottom left (right): θ_K^{cm} versus missing mass before (after) the above cuts.

and assigning the pion mass to them. A cut is then placed at 1.05 GeV, as shown. The ep elastic events can be kinematically isolated in a distribution of θ_K^{cm} versus Q^2, shown in the upper right panel of Fig. 48. The elastics are removed using the cut shown. The lower panels of the same figure shows θ_K^{cm} versus the missing

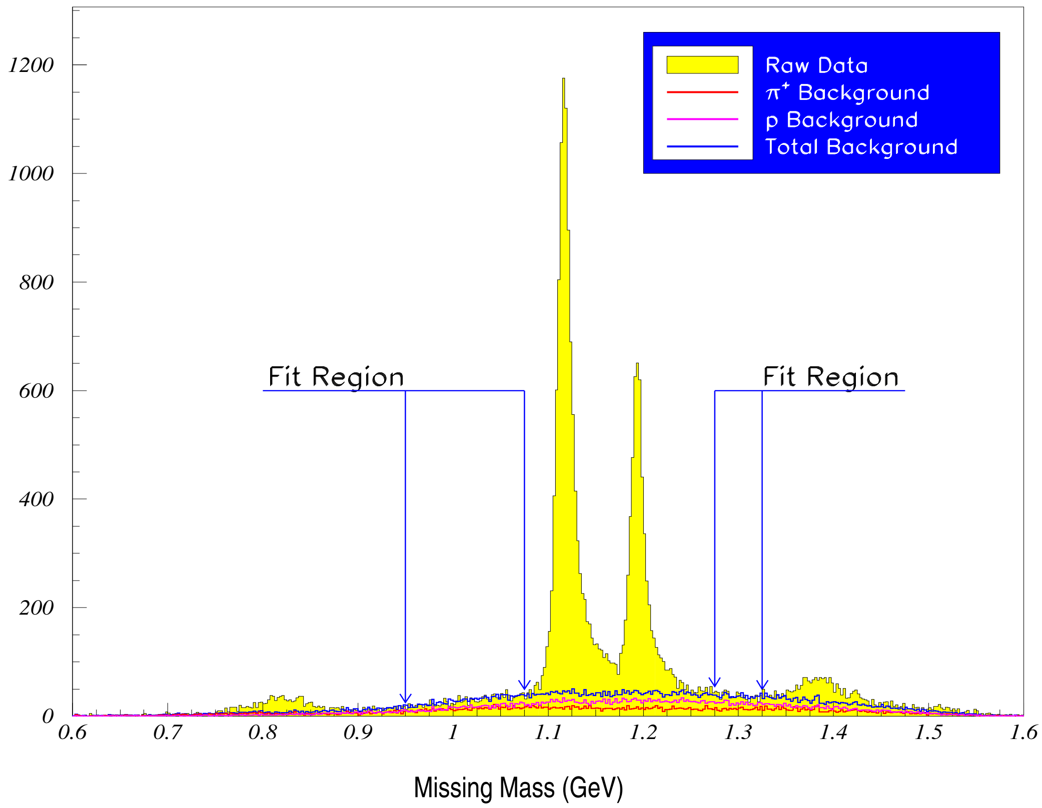

Figure 49: The estimated background phase space using events outside of kaon selection cut. The background distributions from pions and protons are fitted to the data using maximum log likelihood method in the fit regions that most dominate. Each distribution is weighted by the best estimate of its contribution to the fit in order to calculated the total background.

mass before (left) and after (right) the two above cuts. The $e'p\eta$, $e'p\rho^0$, and $e'p\omega$ channels do not make a significant contribution to the background and are removed in the process of subsequent background subtraction. The question of removing the background due to the multi-particle final-state channels such as

– $e + p \to e' + \pi\pi ...$

– $e + p \to e' + p + \pi\pi ...$

is not as trivial as the previously mentioned final-state reactions. These channels are not constrained by the kinematics of the reactions and can have an arbitrary

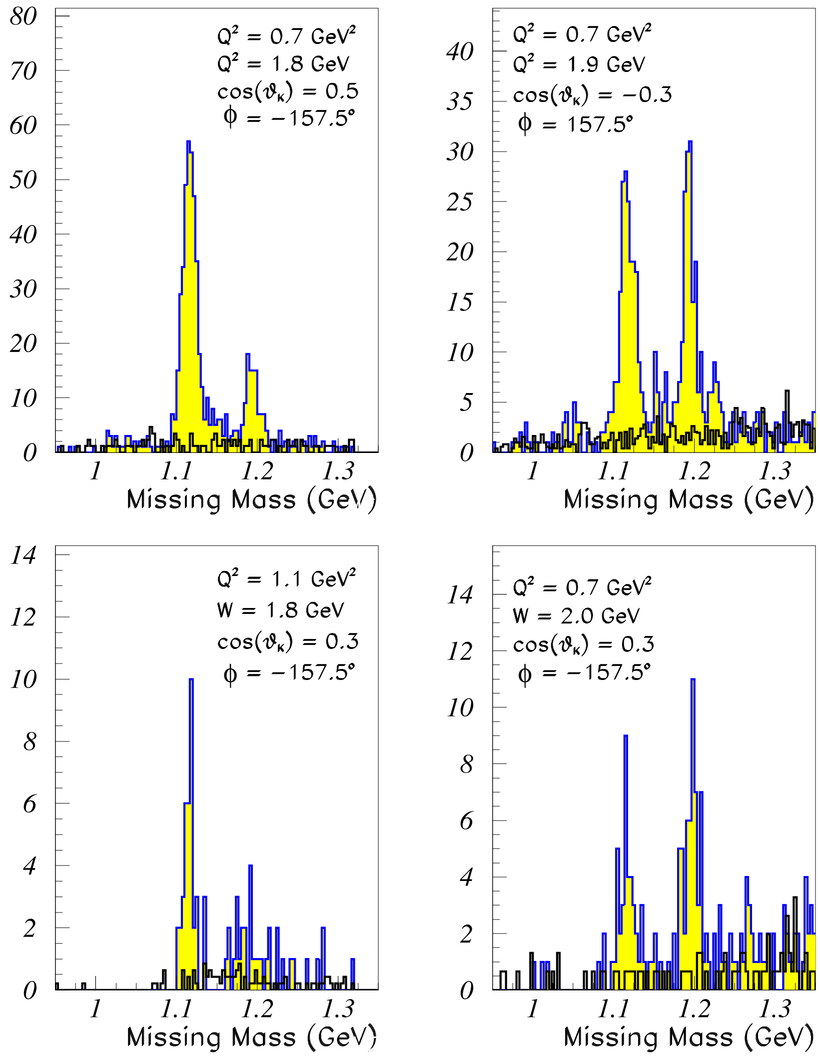

Figure 50: Example of the background fit results for various kinematic bins using fitted background method. The fits are performed in the regions where the phase space dominates.

amount of energy and momentum distributed among the final state particles. These correspond to the uniform background shape and are modeled with a phase space background.

In order to model the phase space background for the missing mass histograms, the contributions of protons and pions outside of the kaon mass cut are used. (Fig. 35). The unskimmed data files were used to select uncorrelated pions and

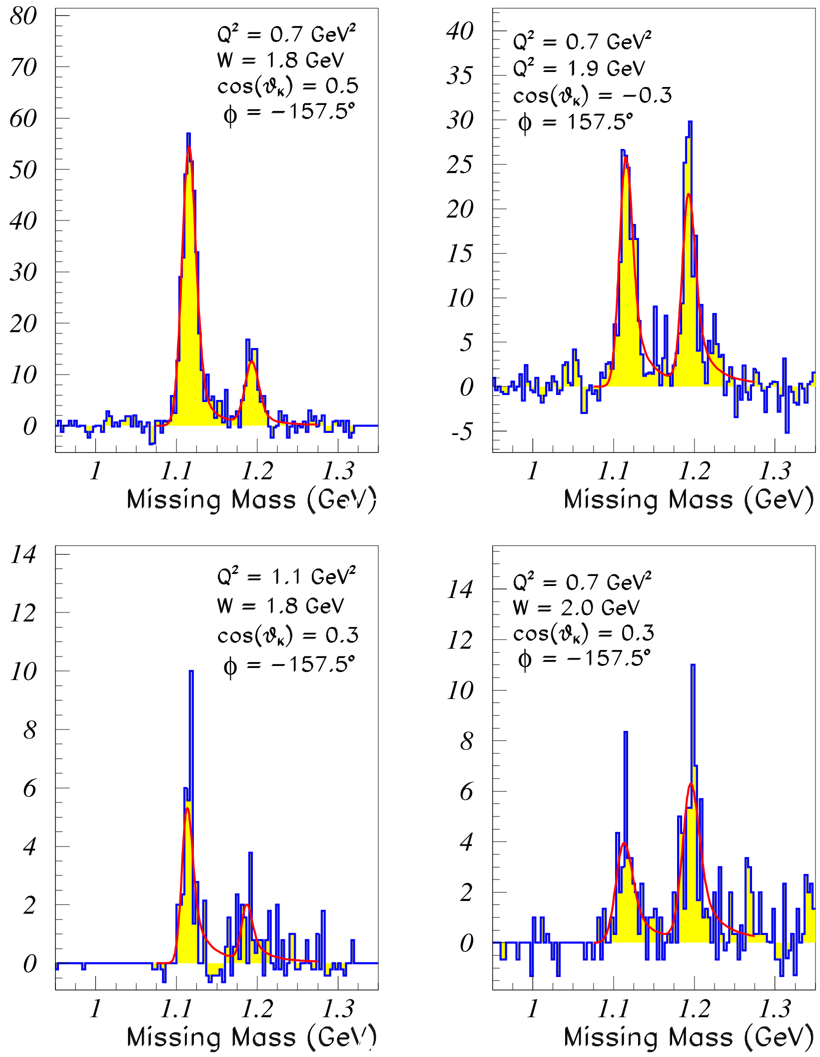

Figure 51: Example of background corrected missing mass plots for various kinematic bins. The signal fits are a convolution of Gaussian and Lorentzian functions but are not used in this analysis.

protons from the complement of kaon mass cut discussed in Section 3.6.2. An additional mass cut from 0.275 to 0.725 GeV effectively selected the tails of the proton and pion mass distributions. These particles were assigned the kaon mass and the missing mass distributions were calculated accordingly. Fig. 49 shows the missing mass distribution with pion, proton and total background contribution overlaid. The two pion and proton background distributions are then fit to the data in the regions of the missing mass distribution where the phase-space background dominates (see Fig. 49). These regions were fit using maximum log likelihood method and the fraction of each distribution present in the data distribution is estimated [54]. The normalized background contributions were finally subtracted from the missing mass distribution formed from good kaons to produce the corrected signal distribution. Fig. 50 and 51 demonstrate examples of the fit results for some low and high statistic kinematical bins. The advantage of the maximum log likelihood fit method is that it includes the statistical fluctuations of the data in the fit, which is useful for the low statistics bins. The background fit could not be performed in some extremely low statistics bins. These yields were rather obtained by counting the number of events within the lambda mass cut without background subtraction. The estimated systematic uncertainty associated with background subtraction should account for such cases (see Chapter 6). The background corrected yields are the number of events that remain within the Λ mass cut.

4.2 Acceptance Corrections

The CLAS detector is a large, nearly 4π sr, acceptance device. However, due to the geometry and the structure of CLAS, there are regions of the solid angle that are not covered in the detector's acceptance. Furthermore, the inefficiencies in the various components of the detector–for example caused by dead or broken wires in the DC or bad TOF scintillators–affect the acceptance and the event reconstruction

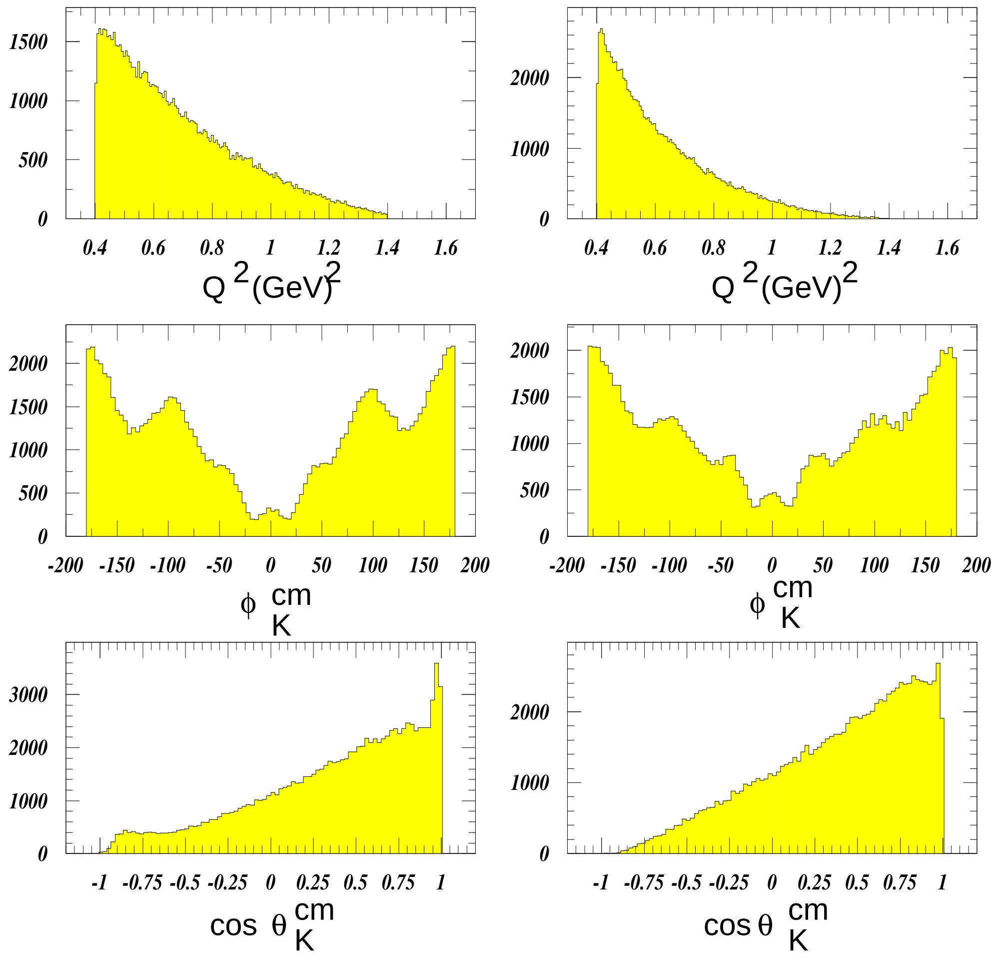

Figure 52: Distribution of the kinematic variables for $e'K^+\Lambda$ for data (left) and GSIM reconstructed Monte-Carlo events (right).

in CLAS. While acceptance and efficiency corrections are expected to largely cancel out in asymmetry measurements, their effects must be considered.

4.2.1 GSIM- Full Monte-Carlo Calculations

In this section a full Monte-Carlo study is presented and the acceptance of the CLAS detector for the reaction of interest is calculated. The GSIM package, a GEANT-based model of CLAS, is used to simulate the response of the detector [55]. This package combines the geometrical configuration with the inefficiencies of the CLAS

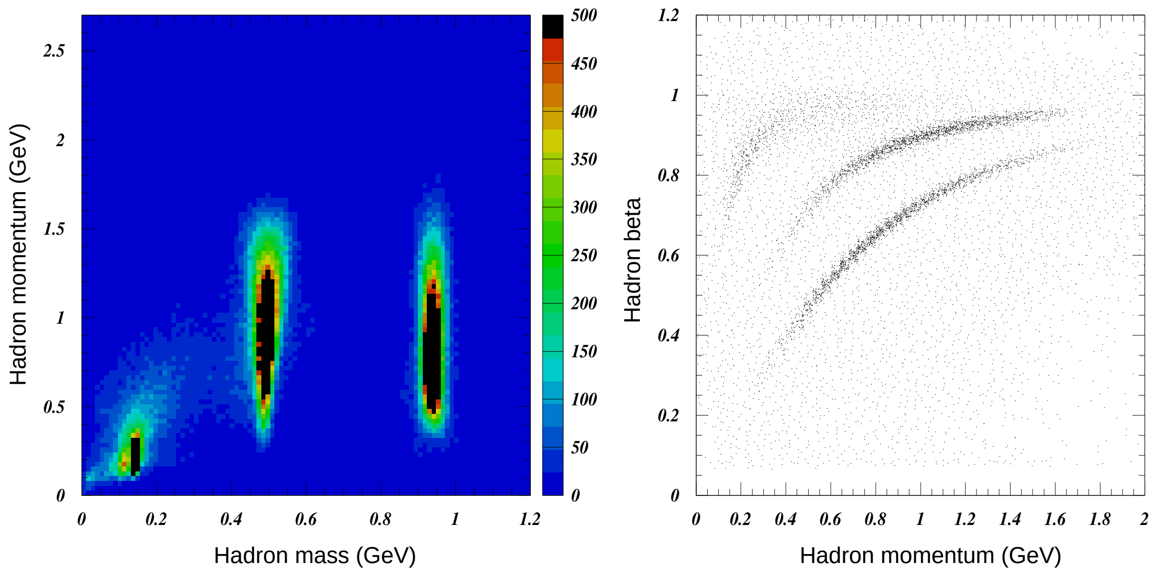

Figure 53: Left: Hadron momentum versus hadron mass, Right: Beta versus momentum for hadrons, GSIM reconstructed Monte-Carlo events.

detector. It includes all the details regarding the geometry and various parts of the CLAS such as beam line components, detector elements, and support structures of CLAS. The RADGEN package is used to generate events as input to GSIM. RADGEN has the ability to employ various theoretical models for meson-baryon electroproduction on a proton target. Radiative effects can also be included. This software was adapted for kaon electroproduction by R. Feuerbach [33]. In this study we have used the latest Mart and Bennhold model [14] which as a generator describes our yield distributions best from among the available models. The distribution of the kinematic variables are shown in Fig. 52 for both data and GSIM results. 20M total events were generated with RADGEN for the two helicity states and the two torus settings–5M events in each setting. The RADGEN output is then processed with GSIM using detector configurations and geometries similar to the

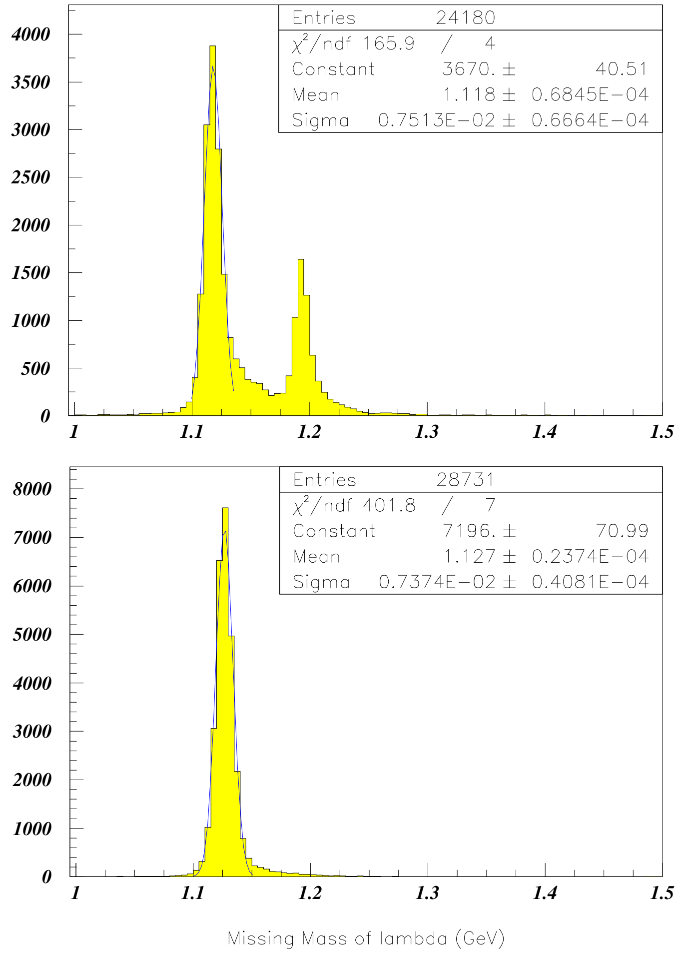

Figure 54: Missing mass of $e'K^+\Lambda$. Top: data, bottom: GSIM simulated Monte-Carlo events for 2250 A torus setting. A small shift is seen in the location of the Λ peak in the GSIM accepted Monte-Carlo events, simulated with realistic resolution.

configurations used during the data-taking period. In this process, hits are produced and the detector response is simulated in each component of the CLAS detector. Additional smearing is also applied to account for those components of the detector with bad signals or poor efficiencies. This is done using the GPP package (GSIM Post Processor) that removes the hits from known dead drift chamber wires and smears the DC and SC detectors by adding random timing offsets to the detector resolutions to produce the resolution determined by the real data. Finally, the

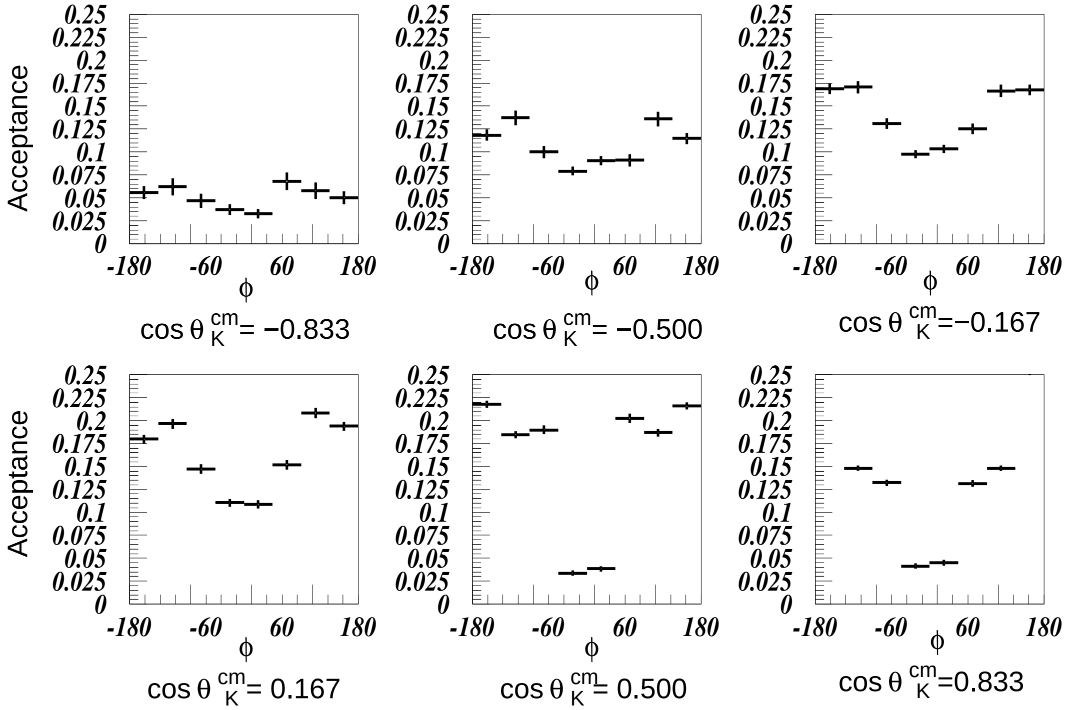

Figure 55: Acceptance correction factors versus ϕ averaged over the two helicity states, $h = \pm 1$. Results are shown for torus setting of 1500 A, $W = 1.825$ GeV and $Q^2 = 0.7$ GeV^2.

simulated events were processed with the same event reconstruction software (a1c) that was used to reconstruct the real data. The data files are converted from the form of BOS files to PAW Ntuples and are analyzed with the same analysis codes and kinematic cuts that are applied to the real data. Fig. 53 shows the hadron momentum distribution versus hadron mass (left) and hadron β versus momentum (right) obtained from the reconstructed Monte-Carlo events after processing with GSIM. Fig. 54 shows the result of missing mass calculation for the simulated CLAS events compared to the data after applying all the cuts.

The acceptance in each bin $(Acc)_i$ is defined as the ratio of the number of reconstructed events $(N_{rec})_i$ in each bin to the number of generated events $(N_{gen})_i$

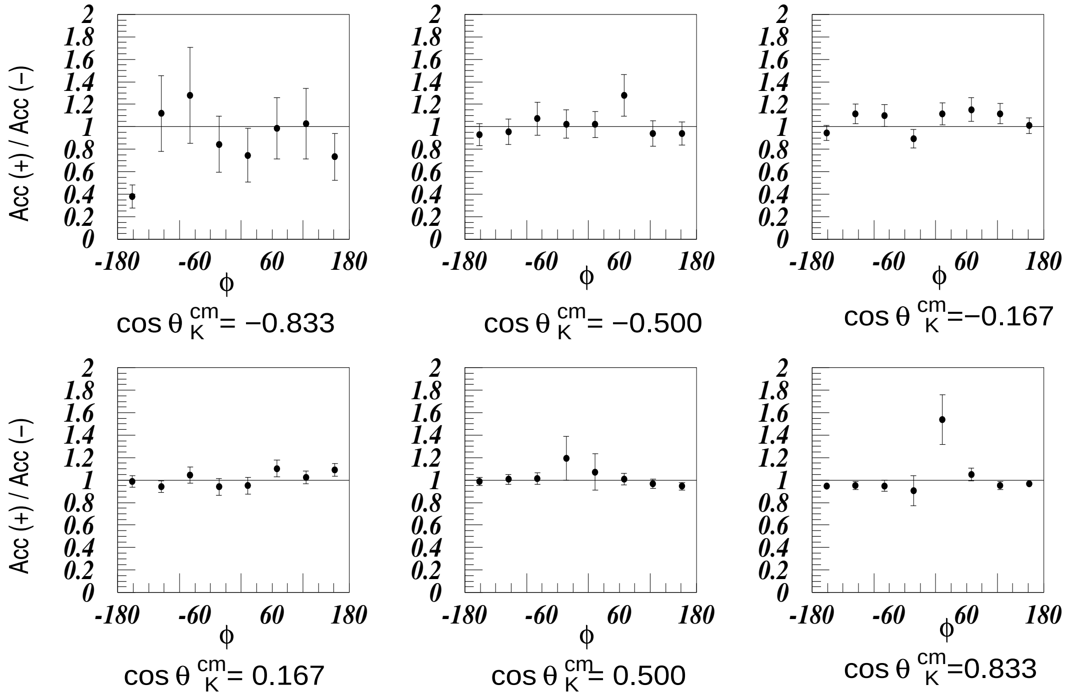

Figure 56: The ratio of the acceptance correction factors for the two helicity states versus ϕ . Results are shown for torus setting of 1500 A, W = 1.825 GeV and $Q^2 = 0.7$ GeV^2.

in the same bin:

$$(Acc)_i = \frac{(N_{rec})_i}{(N_{gen})_i} \tag{44}$$

The uncertainty on the GSIM calculated acceptance is calculated using the binomial distribution:

$$(\delta Acc)_i = \sqrt{\frac{(Acc)_i(1-(Acc)_i)}{(N_{gen})_i}} \tag{45}$$

For this analysis, the acceptance is calculated as a function of four kinematic variables, Q^2, W, θ_K^{cm} and ϕ corresponding to the same binning applied to the real data. Fig. 55 shows the helicity averaged acceptance correction factor for a typical kinematic bin. The ratio of the acceptance correction factors for the two helicity states for a sampling of kinematic bins is shown in Fig. 56. One can see that there is essentially no difference in the acceptance for positive and negative helicities. Indeed, as will be shown in Section 5.4, the acceptance correction has no effect (within the statistical uncertainties) on the asymmetries and has therefore not been applied to the final data.

The acceptance for each torus setting and for the two helicity states in each bin can be applied to the raw yields according to:

$$(N_{corr})_i = \frac{(N_{meas})_i}{(Acc)_i} \tag{46}$$

The uncertainties on the corrected yields for each helicity state (± 1) is a combination of contributions from the yield and the acceptance uncertainties.

$$\delta N_{corr}{}^{\pm} = \sqrt{\frac{{N^{\pm}_{meas}}^2}{{Acc^{\pm}}^4}(\delta Acc^{\pm})^2 + \frac{1}{{Acc^{\pm}}^2} N^{\pm}_{meas}} \tag{47}$$

4.3 Radiative Corrections

In electron scattering experiments, radiative effects apply to the incident and scattered electrons and to the vertices connecting the virtual photon to the electron and hadron currents. Bremsstrahlung photons can be radiated from the incoming and scattered electrons and additional photons can be exchanged between them. In the one-photon exchange approximation, the direct consequence of the radiative processes is that the calculated momenta of the particles at the interaction vertex is different from the actual values. This will result in an inaccurate calculation of the kinematics of the reaction. In addition, the emission of an additional virtual photon, can change the magnitude of the cross section. For example, if a real photon is radiated from the incident electron before exchanging a virtual photon with the proton target, the effective energy of the incident electron on the target would be reduced. Furthermore, if a scattered electron radiates a real photon after interaction with the target, the energy of the electron at the primary vertex is higher than what is observed experimentally. As a result, the missing mass distribution is distorted by the radiative phenomenon. The missing mass that is reconstructed from the events in which the incident or scattered electron radiates a real photon are displaced with respect to the correct value forming a tail as shown in Fig. 57.

Theoretical models do not include the radiative effects. Therefore, it is necessary to correct the experimental yields for these effects in order to determine the single-photon-exchange observables. In order to correct for radiative effects, we have used a recently developed exclusive approach which will be discussed in the following sections.

4.3.1 Exclusive Approach

The approach used here was initially developed and used for exclusive pion electroproduction by I. Akushevich *et al.* [56]. This approach is based on covariant procedure of infrared-divergence cancellation by Bardin and Shumeiko [57]. The classical approach developed by Mo and Tsai [58] for inclusive electron scattering applies an unphysical parameter for distinguishing soft and hard regions of the phase space of the radiated photon. Furthermore, the inclusive calculations do not include any radiative corrections to the polarization asymmetry or any dependency on the outgoing hadron angles. In exclusive electroproduction, a hadron is detected in ad-

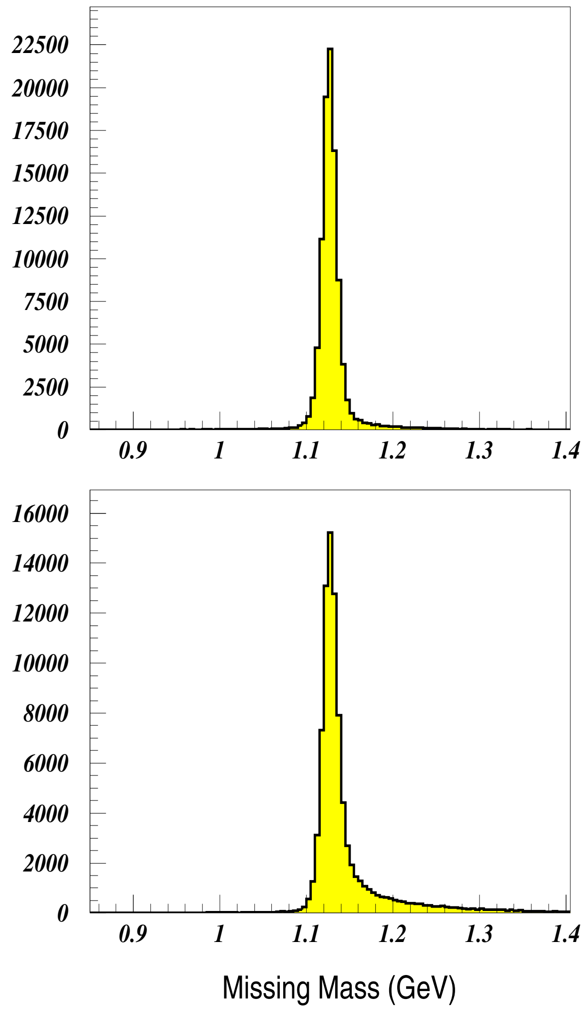

Figure 57: Comparison of the reconstructed missing mass without (top) and with (bottom) radiative effects. The events shown in these plots are generated with the RADGEN Monte-Carlo event generator.

dition to the scattered electron and this reduces the phase space allowed for the final radiated photon. Therefore, the exclusive approach is used to correct the cross sections not only in terms of leptonic variables but also hadronic variables. Unlike the older inclusive approach, which only considers the contribution of two structure functions in the cross section, the exclusive approach has also included contributions of four structure functions for an unpolarized beam and one structure function for

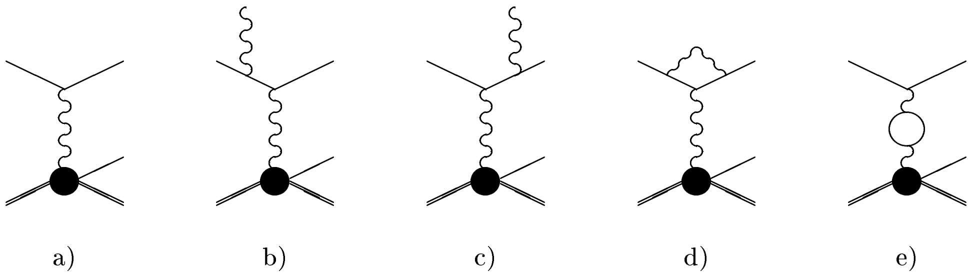

Figure 58: Feynman diagrams for radiative processes. (a) Born process, (b) and (c) Bremsstrahlung, (d) vertex correction, and (e) vacuum polarization.

the case of a polarized beam. Fig. 58 shows the Feynman diagrams contributing to the Born term and higher order radiative processes. These processes include Bremsstrahlung, vertex correction, and vacuum polarization. The cross section of the Born and radiative processes are described by four kinematic variables: Q^2, W, and detected hadron (kaon) angles θ_h and ϕ_h in the center of mass system of the final hadrons. It is important to note that in radiative processes, the undetected hadron energy cannot be determined solely from the measured particles since it depends on the unknown energy of the radiated photons.

The radiative cross section is written as follow:

$$d\sigma_r = \frac{(4\pi\alpha)^3 dQ^2 dW^2 d\Omega_h}{2(4\pi)^7 S^2 W^2} \int d\Omega_k d\nu \frac{\nu\sqrt{\lambda_W}}{f_W^2 Q^4} L^r_{\mu\nu} W_{\mu\nu} \tag{48}$$

where $S = EMp$, Ω_k and Ω_h are the solid angles of the bremsstrahlung photon and detected hadron (kaon) respectively, with

$$\nu = W^2 + m_h^2 - m_u^2 - 2WE_h, \tag{49}$$

$$\lambda_f = (W^2 - m_h^2 - m_u^2 - \nu)^2 - 4m_h^2 W^2, \tag{50}$$

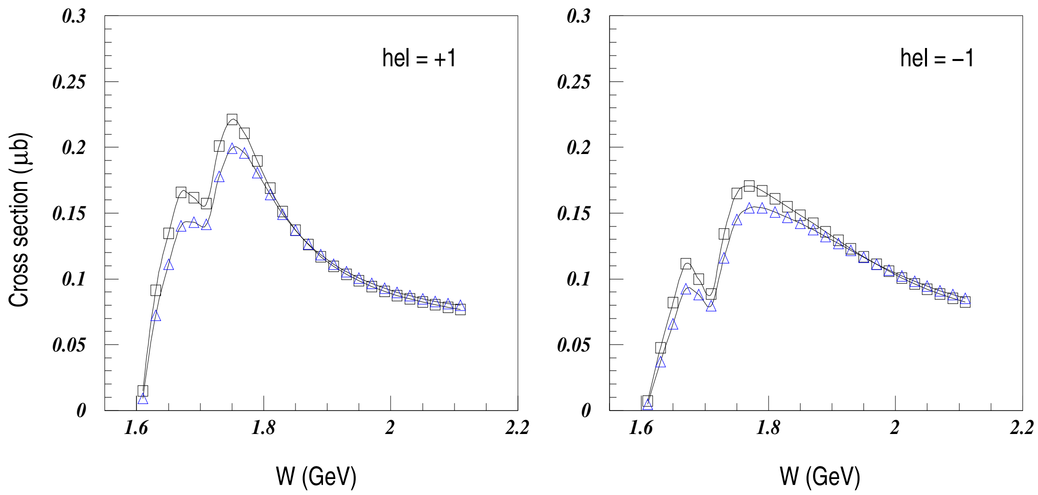

Figure 59: Radiated and Born cross sections in μb versus W in GeV for positive (left) and negative (right) helicity states for a typical kinematical bin of $Q^2 = 0.73$ $(\mathrm{GeV})^2$, $\cos\theta_K^{cm} = 0.4$ and $\phi = 67.5°$. Squares represent the Born cross section and triangles represent the radiated cross section. The radiative effects are maximal just above threshold and become smaller at higher W.

$$f_W = W - E_h + p_h[\cos\theta_h\cos\theta_k + \sin\theta_h\sin\theta_k\cos(\phi_h - \phi_k). \tag{51}$$

Finally, $L^r_{\mu\nu}$ denotes the leptonic tensor for the radiative process. The explicit form of $L^r_{\mu\nu}$ and final form of the radiative cross section is given in Ref. [56].

The radiative corrections have been obtained with the exact calculation and a leading logarithmic (peaking) approximation in which the photons are assumed to be radiated along one of the particles' momentum direction to simplify the integration over the secondary photon's direction. These corrections are expressed as:

$$\delta = \frac{\sigma_{obs}}{\sigma_0} = e^{\delta_{inf}}(1 + \delta_{vr} + \delta_{vac}) + \frac{\sigma_{hard}}{\sigma_0} \tag{52}$$

where δ is the ratio of the observed to Born cross sections, δ_{inf} is the result of infrared cancellation of the vertex function, δ_{vr} and δ_{vac} are due to the vertex and vacuum polarization corrections by leptons and hadrons respectively.

4.3.2 Fortran Code EXCLURAD

The Fortran code EXCLURAD was developed by I. Akushevich *et al.* [56] in order to perform a numerical analysis. For this analysis, EXCLURAD was modified using the cross section for exclusive kaon electroproduction as modeled by Mart and Bennhold [14] with all kinematic variables fixed and suited for the case of kaon electroproduction. The radiative corrections are defined as the ratio of the unradiated cross section to the radiated cross section in each kinematic bin:

$$RC = \frac{\sigma_{unrad}}{\sigma_{rad}} \tag{53}$$

The Born and radiated cross sections are shown in Fig. 59 as a function of W, for a typical kinematic bin and for the two helicity states separately. The corrections are then applied to the helicity-dependent background-corrected yields as follow:

$$N_{RC}^{\pm} = RC^{\pm} N_{meas}^{\pm} \tag{54}$$

where $\pm$ denotes the helicity state, $h = \pm 1$.

4.3.3 EXCLURAD versus RADGEN

The result of the calculation for radiative correction factors obtained by EXCLURAD are compared to those by the RADGEN package. RADGEN includes a model to calculate radiative effects for generated Monte-Carlo events and has the option for switching the radiative effects on or off. This software was written by R. Thompson [59] based on R. Ent's calculations [60] for radiative corrections. This model, is based on a formalism for calculating the radiative corrections to $(e, e'p)$ coincidence reactions that can be modified for any other electroproduction coincidence reaction. However it still applies the assumption of the Mo and Tsai for distinguishing between soft and hard photons i.e. the use of the unphysical parameter Δ. This calculation, uses the peaking approximation, based on the strong peaking of the cross section for the photons emitted in the direction of the electron momentum.

To calculate the radiative correction factors using RADGEN, one again calculates the radiated and unradiated cross sections using a theoretical model. The ratio of the cross sections in each given kinematic bin provides a radiative correction factor for that bin. The model dependency is also reduced by choosing a model that best describes the data (see Fig. 52).

In this approach, the correction factors are calculated by computing the radiated and unradiated cross sections using a Monte-Carlo weighting technique as follows: The uniform phase space was generated and the numerically evaluated cross section at each kinematic point $(W, Q^2, \cos\theta_K^{cm}, \phi_k)$ determined the probability of the event being used. This probability is proportional to the inverse of a constant factor chosen to be larger than the maximum cross section σ_{max} in the complete kinematic region of interest. The cross section in each bin, σ_i is then:

$$\sigma_i = \sigma_{max}\frac{N_i}{T_i} \tag{55}$$

where T_i is the number of attempted throws into a given bin and N_i is the number of entries in that bin that are kept. The statistical uncertainties of the radiated and unradiated cross sections for each bin are calculated as:

$$\delta\sigma_{unrad} = \sigma_{max}\sqrt{\frac{1}{T}\frac{N}{T}(1-\frac{N}{T})} \tag{56}$$

$$\delta\sigma_{rad} = \sigma_{max}\frac{\delta N}{T} = \sigma_{max}\frac{\sqrt{N}}{T} \tag{57}$$

In the case of unradiated cross section, there are no bin migration effects. Therefore the uncertainty is calculated based on a binomial distribution. However, for the radiative cross section, although the bin migration effects are possible, the uncertainties are calculated only by propagating the numerator. The reason is that the number of events thrown in each bin is known and only the number of observed events would fluctuate statistically. Thus, the uncertainties of the calculated correction factors are:

$$\delta RC = \sqrt{(\frac{\delta\sigma_{unrad}}{\sigma_{rad}})^2 + RC^2(\frac{\delta\sigma_{rad}}{\sigma_{rad}})^2} \tag{58}$$

Both exact and leading log approximation calculations with EXCLURAD were compared to the RADGEN outcome. The result of this comparison is shown in Fig. 60 for selected kinematic bins. As seen, the result of the exact calculation is consistent with that of obtained with leading log approximation. However, the result of RADGEN is not in complete agreement with the other two. The radiative correction factors for a typical bin are also plotted versus W in Fig. 61.

It will be shown in the following chapter that the measured asymmetries are relatively insensitive to the radiative corrections. Therefore, the choice of which method to use is somewhat arbitrary. The difference between asymmetries corrected by EXCLURAD and RADGEN will be used to estimate the systematic error associated with radiative corrections. These are generally much smaller than the statistical uncertainties.

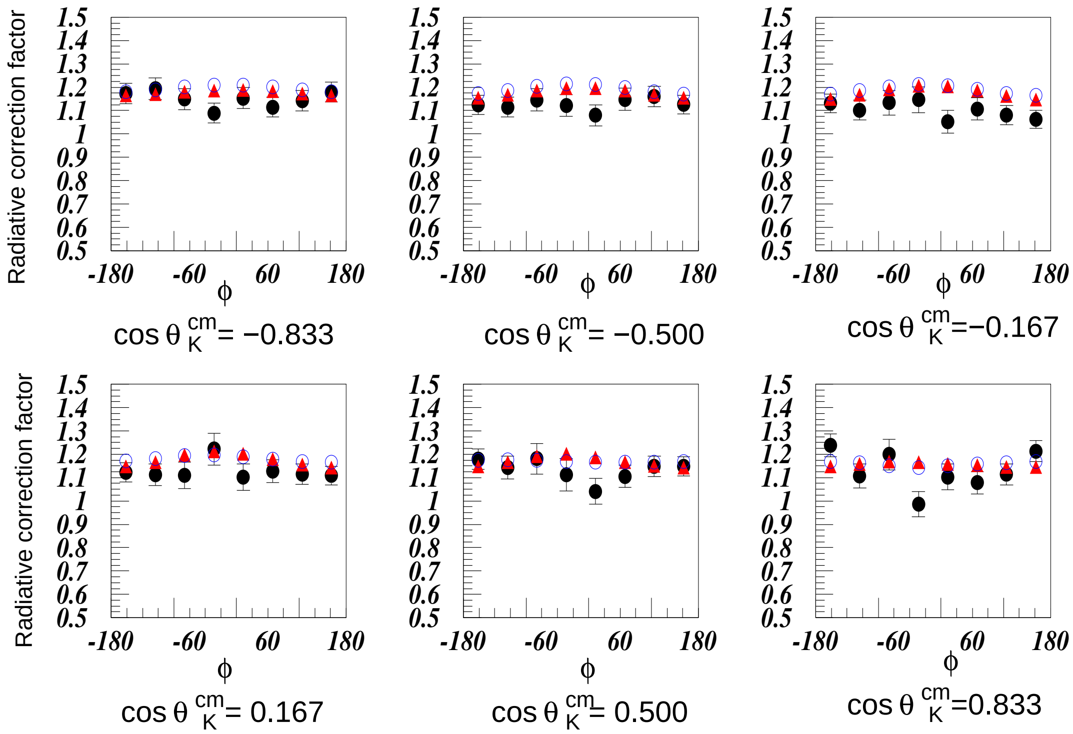

Figure 60: Radiative correction factors versus ϕ obtained with different approaches for $W = 1.675$ GeV and $Q^2 = 0.7$ GeV^2. Result are shown for positive helicity state. The hollow circles: EXCLURAD with exact calculation, the triangles: EXCLURAD with leading log approximation, and full circles: RADGEN.

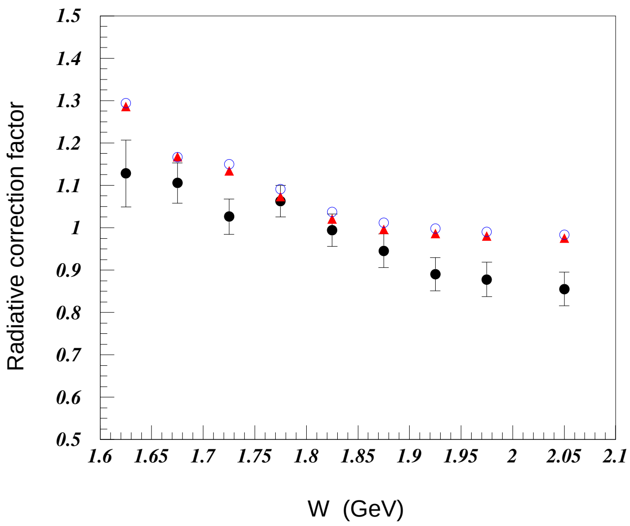

Figure 61: Radiative correction factors versus W in GeV obtained using different approaches. Results are shown for positive helicity, $Q^2 = 0.7$ GeV^2, $cos\theta_K^{cm} = 0.5$, and $\phi = 67.5°$. The hollow circles: EXCLURAD with exact calculation, the triangles: EXCLURAD with leading log approximation, and full circles: RADGEN.

5 Single Spin Asymmetry $A_{LT'}$

The single spin asymmetries are measured by forming the asymmetry for the differential cross section for positive and negative helicity states ($h = \pm 1$) and for each kinematic bin via:

$$A_{LT'} = \frac{\frac{d\sigma}{d\Omega}^{+} - \frac{d\sigma}{d\Omega}^{-}}{\frac{d\sigma}{d\Omega}^{+} + \frac{d\sigma}{d\Omega}^{-}} = \frac{1}{P_b} \frac{N^{+}_{corr} - N^{-}_{corr}}{N^{+}_{corr} + N^{-}_{corr}} \tag{59}$$

where $\frac{d\sigma}{d\Omega}^{\pm}$ is the cross section given by Eq. 15, and N^{+}_{corr} and N^{-}_{corr} are the corrected yields (see chapter 4.1) for positive and negative helicity states, respectively. The electron beam is partially polarized; therefore, the measured asymmetries are also scaled for beam polarization, P_b. A detailed description of beam polarization measurement for E1C run period is given in section 5.3. Furthermore, a correction for beam charge asymmetry (differences in integrated charge for different helicity states of the beam) must be included. The procedure of measuring the beam charge asymmetry is discussed in section 5.2.

5.1 Half-Wave Plate

The beam is prepared at the source in one of the two helicity states. The helicity is typically flipped at a rate of 30 Hz and tagged by a signal indicating the helicity state, which is fed into the data stream of the experiment. During the E1C run period a half-wave plate was frequently inserted into the laser beam at the injector. A half-wave plate is a plate of electro-optical material that serves to rotate the plane of polarization of a light beam. In order to measure the helicity dependent asymmetry, the knowledge of the helicity state of the electron and therefore the

Torus (A)	Run Number	HWP Status
1500	16506-16519	OUT
	16525-16549	IN
	16558-16607	OUT
	16608-16620	IN
2250	16634-16670	IN
	16673-16719	OUT
	16720-16732	IN

Table 3: Status of half-wave plate (HWP) for each run of the 2.567 GeV data.

status of half-wave plate ('in' or 'out') at the injector is very important. This plate was used to reverse the electron-beam helicity state in order to study systematic effects in the Hall C experiment that was running concurrently with Hall B.

In this analysis, the status of the half-wave plate was accounted for on a run by run basis in order to correctly assign the helicity state of the incident electron to each event and to measure the helicity dependent asymmetries. Table 3 summarizes the status of the half-wave plate for the data set analyzed in this work.

5.2 Beam Charge Asymmetry Correction

A difference in the number of incident electrons for different helicity states would contribute a false asymmetry to the physics measurement. This beam charge asymmetry must be accurately measured and an appropriate correction applied to both

Energy (GeV)	Torus (A)	Asymmetry	Stat. Uncertainty
2.567	1500	0.000433	0.000178
2.567	2250	0.000113	0.000249

Table 4: Beam charge asymmetry for E1C running period.

the beam polarization measurement and the physics data. To measure the helicity dependent charge asymmetry during the experiment, *ep* elastic scattering events were used as a monitor. The elastic process has no helicity-dependent asymmetry–apart from a negligible parity violation asymmetry–and thus can be used as a monitor for beam charge asymmetry, A_q [61]. Asymmetries are measured on a run by run basis via:

$$A_q = \frac{Y^+ - Y^-}{Y^+ + Y^-} \tag{60}$$

$$\delta A_q = \sqrt{\frac{4Y^+Y^-}{(Y^+ + Y^-)^3}} \tag{61}$$

where Y^+ and Y^- are the yields for elastic events for positive and negative helicity states. The sign of the asymmetry depends on the status of half-wave plate and the spin precession of the electrons in the accelerator (see reference [61] for more detail). The beam charge asymmetry is shown in Fig. 62 for each run. The weighted average for each torus setting is shown in Table 4. For the data set combined from both torus settings data, the average of these two values normalized to the number of triggers in each data set were used to correct the physics asymmetry, $A_{LT'}$ as follows:

$$A_{LT'}^{corr} = A_{LT'}^{meas} - A_q \tag{62}$$

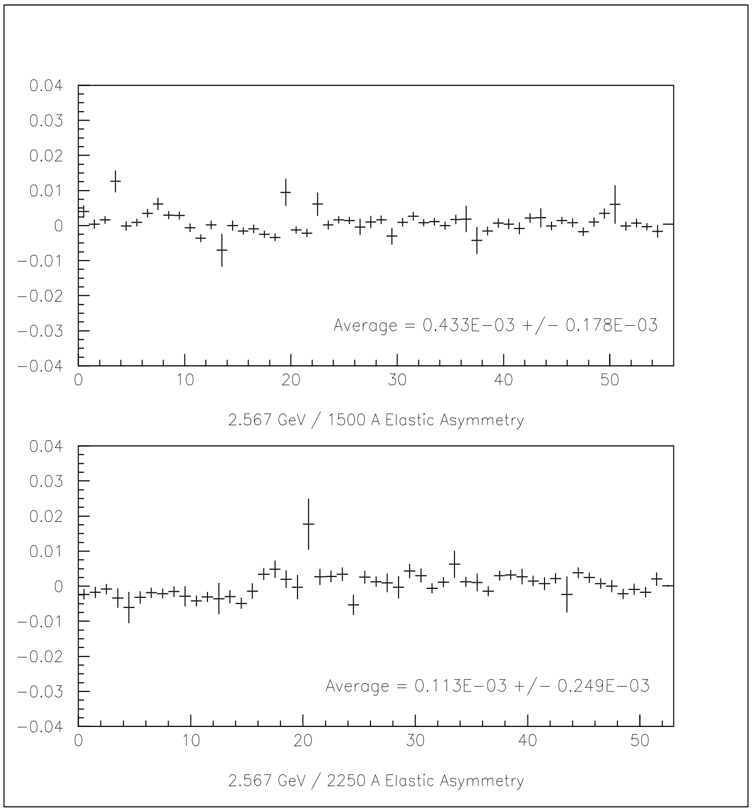

Figure 62: Beam charge asymmetry for 2.567 GeV data for each run (arbitrary run number along the x axis. Top: 1500 torus setting, bottom: 2250 torus setting. The right most point indicates the average asymmetry

This asymmetry is very small, 2.99×10^{-3}, compared to the physics asymmetry and has a negligible effect on the final results.

5.3 Measurement of Electron Beam Polarization

The electron beam polarization is defined as

$$P_b = \frac{N_e^+ - N_e^-}{N_e^+ + N_e^-} \tag{63}$$

where $N_e^{\pm}$ are the number of electrons with spin orientation parallel (+) and antiparallel (−) to the beam direction. Typical CEBAF beam polarization can be

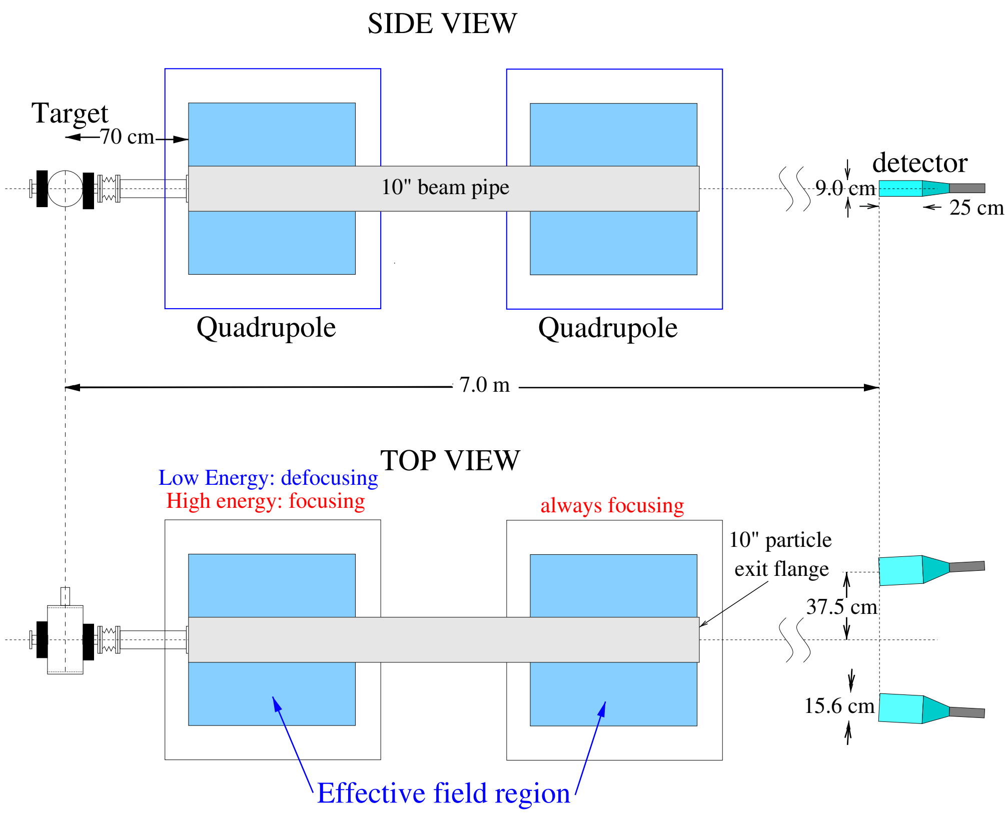

Figure 63: Layout of the Hall B Møller polarimeter.

between 70 and 80%. The beam polarization was measured using the double-arm coincidence Møller polarimeter located upstream of the target position in Hall B. The layout of the Hall B Møller polarimeter is shown in Fig. 63. The Møller target consist of a polarized Permendur foil. The incident electrons elastically scatter off the polarized target electrons. The two scattered electrons are detected in coincidence by two lead scintillator detectors located symmetrically on both sides of the beam line. Two quadrupole magnets are used to focus the scattered electrons on the detectors.

For each energy setting during the E1C run, a separate average beam polarization has been determined along with statistical and systematic uncertainties. Table 5 summarizes the results for the entire running period and the results are also shown in Fig. 64. Results from the other beam energies are included to illustrate the relative stability of the beam polarization for a given energy.

The Hall B Møller polarimeter [62] utilizes $\vec{e} + \vec{e} \rightarrow e + e$ elastic scattering. A detailed description of Møller scattering is presented in Ref. [63]. The beam-helicity dependent asymmetry for longitudinal beam and target polarization is given by

$$A = \frac{\frac{d\sigma}{d\Omega_+} - \frac{d\sigma}{d\Omega_-}}{\frac{d\sigma}{d\Omega_+} + \frac{d\sigma}{d\Omega_-}} = A_{zz}(\theta) P_b^z P_T^z \tag{64}$$

where the $+(-)$ refers to cases where the beam and target spins are aligned (anti-aligned). In principle, one can measure the beam polarization by measuring the above cross-section asymmetry and independently knowing the target polarization. In practice, the asymmetry is formed from angle-integrated yields:

$$A = \frac{N_+ - N_-}{N_+ + N_-} = \bar{A}_{zz} P_b^z P_T^z \tag{65}$$

where $\bar{A}_{zz}$ is the effective analyzing power corrected for the experimental acceptances and atomic-electron motion (Levchuk effect [64]).

5.3.1 Uncertainties in beam polarization

The uncertainty in the measured beam polarization will have contributions from each of the terms given in Eq. 65. The uncertainties for the target polarization and the effective analyzing power have been determined and their method of determination is presented elsewhere [62]. The relative uncertainty due to the target polarization

1.515 GeV					
Date	$1/2\lambda$	P_b (%)	statistical	systematic	total
1/21/99	out	-69.56	0.68	1.32	1.49
1/23/99	in	67.18	1.11	1.28	1.69
1/25/99	out	-71.22	0.83	1.35	1.59
1/29/99	in	68.16	0.53	1.29	1.40
2/01/99	out	-71.07	0.70	1.35	1.52
average		69.41	0.32	1.32	1.36
2.567 GeV					
2/07/99	in	67.05	1.06	1.27	1.66
2/10/99	out	-64.27	1.72	1.22	2.11
2/15/99	in	67.33	0.61	1.28	1.42
average		67.02	0.85	1.27	1.53
4.247 GeV					
2/22/99	in	69.84	4.83	1.33	5.01
2/27/99	in	70.17	0.99	1.33	1.66
average		70.16	0.97	1.33	1.65
4.056 GeV					
3/12/99	in	-64.78	0.95	1.23	1.56
3/19/99	in	-71.36	1.21	1.36	1.81
average		67.29	0.74	1.28	1.48
4.462 GeV					
4/02/99	out	63.31	1.12	1.20	1.64
4/03/99	out	63.38	1.52	1.20	1.94
4/07/99	in	-57.94	1.62	1.10	1.96
4/10/99	in	-60.73	1.19	1.15	1.66
average		61.05	0.94	1.16	1.49

Table 5: Results from Møller run taken during E1C run period. The column labeled $1/2\lambda$ indicates the status of the half-wave plate. The total uncertainty in column 6 is the quadrature sum of the statistical and systematic uncertainties. Details regarding systematic uncertainties and averaging are discussed in the text.

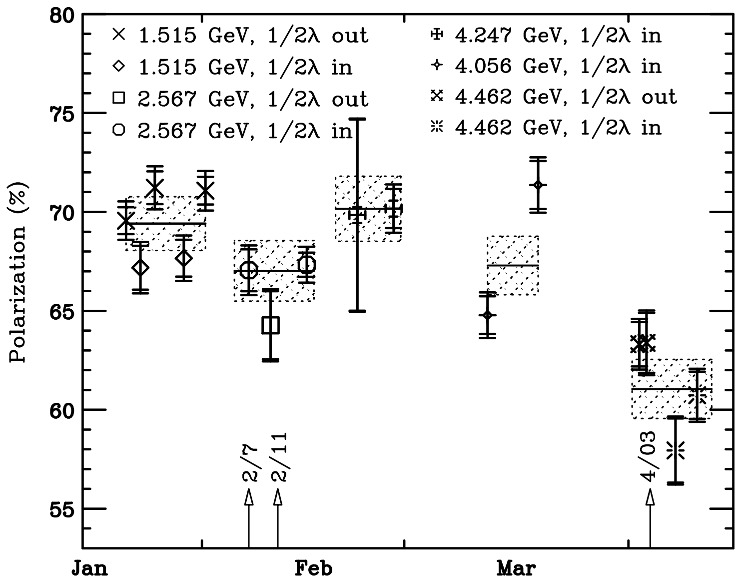

Figure 64: Results of Møller polarimetry measurements of the electron-beam polarization. Each data point reflects a combination of between 1-4 sequential measurements taken at a given time. The inner error bar is statistical only and the outer error bar is statistical combined with the charge-asymmetry correction uncertainty and reflects the total point-to-point uncertainty. The solid lines indicate the average polarization for each of the four beam energies of the E1C run period for which there was good beam polarization. The shaded areas indicate the total uncertainty in the polarization for each energy. Arrows with dates indicate changes in beam conditions that had known effects on the polarization.

is $(\frac{\delta P_b}{P_b})_{tgt} = 0.014$ and the relative uncertainty due to the effective analyzing power is $(\frac{\delta P_b}{P_b})_{A_{zz}} = 0.008$. These uncertainties will result in a systematic uncertainty common to all measurements.

Beam-charge asymmetry

The uncertainty due to the measured Møller asymmetry has two pieces: one piece is just related to the statistical precision of the measurement and is shown in Table 5. The other piece is related to corrections to the Møller asymmetry for the helicity-dependent charge asymmetry of the beam. This is due to differences in the number of beam electrons in the two different helicity states. For E1C, there were four PMTs placed around the beamline to monitor the charge asymmetry. These were read out for every helicity flip. The typical charge asymmetry measured with these monitors was always less than 1% and rarely exceeded 0.5%. The typical correction to the measured beam polarization was less than 2% (absolute).

The uncertainty in beam charge asymmetry measured during beam polarization measurements contributes a relative uncertainty of $(\frac{\delta P_e}{P_e})_{charge} = 0.012$. This was determined by looking at the differences between Møller asymmetry corrected for beam charge asymmetry using different sets of monitoring detectors.

The separate analysis of beam charge asymmetry using elastically scattered electrons, discussed in the previous section, indicates that charge asymmetries measured on a run-by-run basis are comparable to the statistical accuracy to which they can be measured. Over entire running periods, these asymmetries are less than 0.005. These numbers are consistent with what was measured for the Møller runs.

Helicity flipping

The beam helicity flipped at a rate of 30 Hz during this experiment. During the transition from one helicity state to the next, there is a period of approximately 50 μs when the beam polarization is unknown. Fig. 65 schematically summarizes the situation. The transition time amounts to $\frac{0.05 \text{ ms}}{33.3 \text{ ms}} = 0.15\%$ of the total time. In the worst case, assuming the beam is totally unpolarized during the transition, this is still an insignificant correction to measured beam polarization. For a different running period, the measured beam polarization during the transition period was found to be about half of the nominal polarization [65]. Therefore, no correction has

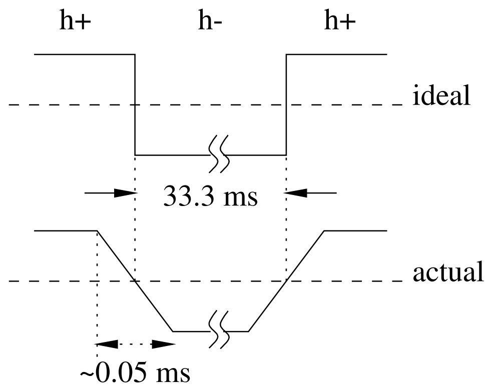

Figure 65: Ideal and actual helicity-flip transition.

been applied to beam polarization measurements and the effect has been ignored in calculating the systematic uncertainty.

Stability of beam polarization

One of the reasons for taking frequent Møller measurements is to monitor the stability of the beam polarization. The contamination of the Hall B beam with beam from the other halls can dilute the polarization. Changes in the beam current delivered to the other halls changes the amount of contamination and therefore can cause instabilities in the polarization. For most of the separate beam energies the Møller measurements indicate a very stable beam polarization. However, there is a rather large discrepancy between the two measurements taken at 4.056 GeV. Furthermore, during that period it was discovered that there was significant contamination of the Hall B beam from the other halls. It is likely that an additional systematic uncertainty should be assigned to the beam polarization for the 4.056 GeV data set to account for this effect but not to the current data set.

Total systematic uncertainty

The point-to-point systematic uncertainty is the combination of the statistical and charge-asymmetry correction uncertainties. The total relative systematic uncertainty is the quadrature sum of the uncertainties discussed above. For the 2.567 GeV data this is estimated to be $\frac{\delta P_e}{P_e} = 0.019$.

5.3.2 Effect of beam polarization uncertainty

Since the corrected asymmetry $A_{LT'}$ is inversely proportional to the beam polarization, the uncertainty in $A_{LT'}$ due to uncertainties in the beam polarization is given by

$$\delta A_{LT'} = |A_{LT'}^{meas}| \frac{\delta P_e}{P_e} = |A_{LT'}| \delta P_e, \tag{66}$$

where

$$A_{LT'}^{meas} = \frac{N^+ - N^-}{N^+ + N^-}. \tag{67}$$

The relative uncertainty for the beam polarization is 2.3% giving a relative systematic uncertainty in $A_{LT'}$ of about 2%. This is again small compared to statistical uncertainties in $A_{LT'}$.

5.4 Measured Asymmetry $A_{LT'}$

The asymmetry, $A_{LT'}$, is measured as a function of four kinematic variables, Q^2, W, $\cos\theta_K^{cm}$ and ϕ, according to Eq. 63. The data are binned over W, from the threshold up to 2.05 GeV, Q^2 from 0.5 to 1.3 GeV^2, and over the full angular coverage of ϕ and θ_K^{cm}, with a total number of 672 bins. The number and the width of each bin is given in Table 6. The complete set of measured asymmetries for all 672 bins are presented in the following section.

Bin	Q^2 GeV^2	W (GeV)	$\cos\theta_K^{cm}$	ϕ (°)
Range	0.5-1.3	1.60-2.05	-1, 1	-180, 180
Number	2	5-9	6	8
Width	0.4	0.050	0.333	45

Table 6: The Range, number, and the width of the kinematical bins.

The effect of the various yield corrections mentioned in Chapter 4 on the measured asymmetries is studied and shown in Fig. 66 to 68 . The results indicate that the measured asymmetries are relatively insensitive to all of these corrections.

Fig. 66 shows the measured raw asymmetry before and after background corrections for a typical W and Q^2 bin. The effect of background corrections on the extracted yields varies depending on the kinematical bin under study where the signal/noise ratio varies with kinematics. It is obvious that some bins have sizable background corrections. In the very low statistical bins, where the background fit procedure fails, the uncorrected yields are used for calculating the asymmetries (the systematic uncertainty due to the lack of this correction for the low statistic bins is given in Chapter 6).

The comparison between acceptance corrected and uncorrected asymmetries is shown in Fig. 67 for a typical W and Q^2 bin. The effect of this correction is seen to be very small. In this analysis, the acceptance corrections were not applied to

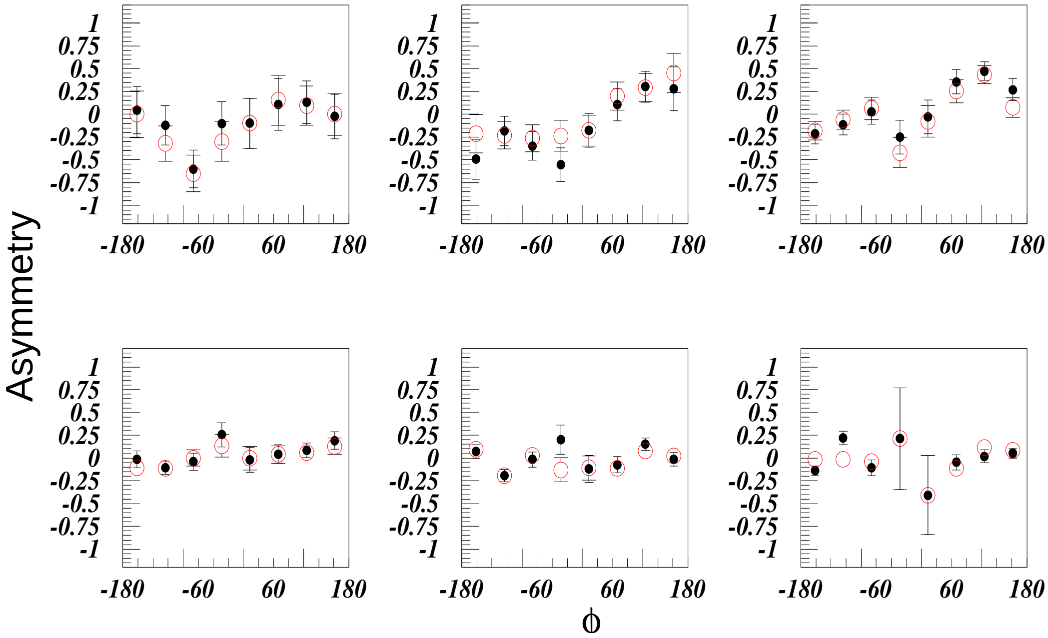

Figure 66: Measured asymmetry before (red circles) and after (black dots) background correction for $\cos\theta_K^{cm}$ = -0.833, -0.50, -0.167, 0.167, 0.50, 0.833 (upper left to lower right), $W = 1.925$ GeV and $Q^2 = 0.7$ GeV^2.

the measured asymmetries since the CLAS acceptance is largely independent of the helicity state of the electron events. The small effect of this correction seen on the asymmetries is mostly due to the statistical fluctuations in GSIM results. It is shown that in the limit of large statistics, this correction has a negligible effect on the measured asymmetries. In order to correct for the acceptance effects, the background corrected yields must be extracted for each torus setting separately. This is due to the fact that the acceptance of CLAS depends on the torus field setting. This would lower the statistics in each kinematic bin and therefore causes fitting problems in the background subtraction procedure. The fact that the asymmetries are not sensitive to the acceptance and efficiency of the detector allows one to combine the data sets for different torus settings and improve the background fit procedure for

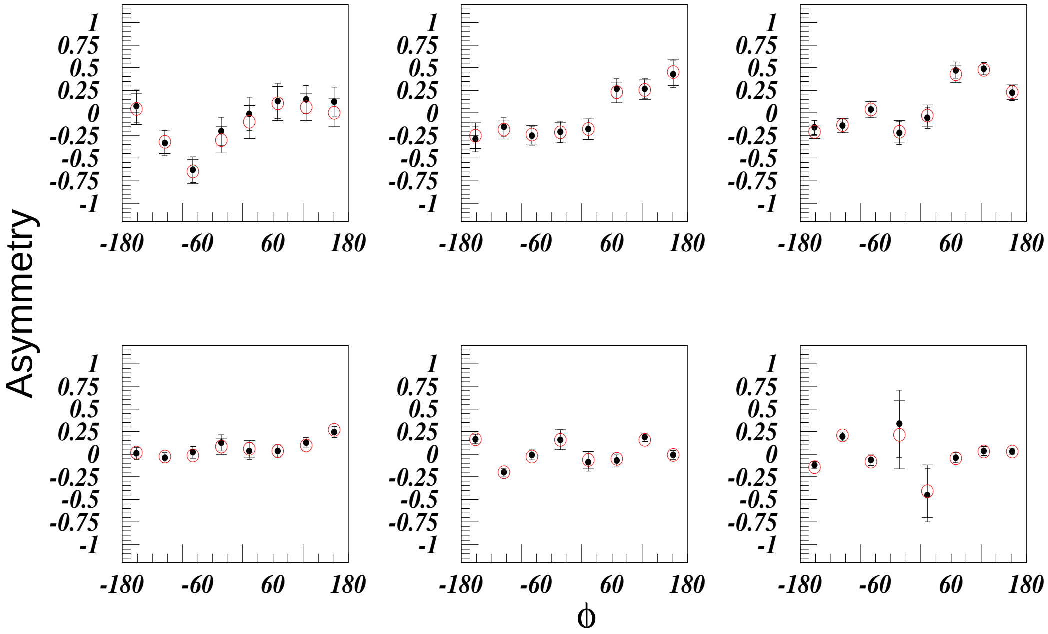

Figure 67: Background corrected asymmetries with (black dots) and without (red circles) CLAS acceptance correction (GSIM). Results are shown for $\cos\theta_K^{cm}$ = -0.833, -0.50, -0.167, 0.167, 0.50, 0.833 (upper left to lower right), , $W = 1.925$ GeV, and $Q^2 = 0.7$ GeV^2.

extracting the reaction yields. This results in smaller total uncertainty even after including systematic uncertainties associated with not doing acceptance corrections (see Chapter 6). The effect of the radiative correction on the measured asymmetries is shown in Fig. 68. As shown the effect of this correction on the measured asymmetries is again very small. However, because of the direct dependence of the cross sections and therefore yields on the radiative effects for each helicity state (see section 4.3), these corrections are applied to the measured asymmetries.

The statistical uncertainties for the measured asymmetries are calculated as follows:

$$\delta A_{LT'} = \frac{1}{P_b}\frac{2}{(N^+_{corr} + N^-_{corr})^2}\sqrt{{N^-_{corr}}^2 \delta {N^+_{corr}}^2 + {N^+_{corr}}^2 \delta {N^-_{corr}}^2} \tag{68}$$

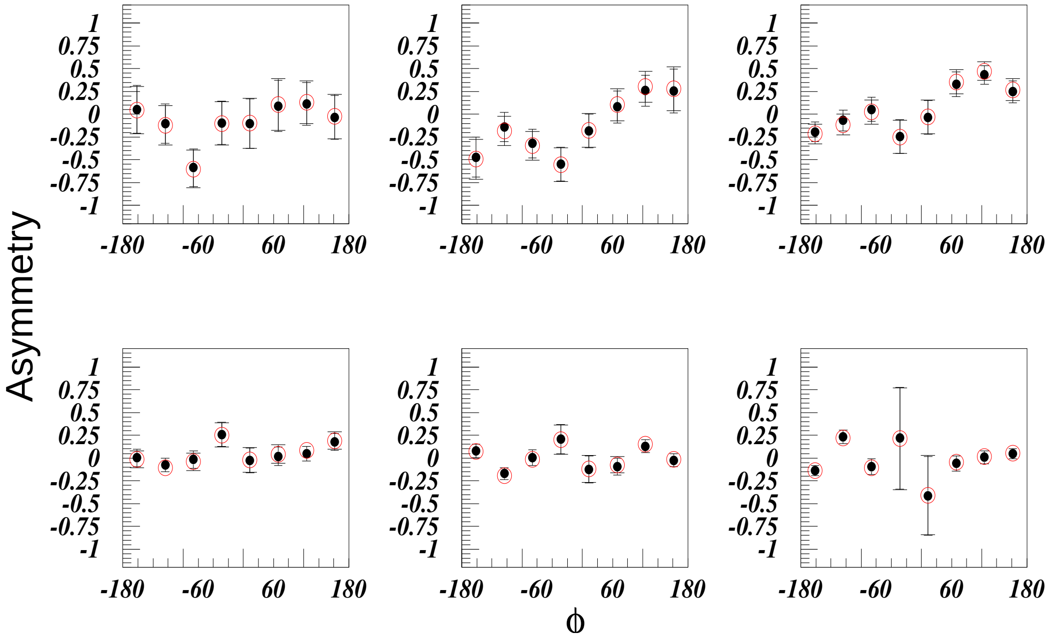

Figure 68: Background corrected asymmetries with (black dots) and without (red circles) radiative corrections (EXCLURAD). Results are shown for $\cos\theta_K^{cm}$ = -0.833, -0.50, -0.167, 0.167, 0.50, 0.833 (upper left to lower right), Q^2 = 0.7 GeV^2, W = 1.925 GeV.

where $N^{\pm}_{corr}$ are the background and radiative corrected yields and $\delta N^{\pm}_{corr}$ are the corresponding uncertainties for positive and negative helicities. There is no statistical uncertainty for radiative correction using the exclusive model, EXCLURAD, since it is an exact calculation. Therefore, the background corrected yields and the uncertainties are scaled by the radiative correction factors for each helicity state.

5.4.1 Asymmetry $A_{LT'}$ Results

In this section we present the complete set of measurement for $A_{LT'}$. The corrected asymmetries are shown in Fig. 69 to 82, plotted versus ϕ for each kinematic bin of Q^2, W, and $\cos\theta_K^{cm}$ and are compared with available theoretical calculations. The missing data points on some of the plots correspond to an asymmetry formed by at least one zero or negative yield in either positive or negative helicity state. These unphysical yields result from statistical fluctuations in the background subtraction procedure. The error bars shown in these plots indicate combined contributions from statistical and systematic uncertainties (see Chapter 6 for details about the estimation of systematic uncertainties for $A_{LT'}$.) The results are also summarized in Appendix E, Table 11 to 24.

5.4.2 Comparison to Theory Calculations

The measured asymmetries are compared to the available theoretical calculations described in Sec. 1.3.1. The calculations are obtained using a code by Mart and Bennhold that can employ various choices of hadron form factors. The calculations presented all use the kaon form factor from Williams [11] and the Λ form factors from Goeke [66]. The elementary KΛ reaction model is then changed to calculate asymmetries and fifth structure functions (see Chapter 7). The results are obtained by averaging the calculations over the kinematical bin sizes.

The agreement between data and the calculations is mixed. The uncertainties of individual $A_{LT'}$ points do not allow for one to immediately determine which model is best. The later Mart and Bennhold model seems to predict larger asymmetries–more in line with what is observed in the data. However, it frequently has the wrong sign. As will be shown in Chapter 7, these results are more useful in distinguishing among the various models–or discounting them all–once $\sigma_{LT'}$ is extracted.

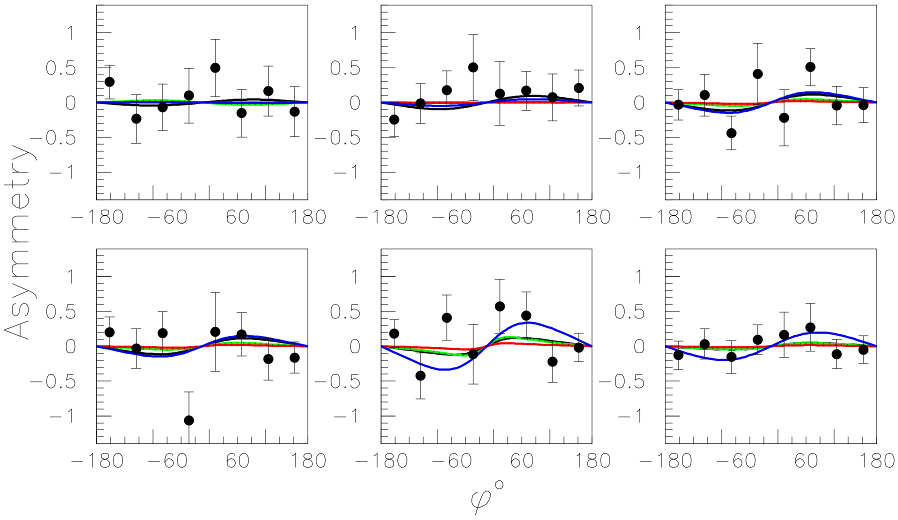

Figure 69: Measured asymmetries versus ϕ for $\cos\theta_K^{cm}$ = -0.833, -0.50, -0.167, 0.167, 0.50, 0.833 (upper left to lower right), Q^2 = 0.7 GeV^2, W = 1.625 GeV. Curves: Adelseck and Wright [9] (black), WJC [11] (green), Mart with hadronic form factors (red), Mart with D13(1900) [14] (blue).

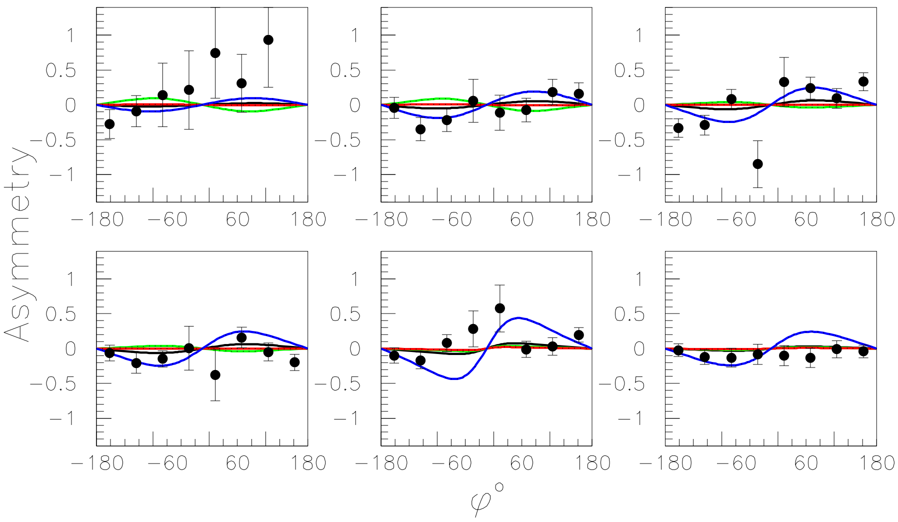

Figure 70: Measured asymmetries versus ϕ for $\cos\theta_K^{cm}$ = -0.833, -0.50, -0.167, 0.167, 0.50, 0.833 (upper left to lower right), Q^2 = 0.7 GeV^2, W = 1.675 GeV. Curves are the same as in Fig. 69.

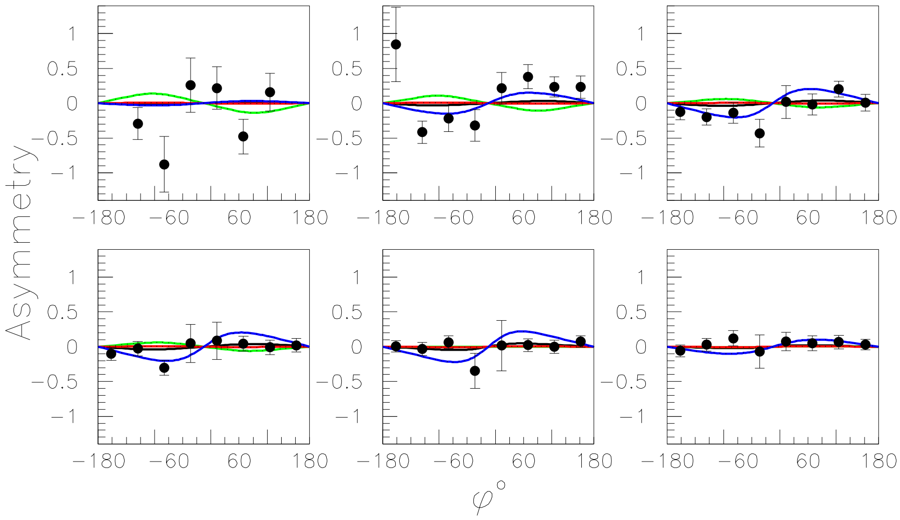

Figure 71: Measured asymmetries versus ϕ for $\cos\theta_K^{cm}$ = -0.833, -0.50, -0.167, 0.167, 0.50, 0.833 (upper left to lower right), $Q^2 = 0.7$ GeV^2, $W = 1.725$ GeV. Curves are the same as in Fig. 69.

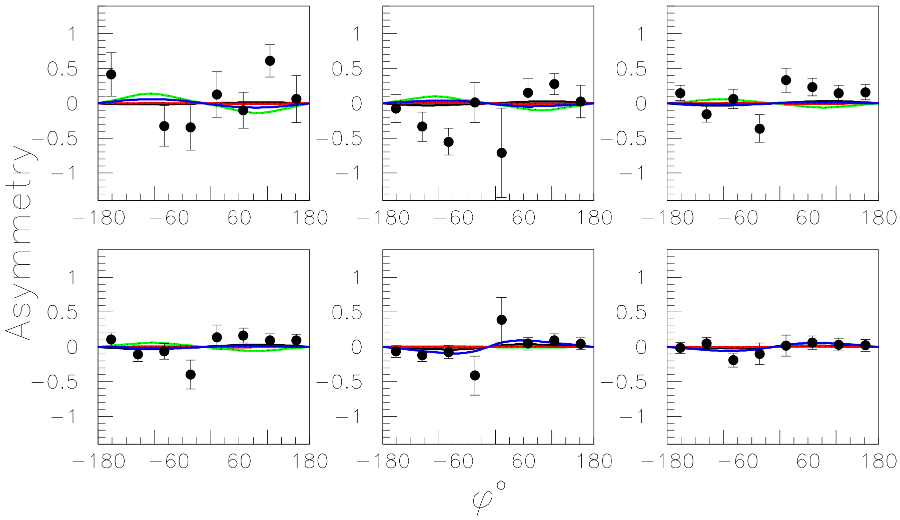

Figure 72: Measured asymmetries versus ϕ for $\cos\theta_K^{cm}$ = -0.833, -0.50, -0.167, 0.167, 0.50, 0.833 (upper left to lower right), $Q^2 = 0.7$ GeV^2, $W = 1.775$ GeV. Curves are the same as in Fig. 69.

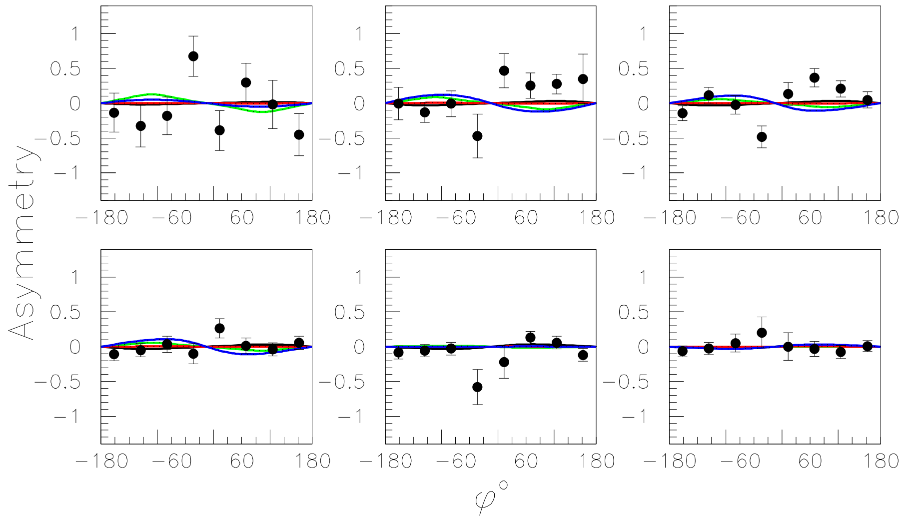

Figure 73: Measured asymmetries versus ϕ for $\cos\theta_K^{cm}$ = -0.833, -0.50, -0.167, 0.167, 0.50, 0.833 (upper left to lower right), $Q^2 = 0.7$ GeV^2, $W = 1.825$ GeV. Curves are the same as in Fig. 69.

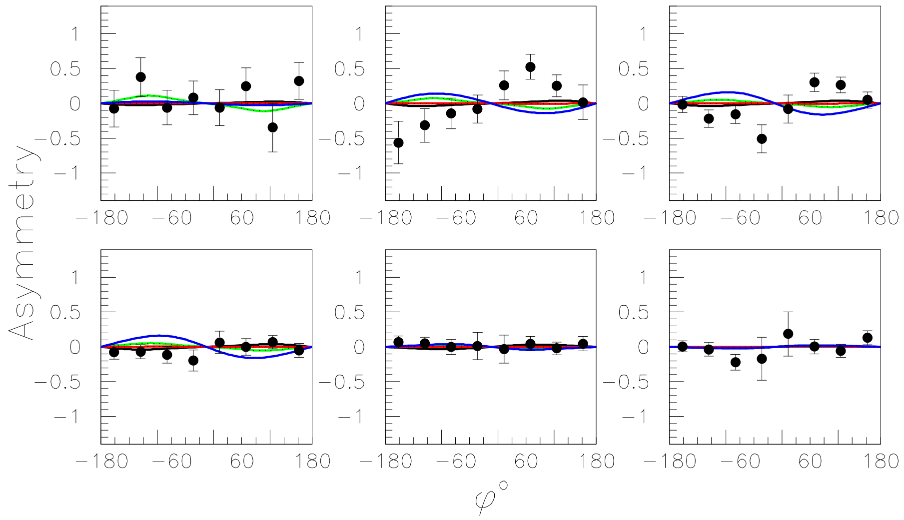

Figure 74: Measured asymmetries versus ϕ for $\cos\theta_K^{cm}$ = -0.833, -0.50, -0.167, 0.167, 0.50, 0.833 (upper left to lower right), $Q^2 = 0.7$ GeV^2, $W = 1.875$ GeV. Curves are the same as in Fig. 69.

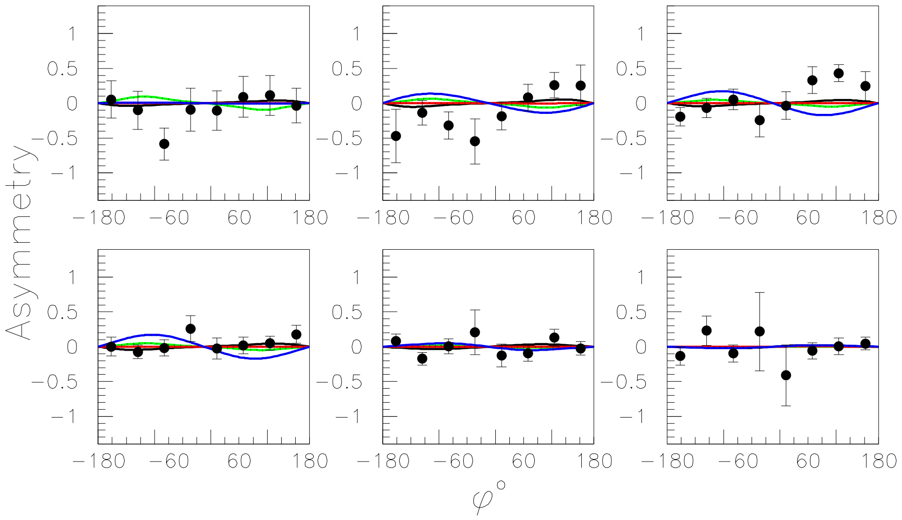

Figure 75: Measured asymmetries versus ϕ for $\cos\theta_K^{cm}$ = -0.833, -0.50, -0.167, 0.167, 0.50, 0.833 (upper left to lower right), $Q^2 = 0.7$ GeV^2, $W = 1.925$ GeV. Curves are the same as in Fig. 69.

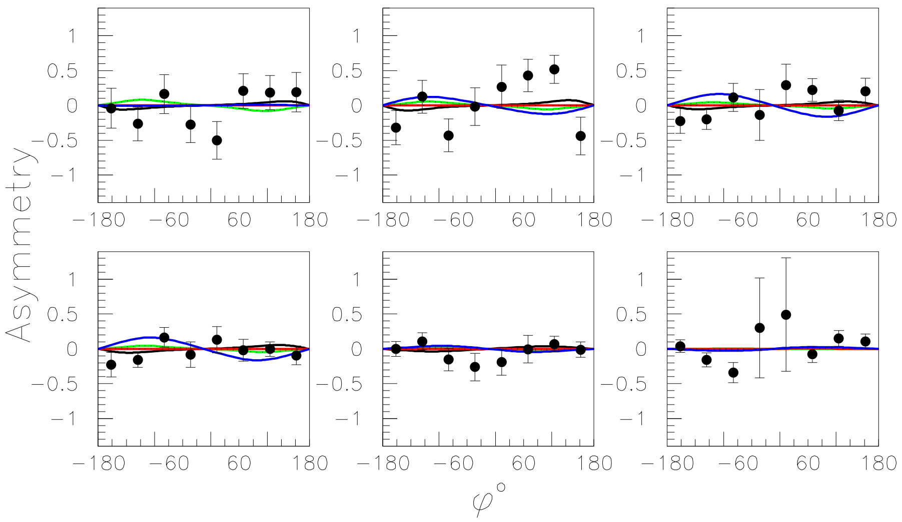

Figure 76: Measured asymmetries versus ϕ for $\cos\theta_K^{cm}$ = -0.833, -0.50, -0.167, 0.167, 0.50, 0.833 (upper left to lower right), $Q^2 = 0.7$ GeV^2, $W = 1.975$ GeV. Curves are the same as in Fig. 69.

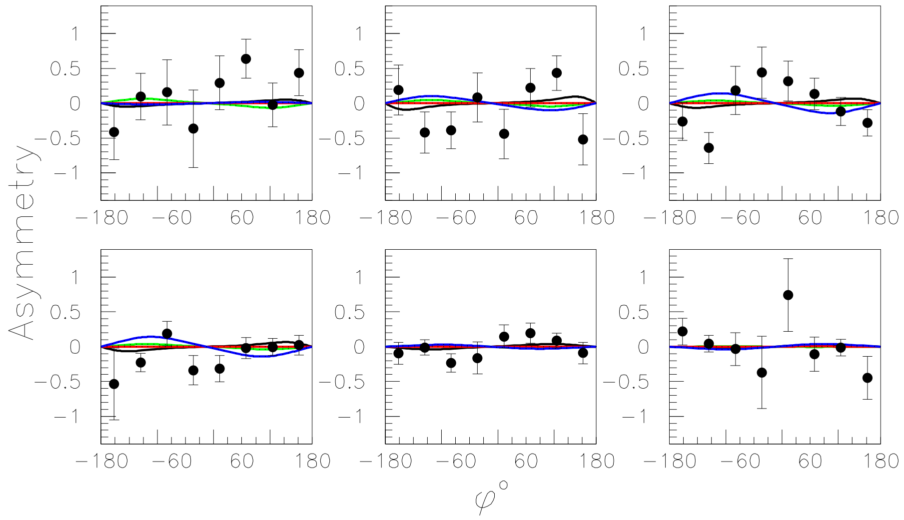

Figure 77: Measured asymmetries versus ϕ for $\cos\theta_K^{cm}$ = -0.833, -0.50, -0.167, 0.167, 0.50, 0.833 (upper left to lower right), $Q^2 = 0.7$ GeV^2, $W = 2.025$ GeV. Curves are the same as in Fig. 69.

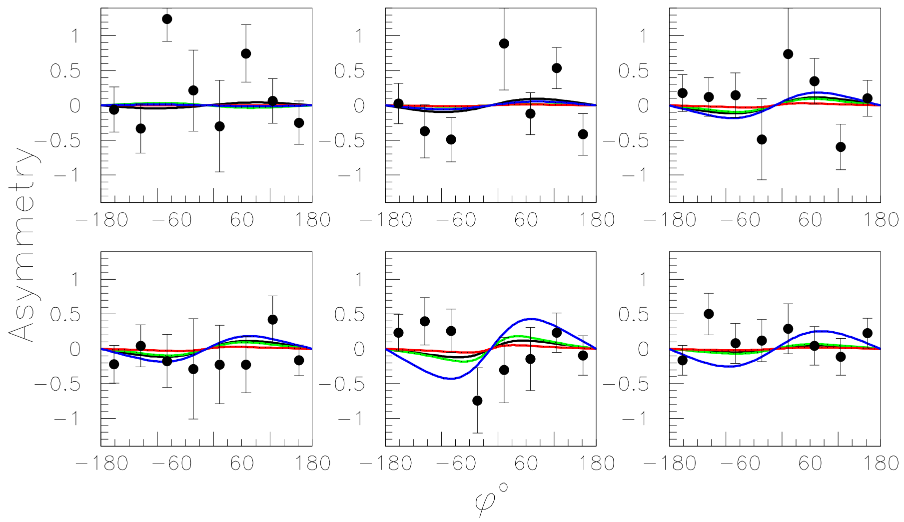

Figure 78: Measured asymmetries versus ϕ for $\cos\theta_K^{cm}$ = -0.833, -0.50, -0.167, 0.167, 0.50, 0.833 (upper left to lower right), $Q^2 = 1.1$ GeV^2, $W = 1.625$ GeV. Curves are the same as in Fig. 69.

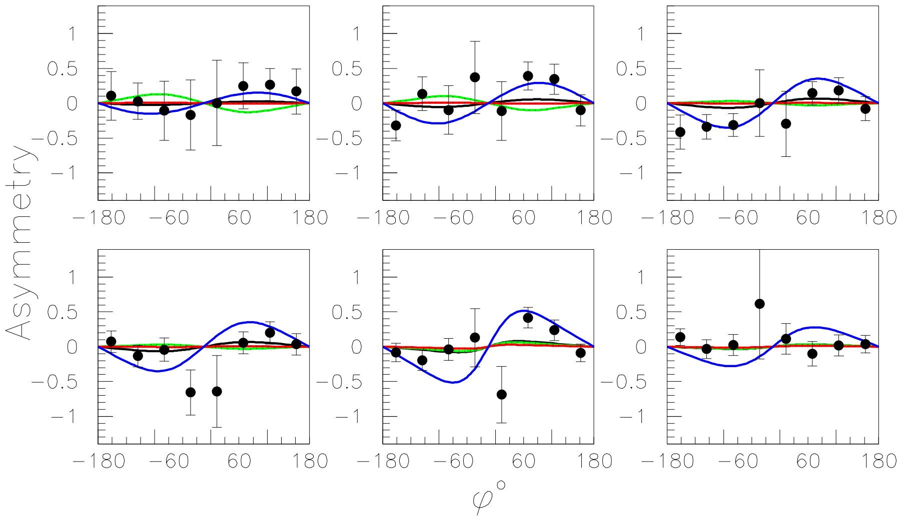

Figure 79: Measured asymmetries versus ϕ for $\cos\theta_K^{cm}$ = -0.833, -0.50, -0.167, 0.167, 0.50, 0.833 (upper left to lower right), $Q^2 = 1.1$ GeV^2, $W = 1.675$ GeV. Curves are the same as in Fig. 69.

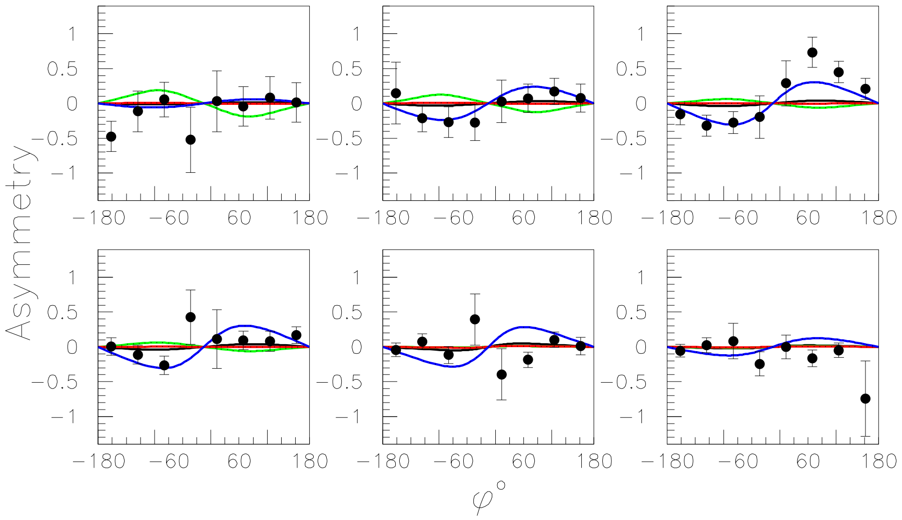

Figure 80: Measured asymmetries versus ϕ for $\cos\theta_K^{cm}$ = -0.833, -0.50, -0.167, 0.167, 0.50, 0.833 (upper left to lower right), $Q^2 = 1.1$ GeV^2, $W = 1.725$ GeV. Curves are the same as in Fig. 69.

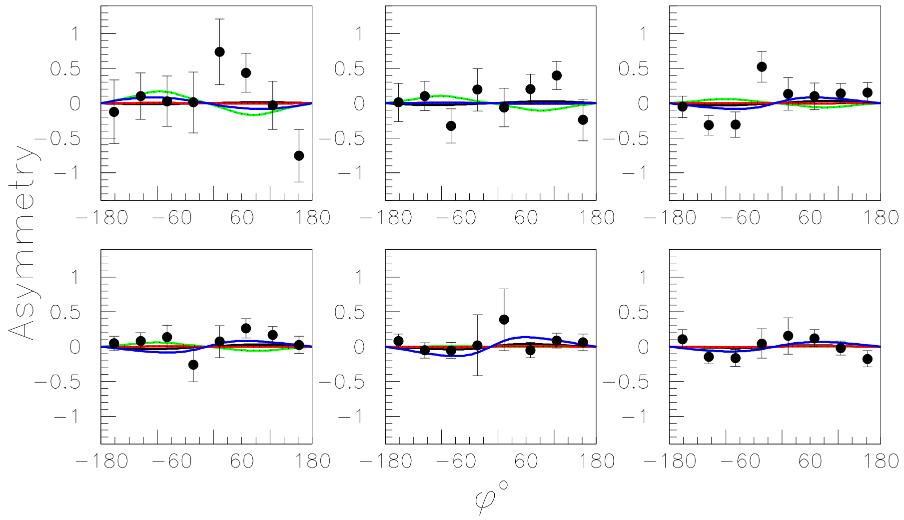

Figure 81: Measured asymmetries versus ϕ for $\cos\theta_K^{cm}$ = -0.833, -0.50, -0.167, 0.167, 0.50, 0.833 (upper left to lower right), $Q^2 = 1.1$ GeV^2, $W = 1.775$ GeV. Curves are the same as in Fig. 69.

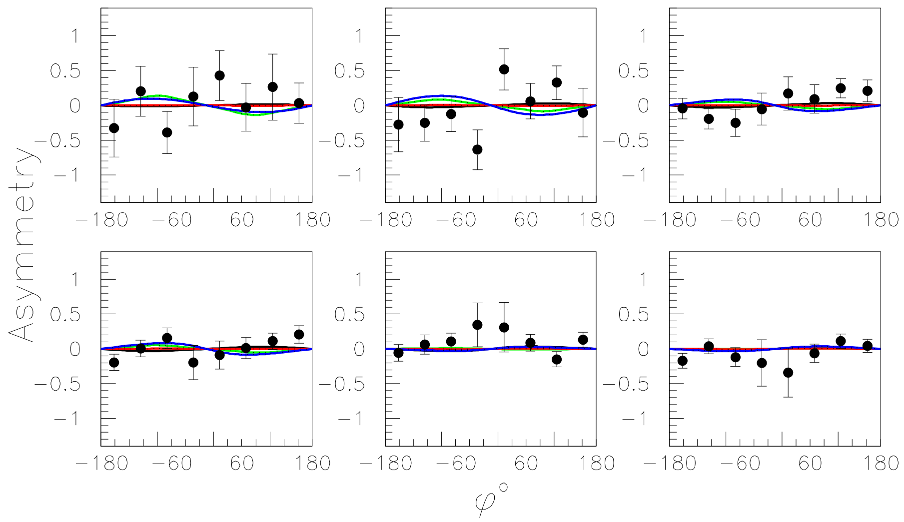

Figure 82: Measured asymmetries versus ϕ for $\cos\theta_K^{cm}$ = -0.833, -0.50, -0.167, 0.167, 0.50, 0.833 (upper left to lower right), $Q^2 = 1.1$ GeV^2, $W = 1.825$ GeV. Curves are the same as in Fig. 69.

6 Systematic Uncertainty Analysis for $A_{LT'}$

There are several sources of systematic uncertainty for $A_{LT'}$. The major sources are:

- Detector acceptance and efficiency.
- Radiative corrections
- Background corrections.
- Effects of fiducial cuts made during the data analysis.
- Beam polarization
- Beam charge asymmetry

The first four items represent sources of point-to-point uncertainties in the $A_{LT'}$ results while the last two will result in a scale uncertainty. In order to estimate the first four systematic uncertainties, the corrected, or nominal asymmetries, A^{nom} are compared to the asymmetries that result from using either alternative corrections or cuts, A^{alt}. The difference $A^{dif} = A^{nom} - A^{alt}$ is used as a measure of the systematic uncertainty. As will be shown, the uncertainties associated with acceptance, radiative corrections and fiducial cuts are small compared to the uncertainty associated with the background corrections and much smaller than the statistical uncertainties. Therefore, it is safe to calculate common uncertainties for all $A_{LT'}$ data points for each of these three effects. The estimated common uncertainty for a given effect is the weighted root-mean-square of A^{dif} for all points:

$$\delta A^{effect} = \sqrt{\frac{\sum (A_i^{dif})^2/(\delta A_i)^2}{\sum 1/(\delta A_i)^2}} \tag{69}$$

where sums are over all data points (i) and δA_i is the statistical uncertainty of the i^{th} data point. As described below, the systematic uncertainty for background corrections is larger and, when possible, has been determined for each asymmetry point.

6.1 Radiative Effects

The effect of the radiative correction on the asymmetry is shown in Fig. 83. The figure shows the uncorrected, EXCLURAD corrected, and RADGEN corrected asymmetries for a typical W and Q^2 bin. As seen, these results agree within the statistical uncertainties. It is expected that in the limit of infinite statistics of the Monte-Carlo events obtained from RADGEN event generator, the results will have a better agreement. This shows that the asymmetry measurement is fairly insensitive to the choice of the method for radiative corrections. The difference between the corrected asymmetries with the two different methods are shown in Fig. 84. In order to obtain a measure of overall systematic uncertainty associated with the radiative correction with EXCLURAD, the weighted average differences of the asymmetries with and without the radiative corrections is calculated by the formula above (Eq. 69). This is determined to be 0.017. The weighted distribution of the differences between corrected and uncorrected asymmetries is also shown in the histogram of Fig. 85 where the weight factor is the statistical uncertainty of each point. The RMS of this distribution is in complete agreement with the result of the calculation, as expected.

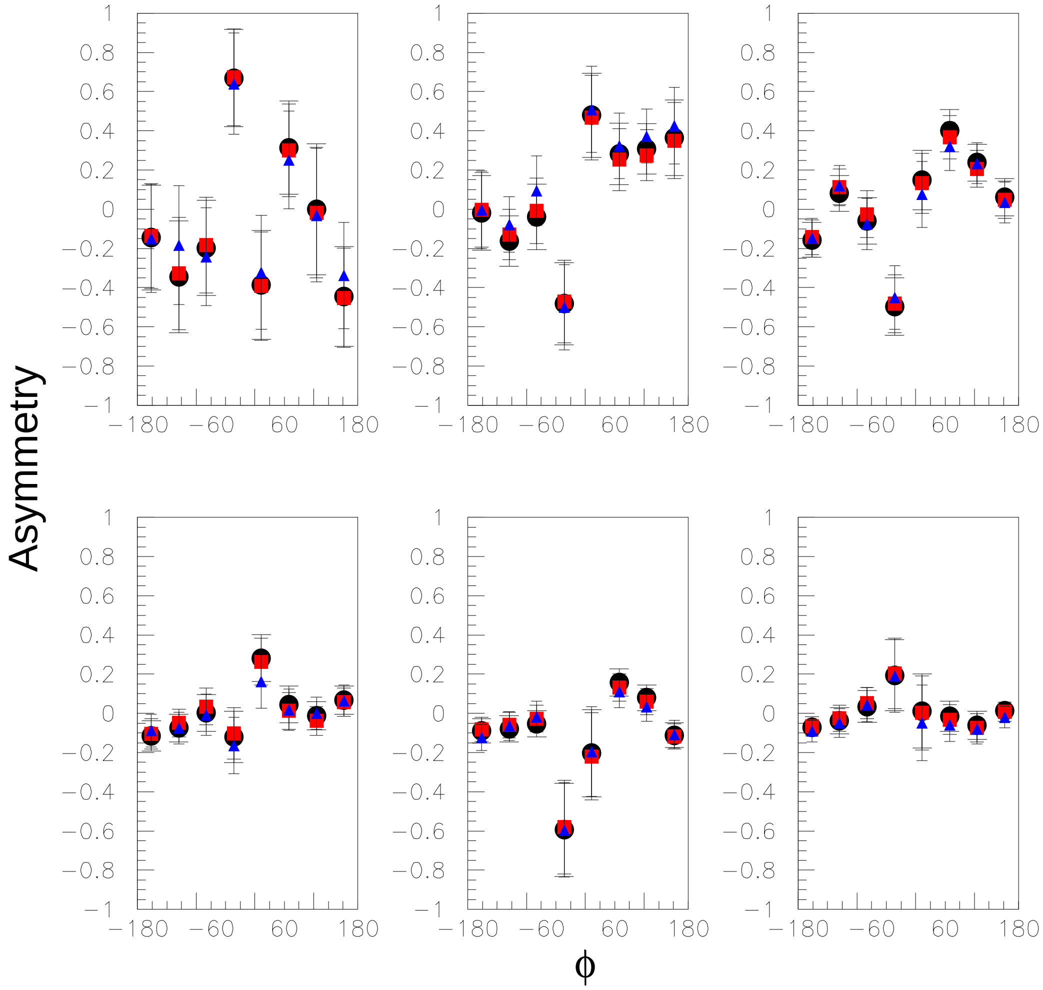

Figure 83: Measured asymmetries for $W = 1.825$ GeV, $Q^2 = 0.7$ (GeV)^2 and $\cos\theta_K^{cm}$ = -0.833, -0.50, -0.167, 0.167, 0.50, 0.833 (upper left to lower right). Black circles: no radiative correction. Red squares: corrected with EXCLURAD. Blue triangles: corrected with RADGEN.

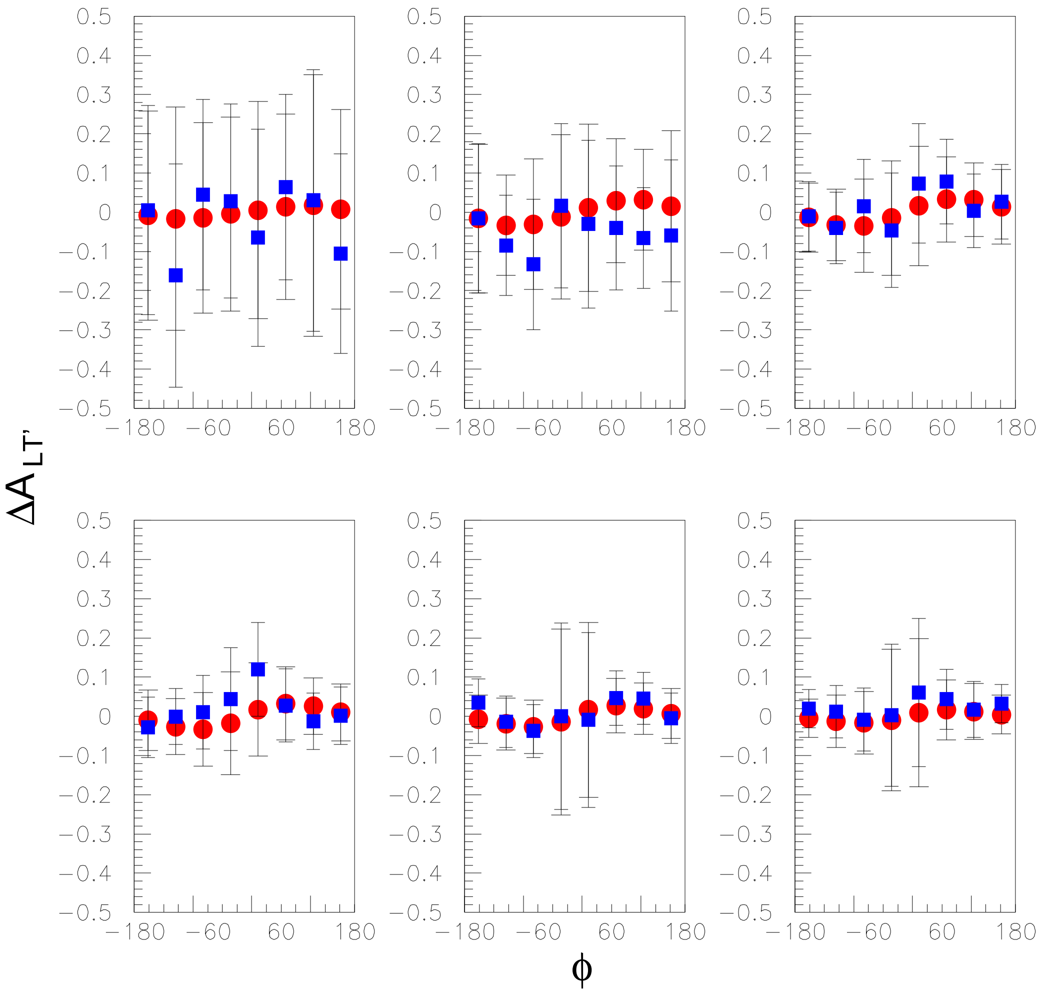

Figure 84: Difference between the uncorrected and corrected asymmetries for radiative effects with EXCLURAD (red circles) and RADGEN (blue squares). Results are shown for $W = 1.825$ GeV, $Q^2 = 0.7$ (GeV)^2 and $\cos\theta_K^{cm}$ = -0.833, -0.50, -0.167, 0.167, 0.50, 0.833 (upper left to lower right).

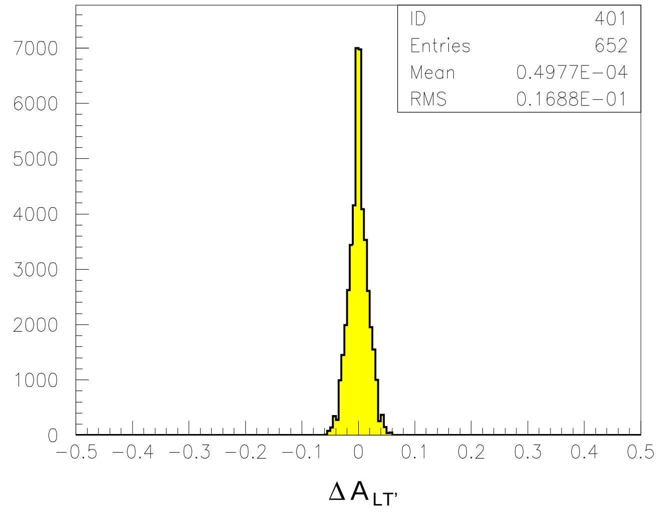

Figure 85: Weighted histogram of the differences between uncorrected and corrected asymmetries for radiative effects. The RMS of the distribution gives a measure of the systematic uncertainty associated with the radiative effects.

6.2 CLAS Efficiency and Acceptance

Two factors are studied in order to estimate the systematic uncertainties due to the CLAS efficiency and acceptance. The first factor is the functional form of the CLAS acceptance corrections obtained by using the GSIM model. The second factor is the volume fiducial cuts employed to select regions of detectors with constant efficiency. The effect of each factor is studied as follows.

6.2.1 Acceptance Function

The result of the asymmetry measurement is relatively insensitive to the acceptance corrections. This is shown in Section 5.4 and also Fig. 86 where the acceptance corrected asymmetries are plotted along with the uncorrected asymmetries for a typical W and Q^2 bin. In our final results, no acceptance correction has been employed. However, in this section, the effect of this correction is studied and the systematic uncertainty associated with CLAS acceptance is estimated. The difference between the corrected and uncorrected asymmetries for acceptance effects is shown in Fig. 87. The weighted RMS of these differences for the entire data set is calculated using the formula in Eq. 69. The result of this calculation is 0.033 which can also be seen as the RMS of the weighted distribution of the differences between corrected and uncorrected asymmetries shown in the histogram of Fig. 88. This is the estimated overall systematic uncertainty assigned to all of the data points.

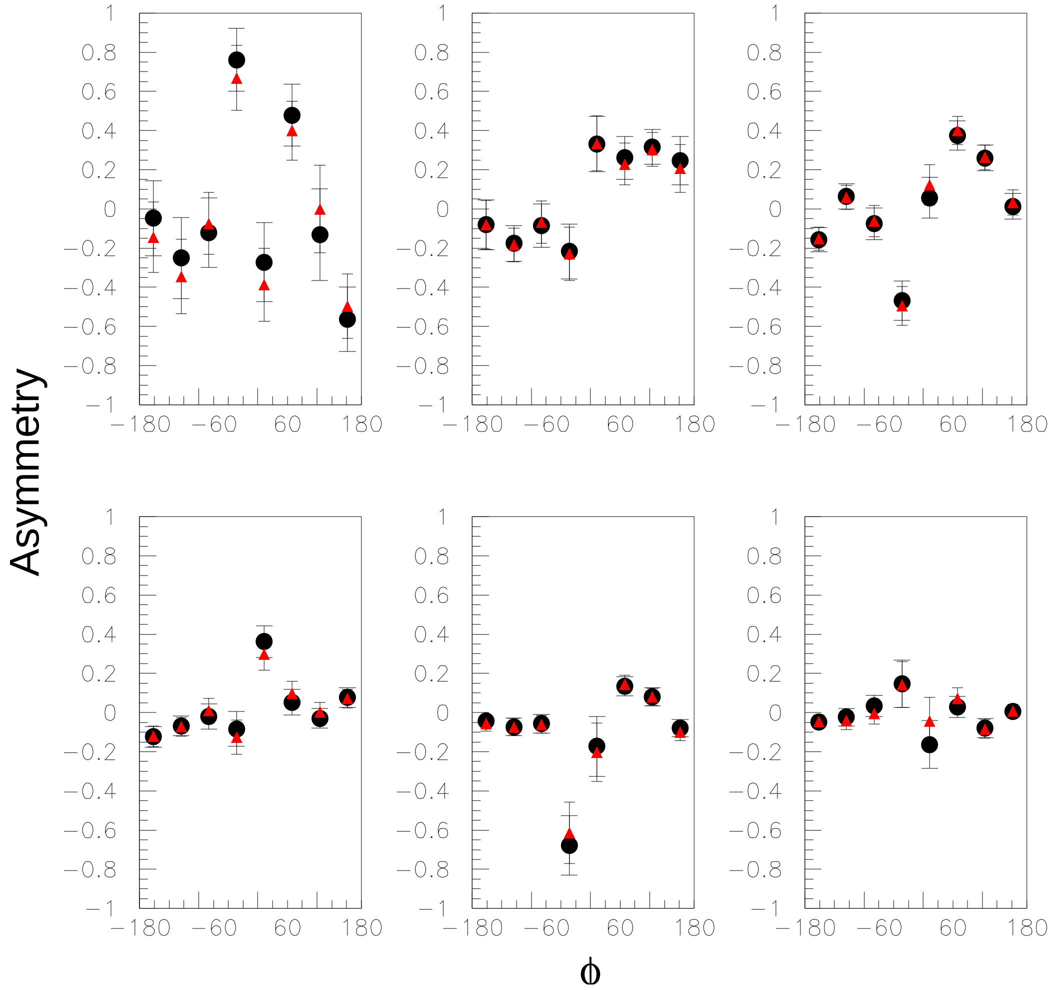

Figure 86: Measured asymmetries for $W = 1.825$ GeV, $Q^2 = 0.7$ $(\mathrm{GeV})^2$ and $\cos\theta_K^{cm}$ = -0.833, -0.50, -0.167, 0.167, 0.50, 0.833 (upper left to lower right). Black circles: no acceptance corrections. Red triangles: corrected with GSIM.

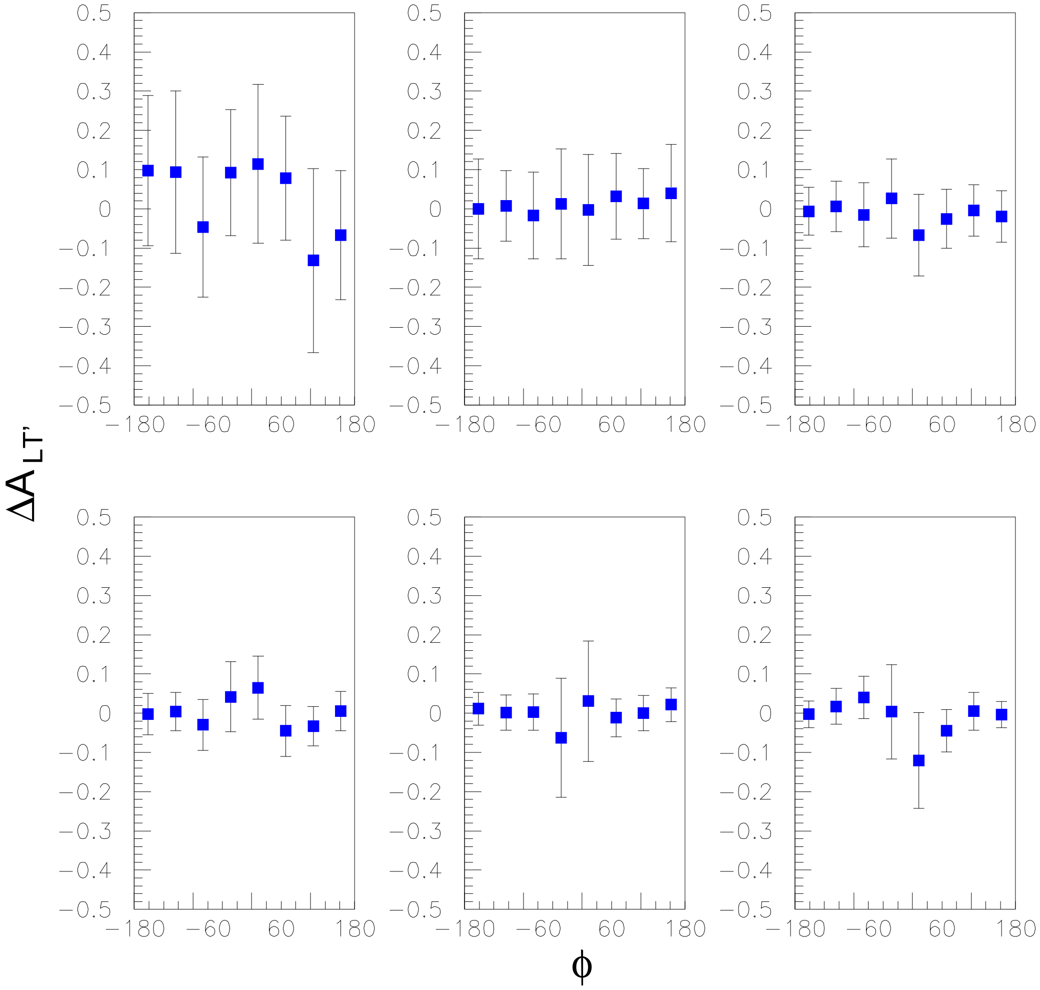

Figure 87: Difference between the uncorrected and corrected asymmetries for acceptance effects with GSIM. Results are shown for W = 1.825 GeV, Q^2 = 0.7 (GeV)^2 and $\cos\theta_K^{cm}$ = -0.833, -0.50, -0.167, 0.167, 0.50, 0.833 (upper left to lower right).

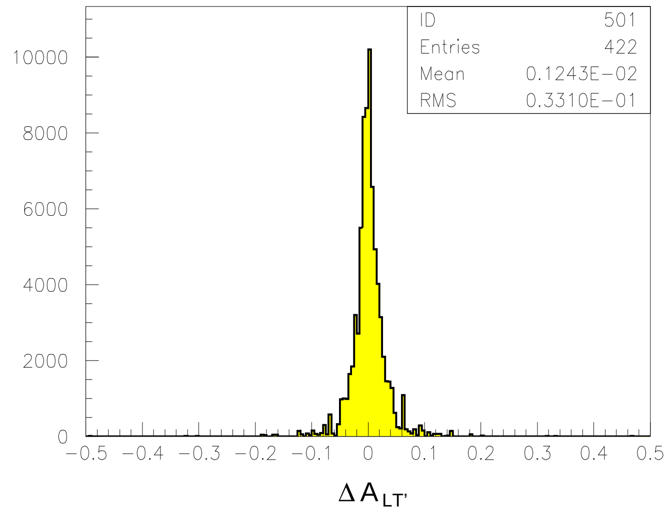

Figure 88: Weighted histogram of the differences between uncorrected and corrected asymmetries for acceptance effects. The RMS of the distribution gives a measure of the systematic uncertainty associated with the acceptance effects.

6.2.2 Fiducial Cuts

The fiducial cuts are defined to select the azimuthal acceptance regions of the edge of the CLAS detector as a function of momentum and angles for electrons and hadrons. The effect of fiducial cuts in the measured asymmetries are studied by altering the nominal cuts used in this analysis (see section 3.8). The asymmetries are then extracted with the altered cuts and the results are compared with the measured asymmetries with the nominal fiducial cuts. There are two altered cuts employed, the "loose" and the "tight" cuts (Fig. 89). The loose cuts allow a larger fiducial area of the detectors, while the tight cut requires smaller area. The asymmetries obtained employing the nominal, loose and tight cuts are plotted versus ϕ in Fig. 90. As seen the effect of choosing an altered cut is small. The differences between the

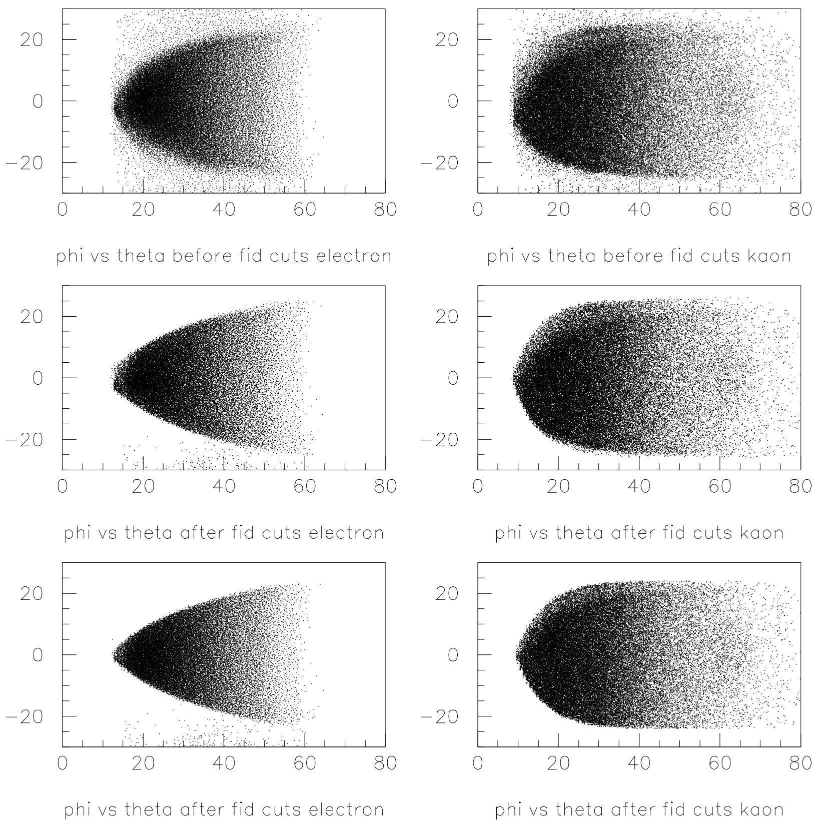

Figure 89: Fiducial cuts for electron (left) and hadron (right) used for systematic uncertainty analysis. Cuts are shown for sector one. Top: before the cuts. Mid: after the loose cuts. Bottom: after the tight cuts.

asymmetries obtained using the nominal cuts and each altered cut are also shown in Fig. 91. The RMS of these differences are calculated using the formula in Eq. 69 for each case. The weighted differences are also plotted in the histograms of Fig. 92. The weighted average of these differences is 0.041 and 0.049 for the loose and tight cuts respectively. The RMS of these two values, 0.045, is then assigned to each data point as the point-to-point systematic uncertainty associated with the fiducial cuts.

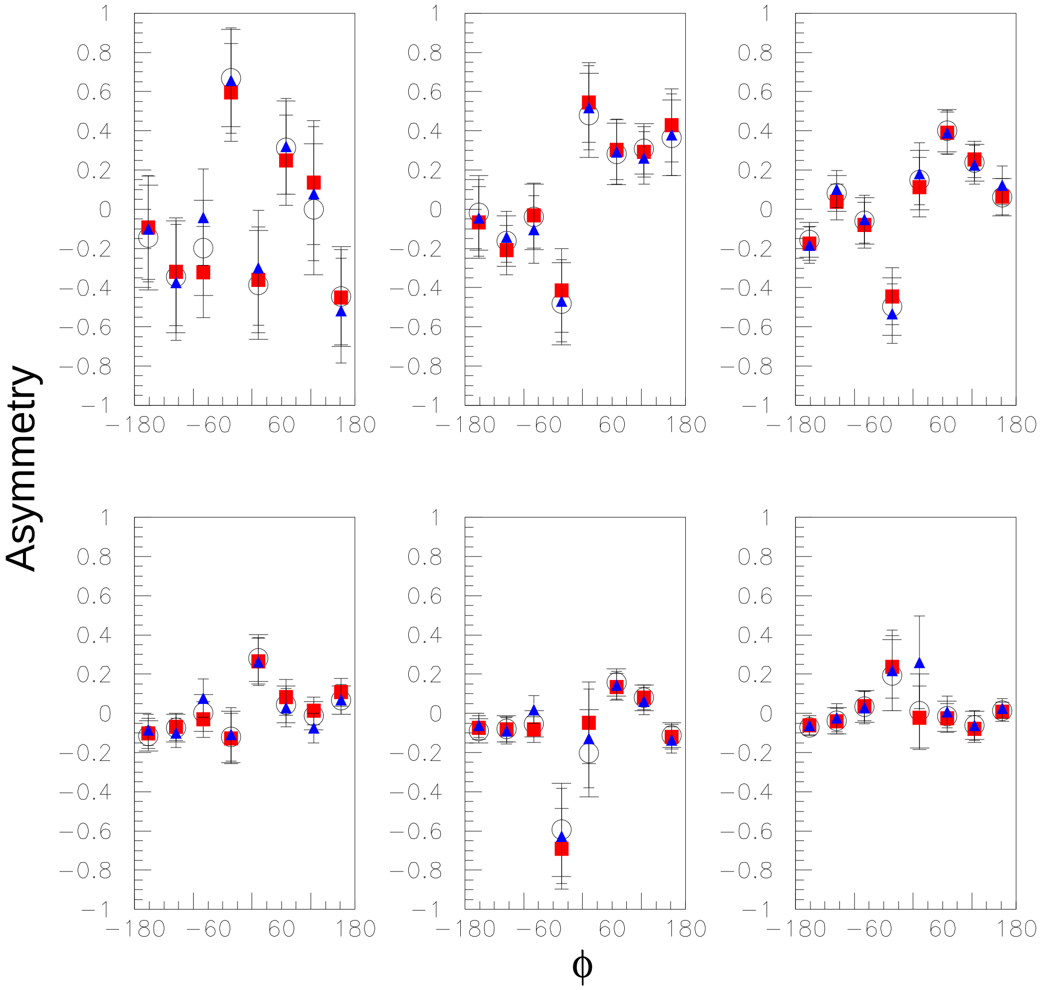

Figure 90: Measured asymmetries for $W = 1.825$ GeV, $Q^2 = 0.7$ (GeV)^2 and $\cos\theta_K^{cm}$ = -0.833, -0.50, -0.167, 0.167, 0.50, 0.833 (upper left to lower right) obtained with the nominal (Black circles), loose (red squares), and tight fiducial cuts (blue triangles).

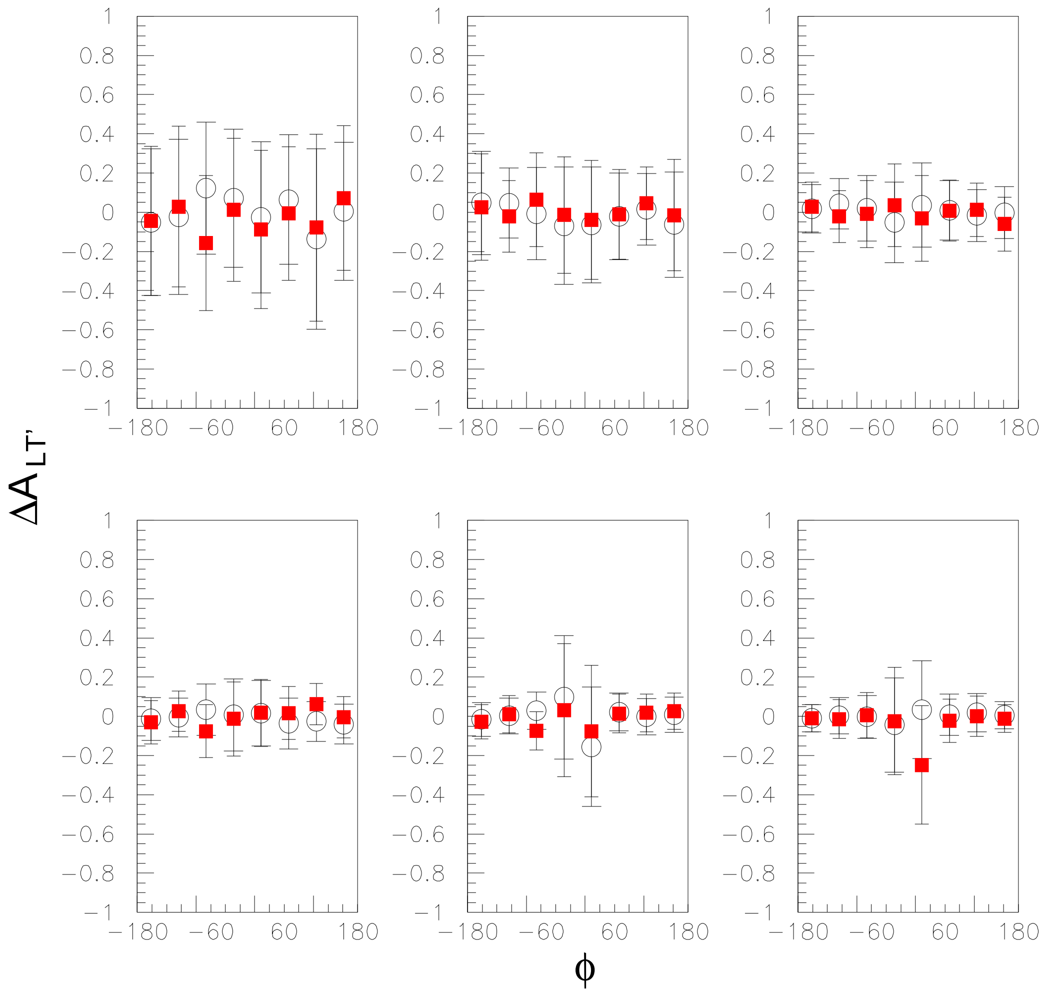

Figure 91: Difference between the asymmetries obtained with nominal fiducial cuts with the loose (black circles) the tight fiducial cuts (red squares). Results are shown for W = 1.825 GeV, Q^2 = 0.7 (GeV)^2 and $\cos\theta_K^{cm}$ = -0.833, -0.50, -0.167, 0.167, 0.50, 0.833 (upper left to lower right).

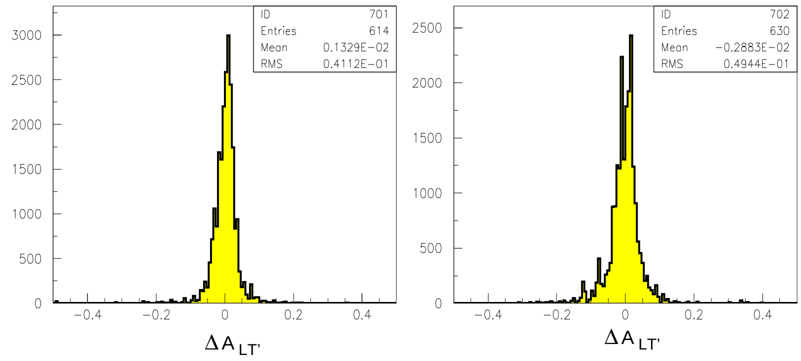

Figure 92: Weighted histograms of differences between asymmetries with the nominal and loose (left), and the nominal and tight (right) fiducial cuts.

6.3 Background Effects

As discussed in section 4.1, the background effects on the missing mass distributions, due to the multi-particle final states are removed by fitting the missing mass distribution to the uniform background shape using a maximum log likelihood method. The phase space background was modeled by selecting pions and protons from hadron mass spectrum and calculating the missing mass by assigning the kaon mass to them. These two distributions were then fitted to the real missing mass spectrum and the best estimate of the fractional contribution of each distribution is obtained.

In order to estimate the systematic uncertainty due to this procedure, two different methods were compared to the original background subtraction method. In the first method, the contribution of the proton background was fixed at zero while modeling the background only with selected pions. In the second method, the background was modeled only by the proton contributions and the pion contribution was fixed at zero. The asymmetries are calculated for both cases and compared with the original method where both distributions are free to contribute to the background model Fig. 93. The differences between the asymmetries obtained using these two alternative background correction models and the nominal model, along with the difference between uncorrected and corrected with the nominal model is shown in Fig. 94.

The RMS of these three differences are calculated for each data point and assigned to that point as the estimated systematic uncertainty.

In very low statistics bins, the background fitting procedure fails. In these bins, the uncorrected yields are used in forming the asymmetry. Therefore, it is not possible to use the above method to determine a background related systematic uncertainty. Instead, the weighted average difference between the uncorrected and corrected asymmetries with each method of background corrections is calculated. The weighted distribution of these differences are shown in the histograms of Fig. 95 with the RMS values of the differences shown in the legend. The RMS of these three values, 0.06, is then assigned, as the systematic uncertainty for background effects, to the points where the background correction is not applied .

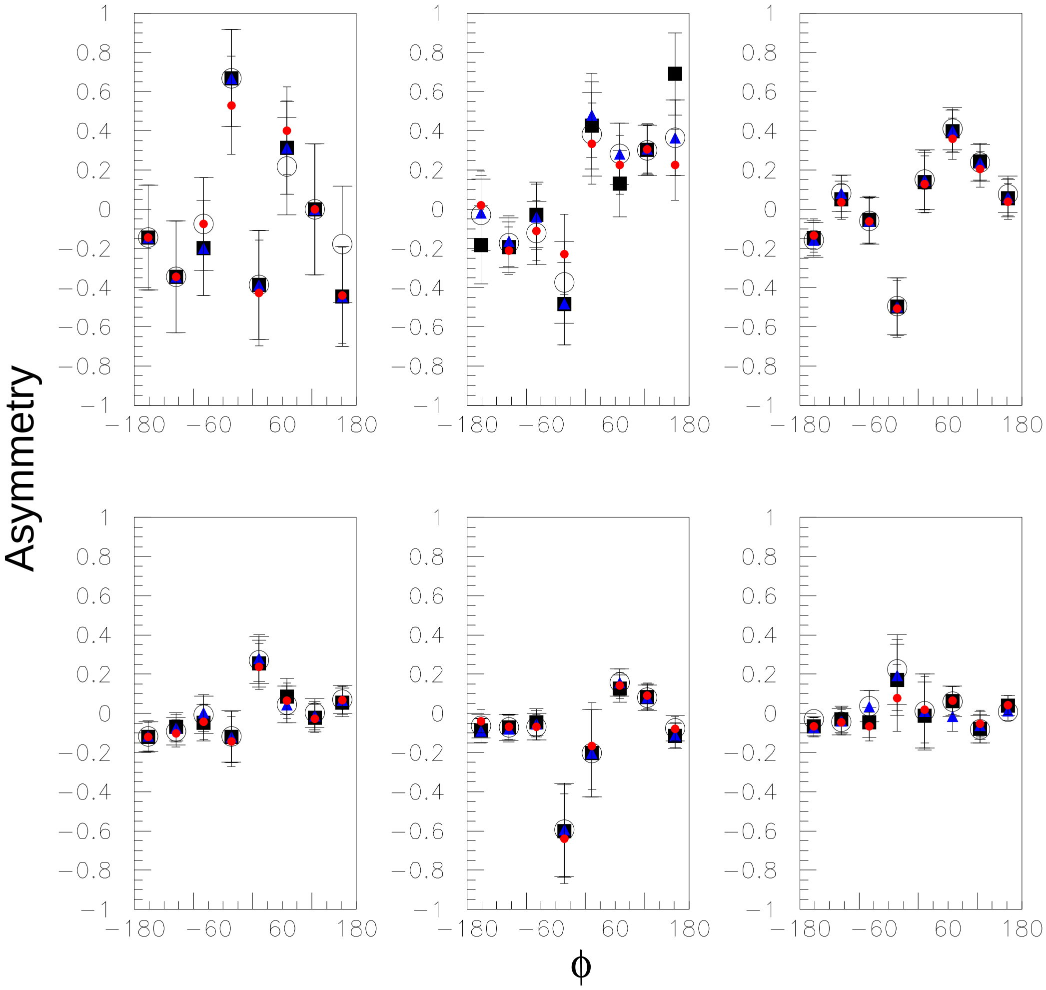

Figure 93: Measured uncorrected (Red dots) and corrected asymmetries for background effects with modeling the background shape from pions (black circles), protons (black squares), and both pions and protons (blue triangles). Data are shown for W = 1.825 GeV, Q^2 = 0.7 (GeV)^2 and $\cos\theta_K^{cm}$ = -0.833, -0.50, -0.167, 0.167, 0.50, 0.833 (upper left to lower right).

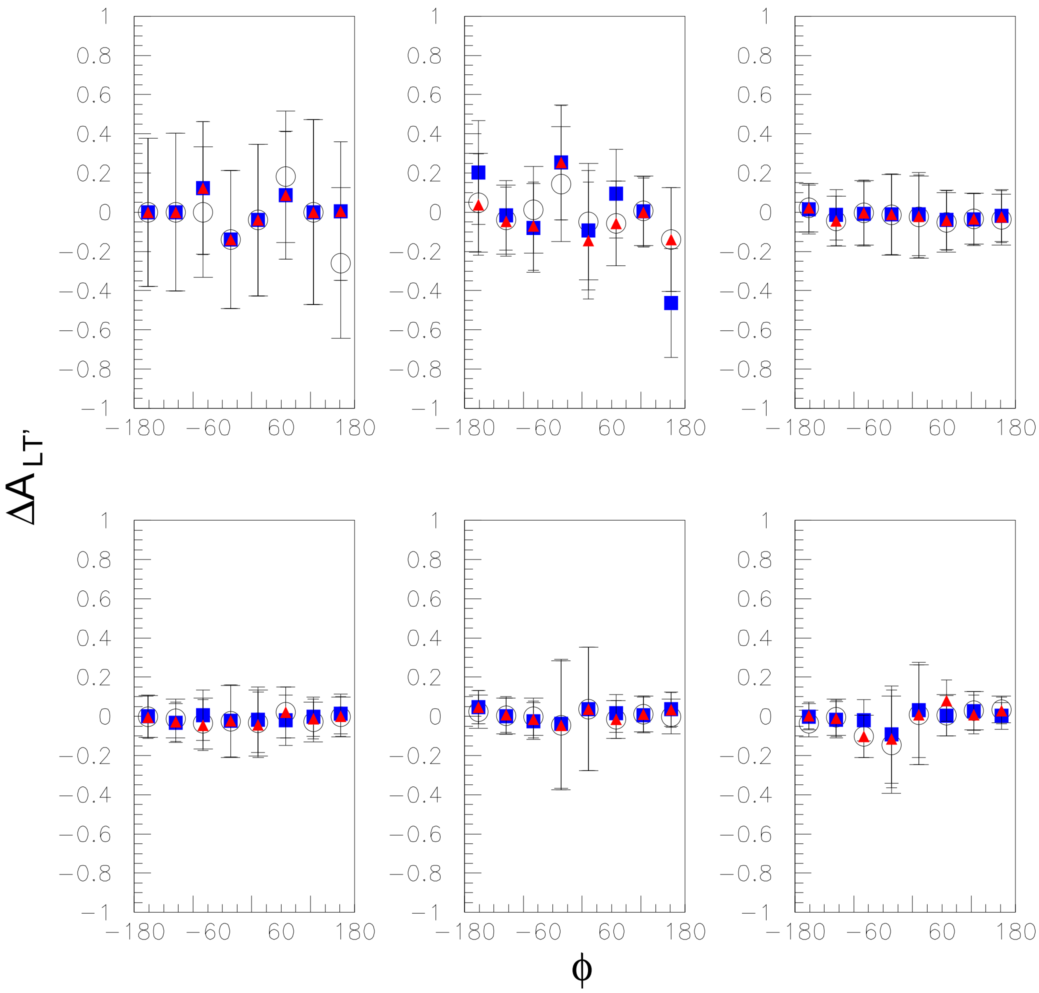

Figure 94: Difference between the corrected asymmetries with the nominal background correction model (using both pions and protons for modeling the background phase space) and the alternative models using only pions (black circles), only protons (blue squares), and uncorrected asymmetries (red triangles). Results are shown for W = 1.825 GeV, Q^2 = 0.7 (GeV)^2 and $\cos\theta_K^{cm}$ = -0.833, -0.50, -0.167, 0.167, 0.50, 0.833 (upper left to lower right).

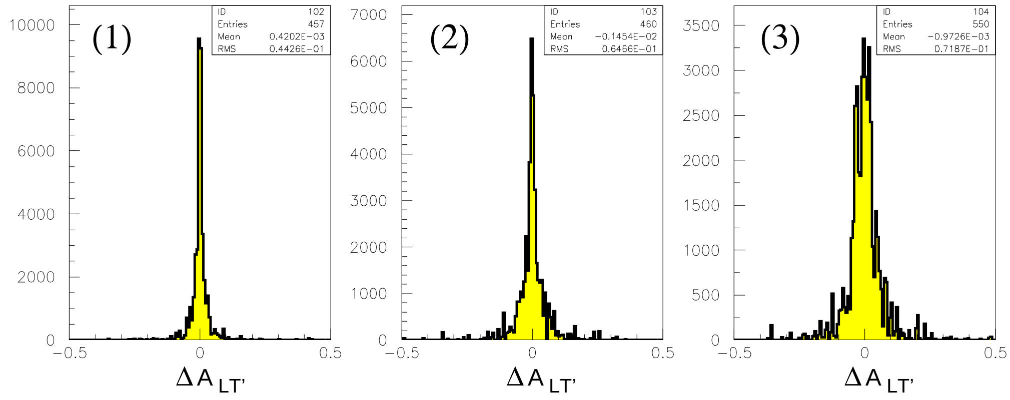

Figure 95: Weighted distribution of differences between background corrected asymmetries using the nominal model (using both pions and protons for modeling the background phase space) and the alternative models using only pions (1), only protons (2), and uncorrected asymmetries (3).

6.4 Beam Related Factors

The beam related factors that contribute to the systematic uncertainties for the asymmetry measurements are due to 1) beam charge asymmetries and 2) beam polarization measurements. These effects have been previously discussed in detail in Section 5.2 and 5.3. The estimated systematic uncertainty from beam charge asymmetry is 2.99×10^{-3}. This is the average of the beam charge asymmetries for the two torus settings normalized to the number of triggers in each set. The systematic uncertainty for the average beam charge asymmetry correction is 1.45×10^{-3}.

The relative systematic uncertainty due to the beam polarization measurement for the data set used in this analysis with beam energy of 2.567 GeV is estimated to be $\frac{\delta P}{P} = 0.023$. The estimated uncertainty for $A_{LT'}$ for the beam polarization is calculated by Eq. 66 where $\delta P = 0.0153$. These results are also summarized in

Table 7.

Source	Description	Systematic Uncertainty $A_{LT'}$
Background effects	Pion Contribution	0.044
	Proton Contribution	0.064
	No correction	0.071
	Over All	0.060
	Point-to-Point	Table 11 to 24
Acceptance and Efficiency	Fiducial Cuts	0.045
	Acceptance function (GSIM)	0.033
Radiative Effects	EXLURAD Model	0.017
Beam Related Factors	Beam Polarization	$\frac{\delta P}{P} = 0.023$
	Beam Charge Asymmetry	1.45×10^{-3}

Table 7: Summary of the result of systematic study for $A_{LT'}$.

7 Extraction of Polarized Structure Function $\sigma_{LT'}$

7.1 Unpolarized Cross Section

The single spin asymmetry, $A_{LT'}$, is directly proportional to the fifth structure function $\sigma_{LT'}$:

$$A_{LT'} = \frac{\sqrt{2\epsilon_L(1-\epsilon)}\sigma_{LT'}\sin\phi_K}{\sigma_0} \tag{70}$$

where σ_0 is the unpolarized cross section give by

$$\sigma_0 = \sigma_T + \epsilon_L\sigma_L + \sqrt{2\epsilon_L(1+\epsilon)}\sigma_{LT}\cos\phi_K + \epsilon\sigma_{TT}\cos 2\phi_K. \tag{71}$$

Inverting Eq. 70 gives

$$A_{LT'}\sigma_0 = \sqrt{2\epsilon_L(1-\epsilon)}\sigma_{LT'}\sin\phi_K \tag{72}$$

The unpolarized differential cross sections, σ_0, for the $p(\vec{e}, e'K^+)\Lambda$ reaction were measured by R. Feuerbach from the same data set [33]. In that analysis, σ_0 was measured as a function of Q^2, W, $\cos\theta_K^{cm}$, and ϕ_K and the structure functions, $\sigma_u = \sigma_T + \epsilon\sigma_L$, σ_{TT} and σ_{LT} were extracted. In order to smooth out the statistical fluctuations of the unpolarized cross section data, a two-dimensional simultaneous fit in ϕ and $\cos\theta_K^{cm}$ of the following functional form is applied to σ_0 data [67]:

$$\sigma_0 = (a_1 + a_2x + a_3x^2 + a_4x^3) + (b_1 + b_2x + b_3x^2 + b_4x^3)\cos\phi$$
$$+(c_1 + c_2x + c_3x^2 + c_4x^3)\cos 2\phi$$

where $x = \cos\theta_K^{cm}$. The original σ_0 data and the resulting fits are shown in Appendix F. In each figure, the solid line is the best fit and the dashed lines represent a 1σ error band around the fit. As expected, the error band is smaller than the uncertainty of the nearby data points. This means that there will be a smaller contribution to the $\sigma_{LT'}$ than if the σ_0 data were used directly.

The measured asymmetries, $A_{LT'}$, are multiplied by the unpolarized cross section, σ_0, obtained by the above fit for each kinematic bin and plotted versus ϕ in Figs. 97 to 110. The statistical uncertainties for $A_{LT'}\sigma_0$, are a combination of the contributions from each part as follows:

$$\delta(A_{LT'}\sigma_0) = \sqrt{\left(A_{LT'}\delta\sigma_0\right)^2 + \left(\sigma_0\delta A_{LT'}\right)^2} \tag{73}$$

where $\delta A_{LT'}$ is the quadrature sum of the statistical and systematic uncertainties for $A_{LT'}$.

A fit of the form of a $a \sin\phi$ is performed and the fit parameter a is obtained for each bin. The fifth structure function, $\sigma_{LT'}$ is then extracted by dividing this parameter by the kinematic factor for a that kinematic bin, $\sqrt{2\epsilon_L(1-\epsilon)}$, as in the Eq. 72. The χ^2 per degrees of freedom of the sine fits are plotted in the Fig. 111. This distribution agrees well with the expected distribution for seven degrees of freedom [68].

7.2 Kinematic Factor

As mentioned in previous section, $\sigma_{LT'}$ is extracted by using Eq. 70 and fitting the ϕ dependence of the measured asymmetries times the unpolarized cross section for each bin. The fifth structure function is then obtained by dividing the fit parameter by the kinematic factor, $\sqrt{2\epsilon_L(1-\epsilon)}$. This kinematic factor has been calculated for each event, then the average value is determined for each kinematic bin. Due to the importance of the kinematic factor in extracting the fifth structure function, we have done the following study in order to account for the effects of the CLAS acceptance in measuring this factor event by event:

For each torus setting and each helicity state, 3M events were generated with RADGEN employing a theoretical model [14] for the kaon electroproduction cross section. The kinematic factor was calculated for Monte-Carlo events and averaged over each kinematic bins. Then the generated events were used as input for the CLAS simulation package to study the effect of the CLAS acceptance and the kinematic factor was again calculated for the accepted events. Fig. 96 shows the comparison between the values obtain for the kinematic factor using the thrown Monte-Carlo events, CLAS accepted Monte-Carlo events, and the real data. The mean value of the kinematic factor distribution is plotted versus $\cos\theta_K^{cm}$ for various bins of Q^2 and W. We noticed that there is a very small field dependence ($< 1\%$) , and the CLAS acceptance effect for the Monte-Carlo events before and after simulation is up to 3% in the worst cases. However, the data shows a percentage difference of up to 5% in the worst cases compared to CLAS accepted Monte-Carlo events. As a result of this study, the following correction is done to the measured kinematic factor from the data:

$$K_{corr} = K_{data} \times \frac{K_{mc}}{K_{acc}} \tag{74}$$

where K_{mc} and K_{acc} are the kinematic factors measured for the Monte-Carlo and CLAS accepted Monte-Carlo events respectively.

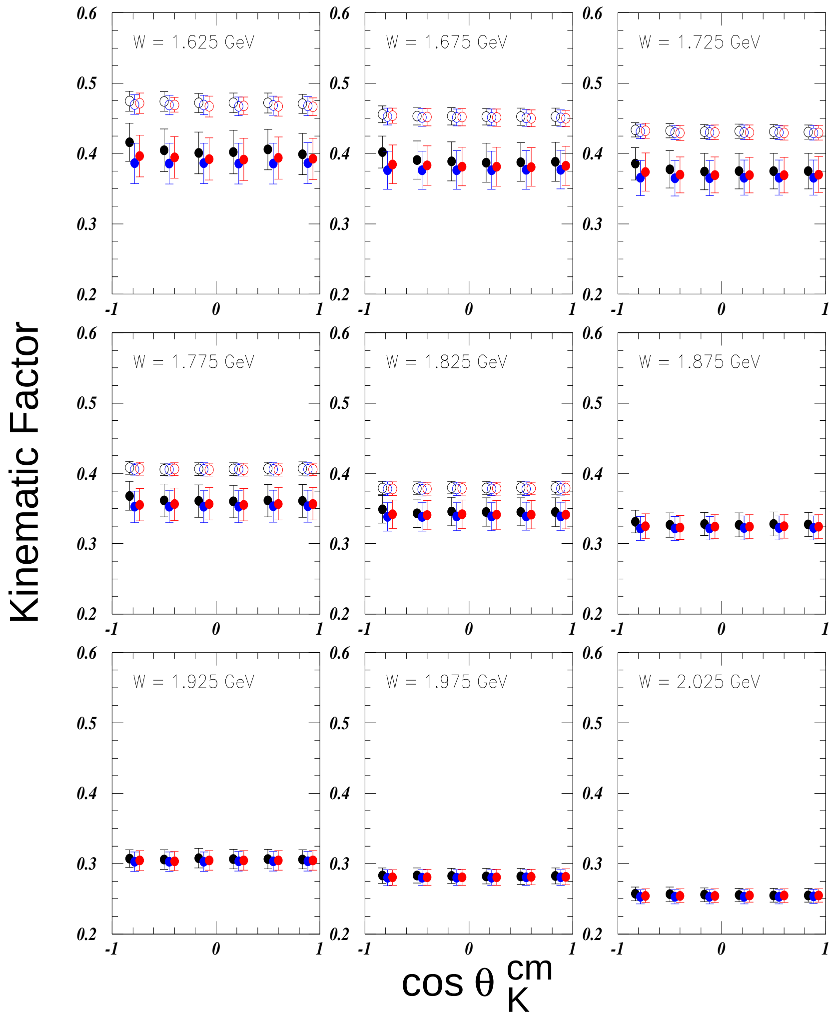

Figure 96: Plots of the kinematic factor, $\sqrt{2\epsilon_L(1-\epsilon)}$ versus $\cos\theta_K^{cm}$ for various W and Q^2 bins. Black = real data, Blue: Monte-Carlo data, Red: GSIM accepted Monte-Carlo data. Filled circles: high $Q^2 = 1.1$ GeV^2, Hollow circles: low $Q^2 = 0.7$ GeV^2. The data were plotted with a small offset on x-axis for better visibility. The horizontal error bars are the width of the distributions.

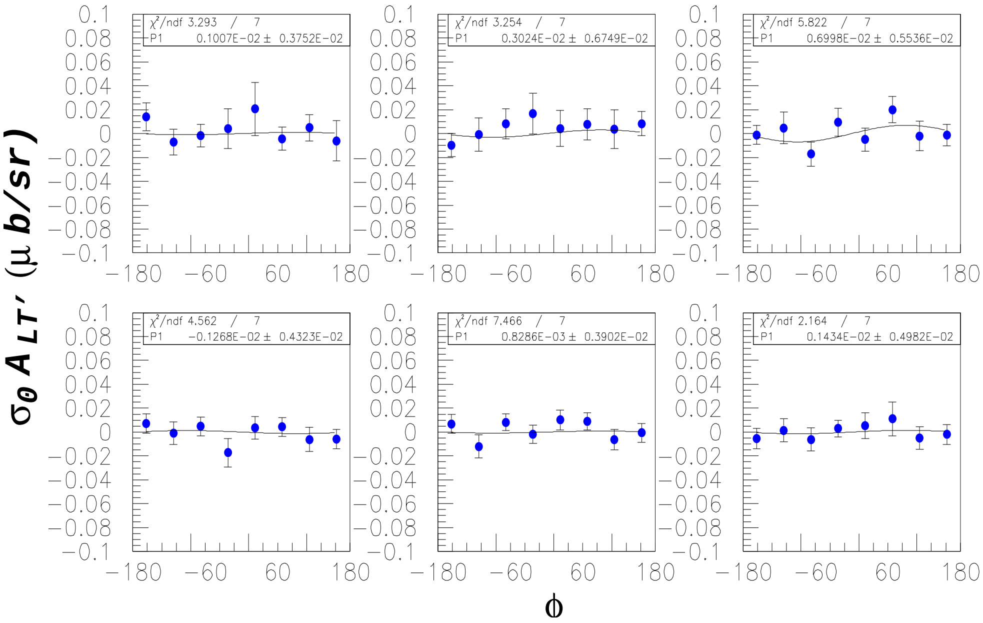

Figure 97: Measured asymmetries multiplied by unpolarized cross section versus ϕ for $\cos\theta_K^{cm}$ = -0.833, -0.50, -0.167, 0.167, 0.50, 0.833 (upper left to lower right), $Q^2 = 0.7$ GeV^2 and $W = 1.625$ GeV. The curves are a fit to $a \sin\phi$.

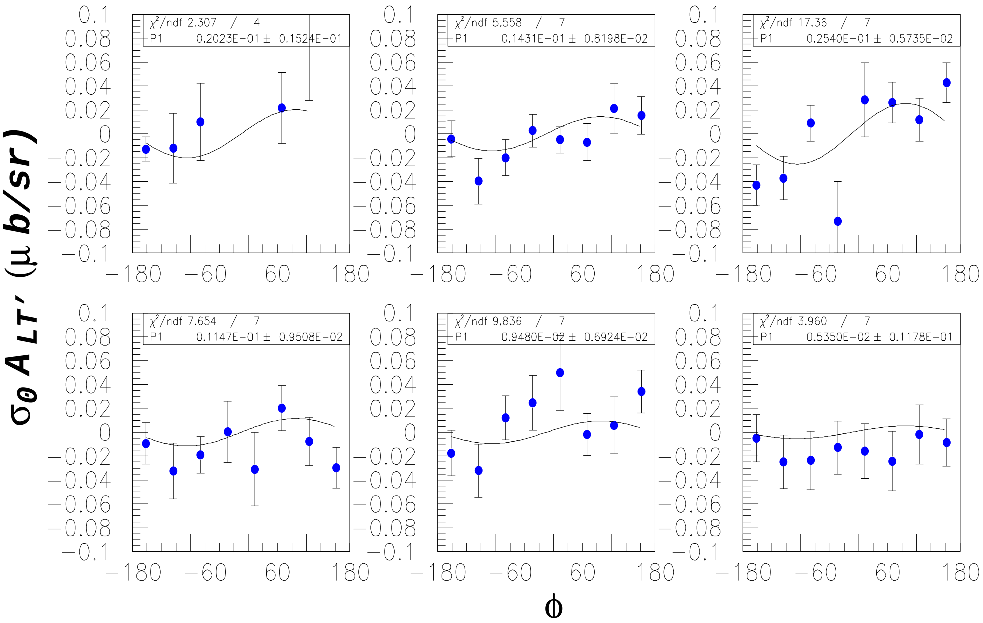

Figure 98: Measured asymmetries multiplied by unpolarized cross section versus ϕ for $\cos\theta_K^{cm}$ = -0.833, -0.50, -0.167, 0.167, 0.50, 0.833 (upper left to lower right), $Q^2 = 0.7$ GeV^2 and $W = 1.675$ GeV. The curves are a fit to $a \sin\phi$.

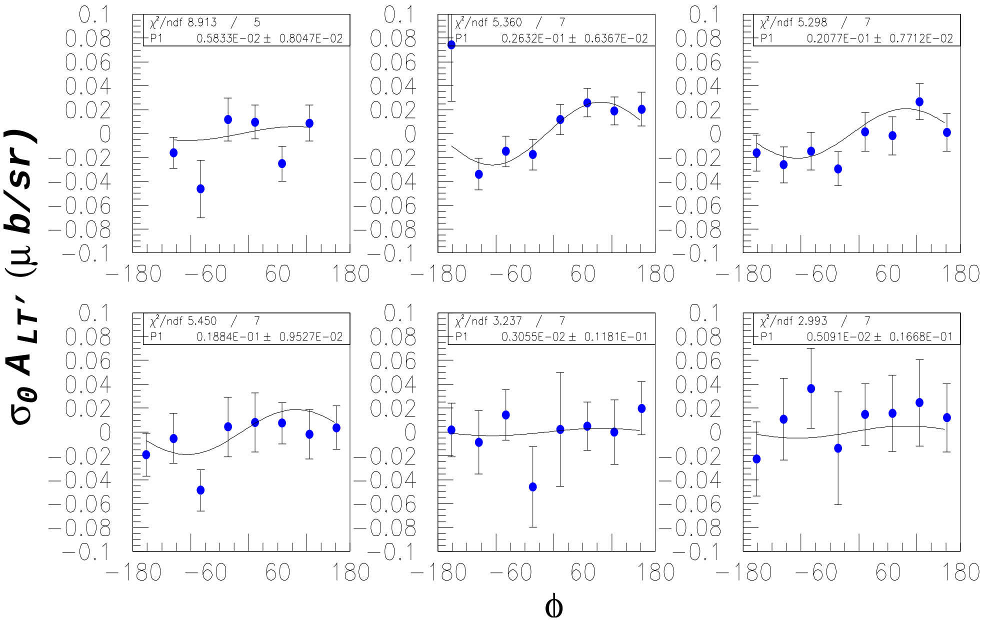

Figure 99: Measured asymmetries multiplied by unpolarized cross section versus ϕ for $\cos\theta_K^{cm}$ = -0.833, -0.50, -0.167, 0.167, 0.50, 0.833 (upper left to lower right), $Q^2 = 0.7$ GeV^2 and $W = 1.725$ GeV. The curves are a fit to $a \sin\phi$.

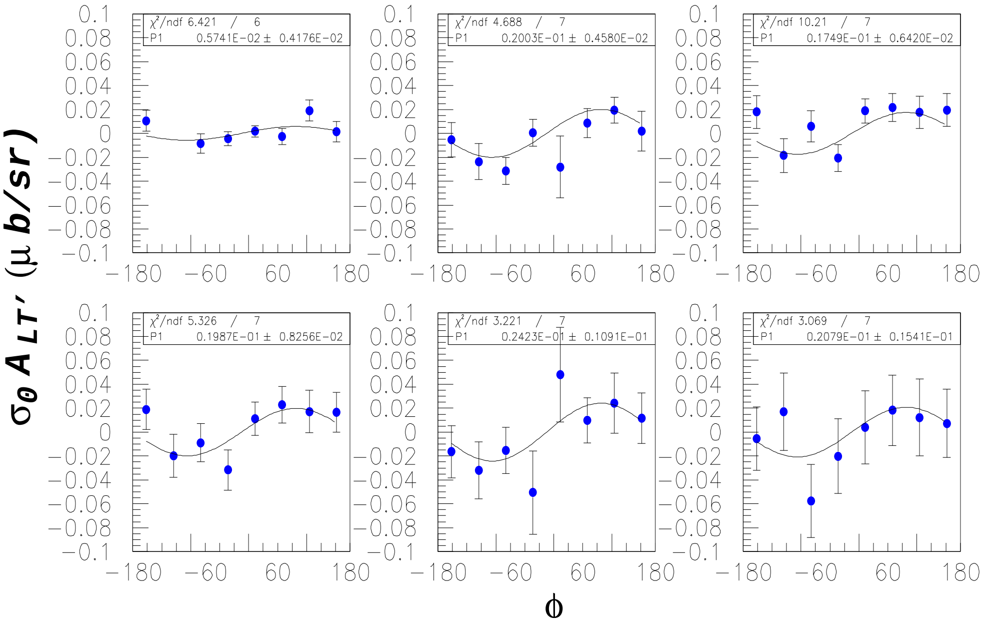

Figure 100: Measured asymmetries multiplied by unpolarized cross section versus ϕ for $\cos\theta_K^{cm}$ = -0.833, -0.50, -0.167, 0.167, 0.50, 0.833 (upper left to lower right), $Q^2 = 0.7$ GeV^2 and $W = 1.775$ GeV. The curves are a fit to $a \sin\phi$.

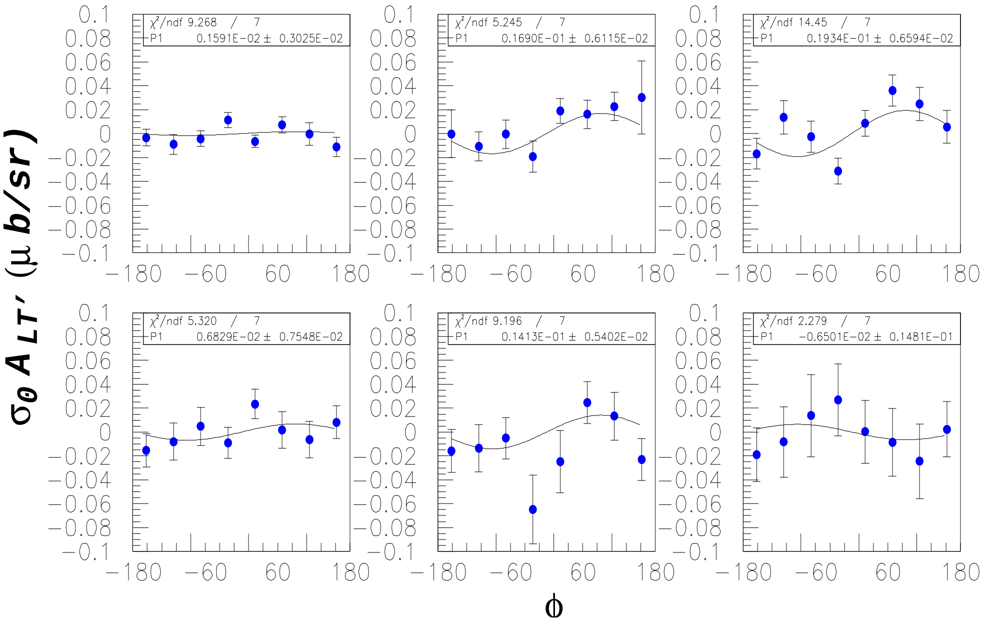

Figure 101: Measured asymmetries multiplied by unpolarized cross section versus ϕ for $\cos\theta_K^{cm}$ = -0.833, -0.50, -0.167, 0.167, 0.50, 0.833 (upper left to lower right), $Q^2 = 0.7$ GeV^2 and $W = 1.825$ GeV. The curves are a fit to $a \sin\phi$.

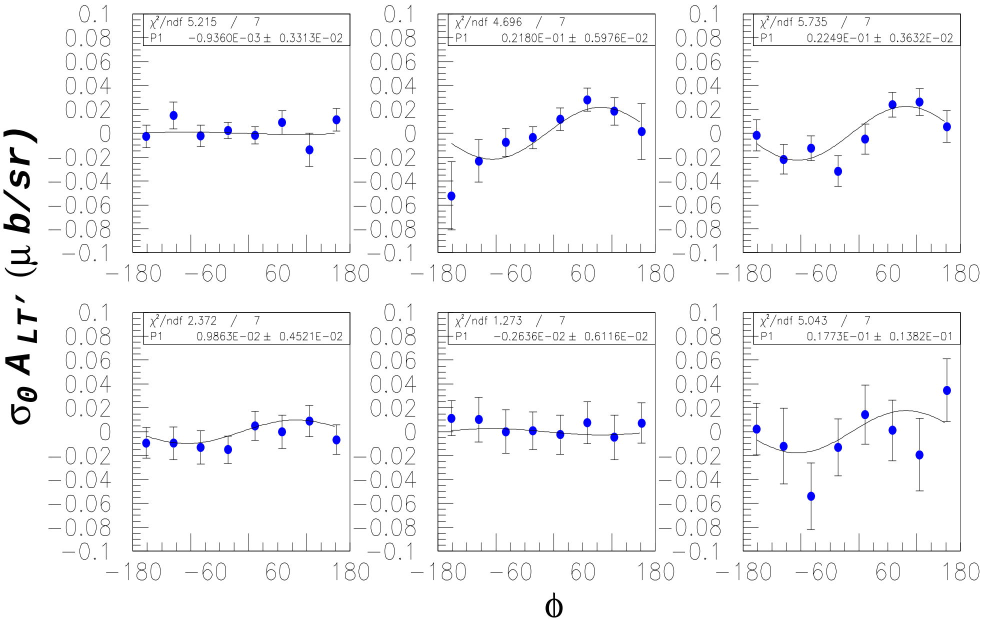

Figure 102: Measured asymmetries multiplied by unpolarized cross section versus ϕ for $\cos\theta_K^{cm}$ = -0.833, -0.50, -0.167, 0.167, 0.50, 0.833 (upper left to lower right), $Q^2 = 0.7$ GeV^2 and $W = 1.875$ GeV. The curves are a fit to $a \sin\phi$.

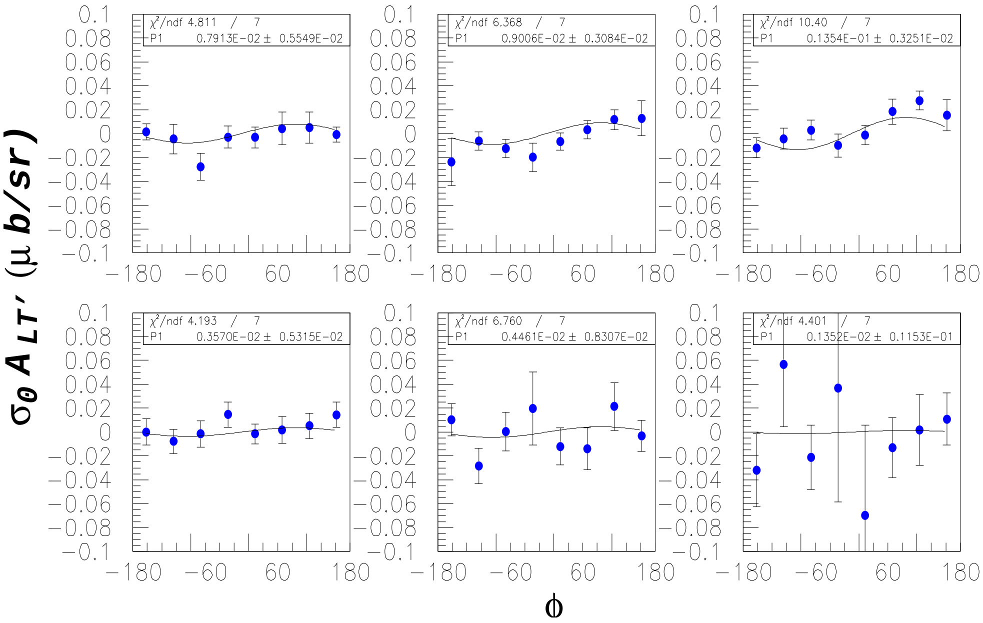

Figure 103: Measured asymmetries multiplied by unpolarized cross section versus ϕ for $\cos\theta_K^{cm}$ = -0.833, -0.50, -0.167, 0.167, 0.50, 0.833 (upper left to lower right), $Q^2 = 0.7$ GeV^2 and $W = 1.925$ GeV. The curves are a fit to $a \sin\phi$.

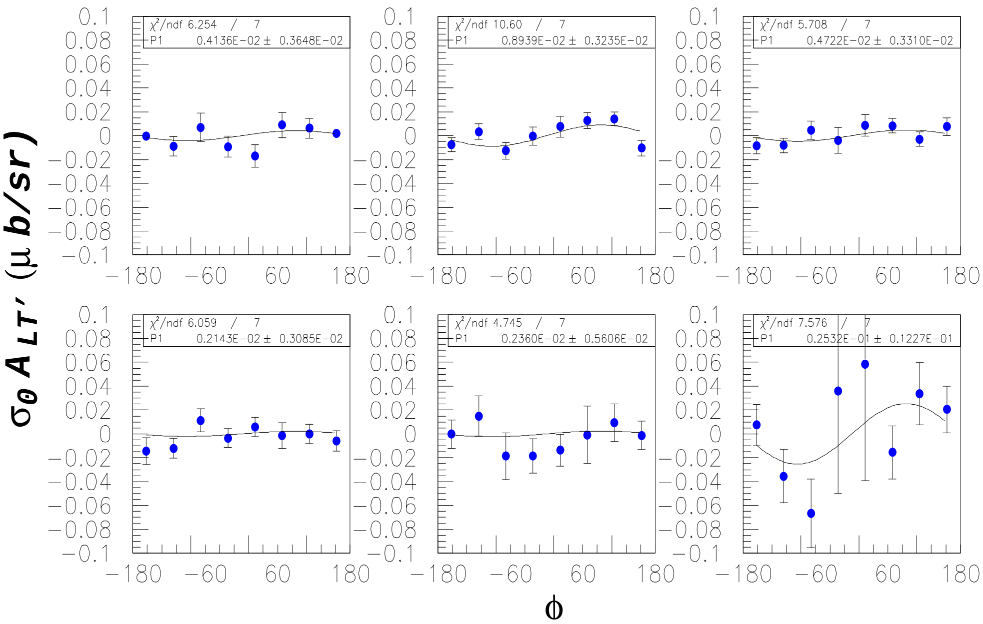

Figure 104: Measured asymmetries multiplied by unpolarized cross section versus ϕ for $\cos\theta_K^{cm}$ = -0.833, -0.50, -0.167, 0.167, 0.50, 0.833 (upper left to lower right), $Q^2 = 0.7$ GeV^2 and $W = 1.975$ GeV. The curves are a fit to $a \sin\phi$.

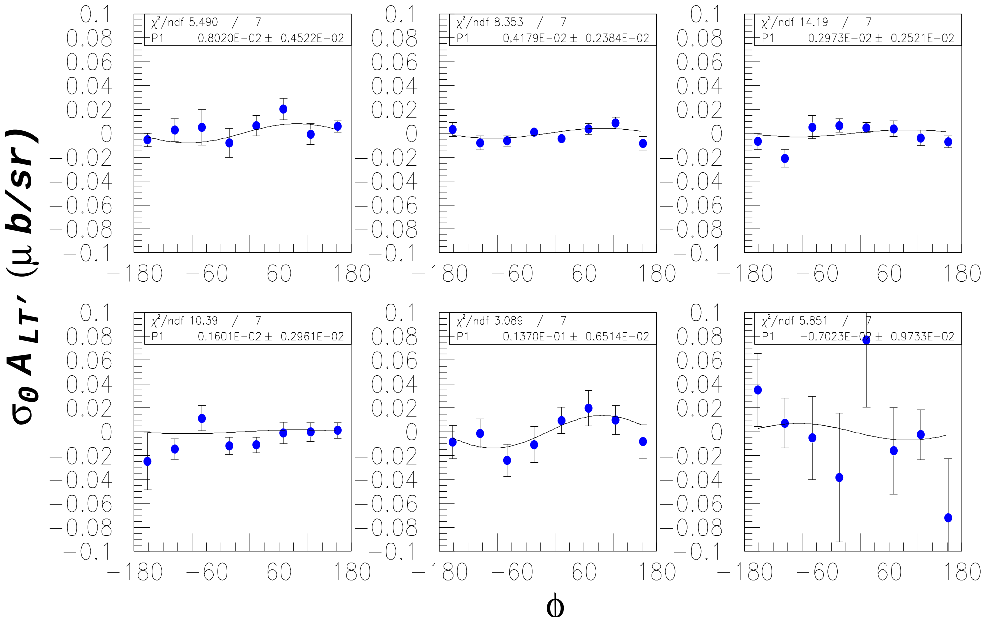

Figure 105: Measured asymmetries multiplied by unpolarized cross section versus ϕ for $\cos\theta_K^{cm}$ = -0.833, -0.50, -0.167, 0.167, 0.50, 0.833 (upper left to lower right), $Q^2 = 0.7$ GeV^2 and $W = 2.025$ GeV. The curves are a fit to $a \sin\phi$.

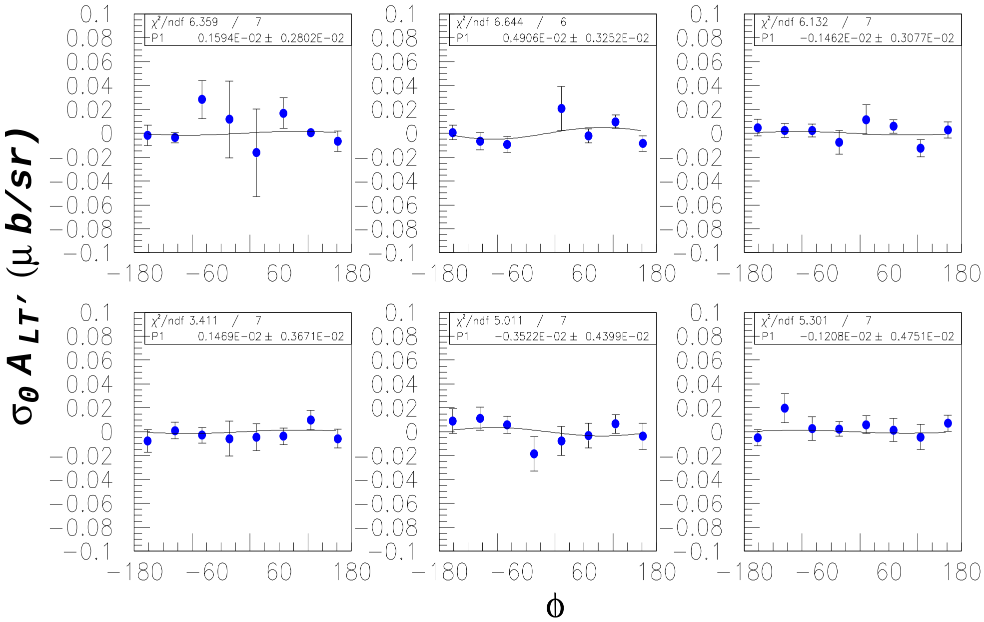

Figure 106: Measured asymmetries multiplied by unpolarized cross section versus ϕ for $\cos\theta_K^{cm}$ = -0.833, -0.50, -0.167, 0.167, 0.50, 0.833 (upper left to lower right), $Q^2 = 1.1$ GeV^2 and $W = 1.625$ GeV. The curves are a fit to $a \sin\phi$.

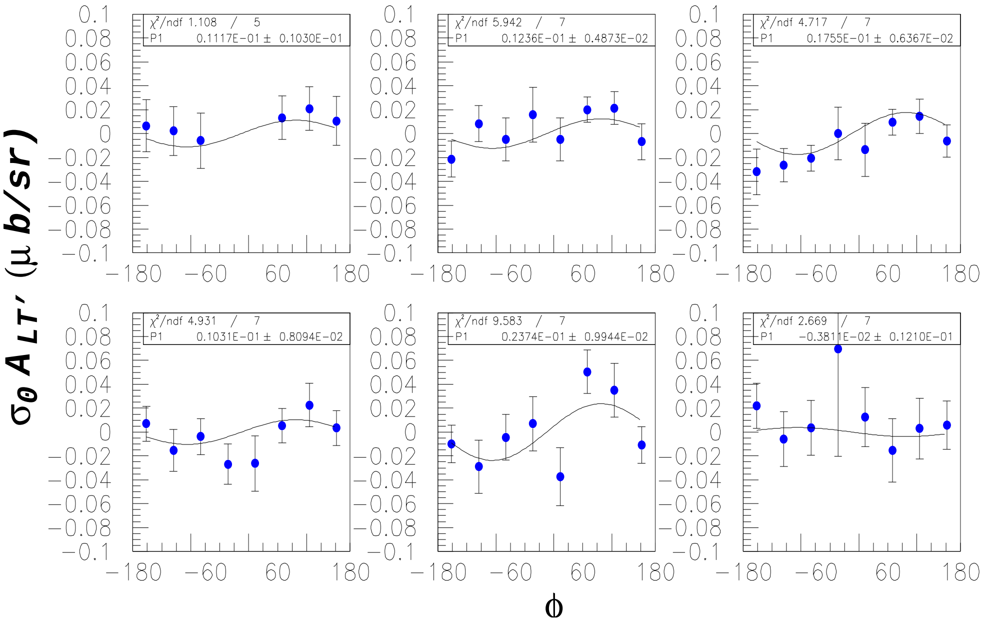

Figure 107: Measured asymmetries multiplied by unpolarized cross section versus ϕ for $\cos\theta_K^{cm}$ = -0.833, -0.50, -0.167, 0.167, 0.50, 0.833 (upper left to lower right), $Q^2 = 1.1$ GeV^2 and $W = 1.675$ GeV. The curves are a fit to $a \sin\phi$.

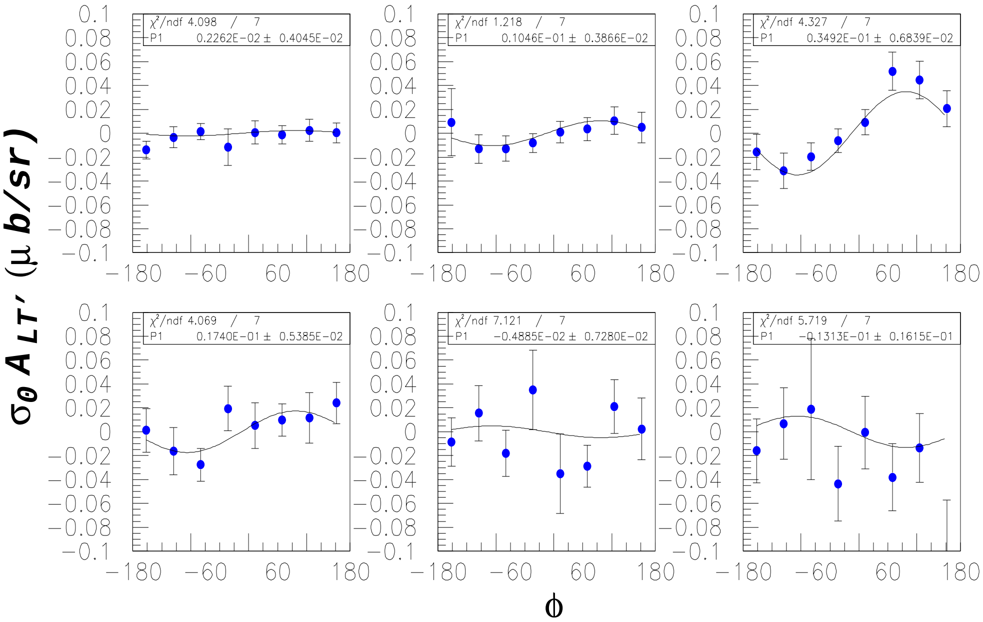

Figure 108: Measured asymmetries multiplied by unpolarized cross section versus ϕ for $\cos\theta_K^{cm}$ = -0.833, -0.50, -0.167, 0.167, 0.50, 0.833 (upper left to lower right), $Q^2 = 1.1$ GeV^2 and $W = 1.725$ GeV. The curves are a fit to $a \sin\phi$.

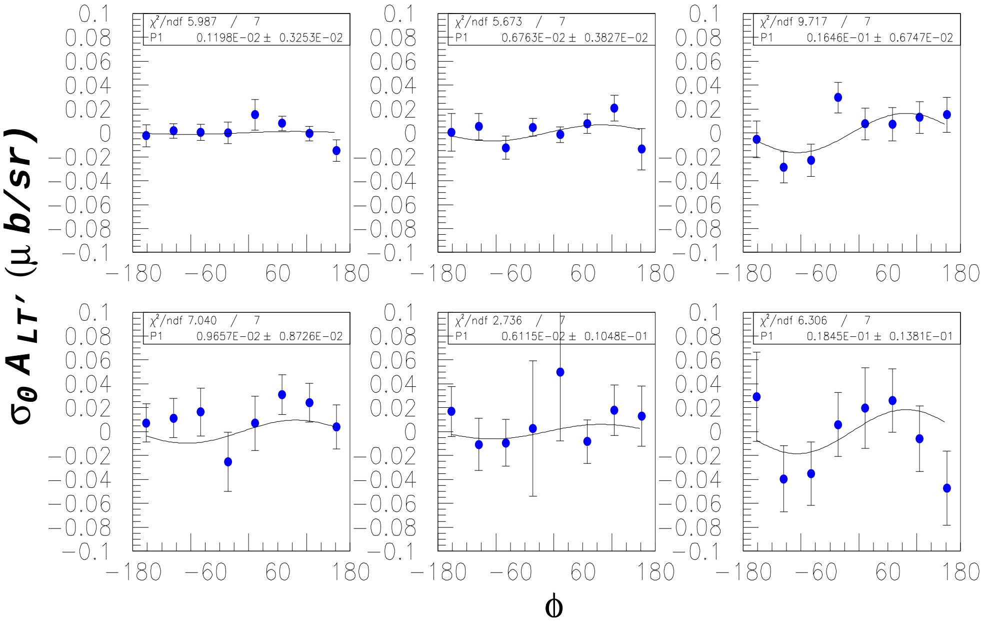

Figure 109: Measured asymmetries multiplied by unpolarized cross section versus ϕ for $\cos\theta_K^{cm}$ = -0.833, -0.50, -0.167, 0.167, 0.50, 0.833 (upper left to lower right), $Q^2 = 1.1$ GeV^2 and $W = 1.775$ GeV. The curves are a fit to $a \sin\phi$.

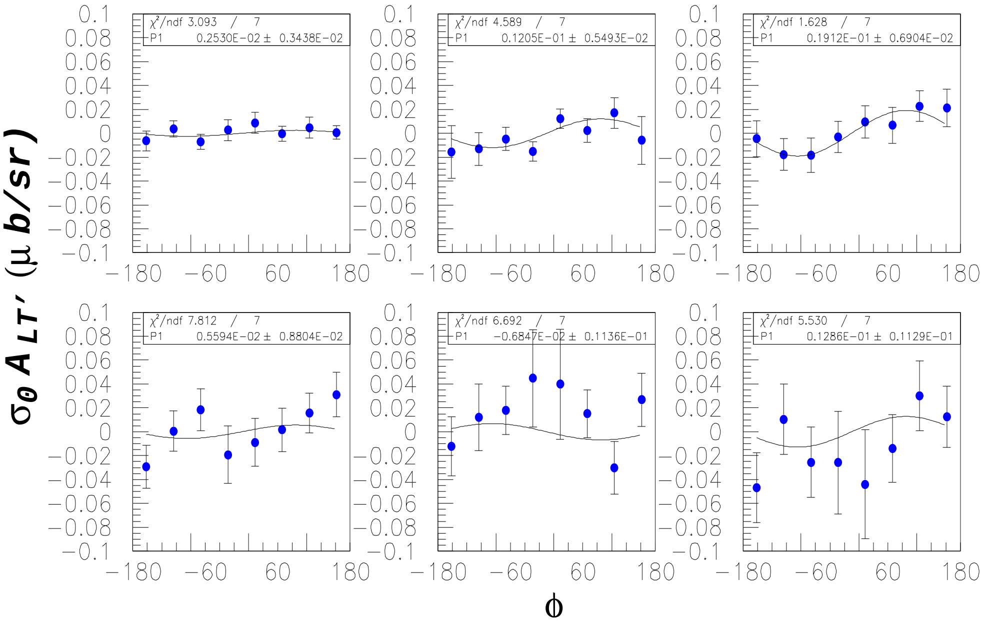

Figure 110: Measured asymmetries multiplied by unpolarized cross section versus ϕ for $\cos\theta_K^{cm}$ = -0.833, -0.50, -0.167, 0.167, 0.50, 0.833 (upper left to lower right), $Q^2 = 1.1$ GeV^2 and $W = 1.825$ GeV. The curves are a fit to $a \sin\phi$.

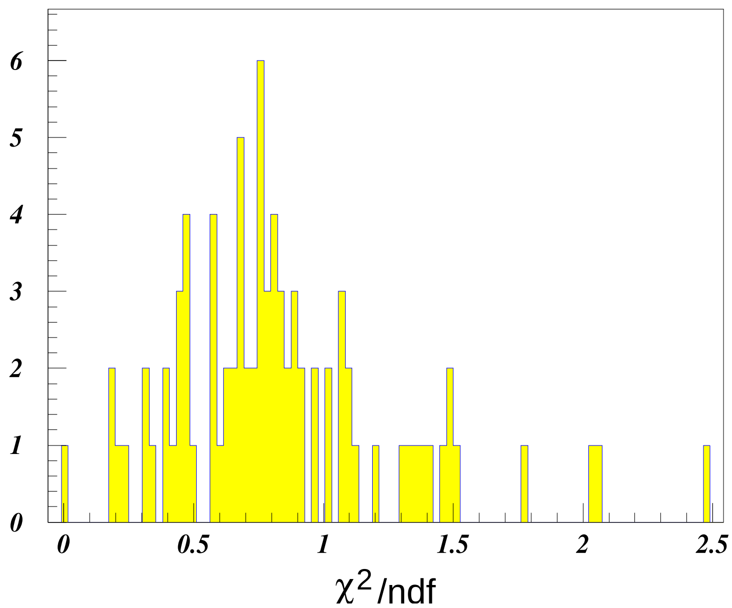

Figure 111: The distribution of χ^2/ndf of the fits to $\sigma_0 A_{LT'}$.

7.3 Fifth Structure function $\sigma_{LT'}$

Figs. 112 to 115 show the result of $\sigma_{LT'}$ measurements along with some of the existing theoretical calculation. The W dependence of the fifth structure function is shown in Fig. 112 and 113 for Q^2 of 0.7 and 1.1 GeV^2 respectively while Fig. 114 and 115 show the $\cos\theta_K^{cm}$ dependence. At $\cos\theta_K^{cm}$=-0.833, the W dependence of the results show a rise above threshold around W=1.675 GeV and at $\cos\theta_K^{cm}$ of -0.50 a rise is seen around 1700 MeV followed by a small bump around 1875 MeV. Similar structure is seen at $\cos\theta_K^{cm}$=-0.167, which likely indicates that these W structures at $\cos\theta_K^{cm}$ of -0.50 and -0.167 are not due to the statistical fluctuations. This is the region where s-channel processes are expected to dominate. However, at $\cos\theta_K^{cm}$=-0.167, the position of the rise and the bump seen at $\cos\theta_K^{cm}$=-0.500 are shifted to a lower W values. This possibly indicates that the interferences seen at these energies are due to more than one resonance or intermediate state. At $\cos\theta_K^{cm}$=0.167 a wide single peak is seen around 1750 MeV and any hint of structure around 1900 MeV is gone. This is also another indication of the interference between the s-channel resonances. The relatively large non-zero values possibly indicate significant contribution from non-resonant amplitudes particularly at $\cos\theta_K^{cm}$ of -0.50, -0.167 and 0.167. The fifth structure function in these bins approaches zero at high W, which is expected since the antisymmetric part of the hadronic tensor vanishes at high W. In the forward kaon scattering angles, at $\cos\theta_K^{cm}$ of 0.50 and 0.833 where the reaction is expected to be dominated by the t-channel exchange, the average of the fifth structure function is zero within the rather large error bars of the data. No obvious interference between resonances or resonant and non-resonant background can be seen here.

At higher value of Q^2, where the range of W is restricted, the W dependence of fifth structure function show similar structures at backward and middle kaon scattering angles seen at the lower values of Q^2. Tables 25 to 27 in Appendix G summarize the results of measurement for fifth structure function.

Plots in Figs. 112 to 115 also include the calculation from Adelseck and Wright [9], WJC [11], Mart model with hadronic form factors, and Mart model with D13(1900) [14]. Comparison to the models shows that, in general, these calculations do not describe these data. As mentioned in Chapter 1, the parameters of these models are generally constrained by the experimental data which do not yet include the recent measurements nor any polarization observables.

Fig. 116 shows again the fifth structure function data for Q^2=0.7 GeV^2 compared to three different versions of Janssen Model [15, 16], model A, B and C. The parameters of these models are obtained by a fit to the recent experimental data that includes the SAPHIR photoproduction data, the measurement of σ_L/σ_T from Hall C, the SPring-8 beam asymmetry data, and the older data from Harvard-Cornell and Orsay. In these calculations, model A and B employ the SU(3) predictions for $g_{K\Lambda N}$ and $g_{K\Sigma N}$ coupling constants while, model C treats all of the coupling constants as free parameters using a χ^2 minimization routine. The intermediate states included in model B are those listed in Appendix B. Model A and C include the same intermediate states as model B except for the hyperonic resonance at 1800 and 1810 MeV. These hyperonic states are included in model B in order to counter-balance the strength of the Born terms. Another difference between the three Janssen models is the difference between the cutoff value used in the functional form of the form factor in Eq. 23. Model A includes a soft hadronic form factor cutoff of Λ=0.43 GeV. This low value for the cutoff mass is one way to significantly reduce the Born term strength. In Model B, since the hyperonic resonances are introduced to reduce the Born term strength, a harder cutoff value of Λ=1.5 GeV is used and finally, the cutoff value used in model C is Λ=2.2 GeV where all the parameters are obtained from the fit to the data. None of the three models correctly predict the fifth structure function data.

Fig. 117 shows the fifth structure function data at Q^2=0.7 GeV^2 compared to the results of the calculations of Janssen Model B, in which several different assumptions are made in order to investigate the structure seen in the published photoproduction total cross section data at a mass of 1900 MeV. These different assumptions are: including no resonance or state at 1900 MeV, a state with quantum numbers of S_{11}, P_{11}, P_{13}, or D_{13}. For each different assumption, the model has been fit to the existing data based as mentioned above [69]. The comparison shows the sensitivity of the fifth structure function to the resonance around 1900 MeV with various quantum numbers. However, the disagreement between the data and this model indicates that there must be contributions from other resonances that have not been included in the model.

7.4 Systematic Uncertainties for $\sigma_{LT'}$

A total uncertainty is assigned to each asymmetry data point which is a convolution of statistical and systematic uncertainties (Table 25 to 27 in Appendix G). These uncertainties are included in the fit for extracting the fifth structure functions from the sine fit to the asymmetry multiplied by unpolarized cross section divided by the kinematic factor. Also included in the fits are the statistical and systematic uncertainties for unpolarized cross section, σ_0.

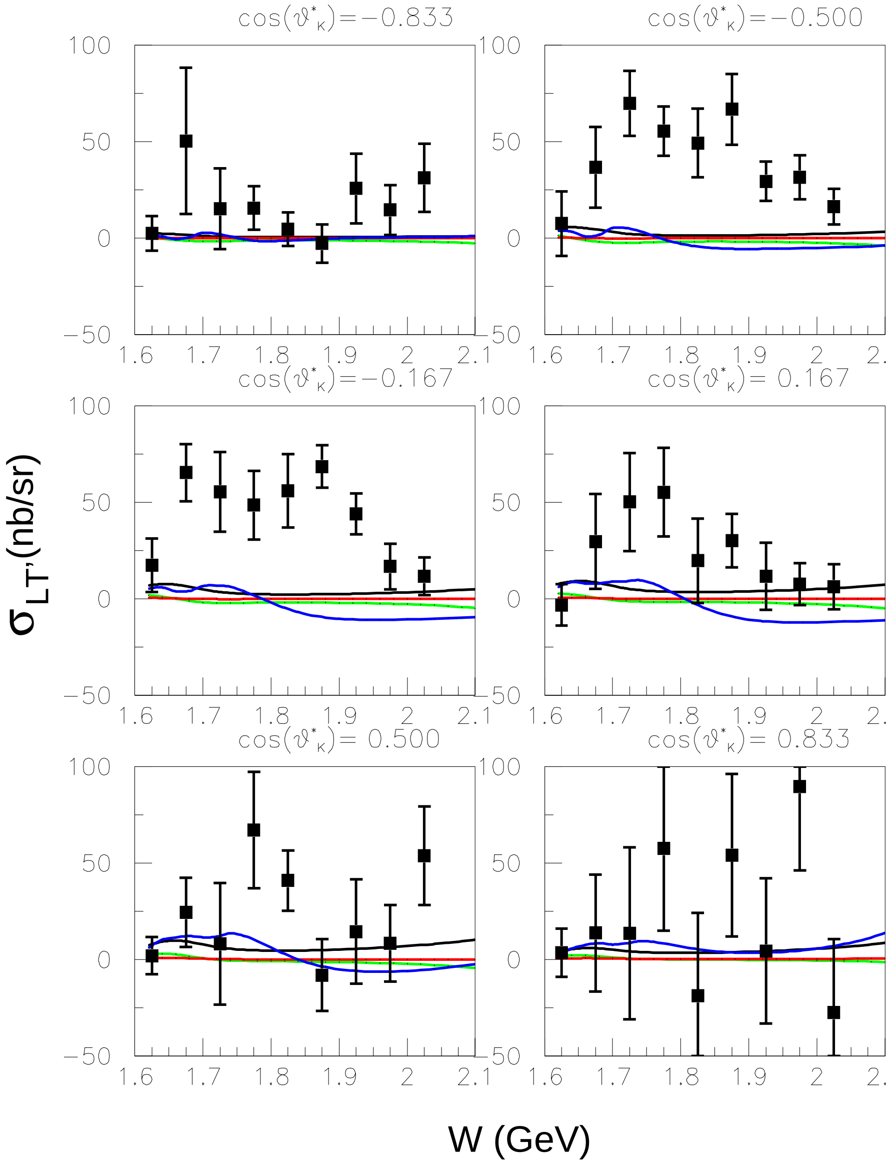

Figure 112: Fifth structure function $\sigma_{LT'}$ (nb/sr), versus W (GeV) for $Q^2 = 0.7$ GeV^2. Curves: Adelseck and Wright [9] (black), WJC [11] (green), Mart with hadronic form factors (red), Mart with D13(1900) [14] (blue).

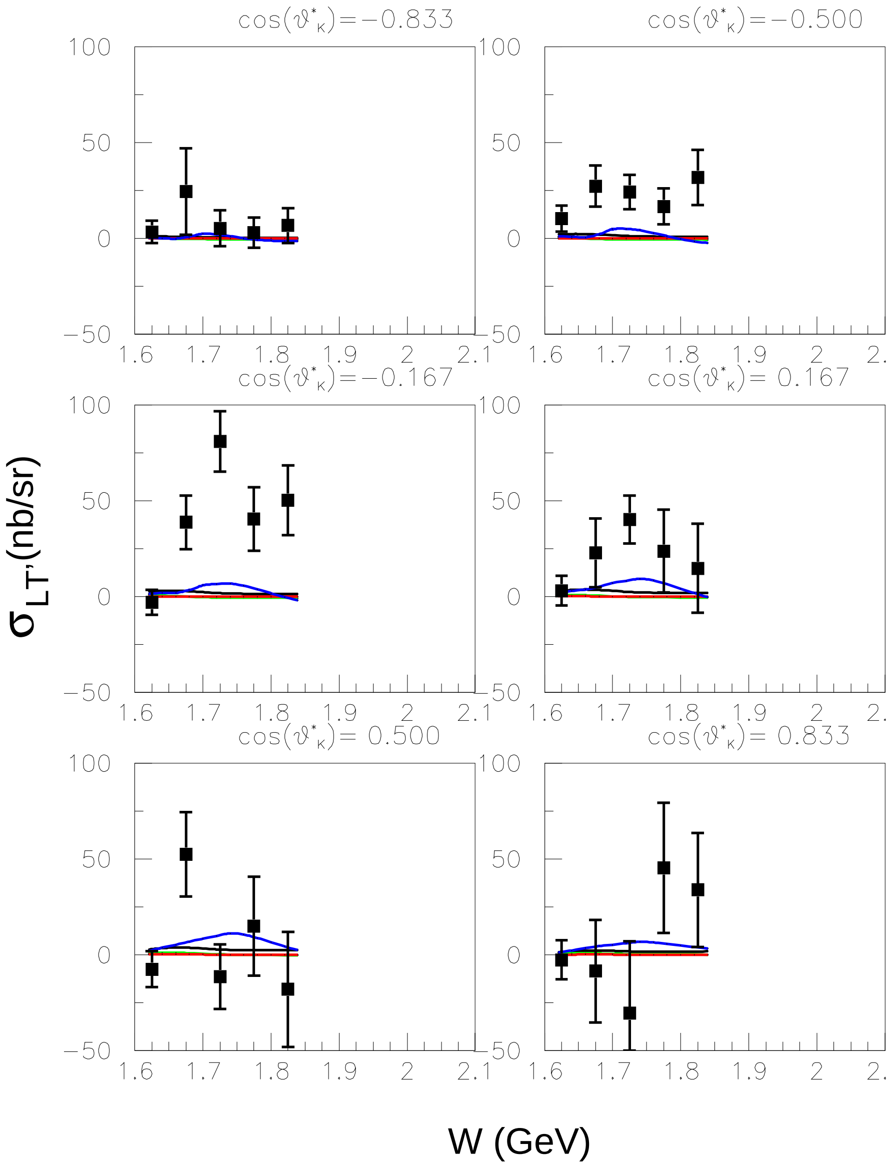

Figure 113: Fifth structure function $\sigma_{LT'}$ (nb/sr),versus W (GeV) for $Q^2 = 1.1$ GeV^2. Curves: Adelseck and Wright [9] (black), WJC [11] (green), Mart with hadronic form factors (red), Mart with D13(1900) [14] (blue) .

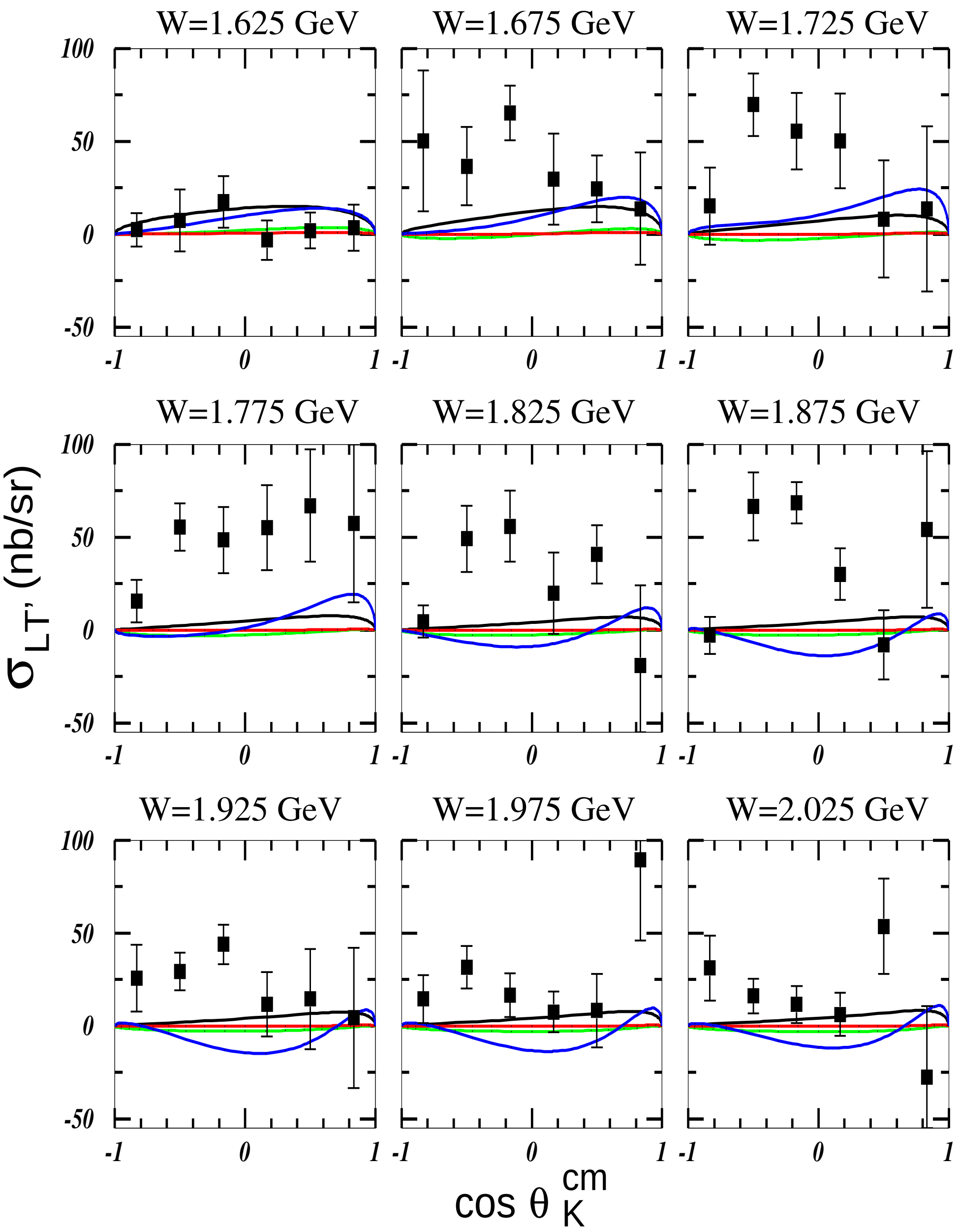

Figure 114: Fifth structure function $\sigma_{LT'}$ (nb/sr), versus $\cos\theta_K^{cm}$ for $Q^2 = 0.7$ GeV^2. Results are shown for $W = 1.625$, 1.675, 1.725, 1.775, 1.825, 1.875, 1.925, 1.975 and 2.025 GeV (upper left to lower right). Curves: Adelseck and Wright [9] (black), WJC [11] (green), Mart with hadronic form factors (red), Mart with D13(1900) [14] (blue).

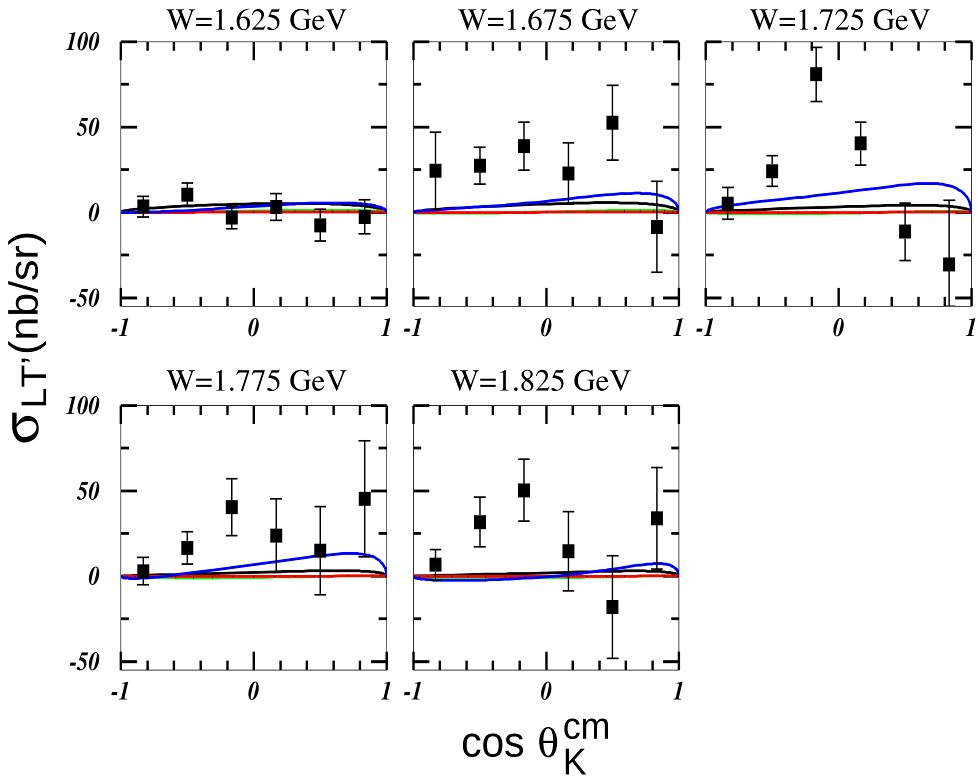

Figure 115: Fifth structure function $\sigma_{LT'}$ (nb/sr), versus $\cos\theta_K^{cm}$ for $Q^2 = 1.1$ GeV^2. Results are shown for $W = 1.625$, 1.675, 1.725, 1.775 and 1.825 GeV (upper left to lower right). Curves: Adelseck and Wright [9] (black), WJC [11] (green), Mart with hadronic form factors (red), Mart with D13(1900) [14] (blue).

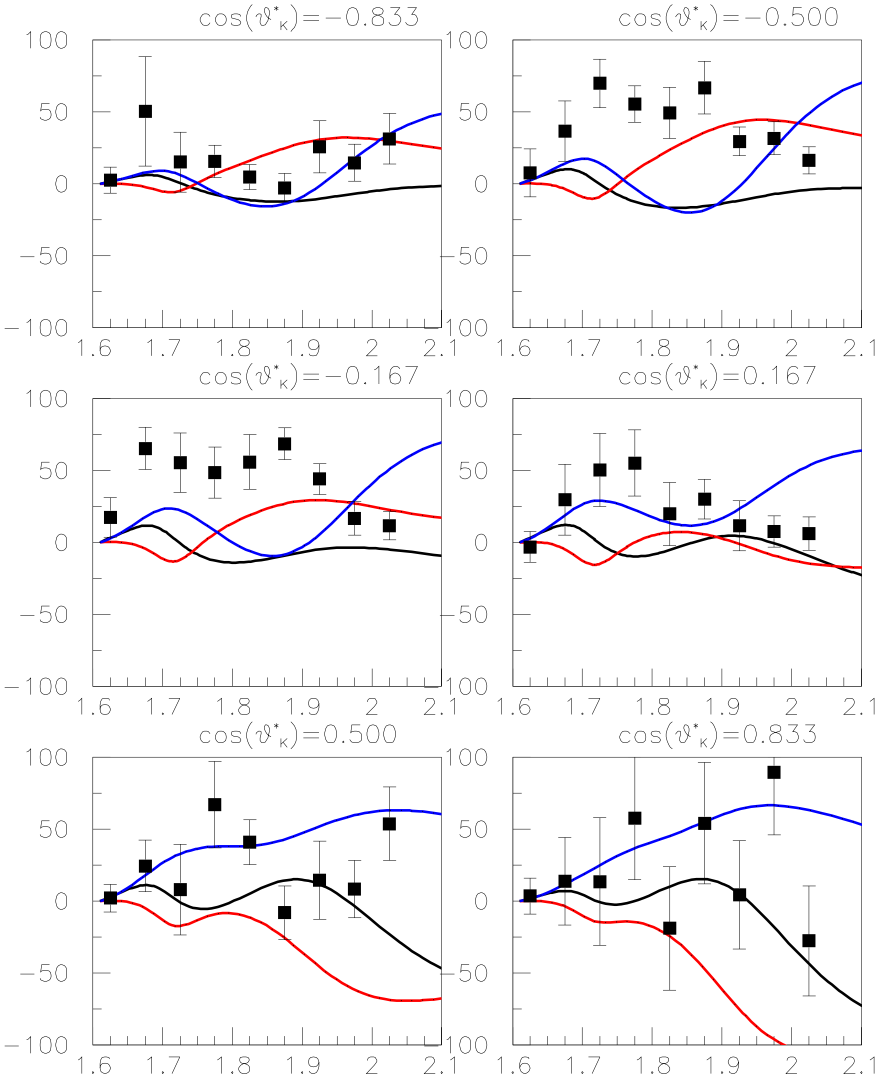

Figure 116: Fifth structure function $\sigma_{LT'}$ (nb/sr), versus W (GeV) for $Q^2 = 0.7$ GeV^2. Curves are from Janssen calculations with model A (black), model B (red), and model C (blue).

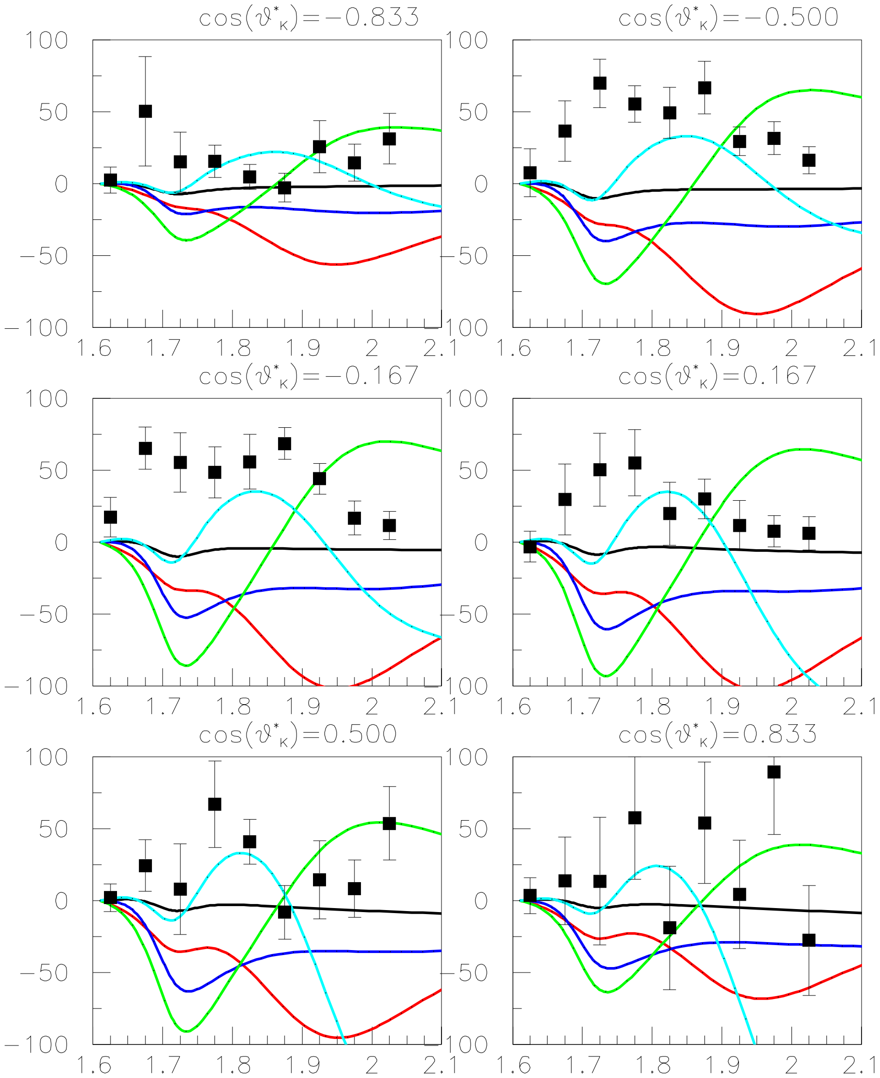

Figure 117: Fifth structure function $\sigma_{LT'}$ (nb/sr), versus W (GeV) for $Q^2 = 0.7$ GeV^2. Curves are from Janssen calculations with model B, and no resonance included around 1900 MeV (black), including $P_{11}(1895)$ (red), $S_{11}(1895)$ (blue), $P_{13}(1895)$ (green), $D_{11}(1895)$ (cyan).

8 Summary

The helicity dependent asymmetries, $A_{LT'}$ and the fifth structure functions, $\sigma_{LT'}$, were measured for $\vec{e}p \to e'K^+\Lambda$ for various kinematical bins. The results of the fifth structure function measurements at the backward and middle kaon scattering angles are consistent with the resonance structure seen around 1700 and 1900 MeV in the photoproduction total cross section and the measurement of structure functions discussed in Chapter 1. This structure indicates a significant interference between resonances and/or resonant and non-resonant amplitudes. The fact that the position of the peaks around 1700 and 1900 MeV shifts with respect to the kaon scattering angle in photoproduction cross section data, indicates that there must be more than one resonance involved in the intermediate states.

The W dependence of $\sigma_{LT'}$ at the backward and middle kaon scattering angles indicate a possible resonance structure that is clearly not predicted by the theoretical calculations. This can be seen where the reaction is mostly dominated by s and u-channel where the interference from various resonances is possible ($\cos\theta_k^{cm}$= -0.50, -0.167, 0.167). The $\sigma_{LT'}$ behavior around W = 1.875 GeV could be a signature of the resonance around 1900 GeV predicted by the quark models.

In the very forward angles where the reaction is dominated by the t-channel, the average $\sigma_{LT'}$ is consistent with zero. There is no indication of the interference between resonances or resonant and non-resonant amplitudes. This might be indicating the dominance of a single t-channel exchange. The theoretical calculations that are compared to the data in this work have all included in the t-channel, the first and second kaon resonance as well as the born kaon exchange amplitudes. It is possible that higher mass t-channel exchange might not contribute significantly to the interference.

The results are compared to the existing theoretical calculations from phenomenological hadrodynamic models such as Adelseck and Wright [9], WJC [11], Mart model with hadronic form factors, Mart model with D13(1900) [14] (Fig. 112 to 115). The comparison shows that the parameters of these models–coupling constants and form factors–have not been constrained enough by the recent data. The fifth structure function results are also compared to the latest Janssen model [15, 16] that includes the recent experimental data (Fig. 116). Study of the sensitivity of the fifth structure function to the resonance around 1900 MeV (Sec. 7.3) shows that these data are highly sensitive to the various assumptions for the quantum number of this resonance (Fig. 117). The comparison also suggests that there must be more than one new resonance involved in the reactions.

The fifth structure function contains amplitudes that do not exist in unpolarized cross section data. Thus, fits to the unpolarized cross section data are not expected to provide strong calculations of the fifth structure function. Including the fifth structure function data to the data base will improve the constraints on the resonances that are known or believed to couple strongly to the $K^+\Lambda$ final states. These results can also be used to find evidence for missing resonances in $N^* \to K^+\Lambda$ final states by adding a particularly sensitive observable.

It is important to note that the unpolarized cross section data from the analysis of Ref. [33], used in the current work, were preliminary at the time of this dissertation. There are few known problems in that analysis which involve the approximations used in the calculations of the virtual photon flux factor and radiative correction factors. These factors were obtained for each kinematical bin by averaging over the bin rather than using the integration formulas. The differences between the averaging and integration methods are largely kinematic dependent. These differences are in the order of 5% and 10% for virtual photon flux calculations and radiative correction factors respectively [70]. Therefore, we expect the final results for $\sigma_{LT'}$ will change once the corrected σ_0 are used in this analysis.

9 Bibliography

References

[1] R. Koniuk and N. Isgur, Phys. Rev. **D21**, 1868 (1980).

[2] S. Capstick, W. Roberts, "$N\pi$ decays of baryons in a relativized model," Phys. Rev. **D47**,1994 (1993).

[3] S. Capstick, W. Roberts, "Quasi-two body decays of nonstrange baryons," Phys. Rev. **D49**,4570 (1994).

[4] S. Capstick, W. Roberts. "Strange decays of nonstrange baryons," Phys. Rev. **D58**,074011 (1998).

[5] S. Boffi, C. Guisti, F. D. Pacati, and M. Radici ,"Electromagnetic response of atomic nulei," Oxford science publications, 1996.

[6] C. W. Akerlof, W. W. Ash, K. berkelman, and C. A. Lichtenstein. "Measurement of the pion form factor," Phys. Rev., **163**(5):1482, 1967.

[7] G. Knochlein, D. Drechsel, and L. Taitor. "Photoproduction and electroproduction of eta mesons," Zeitschrift Phys., A352:327, 1995.

[8] G. Co, A. M. Lallena, T. W. Donnelly, "Nucleon emission induced by polarized electrons at low momentum transfer," Nucl. Phys. **A 469** (1987) 684-716.

[9] R. A. Adelseck, and L. E. Wright. "Electromagnetic production of kaons," Phys. Rev. **D38**,1965 (1988).

[10] R. A. Adelseck, C. Bennhold, and L. E. Wright. " Kaon photoproduction operator for use in nuclear physics," Phys. Rev. **D32**,1681 (1985).

[11] R. A. Williams, C. R. Ji, and S. R. Cotanch. " Hyperon electroproduction in a crossing and duality constrained model," Phys. Rev. **D46**,1617 (1992).

[12] R. A. Adelseck, B. Saghai, "Kaon photoproduction: Data consistency, coupling constants, and polarization observables," Phys. Rev. **D42**,108 (1990).

[13] F. X. Lee, T. Mart, C. Bennhold, H. Haberzettl, and L. E. Wright, "Quasifree kaon photoproduction on nuclei," Nucl. Phys. **A 695**, 237 (2001).

[14] T. Mart and C. Bennhold, "Evidence for a missing nucleon resonance in kaon photoproduction," Phys. Rev. **C61**,012201 (1999).

[15] S. Janssen, J. Ryckebusch, D. Debruyne, and T. V. Cauteren, "Kaon photoproduction: Background contributions, form factors, and missing resonances," Phys. Rev. **C65**,015201 (2001).

[16] S. Janssen, J. Ryckebusch, W. V. Nespen, and T. V. Cauteren, "The role of hyperon resonances in $p(\gamma, K^{+})\Lambda$ processes," Eur. Phys. J. **A 11**,105 (2001).

[17] H. Thom, "Phenomenological analysis of $K^+\Lambda$ photoproduction," Phys. Rev. **151**,1322 (1966).

[18] T. Feuster and U. Mosel, "A unitary model for meson nucleon scattering," Phys. Rev. **D58**,457 (1998).

[19] Wen-tai Chaing, F. Tabakin, T. S. H. Lee, and B. Saghai, "Coupled-channel study of $\gamma p \rightarrow K^+\Lambda$," Phys. Lett. **B 517**,101 (2001).

[20] M. Q. Tran *et al.*, "Measurement of $\gamma p \rightarrow K^+\Lambda$ and $\gamma p \rightarrow K^+\Sigma$ at photon energies up to 2 GeV," Phys. Lett. **B 445**,20 (1998).

[21] B. Saghai, From Known to undiscovered resonances, 2001.

[22] S. Janssen, D. G. Ireland, J. Ryckebusch, "Extraction of N^* information from limited $p(\gamma, K^+)\Lambda$ data set," Phys. Lett. **B 562**51 (2003).

[23] M. Guidal, J.-M. Laget, and M. Vanderhaghen, "Pion and kaon photoproduction at high energies: forward and intermediate angles," Nucl. Phys. **A 627**, 645 (1997).

[24] M. Guidal, J.-M. Laget, and M. Vanderhaghen, "Electroproduction of strangeness above the resonance region," Phys. Rev. **C61**,025204 (2000).

[25] G. Niculescu *et al.*, "Longitudinal and Transverse Cross sections in the $^1H(e, e'K^+)\Lambda$ Reaction," Phys. Rev. Lett. **81**1805 (1998).

[26] C. N. Brown *et al.*, Phys. Rev. Lett. **28**, 16, 1086 (1972).

[27] C. J. Bebek *et al.*, Phys. Rev. Lett. **32**, 1, 21 (1974).

[28] C. J. Bebek *et al.*, Phys. Rev. **D 15**, 3082 (1974).

[29] P. Feller *et al.*, Nucl. Phys. **B 39**, 413 (1972)

[30] R. M. Mohring, *et al.*, "Separation of the longitudinal and transverse cross sections in the $^1H(e, e'K^+)\Lambda$ and $^1H(e, e'K^+)\Sigma^0$," Phys. Rev. **C 67**, 055205 (2003).

[31] D. S. Carman, K. Joo, M. D. Mestayer, and B. A. Raue (CLAS Collaboration), "First Measurement of transferred polarization in the exclusive $\vec{e}p \rightarrow e'K^+\Lambda$ reaction," Phys. Rev. Lett. **90**, 13 (2003).

[32] B. A. Raue and D. S. Carman, " Ratio of σ_L/σ_T for $p(e, e'K^+)\Lambda$ Extracted from Polarization Transfer," nucl-ex/0402024.

[33] R. Feuerbach, PH.D. Thesis. CMU Analysis of Λ and Σ^0 Electroproduction, CLAS Analysis note. To be published.

[34] J. W. C. McNabb *et al.*, Phys. Rev. **C 69**, 042201(R) (2004).

[35] C. K. Sinclair, “Polarized electrons at Jefferson Laboratory,” JLAB-ACT-97-11

[36] M. Crofford *et al.*, “The RF system for the CEBAF polarized photo injector,” Thomas Jefferson National Accelerator Facility.

[37] Jefferson Lab site tour. http://education.jlab.org/sitetour/guidedtour04.html, Jeffeson Laboratory 2003.

[38] B. Mecking *et al.*, Nucl. Instr. and Meth. **A503/3**, (2003)513.

[39] M. D. Mestayer *et al.*, Nucl. Instr. and Meth. **A449**(2000)81-111.

[40] E. S. Smith *et al.*, Nucl. Instr. and Meth. **A432**(1999)265-298.

[41] G.Adams *et al.*, Nucl. Instr. and Meth. **A465**(2001)414.

[42] M. Amarian *et al.,* Nucl. Instr. and Meth. **A460**(2001)239.

[43] V. Blobel *et al.*, CLAS software group, “The BOS system for CLAS detector,” 1995.

[44] J. J. Manak, E.S. Smith, S. McAleer, and S. Barrow. “e1, g1, and g6 Data processing procedures,” CLAS-Note 1999, Jefferson Laboratory.

[45] D. Lawrence, “CLAS Drift Chamber Calibration: Software and Procedures”, CLAS-note 1999-018, Jefferson Laboratory.

[46] E. Smith *et al.*, “Calibration of the CLAS TOF system,” CLAS-note 1999-011, Jefferson Laboratory.

[47] E. Smith and R. Nasseripour, “Systematic Study of Time-walk Correction for the TOF Counters,” CLAS-note 2002-07, Jefferson Laboratory.

[48] K. S. Egiyan, “ Determination of electron energy cut due to the CLAS EC threshold,” CLAS note 99-007, Jefferson Laboratory.

[49] S. Stepanyan, subroutine ec-fid, private communications.

[50] L. Elouadrhiri *et al.*,”Charged particle identification in CLAS,” CLAS-Note 1998-004, Jefferson Laboratory.

[51] S. B. McAleer, “A measurement of the recoil polarization of electroproduced $\Lambda(1116)$,” PHD thesis, Florida State University, 2002.

[52] L. C. Smith and K. Joo, “Measurement of $p(e, e'p)\pi^0$ using CLAS,” Analysis technical report, Jefferson Laboratory, 2001.

[53] K. Y. Kim *et al.*, “General Momentum Correction Form for CLAS: A study of Momentum Corrections for the PROD-1-9 Cooking of e1c Data,” CLAS-Note 2001-18, Jefferson Laboratory.

[54] P. Ambrozewicz, private communications.

[55] CLAS GEANT Simulation, http://www.physics.unh.edu/ maurik/Gsim/gsim-info.shtml

[56] A. Afanasev, I. Akushevich, V. Burkerk, K.Joo, Phys. Rev. **D 66**, 074004 (2002).

[57] D. Y. Bardin and N. M. Shumeiko, Nucl. Phys. **B127**, 242 (1977).

[58] L. W. Mo and Y. Tsai, Rev. Mod. Phys. **41**, 205 (1969).

[59] R. Thompson, "η Electroproduction in the region of the isospin 1/2, spin 1/2, 1535 MeV baryon resonance," PH.D. Thesis, University of Pittsburg, 2000.

[60] R. Ent *et al.,* "Radiative corrections for (e,e'p) reactions at GeV energies," Phys. Rev. **C64**, 054610 (2001).

[61] L. Kramer, R. Nasseripour, and B. Raue, "Analysis of e1c Beam Charge Asymmetries," CLAS-NOTE 2001-012, Jefferson Laboratory.

[62] B. A. Raue *et al.*, Bull. Am. Phys. Soc. **43**, 1543 (1998); R. Nasseripour, B. Raue, L. Kramer, F. Foertter, Bull. Am. Phys. Soc.**45**,91 (2000); see also http://www.fiu.edu/˜baraue/research/moeller/dnp2000.html.

[63] B. Wagner *et al.*, Nucl. Instr. Meth. **A294**, 541 (1990).

[64] L. G. Levchuk, Nucl. Instr. Meth. **A345**, 496 (1994).

[65] A. Freyberger, private communications.

[66] H. Kim *et al.,* "Electromagnetic form factors of the SU(3) octet baryons in the semibosonized SU(3) Nambu-Jona-Lasnio model," Phys. Rev **D53**, 4013 (1996).

[67] B. A. Raue, private communications.

[68] P. R. Bevington and D. K. Robinson. "Data redunction and error analysis for the physical sciences," McGraw-Hill, second edition, P258-259, 1992.

[69] D. S. Carman, private communications.

[70] A. Tkabladze, private communications.

10 Appendices

A Explicit Calculation of the Lepton Tensor Component

L^0_{00}	$L^h_{00} = 0$
$L^0_{01} = L^{0*}_{10} = -L^{0*}_{0-1} = -L^0_{-10}$	$L^h_{01} = L^{h*}_{10} = L^{h*}_{0-1} = L^h_{-10}$
$L^0_{11} = L^{0*}_{-1-1}$	$L^h_{11} = L^{h*}_{-1-1}$
$L^0_{1-1} = L^{0*}_{-11}$	$L^h_{1-1} = L^{h*}_{11} = 0$

Table 8: General structure of the lepton tensor $L_{\lambda\lambda'} = L^0_{\lambda\lambda'} + hL^h_{\lambda\lambda'}$.

$l^0_{00} = \frac{Q^2}{\lvert q\rvert^2}$	$\rho_{00} = \frac{Q^2}{\lvert q\rvert^2} l^0_{00}$	$v_L = \frac{Q^2}{\lvert q\rvert^2} l^0_{00}$
$l^0_{11} = \frac{Q^2}{2\lvert q\rvert^2} + \tan^2\frac{\theta}{2}$	$\rho_{11} = l^0_{11}$	$v_T = l^0_{11}$
$l^0_{01} = \frac{1}{\sqrt{2}}\frac{Q}{\lvert q\rvert}\left(\frac{Q^2}{\lvert q\rvert^2} + \tan^2\frac{\theta}{2}\right)^{\frac{1}{2}}$	$\rho_{01} = \frac{Q}{\lvert q\rvert} l^0_{01}$	$v_{TL} = -\frac{Q}{\lvert q\rvert} l^0_{01}$
$l^0_{1-1} = -\frac{Q^2}{2\lvert q\rvert^2}$	$\rho_{1-1} = l^0_{1-1}$	$v_{TT} = l^0_{1-1}$
$l^h_{01} = \frac{1}{\sqrt{2}}\frac{Q}{\lvert q\rvert}\tan\frac{\theta}{2}$	$\rho'_{01} = \frac{Q}{\lvert q\rvert} l^h_{01}$	$v'_{TL'} = -\frac{Q}{\lvert q\rvert} l^h_{01}$
$l^h_{11} = \tan\frac{\theta}{2}\left(\frac{Q^2}{\lvert q\rvert^2} + \tan^2\frac{\theta}{2}\right)^{\frac{1}{2}}$	$\rho'_{11} = l^h_{11}$	$v'_T = l^h_{11}$

Table 9: Independent components of the lepton tensor in the laboratory frame.

B Table of Resonances Included in the Models

State	New TM	Adelseck/Wright	Williams 92	TM had FF	Janssen
Λ	$\surd$	$\surd$	$\surd$	$\surd$	$\surd$
Σ^0	$\surd$	$\surd$	$\surd$	$\surd$	$\surd$
Σ	$\surd$	$\surd$	$\surd$	$\surd$	$\surd$
$Y(1405)$	-	-	-	-	-
$Y(1670)$	-	-	-	-	-
$Y(1800)$	-	-	-	-	$\surd$
$Y(1810)$	-	-	-	-	$\surd$
$Y(1660)$	-	-	-	-	-
$Y(1750)$	-	$\surd$	-	-	-
p	$\surd$	$\surd$	$\surd$	$\surd$	$\surd$
$N^*(1470)$	-	$\surd$	-	-	-
$N^*(1520)$	-	-	-	-	-
$N^*(1535)$	-	-	-	-	-
$N^*(1650)$	$\surd$	$\surd$	$\surd$	$\surd$	$\surd$
$N^*(1710)$	$\surd$	-	$\surd$	$\surd$	$\surd$
$N^*(1720)$	$\surd$	$\surd$	-	$\surd$	$\surd$
$\Delta(1620)$	-	-	-	-	-
$\Delta(1900)$	-	-	$\surd$	$\surd$	-
$\Delta(1910)$	-	-	$\surd$	-	-
$D13(1895)$	$\surd$	-	-	-	$\surd$
K^+	$\surd$	$\surd$	$\surd$	$\surd$	$\surd$
$K^*(892)$	$\surd$	$\surd$	$\surd$	$\surd$	$\surd$
$K_1(1270)$	$\surd$	-	$\surd$	-	$\surd$
$Q1(1280)$	-	$\surd$	-	-	-

C Data Sets Used in This Analysis

- $I_{beam} = 2.5$ GeV, $I_{torus} = 1500$ A and half-wave plate IN:

  16525 16528 16529 16530 16531 16532 16542 16543 16544 16546 16547 16549 16608 16609 16610 16611 16612 16614 16615 16618 16620

- $I_{beam} = 2.5$ GeV, $I_{torus} = 1500$ A and half-wave plate OUT:

  16509 16510 16513 16514 16515 16516 16517 16518 16519 16558 16559 16560 16561 16565 16566 16567 16569 16576 16577 16581 16582 16583 16584 16585 16586 16587 16588 16589 16590 16595 16597 16598 16600 16601 16602 16603 16604 16605 16606

- $I_{beam} = 2.5$ GeV, $I_{torus} = 2250$ A and half-wave plate IN:

  16634 16635 16637 16647 16648 16649 16651 16652 16653 16654 16655 16656 16657 16668 16669 16670 16720 16726 16731 16732

- $I_{beam} = 2.5$ GeV, $I_{torus} = 2250$ A and half-wave plate OUT:

  16673 16675 16676 16677 16680 16682 16683 16684 16685 16686 16687 16688 16689 16690 16691 16692 16693 16694 16695 16696 16697 16698 16699 16700 16701 16703 16704 16705 16706 16707 16708 16709 16711 16712 16715 16716 16717 16718 16719

D Response functions

β	α	T	L	^{c}TL	^{s}TL	^{c}TT	^{s}TT	^{c}TL$'$	^{s}TL$'$	TT$'$
-	-	R_T^{00}	R_L^{00}	R_{TL}^{00}	0	R_{TT}^{00}	0	0	$R_{TL'}^{00}$	0
-	x	0	0	0	R_{TL}^{0x}	0	R_{TT}^{0x}	$R_{TL'}^{0x}$	0	$R_{TT'}^{0x}$
-	y	R_T^{0y}	R_L^{0y}	R_{TL}^{0y}	0	‡	0	0	$R_{TL'}^{0y}$	0
-	z	0	0	0	R_{TL}^{0z}	0	R_{TT}^{0z}	$R_{TL'}^{0z}$	0	$R_{TT'}^{0z}$
x$'$	-	0	0	0	$R_{TL}^{x'0}$	0	$R_{TT}^{x'0}$	$R_{TL'}^{x'0}$	0	$R_{TT'}^{x'0}$
y$'$	-	$R_T^{y'0}$	‡	‡	0	‡	0	0	‡	0
z$'$	-	0	0	0	$R_{TL}^{z'0}$	0	$R_{TT}^{z'0}$	$R_{TL'}^{z'0}$	0	$R_{TT'}^{z'0}$
x$'$	x	$R_T^{x'x}$	$R_L^{x'x}$	$R_{TL}^{x'x}$	0	‡	0	0	$R_{TL'}^{x'x}$	0
x$'$	y	0	0	0	‡	0	‡	‡	0	‡
x$'$	z	$R_T^{x'z}$	$R_L^{x'z}$	‡	0	‡	0	0	‡	0
y$'$	x	0	0	0	‡	0	‡	‡	0	‡
y$'$	y	‡	‡	‡	0	‡	0	0	‡	0
y$'$	z	0	0	0	‡	0	‡	‡	0	‡
z$'$	x	$R_T^{z'x}$	‡	$R_{TL}^{z'x}$	0	‡	0	0	$R_{TL'}^{z'x}$	0
z$'$	y	0	0	0	‡	0	‡	‡	0	‡
z$'$	z	$R_T^{z'z}$	‡	‡	0	‡	0	0	‡	0

Table 10: Response functions for pseudoscalar meson production [7]. The target (recoil) polarization is indicated by α (β). The last three columns are for when the electron is polarized. ‡ indicates a response function which does not vanish but is related to other response functions. The superscripts c and s refer to the sin or cos terms.

E Asymmetry Results

The following Tables contain the result of $A_{LT'}$ measurements with the statistical, $\delta A_{LT'}$ (stat), systematic $\delta A_{LT'}$ (sys), and total, $\delta A_{LT'}$ (total), uncertainties. The total uncertainty is the quadratic sum of $\delta A_{LT'}$ (stat) and $\delta A_{LT'}$ (sys). Columns labeled as $\delta A_{LT'}$ (sys bg) correspond to the estimated background systematic uncertainty. Bins Where individual background systematic uncertainty could not be determined have been assigned the weighted RMS value of the other points, 0.06 (see Section 6.3).

Q^2 (GeV)^2	W (GeV)	$\cos\theta_K^{cm}$	ϕ (°)	$A_{LT'}$	$\delta A_{LT'}$ (stat)	$\delta A_{LT'}$ (sys bg)	$\delta A_{LT'}$ (sys)	$\delta A_{LT'}$ (total)
0.70	1.625	-0.833	-157.5	0.294	0.234	0.018	0.061	0.242
0.70	1.625	-0.833	-112.5	-0.235	0.338	0.060	0.084	0.348
0.70	1.625	-0.833	-67.5	-0.068	0.325	0.065	0.087	0.337
0.70	1.625	-0.833	-22.5	0.101	0.384	0.060	0.084	0.393
0.70	1.625	-0.833	22.5	0.495	0.406	0.060	0.084	0.415
0.70	1.625	-0.833	67.5	-0.152	0.332	0.060	0.084	0.342
0.70	1.625	-0.833	112.5	0.164	0.350	0.070	0.091	0.361
0.70	1.625	-0.833	157.5	-0.132	0.266	0.231	0.238	0.357
0.70	1.625	-0.500	-157.5	-0.243	0.236	0.040	0.071	0.246
0.70	1.625	-0.500	-112.5	-0.015	0.278	0.048	0.076	0.288
0.70	1.625	-0.500	-67.5	0.179	0.259	0.075	0.095	0.276
0.70	1.625	-0.500	-22.5	0.502	0.468	0.060	0.084	0.475
0.70	1.625	-0.500	22.5	0.130	0.448	0.060	0.084	0.456
0.70	1.625	-0.500	67.5	0.170	0.273	0.029	0.065	0.281
0.70	1.625	-0.500	112.5	0.075	0.324	0.066	0.088	0.336
0.70	1.625	-0.500	157.5	0.209	0.233	0.090	0.107	0.257
0.70	1.625	-0.167	-157.5	-0.032	0.210	0.005	0.059	0.218
0.70	1.625	-0.167	-112.5	0.106	0.293	0.011	0.059	0.299
0.70	1.625	-0.167	-67.5	-0.439	0.235	0.024	0.063	0.244
0.70	1.625	-0.167	-22.5	0.413	0.432	0.060	0.084	0.440
0.70	1.625	-0.167	22.5	-0.220	0.394	0.060	0.084	0.403
0.70	1.625	-0.167	67.5	0.510	0.254	0.058	0.082	0.267
0.70	1.625	-0.167	112.5	-0.045	0.268	0.042	0.072	0.278
0.70	1.625	-0.167	157.5	-0.037	0.240	0.040	0.071	0.250
0.70	1.625	0.167	-157.5	0.199	0.216	0.016	0.061	0.224
0.70	1.625	0.167	-112.5	-0.032	0.278	0.022	0.062	0.284
0.70	1.625	0.167	-67.5	0.187	0.296	0.060	0.084	0.307
0.70	1.625	0.167	-22.5	-1.063	0.397	0.053	0.081	0.405
0.70	1.625	0.167	22.5	0.208	0.559	0.060	0.084	0.565
0.70	1.625	0.167	67.5	0.171	0.297	0.072	0.093	0.311
0.70	1.625	0.167	112.5	-0.186	0.286	0.068	0.089	0.300
0.70	1.625	0.167	157.5	-0.162	0.211	0.051	0.078	0.225
0.70	1.625	0.500	-157.5	0.182	0.189	0.041	0.071	0.202
0.70	1.625	0.500	-112.5	-0.426	0.302	0.125	0.138	0.332
0.70	1.625	0.500	-67.5	0.412	0.305	0.083	0.101	0.322
0.70	1.625	0.500	-22.5	-0.112	0.413	0.098	0.114	0.428
0.70	1.625	0.500	22.5	0.571	0.383	0.060	0.084	0.392
0.70	1.625	0.500	67.5	0.442	0.319	0.092	0.109	0.337
0.70	1.625	0.500	112.5	-0.223	0.256	0.135	0.147	0.296
0.70	1.625	0.500	157.5	-0.018	0.178	0.079	0.099	0.204
0.70	1.625	0.833	-157.5	-0.129	0.165	0.110	0.124	0.206
0.70	1.625	0.833	-112.5	0.033	0.205	0.041	0.071	0.217
0.70	1.625	0.833	-67.5	-0.154	0.210	0.091	0.108	0.236
0.70	1.625	0.833	-22.5	0.093	0.202	0.020	0.062	0.211
0.70	1.625	0.833	22.5	0.164	0.274	0.162	0.172	0.324
0.70	1.625	0.833	67.5	0.272	0.270	0.204	0.212	0.343
0.70	1.625	0.833	112.5	-0.112	0.200	0.036	0.069	0.211
0.70	1.625	0.833	157.5	-0.049	0.190	0.005	0.059	0.199

Table 11: Measured asymmetries and statistical and systematic uncertainties for various kinematic bins (continued).

Q^2 (GeV)^2	W (GeV)	$\cos\theta_K^{cm}$	ϕ (°)	$A_{LT'}$	$\delta A_{LT'}$ (stat)	$\delta A_{LT'}$ (sys bg)	$\delta A_{LT'}$ (sys)	$\delta A_{LT'}$ (total)
0.70	1.675	-0.833	-157.5	-0.276	0.197	0.006	0.059	0.206
0.70	1.675	-0.833	-112.5	-0.093	0.213	0.039	0.070	0.224
0.70	1.675	-0.833	-67.5	0.142	0.259	0.374	0.378	0.458
0.70	1.675	-0.833	-22.5	0.212	0.558	0.060	0.084	0.564
0.70	1.675	-0.833	22.5	0.746	0.646	0.060	0.084	0.651
0.70	1.675	-0.833	67.5	0.309	0.267	0.312	0.318	0.415
0.70	1.675	-0.833	112.5	0.936	0.175	0.660	0.663	0.686
0.70	1.675	-0.833	157.5	—	—	—	—	—
0.70	1.675	-0.500	-157.5	-0.044	0.136	0.037	0.069	0.153
0.70	1.675	-0.500	-112.5	-0.349	0.150	0.044	0.073	0.166
0.70	1.675	-0.500	-67.5	-0.220	0.151	0.012	0.060	0.163
0.70	1.675	-0.500	-22.5	0.059	0.298	0.060	0.083	0.310
0.70	1.675	-0.500	22.5	-0.112	0.242	0.033	0.067	0.251
0.70	1.675	-0.500	67.5	-0.076	0.160	0.012	0.060	0.170
0.70	1.675	-0.500	112.5	0.186	0.156	0.075	0.095	0.183
0.70	1.675	-0.500	157.5	0.156	0.141	0.037	0.069	0.158
0.70	1.675	-0.167	-157.5	-0.334	0.111	0.037	0.069	0.131
0.70	1.675	-0.167	-112.5	-0.292	0.130	0.008	0.059	0.143
0.70	1.675	-0.167	-67.5	0.082	0.123	0.018	0.061	0.137
0.70	1.675	-0.167	-22.5	-0.852	0.328	0.060	0.085	0.338
0.70	1.675	-0.167	22.5	0.329	0.343	0.061	0.085	0.353
0.70	1.675	-0.167	67.5	0.239	0.132	0.059	0.083	0.156
0.70	1.675	-0.167	112.5	0.094	0.127	0.018	0.061	0.141
0.70	1.675	-0.167	157.5	0.332	0.112	0.019	0.062	0.127
0.70	1.675	0.167	-157.5	-0.063	0.098	0.021	0.062	0.116
0.70	1.675	0.167	-112.5	-0.208	0.121	0.062	0.085	0.148
0.70	1.675	0.167	-67.5	-0.148	0.101	0.020	0.062	0.119
0.70	1.675	0.167	-22.5	0.006	0.305	0.060	0.084	0.316
0.70	1.675	0.167	22.5	-0.379	0.360	0.060	0.084	0.370
0.70	1.675	0.167	67.5	0.158	0.105	0.084	0.102	0.147
0.70	1.675	0.167	112.5	-0.049	0.115	0.021	0.062	0.130
0.70	1.675	0.167	157.5	-0.199	0.095	0.024	0.063	0.114
0.70	1.675	0.500	-157.5	-0.100	0.082	0.044	0.073	0.110
0.70	1.675	0.500	-112.5	-0.172	0.099	0.030	0.066	0.119
0.70	1.675	0.500	-67.5	0.080	0.104	0.029	0.065	0.123
0.70	1.675	0.500	-22.5	0.284	0.250	0.029	0.065	0.258
0.70	1.675	0.500	22.5	0.576	0.288	0.166	0.176	0.337
0.70	1.675	0.500	67.5	-0.012	0.101	0.012	0.060	0.117
0.70	1.675	0.500	112.5	0.031	0.108	0.032	0.066	0.127
0.70	1.675	0.500	157.5	0.196	0.082	0.020	0.062	0.103
0.70	1.675	0.833	-157.5	-0.023	0.070	0.014	0.060	0.092
0.70	1.675	0.833	-112.5	-0.121	0.091	0.010	0.059	0.109
0.70	1.675	0.833	-67.5	-0.131	0.118	0.031	0.066	0.135
0.70	1.675	0.833	-22.5	-0.082	0.121	0.050	0.077	0.143
0.70	1.675	0.833	22.5	-0.102	0.129	0.040	0.071	0.147
0.70	1.675	0.833	67.5	-0.134	0.123	0.025	0.063	0.139
0.70	1.675	0.833	112.5	-0.009	0.100	0.037	0.069	0.122
0.70	1.675	0.833	157.5	-0.040	0.068	0.019	0.061	0.091

Table 12: Measured asymmetries and statistical and systematic uncertainties for various kinematic bins (continued).

Q^2 (GeV)^2	W (GeV)	$\cos\theta_K^{cm}$	ϕ (°)	$A_{LT'}$	$\delta A_{LT'}$ (stat)	$\delta A_{LT'}$ (sys bg)	$\delta A_{LT'}$ (sys)	$\delta A_{LT'}$ (total)
0.70	1.725	-0.833	-157.5	—	—	—	—	—
0.70	1.725	-0.833	-112.5	-0.293	0.187	0.120	0.134	0.230
0.70	1.725	-0.833	-67.5	-0.878	0.218	0.332	0.337	0.402
0.70	1.725	-0.833	-22.5	0.262	0.381	0.060	0.084	0.390
0.70	1.725	-0.833	22.5	0.216	0.294	0.060	0.084	0.306
0.70	1.725	-0.833	67.5	-0.478	0.218	0.104	0.119	0.248
0.70	1.725	-0.833	112.5	0.160	0.223	0.142	0.153	0.271
0.70	1.725	-0.833	157.5	—	—	—	—	—
0.70	1.725	-0.500	-157.5	0.846	0.136	0.514	0.517	0.535
0.70	1.725	-0.500	-112.5	-0.417	0.128	0.074	0.095	0.159
0.70	1.725	-0.500	-67.5	-0.218	0.172	0.048	0.075	0.188
0.70	1.725	-0.500	-22.5	-0.320	0.209	0.061	0.085	0.225
0.70	1.725	-0.500	22.5	0.215	0.215	0.031	0.066	0.225
0.70	1.725	-0.500	67.5	0.381	0.158	0.040	0.071	0.173
0.70	1.725	-0.500	112.5	0.234	0.125	0.039	0.070	0.143
0.70	1.725	-0.500	157.5	0.232	0.141	0.049	0.076	0.160
0.70	1.725	-0.167	-157.5	-0.124	0.092	0.034	0.068	0.114
0.70	1.725	-0.167	-112.5	-0.198	0.098	0.006	0.059	0.114
0.70	1.725	-0.167	-67.5	-0.140	0.132	0.037	0.069	0.149
0.70	1.725	-0.167	-22.5	-0.431	0.189	0.025	0.064	0.199
0.70	1.725	-0.167	22.5	0.018	0.220	0.060	0.084	0.235
0.70	1.725	-0.167	67.5	-0.018	0.139	0.009	0.059	0.151
0.70	1.725	-0.167	112.5	0.203	0.099	0.010	0.059	0.115
0.70	1.725	-0.167	157.5	0.009	0.098	0.036	0.069	0.120
0.70	1.725	0.167	-157.5	-0.100	0.075	0.010	0.059	0.096
0.70	1.725	0.167	-112.5	-0.026	0.082	0.027	0.064	0.104
0.70	1.725	0.167	-67.5	-0.304	0.088	0.018	0.061	0.108
0.70	1.725	0.167	-22.5	0.047	0.260	0.060	0.084	0.273
0.70	1.725	0.167	22.5	0.086	0.255	0.060	0.084	0.269
0.70	1.725	0.167	67.5	0.046	0.090	0.002	0.058	0.107
0.70	1.725	0.167	112.5	-0.009	0.085	0.003	0.058	0.103
0.70	1.725	0.167	157.5	0.019	0.076	0.012	0.059	0.096
0.70	1.725	0.500	-157.5	0.006	0.059	0.006	0.059	0.083
0.70	1.725	0.500	-112.5	-0.030	0.073	0.005	0.059	0.093
0.70	1.725	0.500	-67.5	0.064	0.070	0.015	0.060	0.093
0.70	1.725	0.500	-22.5	-0.349	0.230	0.084	0.102	0.252
0.70	1.725	0.500	22.5	0.016	0.252	0.251	0.258	0.361
0.70	1.725	0.500	67.5	0.021	0.068	0.003	0.058	0.090
0.70	1.725	0.500	112.5	0.000	0.074	0.017	0.061	0.096
0.70	1.725	0.500	157.5	0.074	0.059	0.005	0.059	0.083
0.70	1.725	0.833	-157.5	-0.060	0.049	0.031	0.066	0.083
0.70	1.725	0.833	-112.5	0.029	0.066	0.022	0.062	0.091
0.70	1.725	0.833	-67.5	0.122	0.085	0.043	0.073	0.112
0.70	1.725	0.833	-22.5	-0.069	0.118	0.201	0.210	0.241
0.70	1.725	0.833	22.5	0.075	0.110	0.043	0.072	0.132
0.70	1.725	0.833	67.5	0.052	0.083	0.032	0.067	0.107
0.70	1.725	0.833	112.5	0.066	0.066	0.041	0.071	0.097
0.70	1.725	0.833	157.5	0.032	0.048	0.009	0.059	0.076

Table 13: Measured asymmetries and statistical and systematic uncertainties for various kinematic bins (continued).

Q^2 (GeV)^2	W (GeV)	$\cos\theta_K^{cm}$	ϕ (°)	$A_{LT'}$	$\delta A_{LT'}$ (stat)	$\delta A_{LT'}$ (sys bg)	$\delta A_{LT'}$ (sys)	$\delta A_{LT'}$ (total)
0.70	1.775	-0.833	-157.5	0.415	0.305	0.047	0.075	0.314
0.70	1.775	-0.833	-112.5	—	—	—	—	—
0.70	1.775	-0.833	-67.5	-0.326	0.286	0.025	0.064	0.293
0.70	1.775	-0.833	-22.5	-0.347	0.317	0.052	0.078	0.327
0.70	1.775	-0.833	22.5	0.127	0.317	0.071	0.092	0.330
0.70	1.775	-0.833	67.5	-0.103	0.248	0.043	0.072	0.258
0.70	1.775	-0.833	112.5	0.611	0.222	0.043	0.073	0.234
0.70	1.775	-0.833	157.5	0.061	0.325	0.060	0.084	0.336
0.70	1.775	-0.500	-157.5	-0.075	0.180	0.067	0.089	0.201
0.70	1.775	-0.500	-112.5	-0.336	0.137	0.153	0.164	0.213
0.70	1.775	-0.500	-67.5	-0.551	0.173	0.063	0.086	0.194
0.70	1.775	-0.500	-22.5	0.013	0.256	0.116	0.130	0.287
0.70	1.775	-0.500	22.5	-0.712	0.274	0.580	0.583	0.644
0.70	1.775	-0.500	67.5	0.150	0.187	0.079	0.098	0.211
0.70	1.775	-0.500	112.5	0.277	0.137	0.030	0.066	0.152
0.70	1.775	-0.500	157.5	0.026	0.167	0.151	0.162	0.233
0.70	1.775	-0.167	-157.5	0.147	0.093	0.017	0.061	0.111
0.70	1.775	-0.167	-112.5	-0.154	0.100	0.024	0.063	0.118
0.70	1.775	-0.167	-67.5	0.063	0.127	0.017	0.061	0.141
0.70	1.775	-0.167	-22.5	-0.362	0.179	0.057	0.082	0.196
0.70	1.775	-0.167	22.5	0.333	0.157	0.048	0.076	0.175
0.70	1.775	-0.167	67.5	0.234	0.111	0.009	0.059	0.126
0.70	1.775	-0.167	112.5	0.146	0.095	0.001	0.058	0.112
0.70	1.775	-0.167	157.5	0.160	0.092	0.022	0.062	0.111
0.70	1.775	0.167	-157.5	0.105	0.071	0.015	0.060	0.093
0.70	1.775	0.167	-112.5	-0.109	0.076	0.016	0.060	0.097
0.70	1.775	0.167	-67.5	-0.062	0.092	0.029	0.065	0.113
0.70	1.775	0.167	-22.5	-0.399	0.170	0.107	0.122	0.210
0.70	1.775	0.167	22.5	0.141	0.161	0.020	0.062	0.172
0.70	1.775	0.167	67.5	0.161	0.091	0.005	0.059	0.108
0.70	1.775	0.167	112.5	0.093	0.077	0.005	0.059	0.097
0.70	1.775	0.167	157.5	0.091	0.069	0.009	0.059	0.091
0.70	1.775	0.500	-157.5	-0.065	0.058	0.024	0.063	0.086
0.70	1.775	0.500	-112.5	-0.121	0.068	0.009	0.059	0.090
0.70	1.775	0.500	-67.5	-0.074	0.067	0.025	0.063	0.092
0.70	1.775	0.500	-22.5	-0.411	0.272	0.030	0.066	0.280
0.70	1.775	0.500	22.5	0.391	0.308	0.060	0.084	0.319
0.70	1.775	0.500	67.5	0.048	0.067	0.013	0.060	0.090
0.70	1.775	0.500	112.5	0.092	0.067	0.034	0.068	0.096
0.70	1.775	0.500	157.5	0.046	0.059	0.006	0.059	0.083
0.70	1.775	0.833	-157.5	-0.016	0.047	0.019	0.061	0.077
0.70	1.775	0.833	-112.5	0.047	0.065	0.020	0.062	0.089
0.70	1.775	0.833	-67.5	-0.190	0.079	0.020	0.062	0.100
0.70	1.775	0.833	-22.5	-0.099	0.132	0.055	0.080	0.155
0.70	1.775	0.833	22.5	0.020	0.133	0.041	0.071	0.151
0.70	1.775	0.833	67.5	0.060	0.077	0.010	0.059	0.097
0.70	1.775	0.833	112.5	0.034	0.066	0.015	0.060	0.089
0.70	1.775	0.833	157.5	0.021	0.047	0.038	0.070	0.084

Table 14: Measured asymmetries and statistical and systematic uncertainties for various kinematic bins (continued).

Q^2 (GeV)^2	W (GeV)	$\cos\theta_K^{cm}$	ϕ (°)	$A_{LT'}$	$\delta A_{LT'}$ (stat)	$\delta A_{LT'}$ (sys bg)	$\delta A_{LT'}$ (sys)	$\delta A_{LT'}$ (total)
0.70	1.825	-0.833	-157.5	-0.136	0.267	0.060	0.084	0.280
0.70	1.825	-0.833	-112.5	-0.328	0.286	0.060	0.084	0.298
0.70	1.825	-0.833	-67.5	-0.183	0.243	0.101	0.116	0.270
0.70	1.825	-0.833	-22.5	0.673	0.247	0.139	0.151	0.290
0.70	1.825	-0.833	22.5	-0.393	0.277	0.039	0.071	0.286
0.70	1.825	-0.833	67.5	0.300	0.238	0.126	0.139	0.275
0.70	1.825	-0.833	112.5	-0.018	0.334	0.060	0.084	0.344
0.70	1.825	-0.833	157.5	-0.452	0.254	0.150	0.161	0.300
0.70	1.825	-0.500	-157.5	-0.003	0.190	0.122	0.135	0.233
0.70	1.825	-0.500	-112.5	-0.130	0.129	0.037	0.069	0.146
0.70	1.825	-0.500	-67.5	-0.008	0.167	0.063	0.086	0.188
0.70	1.825	-0.500	-22.5	-0.471	0.211	0.223	0.230	0.312
0.70	1.825	-0.500	22.5	0.467	0.215	0.103	0.118	0.245
0.70	1.825	-0.500	67.5	0.253	0.159	0.072	0.093	0.184
0.70	1.825	-0.500	112.5	0.275	0.130	0.005	0.059	0.142
0.70	1.825	-0.500	157.5	0.350	0.194	0.291	0.297	0.354
0.70	1.825	-0.167	-157.5	-0.143	0.088	0.020	0.062	0.108
0.70	1.825	-0.167	-112.5	0.113	0.091	0.037	0.069	0.115
0.70	1.825	-0.167	-67.5	-0.025	0.119	0.005	0.059	0.133
0.70	1.825	-0.167	-22.5	-0.482	0.147	0.012	0.060	0.159
0.70	1.825	-0.167	22.5	0.132	0.153	0.019	0.061	0.165
0.70	1.825	-0.167	67.5	0.367	0.109	0.044	0.073	0.132
0.70	1.825	-0.167	112.5	0.206	0.095	0.035	0.068	0.116
0.70	1.825	-0.167	157.5	0.048	0.095	0.027	0.064	0.115
0.70	1.825	0.167	-157.5	-0.106	0.077	0.003	0.058	0.097
0.70	1.825	0.167	-112.5	-0.049	0.071	0.026	0.064	0.096
0.70	1.825	0.167	-67.5	0.034	0.094	0.034	0.067	0.116
0.70	1.825	0.167	-22.5	-0.102	0.132	0.025	0.063	0.146
0.70	1.825	0.167	22.5	0.264	0.120	0.033	0.067	0.137
0.70	1.825	0.167	67.5	0.012	0.094	0.020	0.062	0.112
0.70	1.825	0.167	112.5	-0.040	0.072	0.018	0.061	0.095
0.70	1.825	0.167	157.5	0.057	0.073	0.007	0.059	0.094
0.70	1.825	0.500	-157.5	-0.082	0.061	0.041	0.071	0.094
0.70	1.825	0.500	-112.5	-0.060	0.066	0.006	0.059	0.088
0.70	1.825	0.500	-67.5	-0.027	0.068	0.017	0.061	0.091
0.70	1.825	0.500	-22.5	-0.581	0.239	0.043	0.073	0.250
0.70	1.825	0.500	22.5	-0.220	0.222	0.038	0.070	0.233
0.70	1.825	0.500	67.5	0.130	0.070	0.016	0.060	0.092
0.70	1.825	0.500	112.5	0.059	0.066	0.010	0.059	0.089
0.70	1.825	0.500	157.5	-0.119	0.064	0.029	0.065	0.091
0.70	1.825	0.833	-157.5	-0.067	0.049	0.021	0.062	0.079
0.70	1.825	0.833	-112.5	-0.025	0.067	0.012	0.060	0.089
0.70	1.825	0.833	-67.5	0.051	0.080	0.085	0.103	0.130
0.70	1.825	0.833	-22.5	0.203	0.181	0.120	0.133	0.225
0.70	1.825	0.833	22.5	0.002	0.189	0.020	0.062	0.198
0.70	1.825	0.833	67.5	-0.032	0.077	0.047	0.075	0.107
0.70	1.825	0.833	112.5	-0.074	0.071	0.023	0.063	0.095
0.70	1.825	0.833	157.5	0.008	0.049	0.026	0.064	0.081

Table 15: Measured asymmetries and statistical and systematic uncertainties for various kinematic bins (continued).

Q^2 (GeV)^2	W (GeV)	$\cos\theta_K^{cm}$	ϕ (°)	$A_{LT'}$	$\delta A_{LT'}$ (stat)	$\delta A_{LT'}$ (sys bg)	$\delta A_{LT'}$ (sys)	$\delta A_{LT'}$ (total)
0.70	1.875	-0.833	-157.5	-0.075	0.228	0.116	0.130	0.262
0.70	1.875	-0.833	-112.5	0.376	0.267	0.060	0.084	0.280
0.70	1.875	-0.833	-67.5	-0.060	0.236	0.060	0.084	0.250
0.70	1.875	-0.833	-22.5	0.080	0.236	0.035	0.068	0.245
0.70	1.875	-0.833	22.5	-0.063	0.207	0.143	0.154	0.258
0.70	1.875	-0.833	67.5	0.244	0.241	0.106	0.121	0.270
0.70	1.875	-0.833	112.5	-0.348	0.341	0.060	0.084	0.351
0.70	1.875	-0.833	157.5	0.324	0.214	0.141	0.153	0.263
0.70	1.875	-0.500	-157.5	-0.563	0.193	0.229	0.236	0.305
0.70	1.875	-0.500	-112.5	-0.317	0.137	0.191	0.200	0.242
0.70	1.875	-0.500	-67.5	-0.142	0.169	0.131	0.143	0.221
0.70	1.875	-0.500	-22.5	-0.079	0.188	0.046	0.075	0.202
0.70	1.875	-0.500	22.5	0.259	0.178	0.086	0.104	0.206
0.70	1.875	-0.500	67.5	0.526	0.155	0.065	0.088	0.178
0.70	1.875	-0.500	112.5	0.252	0.145	0.022	0.063	0.158
0.70	1.875	-0.500	157.5	0.016	0.233	0.068	0.089	0.249
0.70	1.875	-0.167	-157.5	-0.017	0.099	0.019	0.061	0.116
0.70	1.875	-0.167	-112.5	-0.221	0.098	0.053	0.079	0.126
0.70	1.875	-0.167	-67.5	-0.159	0.117	0.020	0.062	0.132
0.70	1.875	-0.167	-22.5	-0.507	0.147	0.125	0.138	0.202
0.70	1.875	-0.167	22.5	-0.081	0.157	0.111	0.126	0.201
0.70	1.875	-0.167	67.5	0.303	0.114	0.034	0.067	0.132
0.70	1.875	-0.167	112.5	0.266	0.096	0.012	0.060	0.113
0.70	1.875	-0.167	157.5	0.050	0.097	0.033	0.067	0.118
0.70	1.875	0.167	-157.5	-0.075	0.080	0.030	0.066	0.104
0.70	1.875	0.167	-112.5	-0.071	0.074	0.030	0.066	0.099
0.70	1.875	0.167	-67.5	-0.113	0.096	0.040	0.071	0.119
0.70	1.875	0.167	-22.5	-0.198	0.129	0.054	0.080	0.151
0.70	1.875	0.167	22.5	0.065	0.132	0.071	0.092	0.161
0.70	1.875	0.167	67.5	-0.002	0.103	0.018	0.061	0.120
0.70	1.875	0.167	112.5	0.066	0.073	0.019	0.061	0.095
0.70	1.875	0.167	157.5	-0.053	0.080	0.006	0.059	0.099
0.70	1.875	0.500	-157.5	0.069	0.065	0.016	0.061	0.089
0.70	1.875	0.500	-112.5	0.050	0.064	0.027	0.064	0.091
0.70	1.875	0.500	-67.5	0.001	0.078	0.046	0.074	0.107
0.70	1.875	0.500	-22.5	0.012	0.176	0.063	0.086	0.196
0.70	1.875	0.500	22.5	-0.031	0.168	0.098	0.114	0.203
0.70	1.875	0.500	67.5	0.045	0.079	0.035	0.068	0.104
0.70	1.875	0.500	112.5	-0.023	0.069	0.014	0.060	0.091
0.70	1.875	0.500	157.5	0.045	0.067	0.052	0.078	0.103
0.70	1.875	0.833	-157.5	0.008	0.051	0.023	0.063	0.081
0.70	1.875	0.833	-112.5	-0.037	0.070	0.036	0.069	0.098
0.70	1.875	0.833	-67.5	-0.221	0.076	0.061	0.085	0.114
0.70	1.875	0.833	-22.5	-0.171	0.297	0.060	0.084	0.308
0.70	1.875	0.833	22.5	0.186	0.309	0.060	0.084	0.320
0.70	1.875	0.833	67.5	0.005	0.079	0.033	0.067	0.104
0.70	1.875	0.833	112.5	-0.060	0.066	0.031	0.066	0.094
0.70	1.875	0.833	157.5	0.131	0.050	0.062	0.085	0.098

Table 16: Measured asymmetries and statistical and systematic uncertainties for various kinematic bins (continued).

Q^2 (GeV)^2	W (GeV)	$\cos\theta_K^{cm}$	ϕ (°)	$A_{LT'}$	$\delta A_{LT'}$ (stat)	$\delta A_{LT'}$ (sys bg)	$\delta A_{LT'}$ (sys)	$\delta A_{LT'}$ (total)
0.70	1.925	-0.833	-157.5	0.054	0.259	0.045	0.074	0.270
0.70	1.925	-0.833	-112.5	-0.103	0.215	0.164	0.174	0.277
0.70	1.925	-0.833	-67.5	-0.587	0.209	0.070	0.092	0.228
0.70	1.925	-0.833	-22.5	-0.095	0.240	0.183	0.193	0.307
0.70	1.925	-0.833	22.5	-0.106	0.272	0.060	0.084	0.284
0.70	1.925	-0.833	67.5	0.091	0.282	0.048	0.075	0.292
0.70	1.925	-0.833	112.5	0.112	0.236	0.150	0.161	0.286
0.70	1.925	-0.833	157.5	-0.035	0.242	0.021	0.062	0.250
0.70	1.925	-0.500	-157.5	-0.471	0.220	0.312	0.317	0.386
0.70	1.925	-0.500	-112.5	-0.139	0.162	0.032	0.067	0.175
0.70	1.925	-0.500	-67.5	-0.322	0.158	0.096	0.112	0.194
0.70	1.925	-0.500	-22.5	-0.549	0.184	0.261	0.268	0.325
0.70	1.925	-0.500	22.5	-0.185	0.184	0.037	0.069	0.197
0.70	1.925	-0.500	67.5	0.080	0.177	0.056	0.081	0.194
0.70	1.925	-0.500	112.5	0.258	0.172	0.029	0.065	0.184
0.70	1.925	-0.500	157.5	0.255	0.243	0.150	0.161	0.291
0.70	1.925	-0.167	-157.5	-0.193	0.108	0.048	0.076	0.132
0.70	1.925	-0.167	-112.5	-0.069	0.114	0.046	0.074	0.136
0.70	1.925	-0.167	-67.5	0.053	0.134	0.031	0.066	0.149
0.70	1.925	-0.167	-22.5	-0.245	0.183	0.140	0.152	0.238
0.70	1.925	-0.167	22.5	-0.036	0.186	0.045	0.074	0.200
0.70	1.925	-0.167	67.5	0.330	0.136	0.125	0.138	0.193
0.70	1.925	-0.167	112.5	0.431	0.104	0.032	0.067	0.124
0.70	1.925	-0.167	157.5	0.246	0.120	0.161	0.171	0.209
0.70	1.925	0.167	-157.5	0.001	0.094	0.079	0.098	0.135
0.70	1.925	0.167	-112.5	-0.075	0.075	0.023	0.063	0.097
0.70	1.925	0.167	-67.5	-0.017	0.094	0.040	0.071	0.118
0.70	1.925	0.167	-22.5	0.259	0.133	0.118	0.132	0.187
0.70	1.925	0.167	22.5	-0.027	0.137	0.017	0.061	0.150
0.70	1.925	0.167	67.5	0.017	0.103	0.020	0.062	0.120
0.70	1.925	0.167	112.5	0.049	0.080	0.027	0.064	0.103
0.70	1.925	0.167	157.5	0.176	0.094	0.067	0.089	0.130
0.70	1.925	0.500	-157.5	0.079	0.074	0.040	0.070	0.102
0.70	1.925	0.500	-112.5	-0.172	0.066	0.022	0.062	0.091
0.70	1.925	0.500	-67.5	0.004	0.084	0.035	0.068	0.108
0.70	1.925	0.500	-22.5	0.208	0.162	0.270	0.276	0.320
0.70	1.925	0.500	22.5	-0.126	0.149	0.023	0.063	0.162
0.70	1.925	0.500	67.5	-0.094	0.091	0.044	0.073	0.117
0.70	1.925	0.500	112.5	0.130	0.069	0.081	0.100	0.122
0.70	1.925	0.500	157.5	-0.025	0.073	0.031	0.066	0.098
0.70	1.925	0.833	-157.5	-0.136	0.054	0.103	0.119	0.130
0.70	1.925	0.833	-112.5	0.230	0.074	0.189	0.198	0.211
0.70	1.925	0.833	-67.5	-0.096	0.086	0.067	0.089	0.124
0.70	1.925	0.833	-22.5	0.219	0.557	0.060	0.084	0.564
0.70	1.925	0.833	22.5	-0.413	0.432	0.060	0.084	0.440
0.70	1.925	0.833	67.5	-0.060	0.083	0.054	0.079	0.115
0.70	1.925	0.833	112.5	0.007	0.070	0.078	0.097	0.120
0.70	1.925	0.833	157.5	0.046	0.054	0.046	0.074	0.092

Table 17: Measured asymmetries and statistical and systematic uncertainties for various kinematic bins (continued).

Q^2 $(GeV)^2$	W (GeV)	$\cos\theta_K^{cm}$	ϕ (°)	$A_{LT'}$	$\delta A_{LT'}$ (stat)	$\delta A_{LT'}$ (sys bg)	$\delta A_{LT'}$ (sys)	$\delta A_{LT'}$ (total)
0.70	1.975	-0.833	-157.5	-0.042	0.277	0.051	0.078	0.288
0.70	1.975	-0.833	-112.5	-0.264	0.227	0.060	0.084	0.242
0.70	1.975	-0.833	-67.5	0.162	0.266	0.060	0.084	0.279
0.70	1.975	-0.833	-22.5	-0.276	0.241	0.060	0.084	0.255
0.70	1.975	-0.833	22.5	-0.503	0.256	0.062	0.086	0.270
0.70	1.975	-0.833	67.5	0.206	0.234	0.060	0.084	0.249
0.70	1.975	-0.833	112.5	0.185	0.236	0.039	0.070	0.246
0.70	1.975	-0.833	157.5	0.189	0.270	0.060	0.084	0.283
0.70	1.975	-0.500	-157.5	-0.319	0.234	0.046	0.074	0.246
0.70	1.975	-0.500	-112.5	0.124	0.190	0.125	0.138	0.235
0.70	1.975	-0.500	-67.5	-0.433	0.185	0.135	0.147	0.236
0.70	1.975	-0.500	-22.5	-0.017	0.223	0.143	0.154	0.271
0.70	1.975	-0.500	22.5	0.268	0.226	0.204	0.213	0.310
0.70	1.975	-0.500	67.5	0.430	0.175	0.140	0.151	0.232
0.70	1.975	-0.500	112.5	0.516	0.182	0.064	0.087	0.202
0.70	1.975	-0.500	157.5	-0.440	0.236	0.113	0.127	0.269
0.70	1.975	-0.167	-157.5	-0.223	0.145	0.090	0.108	0.180
0.70	1.975	-0.167	-112.5	-0.199	0.131	0.040	0.071	0.149
0.70	1.975	-0.167	-67.5	0.116	0.158	0.112	0.127	0.202
0.70	1.975	-0.167	-22.5	-0.138	0.240	0.272	0.278	0.367
0.70	1.975	-0.167	22.5	0.288	0.218	0.205	0.213	0.304
0.70	1.975	-0.167	67.5	0.219	0.151	0.023	0.063	0.164
0.70	1.975	-0.167	112.5	-0.072	0.132	0.027	0.064	0.147
0.70	1.975	-0.167	157.5	0.199	0.149	0.109	0.124	0.193
0.70	1.975	0.167	-157.5	-0.230	0.102	0.131	0.144	0.176
0.70	1.975	0.167	-112.5	-0.156	0.090	0.014	0.060	0.108
0.70	1.975	0.167	-67.5	0.164	0.108	0.069	0.090	0.141
0.70	1.975	0.167	-22.5	-0.084	0.146	0.096	0.112	0.184
0.70	1.975	0.167	22.5	0.132	0.161	0.079	0.099	0.189
0.70	1.975	0.167	67.5	-0.018	0.103	0.104	0.119	0.157
0.70	1.975	0.167	112.5	-0.002	0.083	0.022	0.062	0.104
0.70	1.975	0.167	157.5	-0.092	0.103	0.067	0.089	0.136
0.70	1.975	0.500	-157.5	-0.001	0.087	0.026	0.064	0.108
0.70	1.975	0.500	-112.5	0.108	0.073	0.080	0.099	0.123
0.70	1.975	0.500	-67.5	-0.154	0.095	0.115	0.129	0.161
0.70	1.975	0.500	-22.5	-0.261	0.147	0.121	0.135	0.200
0.70	1.975	0.500	22.5	-0.192	0.154	0.083	0.101	0.184
0.70	1.975	0.500	67.5	-0.006	0.101	0.160	0.170	0.198
0.70	1.975	0.500	112.5	0.068	0.071	0.067	0.089	0.113
0.70	1.975	0.500	157.5	-0.011	0.083	0.038	0.070	0.108
0.70	1.975	0.833	-157.5	0.039	0.060	0.037	0.069	0.091
0.70	1.975	0.833	-112.5	-0.158	0.078	0.013	0.060	0.098
0.70	1.975	0.833	-67.5	-0.341	0.087	0.102	0.117	0.146
0.70	1.975	0.833	-22.5	0.302	0.653	0.298	0.304	0.720
0.70	1.975	0.833	22.5	0.493	0.814	0.060	0.084	0.818
0.70	1.975	0.833	67.5	-0.079	0.093	0.029	0.065	0.114
0.70	1.975	0.833	112.5	0.150	0.076	0.066	0.088	0.116
0.70	1.975	0.833	157.5	0.108	0.060	0.061	0.084	0.104

Table 18: Measured asymmetries and statistical and systematic uncertainties for various kinematic bins (continued).

Q^2 (GeV)^2	W (GeV)	$\cos\theta_K^{cm}$	ϕ (°)	$A_{LT'}$	$\delta A_{LT'}$ (stat)	$\delta A_{LT'}$ (sys bg)	$\delta A_{LT'}$ (sys)	$\delta A_{LT'}$ (total)
0.70	2.025	-0.833	-157.5	-0.416	0.384	0.060	0.084	0.393
0.70	2.025	-0.833	-112.5	0.095	0.325	0.065	0.087	0.336
0.70	2.025	-0.833	-67.5	0.155	0.447	0.136	0.148	0.471
0.70	2.025	-0.833	-22.5	-0.366	0.512	0.207	0.215	0.555
0.70	2.025	-0.833	22.5	0.291	0.378	0.060	0.084	0.387
0.70	2.025	-0.833	67.5	0.640	0.271	0.032	0.067	0.279
0.70	2.025	-0.833	112.5	-0.025	0.304	0.060	0.083	0.316
0.70	2.025	-0.833	157.5	0.437	0.320	0.060	0.084	0.331
0.70	2.025	-0.500	-157.5	0.191	0.348	0.060	0.084	0.358
0.70	2.025	-0.500	-112.5	-0.421	0.283	0.060	0.084	0.295
0.70	2.025	-0.500	-67.5	-0.389	0.252	0.063	0.086	0.266
0.70	2.025	-0.500	-22.5	0.082	0.342	0.060	0.084	0.352
0.70	2.025	-0.500	22.5	-0.443	0.345	0.059	0.083	0.355
0.70	2.025	-0.500	67.5	0.222	0.266	0.060	0.084	0.278
0.70	2.025	-0.500	112.5	0.433	0.234	0.060	0.084	0.248
0.70	2.025	-0.500	157.5	-0.521	0.359	0.060	0.084	0.369
0.70	2.025	-0.167	-157.5	-0.262	0.177	0.198	0.207	0.272
0.70	2.025	-0.167	-112.5	-0.644	0.159	0.143	0.155	0.222
0.70	2.025	-0.167	-67.5	0.184	0.209	0.273	0.279	0.348
0.70	2.025	-0.167	-22.5	0.439	0.346	0.107	0.122	0.367
0.70	2.025	-0.167	22.5	0.319	0.275	0.060	0.084	0.288
0.70	2.025	-0.167	67.5	0.134	0.196	0.101	0.117	0.228
0.70	2.025	-0.167	112.5	-0.119	0.189	0.024	0.063	0.200
0.70	2.025	-0.167	157.5	-0.285	0.158	0.086	0.104	0.189
0.70	2.025	0.167	-157.5	-0.536	0.154	0.489	0.492	0.516
0.70	2.025	0.167	-112.5	-0.228	0.102	0.062	0.086	0.133
0.70	2.025	0.167	-67.5	0.190	0.132	0.103	0.118	0.177
0.70	2.025	0.167	-22.5	-0.339	0.181	0.091	0.108	0.211
0.70	2.025	0.167	22.5	-0.316	0.174	0.032	0.067	0.186
0.70	2.025	0.167	67.5	-0.017	0.129	0.054	0.079	0.151
0.70	2.025	0.167	112.5	-0.004	0.104	0.028	0.065	0.122
0.70	2.025	0.167	157.5	0.023	0.124	0.036	0.069	0.142
0.70	2.025	0.500	-157.5	-0.097	0.120	0.086	0.104	0.159
0.70	2.025	0.500	-112.5	-0.012	0.090	0.023	0.063	0.109
0.70	2.025	0.500	-67.5	-0.234	0.110	0.048	0.076	0.133
0.70	2.025	0.500	-22.5	-0.164	0.162	0.153	0.164	0.231
0.70	2.025	0.500	22.5	0.147	0.148	0.049	0.076	0.167
0.70	2.025	0.500	67.5	0.194	0.113	0.072	0.093	0.146
0.70	2.025	0.500	112.5	0.088	0.084	0.031	0.066	0.107
0.70	2.025	0.500	157.5	-0.091	0.102	0.101	0.117	0.156
0.70	2.025	0.833	-157.5	0.218	0.075	0.166	0.176	0.192
0.70	2.025	0.833	-112.5	0.042	0.095	0.048	0.076	0.122
0.70	2.025	0.833	-67.5	-0.034	0.128	0.189	0.198	0.235
0.70	2.025	0.833	-22.5	-0.371	0.511	0.060	0.084	0.518
0.70	2.025	0.833	22.5	0.744	0.458	0.249	0.256	0.524
0.70	2.025	0.833	67.5	-0.108	0.133	0.196	0.204	0.244
0.70	2.025	0.833	112.5	-0.014	0.094	0.051	0.077	0.121
0.70	2.025	0.833	157.5	-0.450	0.077	0.292	0.298	0.308

Table 19: Measured asymmetries and statistical and systematic uncertainties for various kinematic bins (continued).

Q^2 (GeV)^2	W (GeV)	$\cos\theta_K^{cm}$	ϕ (°)	$A_{LT'}$	$\delta A_{LT'}$ (stat)	$\delta A_{LT'}$ (sys bg)	$\delta A_{LT'}$ (sys)	$\delta A_{LT'}$ (total)
1.10	1.625	-0.833	-157.5	-0.061	0.298	0.116	0.130	0.325
1.10	1.625	-0.833	-112.5	-0.332	0.343	0.060	0.084	0.353
1.10	1.625	-0.833	-67.5	1.243	0.238	0.210	0.219	0.323
1.10	1.625	-0.833	-22.5	0.214	0.558	0.160	0.170	0.583
1.10	1.625	-0.833	22.5	-0.300	0.654	0.060	0.084	0.659
1.10	1.625	-0.833	67.5	0.745	0.323	0.249	0.256	0.412
1.10	1.625	-0.833	112.5	0.065	0.311	0.060	0.084	0.322
1.10	1.625	-0.833	157.5	-0.249	0.300	0.070	0.091	0.314
1.10	1.625	-0.500	-157.5	0.027	0.284	0.032	0.067	0.292
1.10	1.625	-0.500	-112.5	-0.373	0.361	0.110	0.124	0.382
1.10	1.625	-0.500	-67.5	-0.493	0.308	0.060	0.084	0.319
1.10	1.625	-0.500	-22.5	—	—	—	—	—
1.10	1.625	-0.500	22.5	0.891	0.537	0.398	0.402	0.671
1.10	1.625	-0.500	67.5	-0.121	0.292	0.051	0.078	0.302
1.10	1.625	-0.500	112.5	0.536	0.278	0.075	0.095	0.294
1.10	1.625	-0.500	157.5	-0.418	0.286	0.073	0.094	0.302
1.10	1.625	-0.167	-157.5	0.177	0.247	0.074	0.094	0.265
1.10	1.625	-0.167	-112.5	0.119	0.270	0.027	0.064	0.277
1.10	1.625	-0.167	-67.5	0.146	0.316	0.011	0.059	0.322
1.10	1.625	-0.167	-22.5	-0.487	0.577	0.060	0.084	0.583
1.10	1.625	-0.167	22.5	0.737	0.651	0.149	0.161	0.670
1.10	1.625	-0.167	67.5	0.345	0.317	0.060	0.084	0.328
1.10	1.625	-0.167	112.5	-0.599	0.305	0.099	0.116	0.327
1.10	1.625	-0.167	157.5	0.101	0.250	0.021	0.062	0.258
1.10	1.625	0.167	-157.5	-0.224	0.253	0.077	0.097	0.271
1.10	1.625	0.167	-112.5	0.045	0.286	0.085	0.103	0.304
1.10	1.625	0.167	-67.5	-0.174	0.371	0.060	0.084	0.380
1.10	1.625	0.167	-22.5	-0.288	0.656	0.298	0.304	0.723
1.10	1.625	0.167	22.5	-0.225	0.557	0.060	0.084	0.563
1.10	1.625	0.167	67.5	-0.226	0.394	0.085	0.103	0.407
1.10	1.625	0.167	112.5	0.424	0.323	0.072	0.093	0.336
1.10	1.625	0.167	157.5	-0.165	0.214	0.016	0.061	0.222
1.10	1.625	0.500	-157.5	0.232	0.230	0.115	0.129	0.264
1.10	1.625	0.500	-112.5	0.396	0.330	0.060	0.084	0.340
1.10	1.625	0.500	-67.5	0.259	0.300	0.060	0.084	0.311
1.10	1.625	0.500	-22.5	-0.741	0.459	0.060	0.084	0.467
1.10	1.625	0.500	22.5	-0.306	0.461	0.060	0.084	0.469
1.10	1.625	0.500	67.5	-0.146	0.447	0.060	0.084	0.455
1.10	1.625	0.500	112.5	0.231	0.276	0.031	0.066	0.284
1.10	1.625	0.500	157.5	-0.097	0.258	0.105	0.120	0.284
1.10	1.625	0.833	-157.5	-0.166	0.205	0.026	0.064	0.214
1.10	1.625	0.833	-112.5	0.500	0.287	0.060	0.084	0.299
1.10	1.625	0.833	-67.5	0.079	0.254	0.117	0.131	0.286
1.10	1.625	0.833	-22.5	0.117	0.292	0.060	0.084	0.303
1.10	1.625	0.833	22.5	0.289	0.351	0.051	0.078	0.360
1.10	1.625	0.833	67.5	0.043	0.268	0.039	0.070	0.277
1.10	1.625	0.833	112.5	-0.113	0.232	0.115	0.129	0.266
1.10	1.625	0.833	157.5	0.225	0.202	0.043	0.073	0.214

Table 20: Measured asymmetries and statistical and systematic uncertainties for various kinematic bins (continued).

Q^2 (GeV)^2	W (GeV)	$\cos\theta_K^{cm}$	ϕ (°)	$A_{LT'}$	$\delta A_{LT'}$ (stat)	$\delta A_{LT'}$ (sys bg)	$\delta A_{LT'}$ (sys)	$\delta A_{LT'}$ (total)
1.10	1.675	-0.833	-157.5	0.105	0.232	0.253	0.259	0.348
1.10	1.675	-0.833	-112.5	0.027	0.250	0.054	0.079	0.263
1.10	1.675	-0.833	-67.5	-0.109	0.271	0.326	0.331	0.428
1.10	1.675	-0.833	-22.5	-0.169	0.494	0.060	0.084	0.501
1.10	1.675	-0.833	22.5	0.003	0.609	0.060	0.084	0.615
1.10	1.675	-0.833	67.5	0.247	0.301	0.123	0.136	0.331
1.10	1.675	-0.833	112.5	0.268	0.216	0.046	0.075	0.229
1.10	1.675	-0.833	157.5	0.168	0.247	0.205	0.213	0.326
1.10	1.675	-0.500	-157.5	-0.318	0.183	0.108	0.123	0.221
1.10	1.675	-0.500	-112.5	0.135	0.202	0.118	0.132	0.241
1.10	1.675	-0.500	-67.5	-0.098	0.255	0.230	0.237	0.349
1.10	1.675	-0.500	-22.5	0.369	0.511	0.060	0.084	0.518
1.10	1.675	-0.500	22.5	-0.111	0.413	0.060	0.084	0.421
1.10	1.675	-0.500	67.5	0.390	0.187	0.052	0.078	0.203
1.10	1.675	-0.500	112.5	0.346	0.200	0.060	0.084	0.217
1.10	1.675	-0.500	157.5	-0.103	0.162	0.142	0.154	0.224
1.10	1.675	-0.167	-157.5	-0.414	0.153	0.181	0.191	0.244
1.10	1.675	-0.167	-112.5	-0.338	0.165	0.013	0.060	0.175
1.10	1.675	-0.167	-67.5	-0.313	0.149	0.036	0.069	0.164
1.10	1.675	-0.167	-22.5	-0.001	0.472	0.060	0.084	0.479
1.10	1.675	-0.167	22.5	-0.298	0.462	0.060	0.084	0.470
1.10	1.675	-0.167	67.5	0.143	0.154	0.003	0.058	0.164
1.10	1.675	-0.167	112.5	0.184	0.168	0.039	0.070	0.182
1.10	1.675	-0.167	157.5	-0.079	0.160	0.042	0.072	0.175
1.10	1.675	0.167	-157.5	0.073	0.125	0.069	0.091	0.154
1.10	1.675	0.167	-112.5	-0.136	0.141	0.031	0.066	0.155
1.10	1.675	0.167	-67.5	-0.042	0.152	0.039	0.070	0.167
1.10	1.675	0.167	-22.5	-0.659	0.316	0.060	0.084	0.327
1.10	1.675	0.167	22.5	-0.645	0.508	0.060	0.084	0.515
1.10	1.675	0.167	67.5	0.057	0.147	0.012	0.060	0.158
1.10	1.675	0.167	112.5	0.199	0.149	0.015	0.060	0.161
1.10	1.675	0.167	157.5	0.036	0.137	0.039	0.070	0.154
1.10	1.675	0.500	-157.5	-0.082	0.111	0.033	0.067	0.130
1.10	1.675	0.500	-112.5	-0.194	0.131	0.039	0.070	0.149
1.10	1.675	0.500	-67.5	-0.036	0.146	0.014	0.060	0.158
1.10	1.675	0.500	-22.5	0.129	0.412	0.060	0.084	0.420
1.10	1.675	0.500	22.5	-0.690	0.397	0.060	0.084	0.406
1.10	1.675	0.500	67.5	0.417	0.133	0.022	0.063	0.147
1.10	1.675	0.500	112.5	0.236	0.136	0.023	0.063	0.150
1.10	1.675	0.500	157.5	-0.090	0.109	0.022	0.062	0.126
1.10	1.675	0.833	-157.5	0.139	0.096	0.034	0.068	0.118
1.10	1.675	0.833	-112.5	-0.035	0.118	0.034	0.067	0.136
1.10	1.675	0.833	-67.5	0.024	0.132	0.048	0.076	0.152
1.10	1.675	0.833	-22.5	0.619	0.167	0.773	0.775	0.793
1.10	1.675	0.833	22.5	0.112	0.173	0.123	0.136	0.220
1.10	1.675	0.833	67.5	-0.103	0.157	0.054	0.079	0.176
1.10	1.675	0.833	112.5	0.018	0.121	0.067	0.089	0.150
1.10	1.675	0.833	157.5	0.036	0.098	0.055	0.080	0.127

Table 21: Measured asymmetries and statistical and systematic uncertainties for various kinematic bins (continued).

Q^2 (GeV)^2	W (GeV)	$\cos\theta_K^{cm}$	ϕ (°)	$A_{LT'}$	$\delta A_{LT'}$ (stat)	$\delta A_{LT'}$ (sys bg)	$\delta A_{LT'}$ (sys)	$\delta A_{LT'}$ (total)
1.10	1.725	-0.833	-157.5	-0.477	0.205	0.039	0.071	0.217
1.10	1.725	-0.833	-112.5	-0.114	0.229	0.173	0.183	0.293
1.10	1.725	-0.833	-67.5	0.057	0.239	0.034	0.068	0.249
1.10	1.725	-0.833	-22.5	-0.524	0.463	0.060	0.084	0.470
1.10	1.725	-0.833	22.5	0.029	0.431	0.060	0.084	0.439
1.10	1.725	-0.833	67.5	-0.042	0.273	0.060	0.084	0.285
1.10	1.725	-0.833	112.5	0.082	0.245	0.173	0.183	0.305
1.10	1.725	-0.833	157.5	0.014	0.272	0.048	0.076	0.283
1.10	1.725	-0.500	-157.5	0.147	0.198	0.393	0.398	0.444
1.10	1.725	-0.500	-112.5	-0.215	0.175	0.064	0.087	0.196
1.10	1.725	-0.500	-67.5	-0.271	0.193	0.085	0.103	0.219
1.10	1.725	-0.500	-22.5	-0.276	0.244	0.060	0.084	0.258
1.10	1.725	-0.500	22.5	0.028	0.292	0.060	0.084	0.304
1.10	1.725	-0.500	67.5	0.073	0.191	0.045	0.074	0.204
1.10	1.725	-0.500	112.5	0.171	0.163	0.070	0.091	0.187
1.10	1.725	-0.500	157.5	0.077	0.172	0.086	0.104	0.201
1.10	1.725	-0.167	-157.5	-0.158	0.127	0.048	0.076	0.148
1.10	1.725	-0.167	-112.5	-0.318	0.138	0.017	0.061	0.151
1.10	1.725	-0.167	-67.5	-0.277	0.148	0.018	0.061	0.160
1.10	1.725	-0.167	-22.5	-0.196	0.295	0.060	0.084	0.307
1.10	1.725	-0.167	22.5	0.288	0.311	0.060	0.084	0.323
1.10	1.725	-0.167	67.5	0.734	0.147	0.147	0.159	0.216
1.10	1.725	-0.167	112.5	0.451	0.143	0.019	0.062	0.156
1.10	1.725	-0.167	157.5	0.208	0.133	0.044	0.073	0.152
1.10	1.725	0.167	-157.5	0.008	0.104	0.043	0.072	0.126
1.10	1.725	0.167	-112.5	-0.112	0.113	0.051	0.077	0.137
1.10	1.725	0.167	-67.5	-0.265	0.117	0.015	0.060	0.131
1.10	1.725	0.167	-22.5	0.427	0.382	0.060	0.084	0.391
1.10	1.725	0.167	22.5	0.113	0.413	0.060	0.084	0.421
1.10	1.725	0.167	67.5	0.094	0.116	0.020	0.062	0.131
1.10	1.725	0.167	112.5	0.081	0.114	0.069	0.091	0.146
1.10	1.725	0.167	157.5	0.166	0.103	0.015	0.060	0.120
1.10	1.725	0.500	-157.5	-0.042	0.077	0.021	0.062	0.099
1.10	1.725	0.500	-112.5	0.076	0.096	0.019	0.061	0.114
1.10	1.725	0.500	-67.5	-0.116	0.101	0.040	0.071	0.123
1.10	1.725	0.500	-22.5	0.395	0.358	0.060	0.084	0.368
1.10	1.725	0.500	22.5	-0.396	0.358	0.060	0.084	0.368
1.10	1.725	0.500	67.5	-0.186	0.093	0.021	0.062	0.112
1.10	1.725	0.500	112.5	0.103	0.093	0.007	0.059	0.110
1.10	1.725	0.500	157.5	0.011	0.082	0.075	0.095	0.126
1.10	1.725	0.833	-157.5	-0.055	0.068	0.025	0.063	0.093
1.10	1.725	0.833	-112.5	0.025	0.084	0.034	0.067	0.108
1.10	1.725	0.833	-67.5	0.081	0.113	0.221	0.228	0.255
1.10	1.725	0.833	-22.5	-0.245	0.136	0.089	0.106	0.173
1.10	1.725	0.833	22.5	-0.003	0.148	0.059	0.083	0.170
1.10	1.725	0.833	67.5	-0.164	0.101	0.028	0.065	0.120
1.10	1.725	0.833	112.5	-0.049	0.085	0.006	0.059	0.104
1.10	1.725	0.833	157.5	-0.744	0.074	0.535	0.539	0.544

Table 22: Measured asymmetries and statistical and systematic uncertainties for various kinematic bins (continued).

Q^2 (GeV)^2	W (GeV)	$\cos\theta_K^{cm}$	ϕ (°)	$A_{LT'}$	$\delta A_{LT'}$ (stat)	$\delta A_{LT'}$ (sys bg)	$\delta A_{LT'}$ (sys)	$\delta A_{LT'}$ (total)
1.10	1.775	-0.833	-157.5	-0.122	0.449	0.060	0.084	0.456
1.10	1.775	-0.833	-112.5	0.101	0.324	0.060	0.084	0.335
1.10	1.775	-0.833	-67.5	0.028	0.352	0.060	0.084	0.361
1.10	1.775	-0.833	-22.5	0.011	0.431	0.060	0.084	0.439
1.10	1.775	-0.833	22.5	0.737	0.460	0.083	0.102	0.472
1.10	1.775	-0.833	67.5	0.437	0.266	0.060	0.084	0.279
1.10	1.775	-0.833	112.5	-0.030	0.333	0.060	0.084	0.344
1.10	1.775	-0.833	157.5	-0.756	0.370	0.060	0.084	0.379
1.10	1.775	-0.500	-157.5	0.010	0.264	0.060	0.084	0.277
1.10	1.775	-0.500	-112.5	0.103	0.194	0.060	0.084	0.211
1.10	1.775	-0.500	-67.5	-0.326	0.226	0.083	0.101	0.247
1.10	1.775	-0.500	-22.5	0.193	0.296	0.060	0.084	0.307
1.10	1.775	-0.500	22.5	-0.063	0.268	0.045	0.074	0.278
1.10	1.775	-0.500	67.5	0.203	0.189	0.078	0.097	0.212
1.10	1.775	-0.500	112.5	0.399	0.187	0.048	0.076	0.202
1.10	1.775	-0.500	157.5	-0.240	0.288	0.060	0.084	0.300
1.10	1.775	-0.167	-157.5	-0.052	0.124	0.067	0.089	0.153
1.10	1.775	-0.167	-112.5	-0.315	0.127	0.019	0.062	0.141
1.10	1.775	-0.167	-67.5	-0.311	0.169	0.035	0.068	0.182
1.10	1.775	-0.167	-22.5	0.523	0.214	0.015	0.061	0.222
1.10	1.775	-0.167	22.5	0.133	0.223	0.014	0.060	0.231
1.10	1.775	-0.167	67.5	0.099	0.169	0.065	0.087	0.190
1.10	1.775	-0.167	112.5	0.142	0.127	0.036	0.068	0.144
1.10	1.775	-0.167	157.5	0.151	0.122	0.053	0.079	0.146
1.10	1.775	0.167	-157.5	0.048	0.086	0.021	0.062	0.106
1.10	1.775	0.167	-112.5	0.081	0.098	0.030	0.066	0.118
1.10	1.775	0.167	-67.5	0.139	0.124	0.098	0.114	0.168
1.10	1.775	0.167	-22.5	-0.257	0.227	0.080	0.099	0.247
1.10	1.775	0.167	22.5	0.072	0.222	0.024	0.063	0.231
1.10	1.775	0.167	67.5	0.262	0.119	0.045	0.074	0.140
1.10	1.775	0.167	112.5	0.172	0.098	0.012	0.060	0.114
1.10	1.775	0.167	157.5	0.025	0.105	0.024	0.063	0.122
1.10	1.775	0.500	-157.5	0.081	0.076	0.027	0.064	0.100
1.10	1.775	0.500	-112.5	-0.054	0.089	0.025	0.063	0.109
1.10	1.775	0.500	-67.5	-0.056	0.092	0.041	0.071	0.116
1.10	1.775	0.500	-22.5	0.020	0.431	0.060	0.084	0.439
1.10	1.775	0.500	22.5	0.387	0.436	0.060	0.084	0.444
1.10	1.775	0.500	67.5	-0.050	0.093	0.005	0.059	0.110
1.10	1.775	0.500	112.5	0.089	0.085	0.024	0.063	0.106
1.10	1.775	0.500	157.5	0.063	0.080	0.068	0.089	0.120
1.10	1.775	0.833	-157.5	0.107	0.067	0.105	0.120	0.138
1.10	1.775	0.833	-112.5	-0.144	0.082	0.007	0.059	0.101
1.10	1.775	0.833	-67.5	-0.163	0.108	0.017	0.061	0.124
1.10	1.775	0.833	-22.5	0.046	0.198	0.035	0.068	0.209
1.10	1.775	0.833	22.5	0.154	0.248	0.060	0.084	0.261
1.10	1.775	0.833	67.5	0.121	0.103	0.035	0.068	0.123
1.10	1.775	0.833	112.5	-0.021	0.080	0.011	0.059	0.100
1.10	1.775	0.833	157.5	-0.174	0.070	0.068	0.090	0.114

Table 23: Measured asymmetries and statistical and systematic uncertainties for various kinematic bins (continued).

Q^2 (GeV)^2	W (GeV)	$\cos\theta_K^{cm}$	ϕ (°)	$A_{LT'}$	$\delta A_{LT'}$ (stat)	$\delta A_{LT'}$ (sys bg)	$\delta A_{LT'}$ (sys)	$\delta A_{LT'}$ (total)
1.10	1.825	-0.833	-157.5	-0.327	0.405	0.060	0.084	0.414
1.10	1.825	-0.833	-112.5	0.202	0.347	0.070	0.091	0.359
1.10	1.825	-0.833	-67.5	-0.391	0.290	0.060	0.084	0.301
1.10	1.825	-0.833	-22.5	0.125	0.412	0.060	0.084	0.421
1.10	1.825	-0.833	22.5	0.429	0.347	0.060	0.084	0.357
1.10	1.825	-0.833	67.5	-0.030	0.333	0.060	0.084	0.344
1.10	1.825	-0.833	112.5	0.262	0.467	0.060	0.084	0.474
1.10	1.825	-0.833	157.5	0.032	0.277	0.051	0.078	0.288
1.10	1.825	-0.500	-157.5	-0.275	0.380	0.060	0.084	0.389
1.10	1.825	-0.500	-112.5	-0.254	0.209	0.143	0.154	0.260
1.10	1.825	-0.500	-67.5	-0.124	0.233	0.083	0.101	0.255
1.10	1.825	-0.500	-22.5	-0.638	0.272	0.060	0.084	0.284
1.10	1.825	-0.500	22.5	0.517	0.281	0.060	0.084	0.294
1.10	1.825	-0.500	67.5	0.060	0.239	0.060	0.084	0.253
1.10	1.825	-0.500	112.5	0.327	0.211	0.105	0.120	0.242
1.10	1.825	-0.500	157.5	-0.104	0.341	0.060	0.084	0.351
1.10	1.825	-0.167	-157.5	-0.045	0.133	0.033	0.067	0.149
1.10	1.825	-0.167	-112.5	-0.194	0.130	0.014	0.060	0.143
1.10	1.825	-0.167	-67.5	-0.252	0.161	0.093	0.109	0.195
1.10	1.825	-0.167	-22.5	-0.053	0.221	0.012	0.059	0.229
1.10	1.825	-0.167	22.5	0.169	0.224	0.061	0.084	0.240
1.10	1.825	-0.167	67.5	0.091	0.191	0.045	0.074	0.205
1.10	1.825	-0.167	112.5	0.248	0.125	0.015	0.060	0.138
1.10	1.825	-0.167	157.5	0.210	0.140	0.039	0.070	0.157
1.10	1.825	0.167	-157.5	-0.194	0.098	0.031	0.066	0.118
1.10	1.825	0.167	-112.5	0.004	0.105	0.017	0.061	0.121
1.10	1.825	0.167	-67.5	0.154	0.135	0.015	0.060	0.147
1.10	1.825	0.167	-22.5	-0.196	0.207	0.114	0.128	0.244
1.10	1.825	0.167	22.5	-0.091	0.191	0.032	0.066	0.202
1.10	1.825	0.167	67.5	0.013	0.136	0.036	0.069	0.153
1.10	1.825	0.167	112.5	0.110	0.102	0.018	0.061	0.119
1.10	1.825	0.167	157.5	0.206	0.105	0.028	0.065	0.124
1.10	1.825	0.500	-157.5	-0.059	0.091	0.049	0.076	0.119
1.10	1.825	0.500	-112.5	0.061	0.094	0.084	0.103	0.139
1.10	1.825	0.500	-67.5	0.108	0.100	0.034	0.067	0.121
1.10	1.825	0.500	-22.5	0.346	0.302	0.060	0.084	0.313
1.10	1.825	0.500	22.5	0.309	0.345	0.060	0.084	0.355
1.10	1.825	0.500	67.5	0.090	0.104	0.012	0.060	0.120
1.10	1.825	0.500	112.5	-0.150	0.088	0.030	0.066	0.110
1.10	1.825	0.500	157.5	0.128	0.088	0.015	0.060	0.107
1.10	1.825	0.833	-157.5	-0.172	0.075	0.049	0.076	0.107
1.10	1.825	0.833	-112.5	0.038	0.090	0.010	0.059	0.108
1.10	1.825	0.833	-67.5	-0.119	0.115	0.046	0.074	0.137
1.10	1.825	0.833	-22.5	-0.202	0.323	0.060	0.084	0.334
1.10	1.825	0.833	22.5	-0.343	0.342	0.060	0.084	0.352
1.10	1.825	0.833	67.5	-0.065	0.112	0.040	0.071	0.133
1.10	1.825	0.833	112.5	0.110	0.087	0.015	0.060	0.106
1.10	1.825	0.833	157.5	0.046	0.072	0.016	0.060	0.094

Table 24: Measured asymmetries and statistical and systematic uncertainties for various kinematic bins.

F Unpolarized Cross Section fits

Results of the two-dimensional fits in ϕ and $\cos\theta_K^{cm}$ to the unpolarized cross section data from Ref. [33] for various W and Q^2. The solid line is the best fit and the dashed lines represent the 1σ error band around the fit [67].

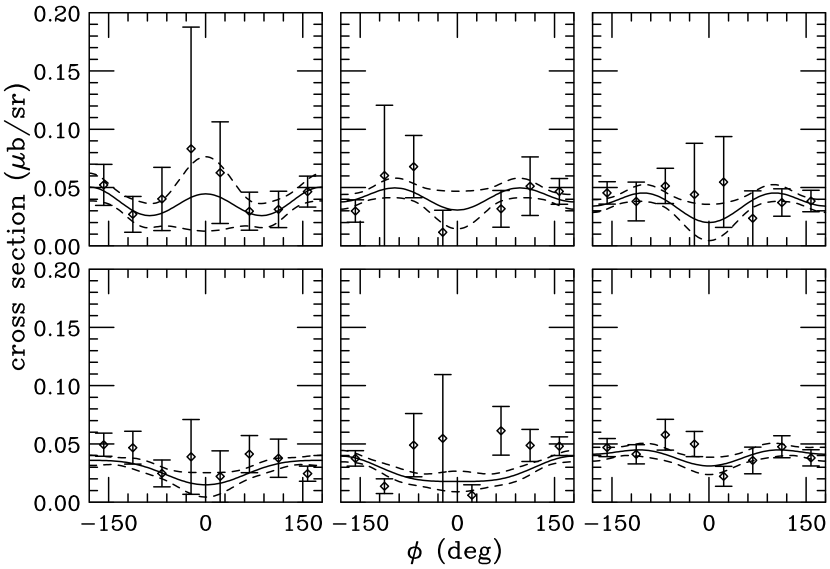

Figure 118: Fits to σ_0 versus ϕ for $\cos\theta_K^{cm}$ = -0.833, -0.50, -0.167, 0.167, 0.50, 0.833 (upper left to lower right), $W = 1.675$ GeV and $Q^2 = 0.7$ GeV^2 with $\chi^2/ndf = 1.12$.

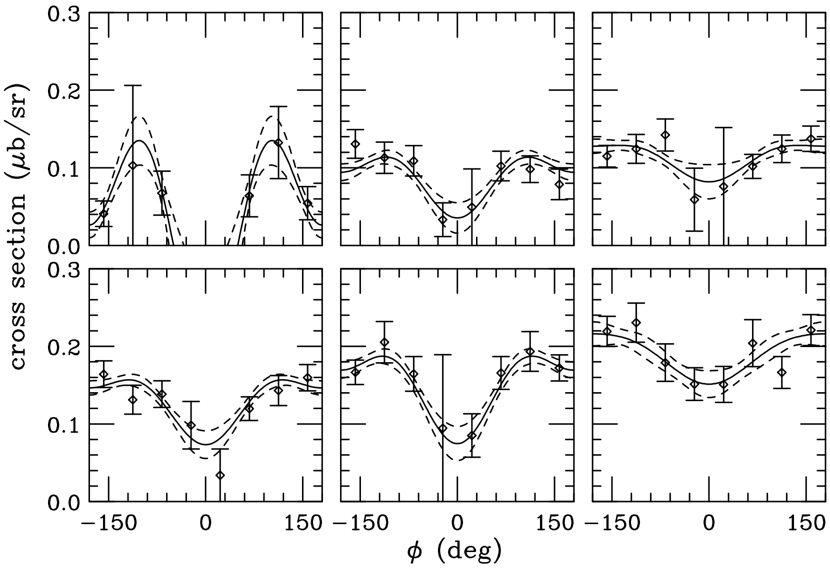

Figure 119: Fits to σ_0 versus ϕ for $\cos\theta_K^{cm}$ = -0.833, -0.50, -0.167, 0.167, 0.50, 0.833 (upper left to lower right), $W = 1.675$ GeV and $Q^2 = 0.7$ GeV^2 with $\chi^2/ndf = 0.72$.

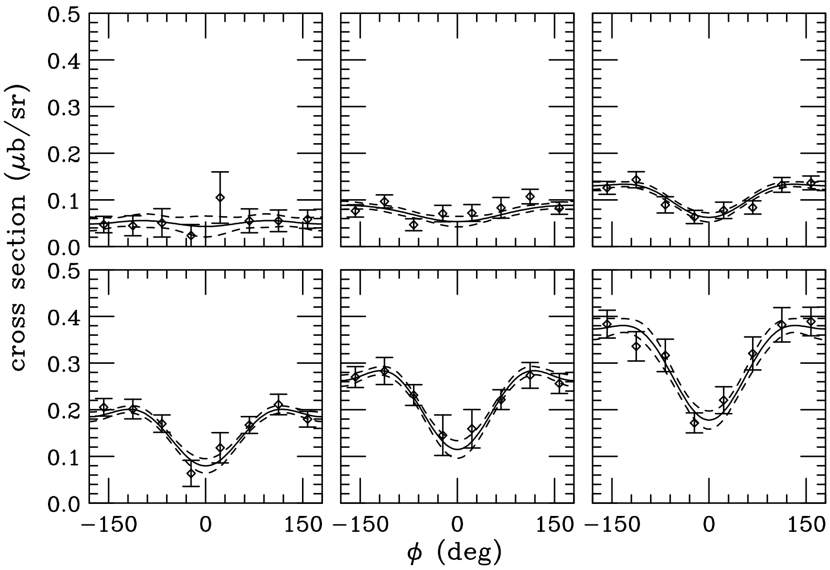

Figure 120: Fits to σ_0 versus ϕ for $\cos\theta_K^{cm}$ = -0.833, -0.50, -0.167, 0.167, 0.50, 0.833 (upper left to lower right), $W = 1.725$ GeV and $Q^2 = 0.7$ GeV^2 with $\chi^2/ndf = 0.71$.

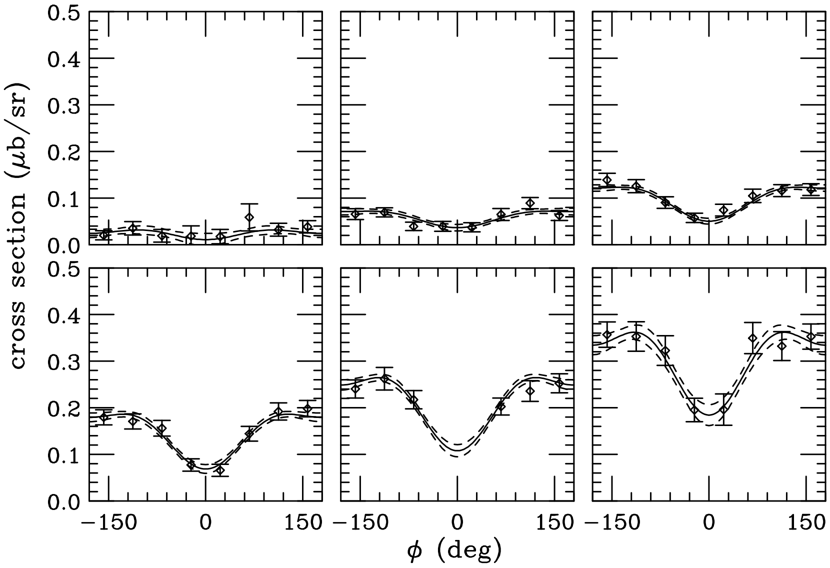

Figure 121: Fits to σ_0 versus ϕ for $\cos\theta_K^{cm}$ = -0.833, -0.50, -0.167, 0.167, 0.50, 0.833 (upper left to lower right), $W = 1.775$ GeV and $Q^2 = 0.7$ GeV^2 with $\chi^2/ndf = 0.74$.

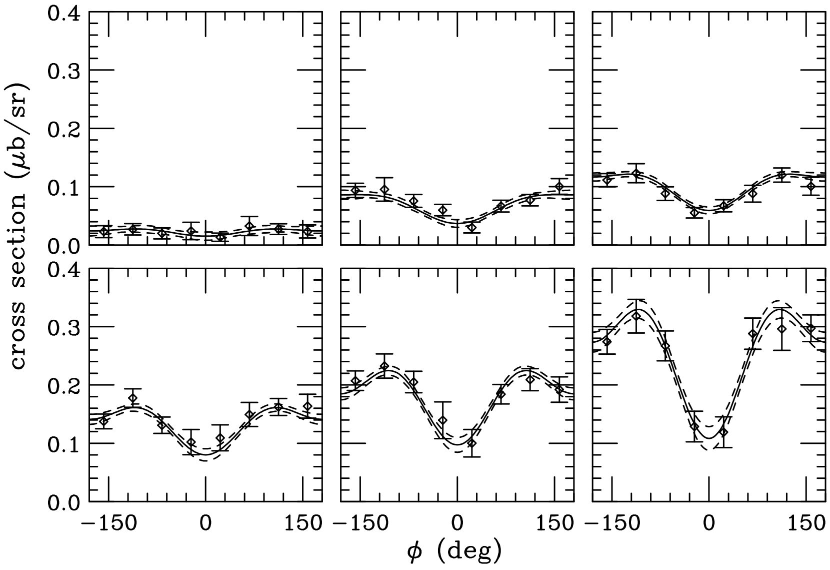

Figure 122: Fits to σ_0 versus ϕ for $\cos\theta_K^{cm}$ = -0.833, -0.50, -0.167, 0.167, 0.50, 0.833 (upper left to lower right), $W = 1.825$ GeV and $Q^2 = 0.7$ GeV^2 with $\chi^2/ndf = 0.66$.

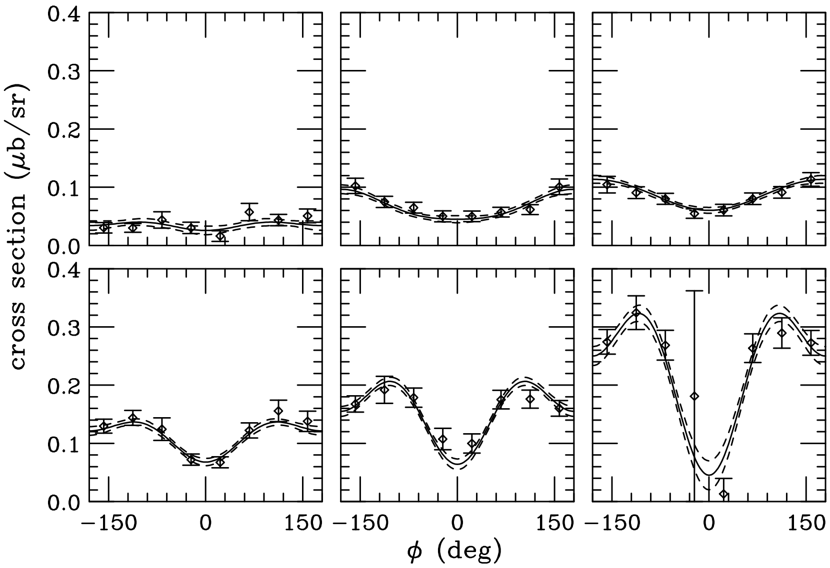

Figure 123: Fits to σ_0 versus ϕ for $\cos\theta_K^{cm}$ = -0.833, -0.50, -0.167, 0.167, 0.50, 0.833 (upper left to lower right), $W = 1.875$ GeV and $Q^2 = 0.7$ GeV^2 with $\chi^2/ndf = 0.99$.

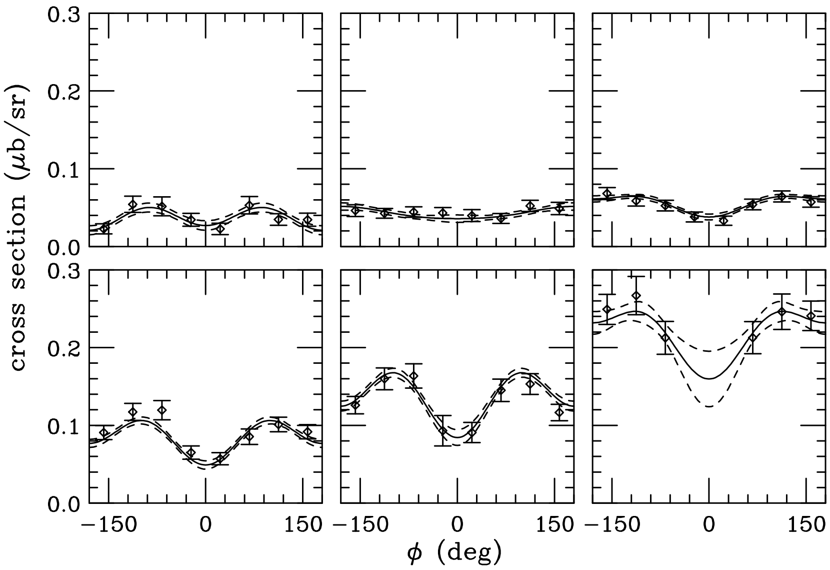

Figure 124: Fits to σ_0 versus ϕ for $\cos\theta_K^{cm}$ = -0.833, -0.50, -0.167, 0.167, 0.50, 0.833 (upper left to lower right), $W = 1.925$ GeV and $Q^2 = 0.7$ GeV^2 with $\chi^2/ndf = 0.86$.

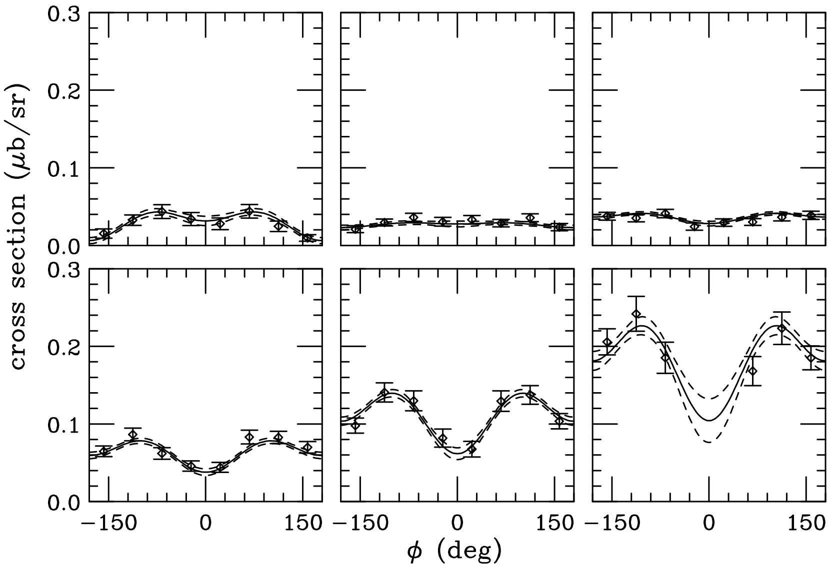

Figure 125: Fits to σ_0 versus ϕ for $\cos\theta_K^{cm}$ = -0.833, -0.50, -0.167, 0.167, 0.50, 0.833 (upper left to lower right), $W = 1.975$ GeV and $Q^2 = 0.7$ GeV^2 with $\chi^2/ndf = 0.91$.

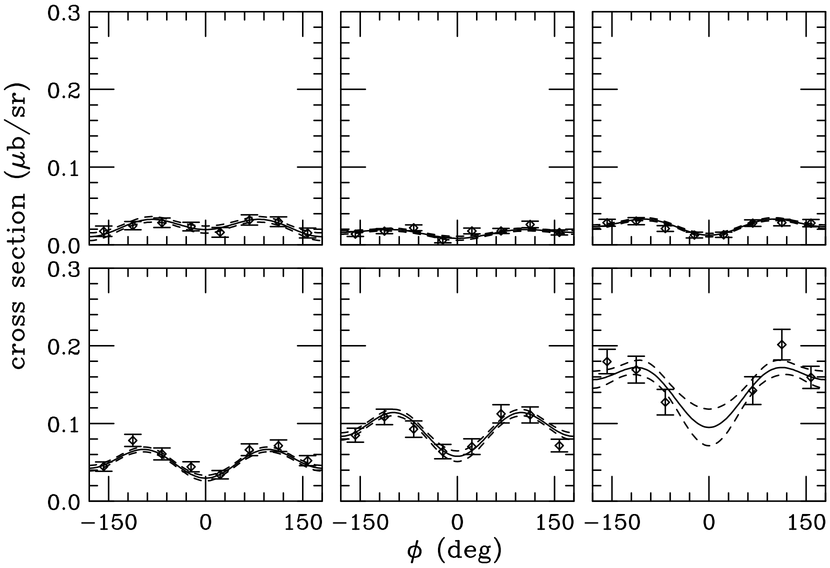

Figure 126: Fits to σ_0 versus ϕ for $\cos\theta_K^{cm}$ = -0.833, -0.50, -0.167, 0.167, 0.50, 0.833 (upper left to lower right), $W = 2.025$ GeV and $Q^2 = 0.7$ GeV^2 with $\chi^2/ndf = 1.20$.

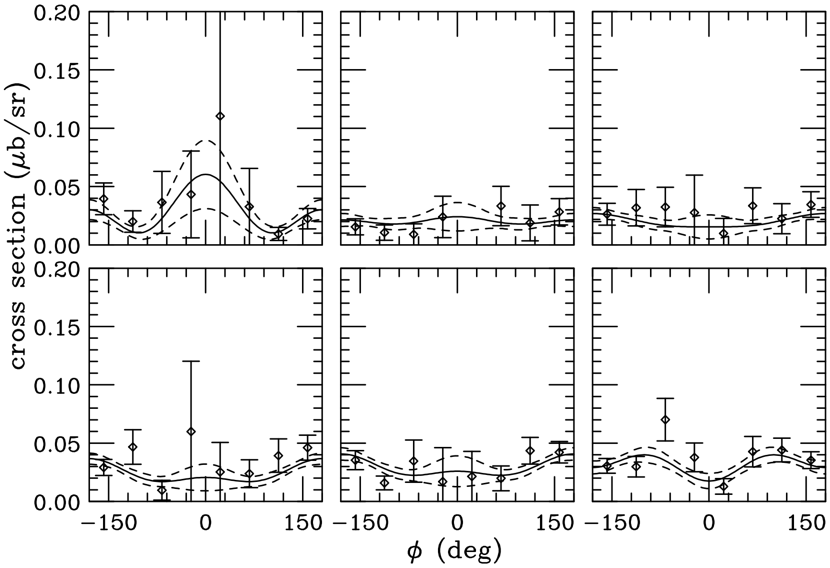

Figure 127: Fits to σ_0 versus ϕ for $\cos\theta_K^{cm}$ = -0.833, -0.50, -0.167, 0.167, 0.50, 0.833 (upper left to lower right), $W = 1.625$ GeV and $Q^2 = 1.1$ GeV^2 with $\chi^2/ndf = 0.97$.

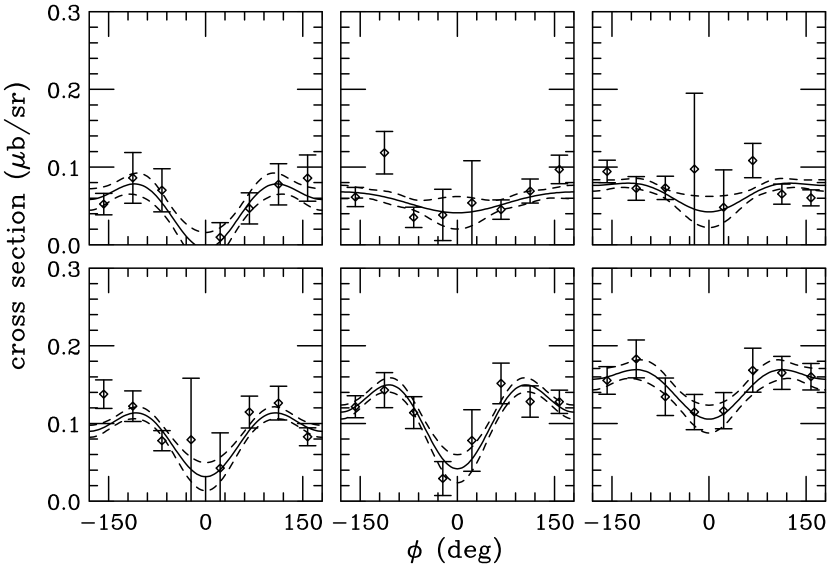

Figure 128: Fits to σ_0 versus ϕ for $\cos\theta_K^{cm}$ = -0.833, -0.50, -0.167, 0.167, 0.50, 0.833 (upper left to lower right), $W = 1.675$ GeV and $Q^2 = 1.1$ GeV^2 with $\chi^2/ndf = 1.03$.

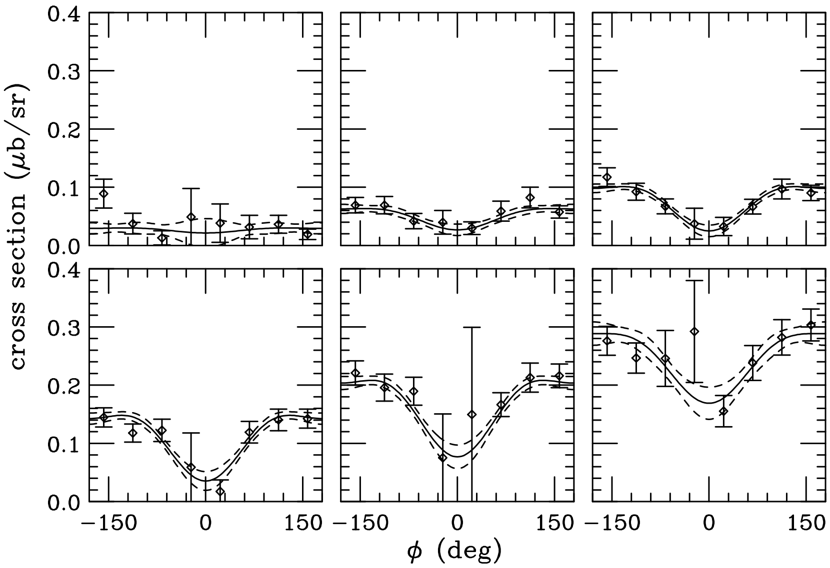

Figure 129: Fits to σ_0 versus ϕ for $\cos\theta_K^{cm}$ = -0.833, -0.50, -0.167, 0.167, 0.50, 0.833 (upper left to lower right), W = 1.725 GeV and Q^2 = 1.1 GeV^2 with χ^2/ndf = 0.82.

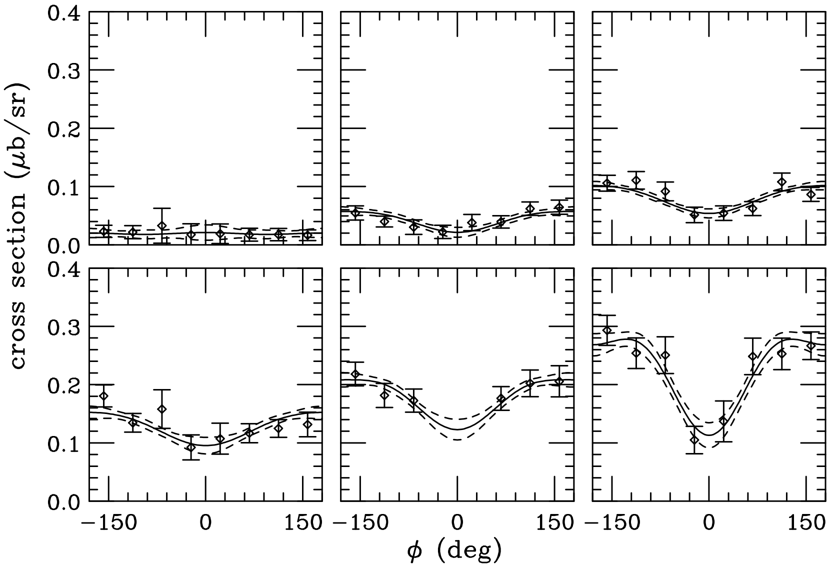

Figure 130: Fits to σ_0 versus ϕ for $\cos\theta_K^{cm}$ = -0.833, -0.50, -0.167, 0.167, 0.50, 0.833 (upper left to lower right), W = 1.775 GeV and Q^2 = 1.1 GeV^2 with χ^2/ndf = 0.72.

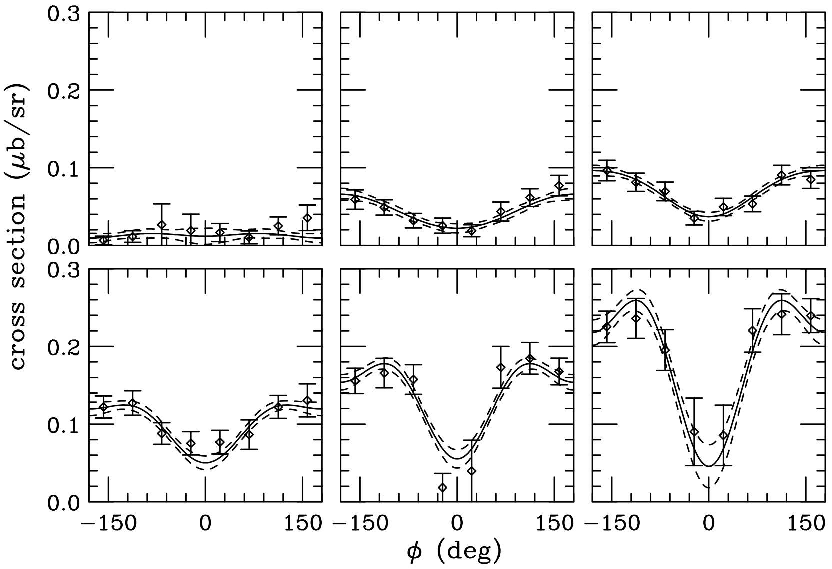

Figure 131: Fits to σ_0 versus ϕ for $\cos\theta_K^{cm}$ = -0.833, -0.50, -0.167, 0.167, 0.50, 0.833 (upper left to lower right), $W = 1.825$ GeV and $Q^2 = 1.1$ GeV^2 with $\chi^2/ndf = 0.81$.

G Fifth Structure Function Results

$\cos\theta_K^{cm}$	W (GeV)	$\sigma_{LT'}$ (nbarn/sr)	$\delta\sigma_{LT'}$ (nbarn/sr)
-0.833	1.625	2.421	9.021
	1.675	50.315	37.897
	1.725	15.137	20.883
	1.775	15.601	11.348
	1.825	4.560	8.669
	1.875	-2.824	9.998
	1.925	25.769	18.070
	1.975	14.613	12.890
	2.025	31.194	17.587
-0.500	1.625	7.471	16.674
	1.675	36.636	20.985
	1.725	69.791	16.879
	1.775	55.441	12.677
	1.825	49.245	17.821
	1.875	66.755	18.300
	1.925	29.453	10.085
	1.975	31.585	11.430
	2.025	16.293	9.295
-0.167	1.625	17.463	13.813
	1.675	65.378	14.758
	1.725	55.512	20.614
	1.775	48.509	17.804
	1.825	55.939	19.073
	1.875	68.560	11.069
	1.925	44.025	10.575
	1.975	16.725	11.722
	2.025	11.629	9.862

Table 25: Extracted $\sigma_{LT'}$ and total uncertainties for various kinematic bins at $Q^2 = 0.7$ GeV^2 (continued).

$\cos\theta_K^{cm}$	W (GeV)	$\sigma_{LT'}$ (nbarn/sr)	$\delta\sigma_{LT'}$ (nbarn/sr)
0.167	1.625	-3.155	10.754
	1.675	29.655	24.579
	1.725	50.233	25.397
	1.775	55.201	22.931
	1.825	19.794	21.881
	1.875	30.162	13.826
	1.925	11.655	17.352
	1.975	7.600	10.937
	2.025	6.278	11.607
0.500	1.625	2.043	9.620
	1.675	24.445	17.854
	1.725	8.144	31.489
	1.775	67.053	30.186
	1.825	40.919	15.643
	1.875	-8.037	18.644
	1.925	14.551	27.094
	1.975	8.368	19.880
	2.025	53.721	25.548
0.833	1.625	3.591	12.481
	1.675	13.779	30.336
	1.725	13.570	44.472
	1.775	57.600	42.674
	1.825	-18.853	42.938
	1.875	54.137	42.195
	1.925	4.417	37.673
	1.975	89.612	43.422
	2.025	-27.554	38.188

Table 26: Extracted $\sigma_{LT'}$ and total uncertainties for various kinematic bins at $Q^2 = 0.7$ GeV^2 (continued).

$\cos\theta_K^{cm}$	W (GeV)	$\sigma_{LT'}$ (nbarn/sr)	$\delta\sigma_{LT'}$ (nbarn/sr)
-0.833	1.625	3.360	5.906
	1.675	24.523	22.596
	1.725	5.214	9.325
	1.775	2.936	7.974
	1.825	6.675	9.070
-0.500	1.625	10.349	6.860
	1.675	27.287	10.755
	1.725	24.209	8.946
	1.775	16.678	9.437
	1.825	31.802	14.501
-0.167	1.625	-3.098	6.522
	1.675	38.759	14.060
	1.725	80.957	15.857
	1.775	40.532	16.616
	1.825	50.333	18.177
0.167	1.625	3.112	7.777
	1.675	22.803	17.894
	1.725	40.303	12.477
	1.775	23.776	21.484
	1.825	14.745	23.207
0.500	1.625	-7.465	9.322
	1.675	52.498	21.986
	1.725	-11.336	16.893
	1.775	15.033	25.767
	1.825	-18.034	29.930
0.833	1.625	-2.566	10.095
	1.675	-8.425	26.748
	1.725	-30.508	37.533
	1.775	45.350	33.937
	1.825	33.888	29.737

Table 27: Extracted $\sigma_{LT'}$ and total uncertainties for various kinematic bins at $Q^2 = 1.1$ GeV^2.

VITA

RAKHSHA NASSERIPOUR

Born In 1966, Tehran, Iran

2001-2004	Ph. D. Candidate (Physics), Florida International University.
1998-2001	M. Sc. (Physics), Florida International University.
1986-1990	B. Sc. (Applied Physics), Amir Kabir University of Technology, Tehran, Iran.
2001-	Member of American Physical Society (APS).
1999-	Member of Thomas Jefferson National Accelerator Facility User Group.
1999-	Term Member of CEBAF Large Acceptance Spectrometer (CLAS) Collaboration.
1999-	Participating in kaon electroproduction experiments and data analysis, Thomas Jefferson National Laboratory, Newport News, VA.
1999-	Research/Teaching assistant, Physics Department, Florida International University.
Aug. 2001	Intensive Teaching Workshop, The Academy for the Art of Teaching, Florida International University.
1990-1998	Gamma spectroscopy, nuclear detector calibration, radionuclidic quality control of radiopharmaceuticals, Radioisotope Department, Nuclear Research Center, Tehran, Iran.
Jan. 1992- **Sept. 1992**	Nuclear electronics and detectors training, Nuclear Research Center, Tehran, Iran.
Oct. 1990- **Feb. 1991**	Health physics and radiation protection training, Nuclear Research Center, Tehran, Iran.

CONTRIBUTED TALKS

1. Measurement of the Polarized Structure Function $\sigma_{LT'}$ for Kaon Electroproduction in the Exclusive $p(\vec{e}, e'K^+)\Lambda$ Reaction, Rakhsha Nasseripour and Brian A. Raue, **Bull. Am. Phys. Soc. 48** 9, 12 (2003).

2. Measurement of the Single Spin Asymmetry and Polarized Structure Function $\sigma_{LT'}$ for Kaon Electroproduction in the Exclusive $p(\vec{e}, e'K^+)\Lambda$ Reaction, Rakhsha Nasseripour and Brian A. Raue, **8th International Conference on Hypernuclear and Strange Particle Physics, Hyperon 2003** , Thomas Jefferson National Laboratory, October, 2003.

3. Kaon Electroproduction using CLAS at Jefferson Lab, Pawel Ambrozewicz, Rakhsha Nasseripour, and Brian Raue, **Bull. Am. Phys. Soc. 48** (2003).

4. Measurement of $A_{LT'}$ for $K\Lambda$ electroproduction with CLAS, Brian Raue, Rakhsha Nasseripour, and Daniel Carman, **Bull. Am. Phys. Soc. 47** 52 (2002).

5. Hyperon Double Polarization Observables from CLAS for $p(\vec{e}, e'K^+)Y$ Reaction, Daniel S. Carman, Matthias Mozer, Brian Raue and Rakhsha Nasseripour, **Bull. Am. Phys. Soc. 47** 52 (2002).

6. Single Spin beam asymmetry measurements for kaon electroproduction with CLAS, Rakhsha Nasseripour and Brian Raue, **Bull. Am. Phys. Soc. 46** 14 (2001).

7. Measurement of beam-helicity dependent asymmetries for $p(\vec{e}, e'K^+)\Lambda$ with CLAS, Brian Raue, Rakhsha Nasseripour, and Daniel Carman, **Bull. Am. Phys. Soc. 46** 36 (2001).

8. Polarization Measurements and Systematic Studies for the Hall B Møller Polarimeter, Rakhsha Nasseripour, Brian Raue, Laird Kramer, Fernanda Foertter, **Bull. Am. Phys. Soc. 45** 91 (2000).

9. Hyperon Double-Polarization Observables from CLAS for the $p(\vec{e}, e'K^+)Y$ Reaction, Daniel S. Carman, Brian A. Raue, Rakhsha Nasseripour, and Kyungseon Joo, **Bull. Am. Phys. Soc. 45** 86 (2000).